Mechanisms of Carbide Precipitation and Carbon Solubility in High Nb Containing TiAl Alloys

Von der Fakultät für Maschinenbau, Elektrotechnik und Wirtschaftsingenieurwesen
der Brandenburgischen Technischen Universität Cottbus zur Erlangung des
akademischen Grades eines Doktor-Ingenieurs
genehmigte Dissertation

vorgelegt von

Master of Engineering

Li Wang

Geboren am 29. Mai 1986 in Hunan, China

Vorsitzender: Prof. Dr. Sabine Weiss

Gutachter: Prof. Dr. Florian Pyczak

Gutachter: Prof. Dr. Helmut Clemens

Tag der mündlichen Prüfung: 23. Mai 2014

Acknowledgements

There are many people I would like to thank for their contributions and efforts to this PhD thesis.

I would first like to express my sincere appreciation to Prof. Florian Pyczak, head of Material Physics department in Helmholtz-Zentrum Geesthacht for accepting me as a PhD student and for his instructions and continuous support on my PhD work in Helmholtz-Zentrum Geesthacht, and also for his patience, trust and encouragement during the whole PhD study. His easy-going, thoughtful consideration and enthusiasm on the project make me feel comfortable and I cannot image a much better advisor.

My regards also to Prof. Helmut Clemens for being a reviewer of my thesis and defense, and for his valuable suggestion and encouragement. Many thanks to Prof. Sabine Weiss to be the chairman of my defense committee and for her valuable feedback.

I am also very grateful to Dr. Heike Gabrisch for her instructions on TEM investigations and suggestions during discussions. Many thanks I would like to give to Dr. Andreas Stark for his help in doing HEXRD experiments and his suggestions on analyzing and discussing HEXRD data. My heartfelt thanks to Dr. Jonathan Paul for his unconditional help and suggestions on my PhD work, and also for his efforts to modify the English of the thesis. Very particular thanks are to Dr. Michael Oehring for his sincere help in experiments and discussions on the experiment results. I am deeply grateful to Uwe Lorenz for his help on experiments and support during my whole stay in Helmholtz-Zentrum Geesthacht. My sincere gratitude also belongs to Dr. Frank-Peter Schimansky for making the primary materials for my work and suggestions during the discussion. I am very thankful that Dr. Ulrich Fröbel provides help on TEM operations and suggestions for the experiments. Many thanks to Stefan Eggert for his help in preparing TEM specimens, to Dirk Herrmann for making primary materials for my work, and to Dr. Fritz Appel for his comments on results. Many thanks also to other colleagues in our department and in Helmholtz-Zentrum Geesthacht.

I sincerely thank Prof. Yong Liu (Central South University) for his selfless help and encouragement.

The CSC-Helmholtz program is much acknowledged for funding my PhD work in Helmholtz-Zentrum Geesthacht.

Finally yet also importantly, I would like to thank my parents for giving my birth, developing me and educating me. Without them I will have no chance to go abroad and to do what I am interested in. I also thank my boyfriend, my brother and sister-in law, and all my friends for giving me help and encouragement.

Abstract

TiAl alloys with a high addition of Nb have recently been applied in the aerospace and automotive fields due to their excellent high-temperature properties. The C additions to TiAl alloys have been reported to improve their strength and creep resistance through solid-solution hardening and / or precipitation hardening. In this work powder metallurgy (PM) based Ti-45Al-5Nb-xC (x=0, 0.5 0.75 and 1.0 at. %) alloys were systematically investigated after different heat treatments. The research is mainly concerned with the temperature range from 800 to 1000ºC which is interesting for processing as well as applications. The results show that the addition of C influences the phase transformations in Ti-45Al-5Nb and that the addition of Nb may influence the carbon solubility in TiAl alloys at high temperatures. The carbon solubility in Ti-45Al-5Nb is > 1.0 at. % at 1400°C, but between 0.5 and 0.75 at. % at 1000°C, and less than 0.5 at. % at 800°C. The carbide precipitation and development of carbide morphology are discussed in great detail. The thermal stability of P-Ti_3AlC carbides in Ti-45Al-5Nb-xC alloys is increased, which might be attributed to the addition of high amounts of Nb, or the high amount of carbon, or a combination of both. In heat-treated Ti-45Al-5Nb-0.5C and Ti-45Al-5Nb-0.75C, H-type carbides are not detected to form during annealing. The addition of Nb may increase the formation temperature of the H-Ti_2AlC precipitate phase.

Zusammenfassung

TiAl-Legierungen mit hohem Nb-Gehalt werden in letzter Zeit für Anwendungen in der Luftfahrt und dem Automobilbereich eingeführt. Dabei profitieren sie von ihren exzellenten Hochtemperatureigenschaften. In der Literatur wird berichtet, dass sich durch die Zugabe von Kohlenstoff die Festigkeit und der Kriechwiderstand weiter steigern lässt, wobei Kohlenstoff entweder als Mischkristallhärter oder über die Ausscheidung von Karbiden wirkt. In dieser Arbeit werden pulvermetallurgisch hergestellte TiAl-Legierungen der Zusammensetzung Ti-45Al-5Nb-xC (x=0, 0.5 0.75 und 1.0 at. %) systematisch im Anschluss an verschiedene Wärmebehandlungen untersucht. Der wichtige Temperaturbereich liegt dabei zwischen 800 und 1000°C, da dies typische Temperaturen in der Anwendung und für Wärmebehandlungen sind. Es zeigte sich, dass Kohlenstoff die Phasenübergänge in Ti-45Al-5Nb beeinflusst und dass die Zugabe von Niob Auswirkungen auf die Kohlenstofflöslichkeit bei hohen Temperaturen haben kann. Die Kohlenstofflöslichkeit in Ti-45Al-5Nb ist größer als 1.0 at. % bei 1400°C, aber nimmt auf 0.5 bis 0.75 at. % bei 1000°C ab und weniger als 0.5 at. % ist bei 800°C löslich. Die Ausscheidungssequenz von Karbiden sowie die Entwicklung der Karbidmorphologie werden im Detail diskutiert. Die thermische Stabilität von P-Ti_3AlC Karbiden in Ti-45Al-5Nb-xC Legierungen ist erhöht, was ein Effekt des hohen Niobgehaltes oder des hohen Kohlenstoffgehaltes oder eine Kombination von beiden sein kann. Nach der Wärmebehandlung wurden keine H-Karbide mehr in Ti-45Al-5Nb-0.5C und Ti-45Al-5Nb-0.75C gefunden. Die Zugabe von Nb erhöht vermutlich die Bildungstemperatur der H-Ti_2AlC Karbidphase.

1. Introduction

With the development of aerospace science, researchers are paying more and more attention to the study of high-temperature engineering materials. In order to reduce the weight of components and thus improve the energy efficiency of new engines, highly advanced new materials are required. The service temperature and air compression ratio of aero-engines are directly related to the consumption rate of fuel and the thrust of engines. Improved engines efficiency can be achieved by increasing the temperature within the combustion chambers to obtain a higher combustion efficiency. Alternatively reducing the weight of components to decrease engine weight will increase the thrust to weight ratio. Advanced aerospace engineering materials are required to meet the following properties: high strength and low weight, high fatigue strength, high creep resistance, high fracture toughness and excellent oxidation resistance.

In intermetallic compounds the bonds have both metallic and covalent character and thus exhibit high strength, high creep resistance, high-temperature microstructure stability as well as high elastic modulus. Therefore they have the potential to be used as high-temperature materials. Over the past few decades the research on intermetallic compounds such as A_3B and AB types in Ni-Al, Ti-Al and Fe-Al systems, has made significant progress (Yamaguchi 2000). γ-TiAl alloys are considered as an ideal aerospace structural material because they meet the above mentioned requirements for high-temperature engineering materials (Kim 1991, Kim 1994, Kim 1995, Kim 1995, Dimiduk 1999, Yamaguchi 2000).

Table 1 Properties of potential advanced high-temperature alloys for jet engines (Kumpfert 2005)

	Near-α Ti	Ni-base	γ-TiAl
Density	+	-	++
Specific tensile strength	+	-	+/-
High-temperature Young's modulus	+/-	+	++
Room-temperature ductility	+	+	-
Formability	+	+	-
Creep resistance	-	++	++
Room-temperature fracture toughness	+	++	-
Room-temperature crack growth	+	+	-
Specific fatigue strength	+	-	+/-
Oxidation resistance	-	++	++
High-temperature embrittlement	-	+	+/-

Table 1 (Kumpfert 2005) and **Figure 1** (Dimiduk 1999, Appel 2011) show the comparison between γ-TiAl alloys and other high-temperature alloys. Compared with Ni-Al, Ti, and Ni-base alloys, the γ-TiAl alloys have high specific modulus (modulus divided by density) over the temperature range from 300 to 1100K. The specific strength also exceeds those of Ti and superalloys over the corresponding temperature

range. Meanwhile γ-TiAl alloys exhibit excellent creep and oxidation resistance. From this data, it can be seen that γ-TiAl alloys have great advantages compared to other high-temperature alloy systems except for the low room-temperature ductility and fracture toughness (Kim 1989, Liu 1996).

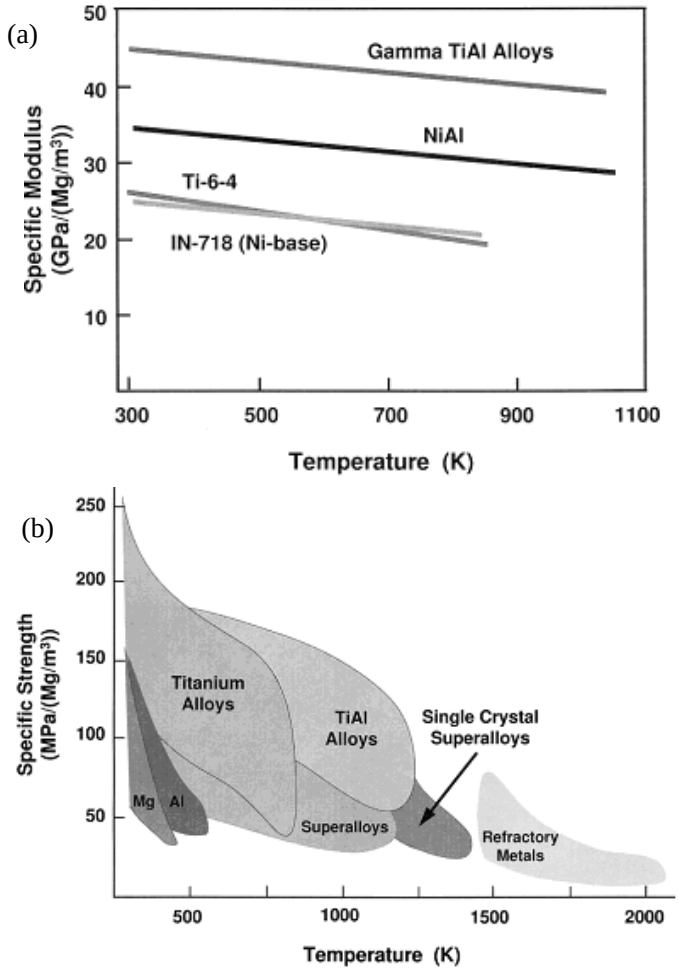

Figure 1 Comparison of (a) Specific modulus and (b) Specific strength between γ-TiAl alloys and other structural materials as a function of temperature (Dimiduk 1999). The data indicates that TiAl alloys possess advantages compared with other structural materials.

1.1 Development and application of TiAl alloys

The first report on the mechanical properties of TiAl alloys traces back to the 1950's. At that time McAndrew and Kessler (McAndrew 1956) found that the as-cast binary TiAl alloys possessed good oxidation resistance and high-temperature strength. However due to their low room-temperature ductility and fracture toughness, these alloys did not attract broad interest from researchers towards industrial application for a long period. Up to now TiAl based alloys have developed over three generations. The chemical compositions of such alloys can be summarized as Ti-(42-49)Al-(0-4)Cr, Mn, V-(0-10)Nb, Ta, W, Mo-(0-1)Si, B, C (in atomic percent, at. %) (Appel 2000).

A representative of the first generation of TiAl based alloys is the Ti-48Al-1V-0.3C (at. %) alloy developed by the US Air Force Materials Lab and Pratt & Whitney (P&W) between 1975 and 1983 (Blackburn 1981, Blackburn 1982). Its ductility reached 1.5%, but the comprehensive performance could not meet the requirements for an aerospace engine. Thus the development was limited to laboratory research.

Considered as a second generation alloy, as-cast Ti-48Al-2Cr-2Nb (at. %) developed by General Electric (GE) (Huang 1991) had better room temperature ductility, strength and oxidation resistance than Ti-48Al-1V-0.3C (at. %). However this alloy showed poor tensile properties at room temperature for a coarse-grained fully lamellar microstructure (Kim 1992, Kim 1995). Other examples of second-generation TiAl alloys are γ-TAB: Ti-47Al-4(Nb, Mn, Cr, Si, and B) (at. %) developed by Helmholtz-Zentrum Geesthacht (HZG, previously called GKSS) (Çam 1996) and γ-Met Ti-46.5Al-4(Cr, Nb, Ta, and B) (at. %) designed by Plansee (Clemens 1999). Such alloys exhibited outstanding high-temperature properties at 760°C (specific stiffness, high-temperature strength, creep resistance, oxidation resistance and corrosion resistance), which were better than or equaled to those of high-temperature Ni-based alloys (Appel 2000).

Recently, research on alloy design, manufacturing and processing of TiAl based alloys resulted in significant achievements with the so-called third generation alloys which have improved yield strength, creep strength and oxidation resistance at higher temperatures. The representative alloys are γ-TNB (Ti-45Al-(5-10)Nb-x(C, B), at. %) alloy designed by HZG (Appel 2000) and γ-TNM (Ti-(42-45)Al-(3-5)Nb-(0.1-2)Mo-(0.1-0.2)B, at. %) alloy developed by MUL (Montan Universität Leoben) (Chladil 2006, Clemens 2008). For example, hot extruded Ti-45Al-(5-10)Nb alloy had a room-temperature tensile strength over 1100MPa and a plastic fracture strain more than 2% (Kestler 2005, Appel 2011). The addition of carbon in this alloy improved the creep resistance via the precipitation of P-Ti_3AlC carbides.

Current worldwide research on TiAl alloys shows several tendencies: (1) development of new TiAl intermetallic alloys with a higher melting point for applications up to around 900°C, mainly with Nb, W, Mo and Ta additions (Appel 2000); (2) development of γ-TiAl composites, usually incorporating SiC, Al_2O_3 fibers or TiB_2, TiC strengthening phases to enhance the γ-TiAl matrix (Wrzesinski 1990, Rao 2000, Djanarthany 2001, Wu 2013); (3) optimizing the microstructure and mechanical properties of TiAl alloys by (a) adding light elements, such as a B to refine the microstructure (Hu 2001), adding Si and C to improve the creep resistance by precipitation hardening and solid-solution hardening (Kim 1989, Tian 1993, Noda 1995, Tian 1997), combined with (b) advanced hot processing together with subsequent heat treatments (Liu 1996, Clemens 2000, Tetsui 2003, Gerling 2004, Huang 2005); (4) development of new forming technologies, such as metal powder injection molding (MIM) (Terauchi 2000, Gerling 2001, Gerling 2006, Zhang 2009) and spark plasma sintering (SPS) (Matsugi 1996, Molénat 2007, Jabbar 2010, Guyon 2013, Kennedy 2013, Voisin 2013).

In view of the performance characteristics of TiAl alloys, they have application prospects in aircraft engines (Kestler 2005). In 1992 MTU Aero Engines GmbH (Germany) successfully conducted the first spin test of an as-cast γ-TiAl blade in a low pressure turbine at 700°C and with 16000rpm (Smarsly 1994). In 1993 the first engine test of γ-TiAl alloys was conducted by General Electric (Austin 1995). A full set of 98 low pressure turbine blades were installed in a CF-80C2 engine which is used in large commercial aircraft. The blades were produced by Howmet with an actual composition of Ti-46.5Al-2Cr-2Nb (at. %). The test included over 1000 simulated flight cycles as part of a normal endurance test, which was considered as a milestone in the development history of TiAl alloys. Recently Bewlay et al. (Bewlay 2013) reported that the GEnx^{TM} engine was equipped with γ-TiAl blades which resulted in a 20% reduction in fuel consumption, a 50% reduction in noise, and an 80% reduction in NOx emissions compared with prior engines in its class. Up to now, over 40,000 TiAl low-pressure turbine blades have been manufactured for the GEnx^{TM} 1B (Boeing 787) and the GEnx^{TM} 2B (Boeing 747-8) engines.

TiAl alloys can be also applied in the automotive field and have been used to make turbocharger wheels (Noda 1998, Tetsui 1999, Tetsui 2001, Tetsui 2002, Jovanović 2005, Tetsui 2012). The first commercial turbocharger application of TiAl alloys was in a Mitsubishi sports car in 1999 (Tetsui 1999). Tetsui (Tetsui 2007) developed an optimized TiAl alloy composition for turbocharger applications which had excellent creep strength and low manufacturing costs. The application temperature was higher than that of an Inconel 713C turbocharger, and the cost was decreased compared with other TiAl turbochargers. Due to their approximately half less density and higher elevated temperature strength than steel, TiAl alloys have another ideal application in exhaust engine valves (Keller 1997, Eylon 1998, Badami 2006, Gebauer 2006, Fu 2008). An engine test conducted by Blum et al. (Blum 1999) in a 4 cyclinder/16 valve BMW-engine showed all TiAl valves completed the test successfully.

In a summary, TiAl alloys have broad application in aerospace and automotive fields. They attract great interest from researchers as light-weight and high-strength structural materials.

1.2 Overview: optimization of microstructure and properties of TiAl alloys

At present there are three main routes to optimize the microstructure and properties of TiAl alloys.

(1) Through optimizing the procedure to manufacture raw materials.

Up to now the main manufacturing processes for TiAl alloys are generalized as ingot metallurgy (IM) and powder metallurgy (PM) (Kim 1994, Clemens 2000). The microstructure produced by IM usually has a large grain size, porosity and severe elemental segregation (Clemens 2000). Further heat treatments should be applied to refine the microstructure (Kim 1994, Clemens 1995). Compared with IM, PM can manufacture TiAl alloys with uniform composition, fine grains, and low defects. As a

consequence PM TiAl alloys can be further hot processed without prior homogenizing heat treatments (Clemens 1999). The primary material is pre-alloyed powders. **Figure 10** in **Section 2.1** shows the Plasma Melting Inert Gas Atomization (PIGA) equipment in HZG which is used to produce pre-alloyed TiAl powders in large quantities by means of argon gas atomization under high pressure. HIPing is the most effective consolidation processes to manufacture PM TiAl billets. There also exist other PM technologies. Metal powder injection molding (MIM) for example has the obvious advantage that near-net shape manufacture of TiAl based components is possible (Merhar 1990, Gerling 2001, Gerling 2002, Gerling 2006). Additionally the spark plasma sintering (SPS) process is now considered as a promising route because it can develop TiAl alloys with fine microstructure and properties (Molénat 2007, Couret 2008, Lu 2009, Jabbar 2011). However, these two latter powder techniques are under development and need further research.

(2) Through thermo-mechanical processing & subsequent heat treatments.

The thermomechanical processing commonly applied to develop TiAl alloys includes isothermal forging, hot-pack forging, hot extrusion, isothermal rolling and hot-pack rolling et al. (Liu 1996, Liu 1998, Clemens 1999, Clemens 2000, Tetsui 2003, Huang 2005, Tetsui 2005, Appel 2006, Chaudhari 2010, Wang 2011). After thermo-mechanical processing and subsequent heat treatments (parameters based on practical requirements to get the ideal microstructure), the microstructures are refined and properties are optimized. This makes the final shaping technique being implemented easily, such as sheet rolling, superplastic deformation, and near-net isothermal forging. Hot rolling has been applied by Gerling et al. (Gerling 2004) to produce TiAl sheets with dimensions of approximately 600×300×1 mm^3 successfully. The canned HIP compacts were multi-pass rolled at Plansee AG within the (α+γ) phase field, and subsequently the sheets were heat treated at 1000°C for 3h under vacuum condition to stabilize the microstructure and reduce the residual stress. The resulting near γ microstructure had a very fine grain size of about 5μm. The yield strength could reach 750MPa and plastic elongation was up to 2% at room temperature. At 1000°C the ultimate tensile strength was around 85MPa and the elongation was about 93%.

(3) Through control of microstructure and mechanical properties via composition.

The ductility of binary TiAl alloy at room temperature varies as Al content changes and reaches maximum at an Al concentration of 48 at. % (Kim 1989). However, the creep properties and oxidation behavior of these alloys cannot meet the requirements for application. Thereby other ternary or quaternary elements are added to further modify the microstructure and properties. Based on a huge amount of research, the addition elements can be divided into three types in terms of their effects on properties:

- Cr, V and Mn strengthen TiAl alloys by substitutional solid solution (Kim 1994, Kawabata 1998). They also increase the ductility of TiAl alloys. Cr improved the

ductility by decreasing the tetragonality and thus reducing the difference in mobility between ordinary dislocations and superdislocations (Kawabata 1993). The ductility refinement of V was caused by the modification of the TiAl bonds and the promotion of twin formation (Huang 1991). Mn increased the ductility of TiAl based alloys at room temperature via microstructural refinement and easier twinning formation (Hashimoto 1990).

- W, Nb, Mo, and Ta slow down the kinetics of phase transformations and greatly improve the strength and the creep resistance (Shida 1993, Tetsui 1999, Appel 2000, Chen 2002, Hodge 2004). Nb also reduces the stacking fault energy and thus improves the ductility of the alloys at room temperature through increased activity of mechanical twinning (Woodward 1992, Zhang 2002, Yuan 2006). Moreover Nb can significantly improve the oxidation resistance by retarding the diffusion process and modifying the structure of the oxidation layer (Yoshihara 1995). Ta is effective in improving the oxidation resistance of TiAl based alloys (Vojtěch 2011).

- B, Si, and C can improve the strength and creep resistance. Boron addition of 0.1 to 1.0 at. % can refine the microstructure by the formation of borides at grain boundaries confine grain growth (Larsen 1991, Hu 2001, Gosslar 2010) or by borides acting as inoculants for α grains in the β/α transformation (Hecht 2008). Small amounts of Si can increase both creep resistance and oxidation behavior. However, the fraction of Si should be in the range of 0.2-0.65 at. %, otherwise the microstructure loses thermal stability (Kim 1989, Kim 1994). C and Si can form strengthening phases, such as Ti_3AlC and Ti_5Si_3, which prevent dislocation gliding and grain boundary sliding and thus improve the creep resistance (Nemoto 1992, Noda 1995, Tian 1995, Worth 1995, Christoph 1997, Tian 1997, Gouma 1998, Gouma 1998, Karadge 2003).

In order to improve the capabilities of γ-TiAl alloys towards higher temperatures, more attention is concentrated on the high Nb containing as well as carbon doped TiAl alloys (Noda 1998, Appel 2000, Clemens 2000). Thus the effects of Nb and C additions in TiAl alloys will be described separately in the following sections.

1.3 Nb additions to TiAl alloys

The early research by Huang (Huang 1993) and Chen et al. (Chen 1993, Chen 2002, Liu 2002, Zhang 2002) suggested that a high Nb addition up to 10 at. % could achieve significant strengthening in the Ti-45Al alloy at both room temperature and high temperatures. From the systematic research of Paul and Appel et al. (Paul 1998, Appel 2000), these high Nb containing TiAl alloys showed a good balance of properties and excellent oxidation behavior at elevated temperatures (Yoshihara 1995, Taniguchi 1998, Lin 2011). Thus they have potential to expand the application range of TiAl based alloys towards higher temperatures.

1.3.1 Influence of Nb on the Ti-Al phase diagram

Chen et al. (Chen 1999) studied the influence of Nb additions on the phase transformations in TiAl alloys, as shown in the phase diagrams (**Figure 2**). It should be noted that these phase diagrams might be a little different from the thermodynamic equilibrium condition due to the limited heat treatment times.

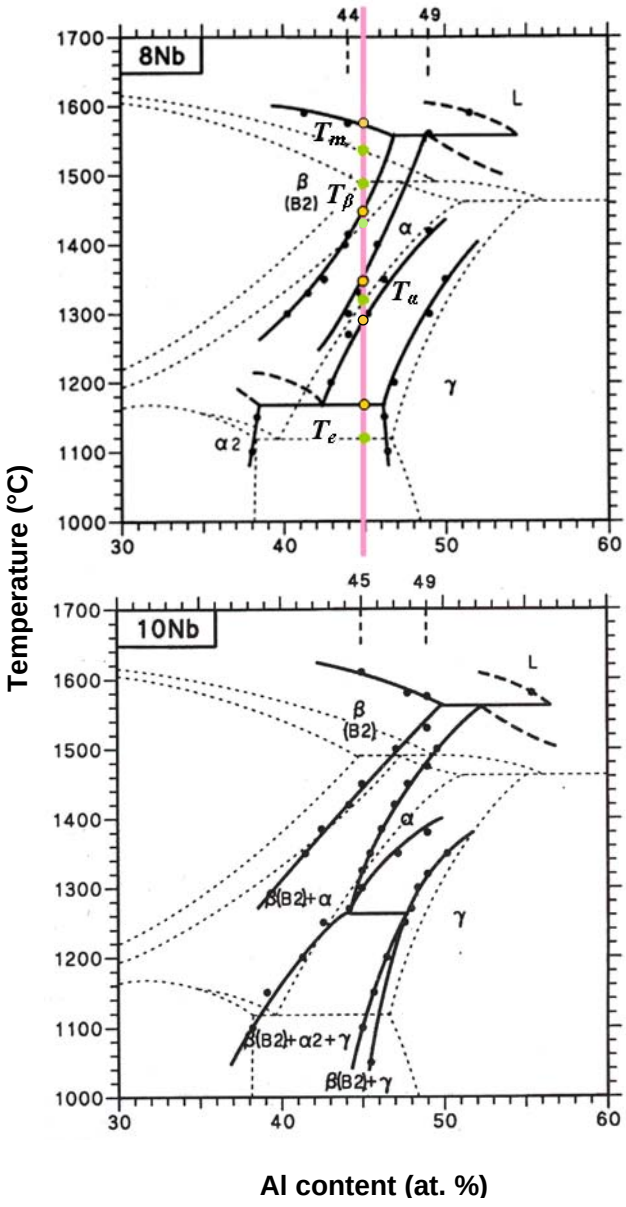

Figure 2 Quasi-binary phase diagrams showing the influence of 8 and 10 at. % Nb additions on the Ti-Al phase diagram. The reference Ti-Al phase diagram is displayed with dotted lines and the TiAl-8Nb and TiAl-10Nb phase diagrams are shown with solid lines. Due to the limited heat treatment times these phase diagrams might differ from the thermodynamic equilibrium condition (Chen 1993, Chen 1999).

An 8-10 at. % Nb addition to TiAl alloys had pronounced effects on the phase relationships (Chen 1999): (1) at high temperatures the phase fields were shifted to a higher Al content, (2) the α phase field, and (β+α) and (α+γ) two phase regions got narrower; (3) the melting point was increased about 100°C; (4) the transformation

temperature from α phase to γ phase (T_α) was decreased, while the transformation temperature from α phase to α_2 phase (T_e) was increased; and (5) the B2 phase could be stabilized at low temperatures when the Nb concentration exceeded 9.5 at. %. The recent study of Chladil et al. (Chladil 2006) on Ti-45Al-5Nb and Ti-45Al-7.5Nb showed a similar tendency that Nb increased the eutectoid temperature (T_e). In contrast, it indicated little influence on the α-transus temperature (T_α).

1.3.2 Strengthening effects of Nb additions in TiAl alloys

From the research of Paul and Appel et al. (Paul 1998, Appel 2000) on Ti-45Al-10Nb (at. %) alloy extruded at 1300°C, the yield strength could reached levels above 1000MPa at room temperature and 679MPa at 700°C. However for Ti-48.5Al-2Cr-0.2C (at. %) extruded at the same temperature, its yield strength was somewhat lower, 578MPa at room temperature and 485MPa at 700°C. When considering the specific yield strength, as displayed in **Figure 3**, Ti-45Al-10Nb showed impressive tensile properties. Over the whole temperature range from 25 to 800°C, Ti-45Al-10Nb had significantly higher specific yield strength than traditional TiAl alloys, such as Ti-48.5Al-2Cr-0.2C and Ti-47Al-2Cr-0.2Si, at. %. Additionally the specific yield strength of the Ti-45Al-10Nb alloy also exceeded those of high-temperature Ti alloys and superalloys up to 750°C.

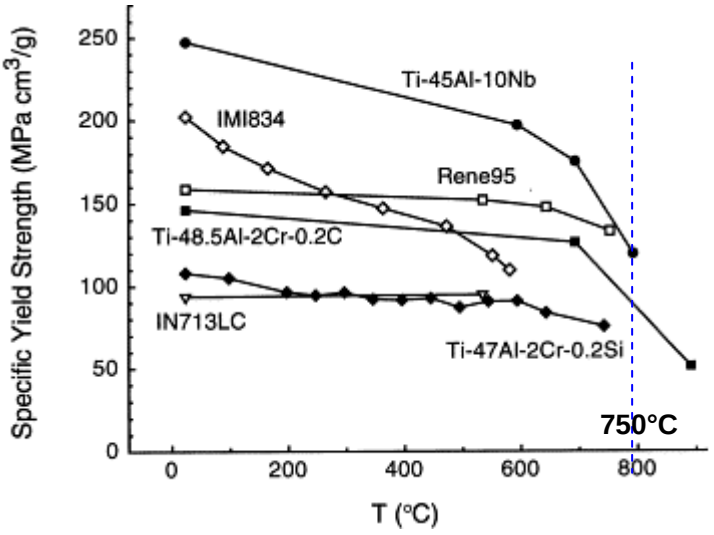

Figure 3 Specific yield strength as a function of temperature for selected TiAl alloys and other commercially available high-temperature alloys. Ti-45Al-10Nb and Ti-48.5-2Cr-0.2C were extruded at 1300°C. The Ti-47Al-2Cr-0.2Si alloy was isothermally forged and transformed to a fully-lamellar microstructure (Appel 2000).

The strengthening mechanism could be partly attributed to an increase of the α_2 lamellae fraction and the refinement of lamellar spacing by the high Nb additions. The high density of lamellar interfaces could impede dislocation gliding. However solid-solution hardening, caused by the very small lattice misfit between Ti and Nb atoms and the short-range dislocation interaction with solute Nb atoms, was relatively small and not important (Appel 2000). Furthermore the addition of Nb decreases the stacking fault energies of TiAl alloys. Thus mechanical twinning is relatively easy in

high Nb containing TiAl alloys, which reduces the plastic anisotropy. All the above mentioned mechanisms help to explain why optimized Nb containing TiAl alloys show room-temperature tensile yield strengths above 1000MPa and elongations of 2-3% which are by 1% higher than those of other traditional alloys tested under the same parameters (Appel 2003). Tracer measurements for Nb solute diffusion in TiAl alloys suggested that Nb was a slow diffuser (Herzig 2001). This means that diffusion-assisted dislocation climbing might be impeded in these alloys, which explains why these alloys possess high yield stresses and excellent creep resistance at elevated temperatures. However from the research on the diffusion of Ti and Nb atoms in binary and ternary high Nb containing TiAl alloys by Divinski et al. (Divinski 2005), it was shown that diffusion of Ti and Nb atoms was faster in ternary alloys than that in binary TiAl alloys at $T > 1000$K. This is believed to be due to the elastic distortion of the $L1_0$ structure of the γ phase introduced by Nb alloying. The superior creep resistance of TiAl-10Nb alloys may be related to the reduced bulk diffusion at low temperatures.

High Nb additions to TiAl alloys can also improve their oxidation resistance. According to the research of Lin et al. (Lin 2011), TiAl-8Nb (at. %) alloy showed much better oxidation resistance than binary TiAl alloys at 900°C for 100h for the following reasons: (1) Nb could suppress the growth of a porous TiO_2 layer and the formation of a (Ti, Nb)O_2-rich layer was much denser and more protective, (2) Nb reduced the critical Al content required to form a dense external alumina by changing the activities of Ti and Al atoms, and (3) Nb slowed down the diffusion of atoms and the oxidation process.

1.4 C additions to TiAl alloys

As mentioned above, in order to improve the mechanical properties, especially the creep resistance, some light elements, such as Si and C, are added in TiAl alloys. From literature it is known that carbon occupies the interstices in crystal lattices of the α_2 and γ phases. When the carbon concentration exceeds the solid solubility in the matrix, carbides will precipitate.

1.4.1 Carbide types and morphologies in TiAl alloys

To date two types of carbides are reported to be effective for improving the mechanical properties of TiAl alloys. These are Perovskite P-type carbides (Ti_3AlC, space group Pm-3m, a=4.162Å) and hexagonal H-type carbides (Ti_2AlC, space group $P6_3/mmc$, a= 3.056Å and c=13.62Å) (Schuster 1980). P-type carbides have a similar crystal structure to the γ-TiAl phase, as shown in **Figure 4(a)**. It can be formed from the $L1_0$ γ-TiAl unit cell by simply replacing the base-centered Al atoms with Ti atoms, together with the carbon atoms being situated in the Ti_6 octahedral interstices. Usually the formula of P-type carbides is taken as Ti_3AlC, but in fact carbon atoms do not occupy fully all the interstices. This is why in ref. (Pietzka 1994), the formula Ti_3AlC_{1-x} ($0<x<1$) was proposed for P-type carbides. H-type carbides have a more

complicated structure, as described in **Figure 4(b)**. The close-packed Ti and Al atom layers alternately stack along the c-axis. Carbon atoms are located at the octahedral interstices with a repeating distance of c/2 (Xiao 1992).

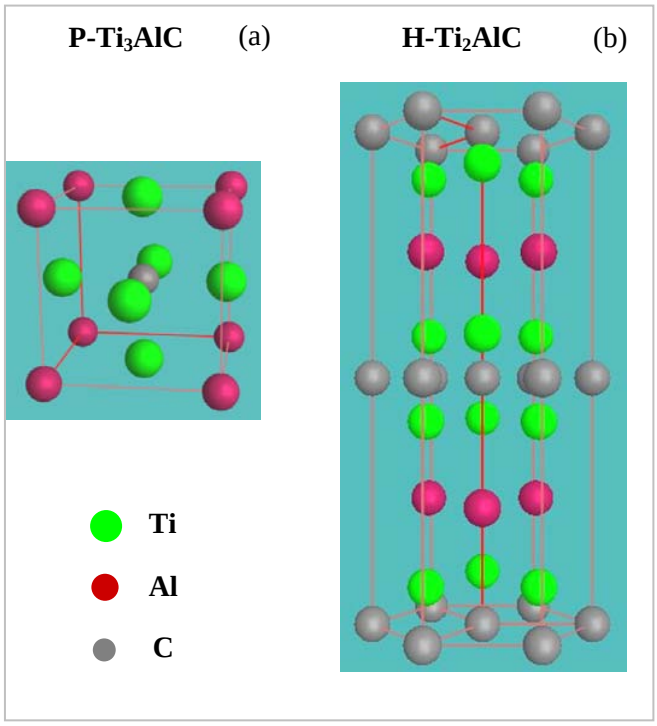

Figure 4 Crystal structures of (a) P-Ti_3AlC and (b) H-Ti_2AlC carbides.

There are many reports about the formation of carbides in various TiAl alloys (mainly Nb free or low Nb containing TiAl alloys). Tian et al. (Tian 1993, Tian 1997) reported that in TiAl alloys with 0.5 mol % carbon, P-type carbides appeared in the γ matrix as a needle-like morphology after aging at 800 and 900°C for various periods. As shown in **Figure 5(a)**, the carbides exhibited needle-like projections viewed from the [100] direction and dot-like cross sections in [001] direction. Long-range carbon-vacancy ordering even existed in the perovskite carbides and two ordered domain variants coexisted in a single needle at 800°C. After aging at higher temperatures or for longer periods at 800°C, plate-like H-type carbides formed. In Ti-(48-50)Al-2.1Nb and Ti-(48-50)Al-2.6V (at. %) alloys with a carbon content of 600-700 at. ppm investigated by Chen et al. (Chen 1992), P-type carbides formed at grain boundaries, at dislocations and in the γ matrix at 750 and 815°C. H-type carbides were also found to nucleate at grain boundaries and formed at dislocations in the γ matrix at the expense of P-type carbides at 750 and 815°C after 168h. They eventually replaced P-type carbides completely after 264h at 850°C and 168h at temperatures above 900°C. The orientation relationship of carbides with the γ matrix was reported as (Chen 1992):

$$[100]_P//[100]_\gamma \text{ and } (001)_P//(001)_\gamma,$$

$$[11\text{-}20]_H//[1\text{-}10]_\gamma \text{ and } (0001)_H//(111)_\gamma.$$

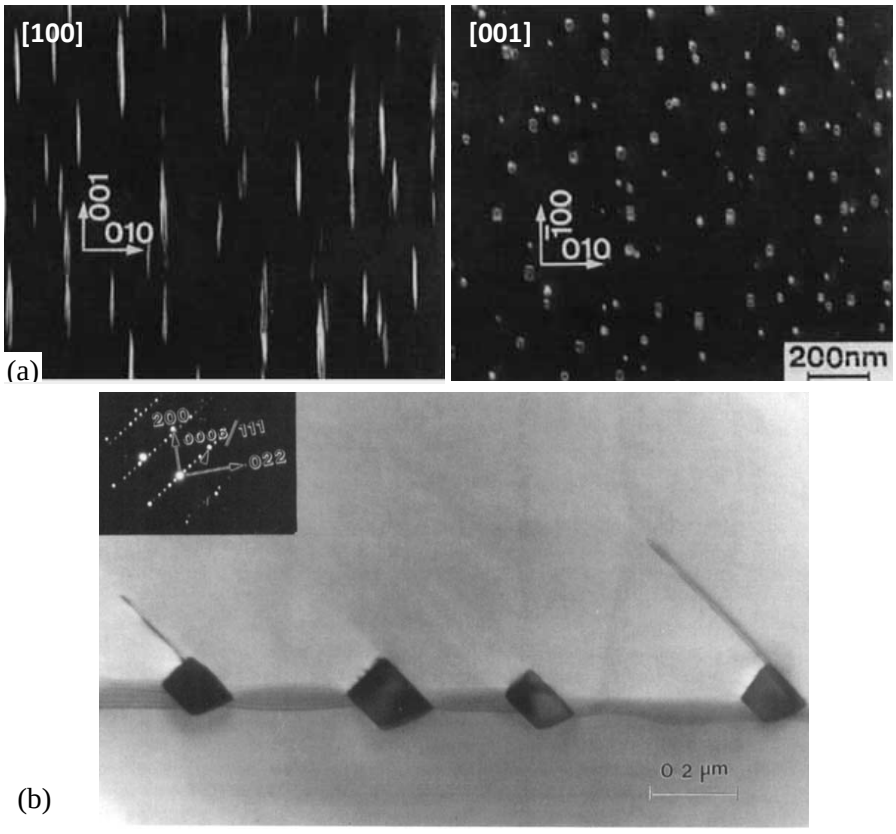

Figure 5 (a) Typical morphology of P-type carbides as reported in literature (Tian 1993), exhibiting needle-like projections along the [100] direction and dot or square cross sections along the [001] direction, (b) H-type carbides with a plate-like morphology formed at grain boundaries, together with the associated diffraction pattern viewed along the $[11\text{-}20]_H$ and $[1\text{-}10]_\gamma$ directions (Xiao 1992).

In a Ti-48Al-1V-0.2C (at. %) alloy investigated by Worth et al. (Worth 1995), P type carbides nucleated at grain boundaries, at dislocations and in γ grains after annealing at 750°C. However, after aging at 815°C, precipitates only heterogeneously nucleated at grain boundaries and along dislocations within γ grains. Wu et al. (Wu 2003) reported that in a Ti-46.6Al-1.4Mn-2Mo-0.3C (at. %) alloy acicular P-type carbides were observed at α_2/γ grain boundaries at 800°C and plate-like H-type carbides were also observed along prior α grain boundaries and at dislocations within the γ phase after aging at 800°C for 36h. Gouma et al. (Gouma 1998) did not observe perovskite precipitates in K5SC alloy (Ti-46Al-3Nb-1.8Cr-0.2W-0.2Si-0.1C, at. %) after aging at 900°C for 8, 24 and 48h and only found H-type carbides with long platelets at the γ-γ lath boundaries. Simpkins et al. (Simpkins II 2007) investigated Ti-47Al-2Nb-2Mn-0.08TiB_2 (at. %) with 0.1 wt. % C after annealing at temperatures between 950 and 1100°C for 2 to 40h. They found that carbides changed their morphology from a coherent spherical shape to rod shape in a complex way which depended on the annealing time and temperature, although the type of carbides was not indicated. In a Ti-52Al-3C (at. %) alloy investigated by Xiao et al. (Xiao 1992), only H-type carbides were observed to heterogeneously nucleate at γ grain boundaries, as shown

in **Figure 5(b)**. They also had the following orientation relationship with the γ matrix: $[11\text{-}20]_H//[1\text{-}10]_\gamma$ and $(0001)_H//(111)_\gamma$.

From the above references it can be concluded for carbon doped TiAl alloys that P- and H-type carbides form at different heat treatment temperatures and times. Usually P-type carbides form within the temperature range of 750-900°C, while H-type carbides form at the expense of P-type carbides at temperatures ≥ 900°C or at lower temperatures with longer annealing times.

1.4.2 Influence of carbon on phase transformations

The addition of carbon to TiAl alloys stabilizes the α_2 phase, which is confirmed in **Figure 6** (Chladil 2005). From the investigation of Chladil et al. (Chladil 2005) on Ti-45Al-7.5Nb alloys with 0, 0.25 and 0.5 at. % C, carbon clearly raised T_e ($\alpha_2+\gamma\rightarrow\alpha$). But as carbon content was increased, its impact on of T_e became less significant. Meanwhile, C also has little influence on T_α ($\gamma\rightarrow\alpha$). However Park et al. (Park 1999) reported that a 0.3 at. % carbon addition stabilized the high-temperature α phase, thereby decreasing T_α in a Ti-46.6Al-1.4Mn-2Mo-0.3C (at. %) alloy. But as the results indicated that T_α dropped from 1367 to only 1361°C, this statement should be treated carefully. McCullough et al. (McCullough 1990) studied the microstructural evolution in Ti-48Al and Ti-45Al (at. %) powders with different carbon contents and found carbon changed the phase selection from primary β phase to primary α phase during solidification. In an investigation by Wu et al. (Wu 2003) on Ti-46.6Al-1.4Mn-2Mo-xC (at. %) alloy, the microstructure changed from nearly lamellar (NL) to near gamma (NG) as the carbon concentration increased from 0.3 to 0.6 at. %. The same phenomenon occurred in 47XD alloys that contained varying carbon contents investigated by McQuay et al. (McQuay 1999). When the carbon content was increased from 0.02 to 0.36 at. %, the lamellar fraction decreased from 70% to 30%, and the grain size was refined.

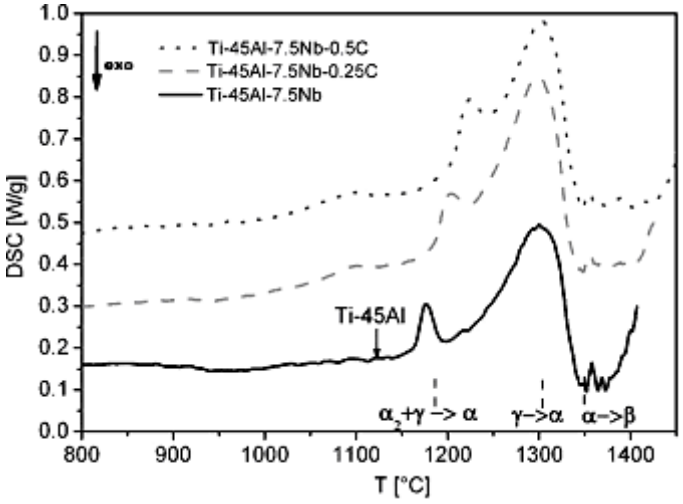

Figure 6 The influence of carbon on phase transformations in the Ti-45Al-7.5Nb (at. %) alloy. The DSC curves were measured with a heating rate of $20K\cdot min^{-1}$ (Chladil 2005).

1.4.3 Influence of carbon on properties

The addition of carbon to TiAl alloys was reported to enhance the strength and creep resistance, as seen in **Figure 7** (McQuay 1999). The TiAl alloys showed enhanced creep resistance with increasing carbon content up to 0.065 wt. %. However, when the carbon concentration was increased further to 0.110 wt. %, the creep resistance decreased.

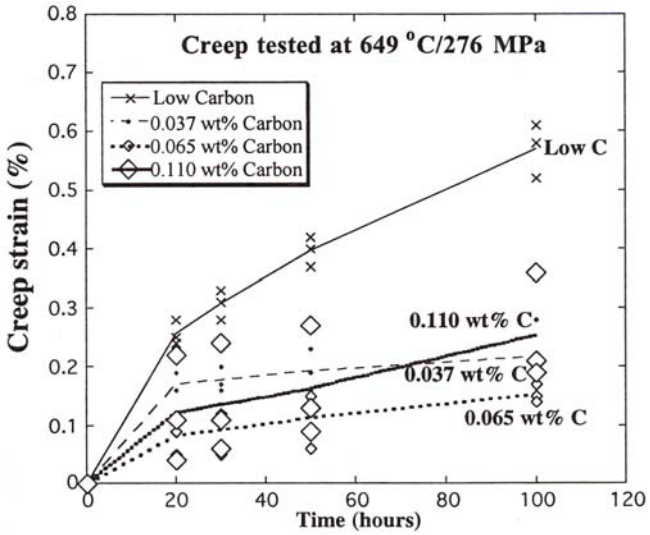

Figure 7 Creep properties of Ti-47Al-2Mn-2Nb-1B-xC (x= low, 0.037, 0.065 and 0.110 wt. %) alloys tested at 649°C and 276MPa (McQuay 1999).

The strengthening might be caused by solid-solution hardening or/and precipitation hardening. In Ti-48Al-4V-0.3C (at. %) reported by Worth at al. (Worth 1995), the solute atmosphere drag mechanism might be responsible for the improvement in creep properties rather than carbide precipitation hardening. However from the study of Gouma et al. (Gouma 1998, Gouma 1998, Karadge 2003) on the K5SC system, carbides forming mainly at the lamella interfaces were quite stable and could prevent the movement of interfacial dislocations. Thus the improved creep resistance was attributed to the carbide precipitation. Tian et al. (Tian 1993, Tian 1997) also supported the idea that the increased creep resistance in carbon doped alloys resulted from Orowan pinning of the dislocations by perovskite Ti_3AlC precipitates. Appel et al. (Christoph 1997, Appel 2000) reported that carbon in solid solution only acted as weak glide obstacle and was easily overcome by thermal activation in a Ti-48.5Al-0.37C (at. %) alloy. Ti_3AlC perovskite precipitates formed after aging acted as glide obstacles with long-range stress fields and could not be overcome with the aid of thermal activation. In Ti-46.6Al-1.4Mn-2Mo-xC investigated by Park et al. (Park 2001) the improvement in strength and creep resistance was attributed to microstructure refinement and precipitation hardening by the Ti_3AlC phase. However, P-Ti_3AlC carbides are not stable during annealing and coarsen easily by Ostwald ripening. The work of Gouma et al. (Gouma 1998) showed that fine H-Ti_2AlC carbides at γ-γ lamellae interfaces played an effective role in improving the strength

and creep resistance of PM Ti-48Al-2Mn-2Nb-0.8C (at. %) alloy, although at the expense of tensile ductility. However H-Ti_2AlC carbides usually form at higher temperatures with a large size, this makes them less effective compared with P-Ti_3AlC carbides for improving the mechanical performances. Thus it is important to improve the thermal stability of P-Ti_3AlC carbides and/or try to obtain fine H-Ti_2AlC carbides.

1.4.4 Carbon solubility in TiAl alloys

Menand et al. (Menand 1996) carried out interstitial concentration measurements by atom probe in TiAl alloys with two-phase (α_2+γ) and single-phase γ microstructures. They found that the solubility limit of carbon in the γ phase of different binary Ti-Al alloys as well as in various ternary Ti-Al-X systems (X= 3 and 5 at. % Cr, Mn, Nb) was very low, ranging from 200 to 300 at. ppm. At temperatures between 1000 and 1300°C, the solid solubility of carbon did not vary too much, but it decreased significantly from 1000 to 800°C, as shown in **Table 2**. The carbon solubility in the α_2 phase was almost ten times higher than in the γ phase. This may be attributed to the octahedral interstices surrounded by six Ti atoms in the DO_{19} structure of the α_2 phase, which are preferred sites for carbon atoms. In the γ phase, there are only Ti_2Al_4-type or Ti_4Al_2-type interstices, as shown in **Figure 8**. Although in the γ phase some Ti atoms can replace Al atoms in (002) planes to form Ti_6 octahedral sites, the number is still far fewer than in the α_2 phase. As a consequence the solubility limit of carbon in the γ phase is quite low. This also indicates that the stoichiometry of the matrix phases plays a role in the solubility of the interstitial elements, such as carbon.

Table 2 Carbon solubility in the γ phase of the Ti-52Al (at. %) alloy (Menand 1996)

Temperature (°C)	800	900	1000
Carbon solubility (at. ppm)	90±50	220±80	250±90

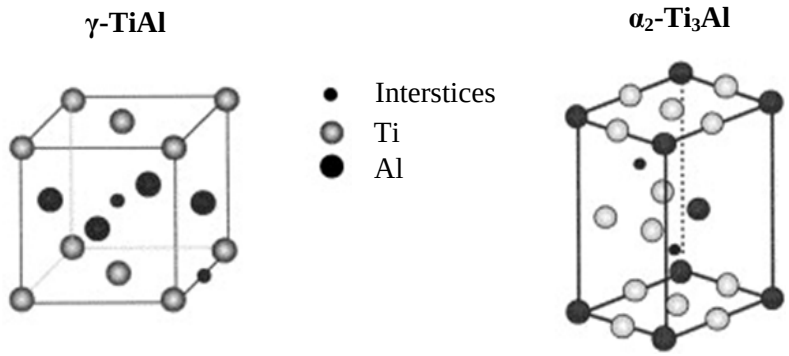

Figure 8 Octahedral interstices in the $L1_0$ structure of the γ phase and in the DO_{19} structure of the α_2 phase. In the γ-TiAl phase the chemical surroundings of the octahedral cavities are Ti_4Al_2 and Ti_2Al_4 types, while in the α_2-Ti_3Al phase they are Ti_6 and Ti_4Al_2 types (Menand 1998).

In other ternary and multinary systems, as shown in **Table 3,** the carbon solubility is also low. Carbide precipitates were found in Ti-48.7Al-2.1Nb-0.06C and Ti-47Al-2Mn-2Nb-1B-0.12C (at. %) alloys. In rapidly solidified Ti-45Al and Ti-48Al (at. %)

powders investigated by McCullough et al. (McCullough 1990), carbides were observed when Ti-45Al-xC (x>0.64 at. %) and Ti-48Al-xC (x>1 at. %).

Table 3 Carbon existence form in various TiAl alloys from literature data

Alloy composition (at. %)	Thermal processing	Carbon existence form
Ti-48.7Al-2.1Nb-0.06C (Chen 1992)	4h@1250ºC, FC	solute+ precipitate
Ti-47Al-2Mn-2Nb-1B-0.12C (McQuay 1999)	4h@1260ºC + 50h@1010ºC	solute+ precipitate
Ti-45Al-xC (McCullough 1990)	Rapid solidification	solute (x<0.64)
Ti-48Al-xC (McCullough 1990)		solute (x<1)
Ti-45Al-5Nb-0.5C (Scheu 2009)	2h@1270ºC + 2h@1050ºC	solute

However in recent work by Gerling et al. (Gerling 2008), no presence of carbides was observed in a PM Ti-45Al-5Nb-0.5C (at. %) alloy. Scheu et al. (Scheu 2009) also reported that carbon was in solution in the Ti-45Al-5Nb-0.5C (at. %) alloy. Through atom probe analysis, the carbon concentration in the γ phase was about 0.25 at. %, which was almost ten times higher than the solubility reported for the γ phase in other TiAl alloys. Moreover they did not find carbides but some carbon enriched regions, as shown in **Figure 9**. Such regions were proposed to act as Cottrell atmospheres surrounding dislocation cores. These investigations were performed on the PM Ti-45Al-5Nb-0.5C alloy after hot rolling and primary annealing at 1050°C for 2h, which resulted in a microstructure composed of about 80 vol. % γ phase and 20 vol. % α_2 phase. The high solubility of carbon in the γ phase was attributed to the addition of Nb which modified the surrounding of the interstitial sites where carbon atoms were situated. Nevertheless, Appel et al. (Appel 2011) reported the presence of carbides precipitated at dislocations in Ti-45Al-8Nb-0.2C (at. %) after extrusion.

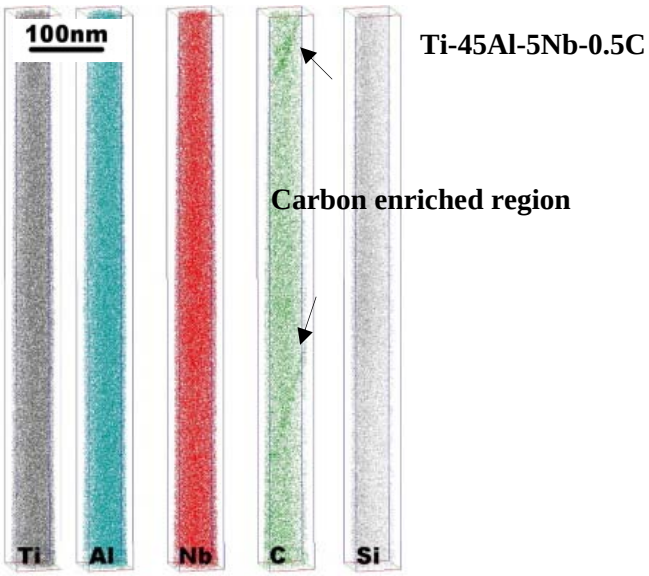

Figure 9 Atom probe investigation in the Ti-45Al-5Nb-0.5C (at. %) alloy (HIPed @ 1270°C, 2h + hot-rolled + annealed @ 1050°C, 2h). No carbides were detected but some carbon enriched regions were proposed to act as Cottrell atmospheres surrounding dislocation cores (Scheu 2009).

1.5 Objectives and methods of research

The objective of this research is to confirm whether Nb has an influence on the carbon solubility in TiAl alloys and to investigate carbide precipitation in high Nb containing TiAl alloys. Up to know no detailed information about carbide precipitation and the thermal stability of carbides in high Nb containing TiAl alloys is reported. The research of Gerling et al. (Gerling 2008) and Scheu et al. (Scheu 2009) only focused on Ti-45Al-5Nb-0.5C (at. %) alloy after hot rolling and subsequent annealing at 1050°C for 2h. Therefore their results only consider one carbon concentration and one specimen state. For a broader understanding of the effects of carbon addition in high Nb containing TiAl alloys it is very important to investigate: **(1)** the influence of carbon content on phase transformations, **(2)** the influence of Nb on carbon solubility and **(3)** carbide precipitation and the thermal stability of carbides in these alloys. This will help to understand the effects of carbon addition on the mechanical properties. In this work PM Ti-45Al-5Nb-xC alloys (x=0, 0.5, 0.75 and 1.0 at. %) were systematically investigated in different heat-treated states. This research mainly concerns the temperature range from 800 to 1000ºC which is interesting for processing as well as applications. The microstructures and especially the carbides have been investigated in detail using high energy X-ray diffraction (HEXRD), scanning electron microscope (SEM), transmission electron microscope (TEM) and high resolution TEM (HRTEM). HRTEM images have been simulated by JEMS software using the Bloch wave method to interpret the experimental images. In this research, due to the difficulty in measuring the carbon concentration in the matrix, it was assumed that the carbon solubility was exceeded if carbides were precipitated. In this way we can obtain an understanding for the carbon solubility in high Nb containing TiAl alloys. The carbide precipitation, and the morphology development and thermal stability of carbides in high Nb containing TiAl alloys were studied in a great detail.

2. Experimental

2.1 Materials

The Ti-45Al-5Nb-xC pre-alloyed powders (x=0, 0.5, 0.75 and 1.0 at. %) used in this research were produced by powder metallurgy (PM) technology, using the plasma melting induction guiding gas atomization (PIGA) technique (see **Figure 10**). More details about powder production can be found in Ref. (Gerling 2004).

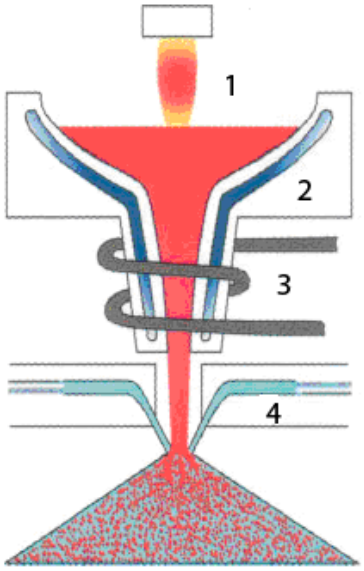

Figure 10 Schematic illustration of the plasma melting induction guiding gas atomization (PIGA) technique (Gerling 2004). (1) Plasma torch, (2) cold copper crucible, (3) induction-heated cold copper funnel, and (4) gas nozzle.

Table 4 shows the concentration levels of light elements (C, N and O) in the pre-alloyed powders. The actual contents of C in the Ti-45Al-5Nb-0.5C, Ti-45Al-5Nb-0.75C and Ti-45Al-5Nb-1.0C powders are very close to the nominal concentrations. The O and N contents are controlled below 586 and 56 μg/g respectively. The fraction of powder particles with diameters < 180μm was separated by sieving, then filled into Ti cans, degassed, sealed and consolidated by hot isostatic pressing (HIP) at 1250°C and 200MPa for 2h.

Table 4 Chemical analysis of the pre-alloyed Ti-45Al-5Nb-xC (x= 0.5, 0.75 and 1.0 at. %) powders

Pre-alloyed powders for HIP (0-180μm)	C (μg/g)	O (μg/g)	N (μg/g)
Ti-45Al-5Nb-0.5C	1535 (1480)	381	56
Ti-45Al-5Nb-0.75C	2170 (2210)	512	48
Ti-45Al-5Nb-1.0C	2850 (2950)	586	39

* The values in brackets are nominal concentrations for carbon.

2.2 Heat treatments

- Solution treatments

In order to dissolve the primary carbides and distribute carbon more homogeneously in the matrix, the HIPed Ti-45Al-5Nb-xC alloys were heat treated at various temperatures between 1250 and 1400°C for different times, as summarized in **Table 5**.

- Annealing treatments

In order to investigate the carbide precipitation at low temperatures, annealing treatments at 800-1000°C were applied to the Ti-45Al-5Nb-0.5C and Ti-45Al-5Nb-0.75C alloys that had been HIPed and Solution treated, see **Table 5**.

Table 5 Heat treatments for the Ti-45Al-5Nb-xC (x=0.5, 0.75 and 1.0 at. %) alloys

	Starting alloy (at. %)	Heat treatment conditions	Heat-treated alloys (at. %)
Solution treatments	HIPed Ti-45Al-5Nb-1.0C	5, 24, 48, 72, 96h @1250°C, OQ	Solution treated Ti-45Al-5Nb-1.0C
		24h @1280°C, OQ	
		24h @1300°C, OQ	
		1h @1320°C, WQ	
		5h @1350°C, WQ	
		1h @1400°C, OQ	
	HIPed Ti-45Al-5Nb-0.75C	5, 24, 48h @1250°C, OQ	Solution treated Ti-45Al-5Nb-0.75C
		2, 5, 10, 24h @1280°C, OQ	
		24h @1300°C, WQ	
		1h @1400°C, OQ	
	HIPed Ti-45Al-5Nb-0.5C	5h @1250°C, OQ	Solution treated Ti-45Al-5Nb-0.5C
Annealing treatments	HIPed Ti-45Al-5Nb-0.75C	24, 48, 96, 168h @ 800°C, FC	HIPed & Annealed Ti-45Al-5Nb-0.75C
		24, 48, 96, 168h @ 900°C, FC	
		24, 48, 96, 168h @ 1000°C, FC	
	HIPed Ti-45Al-5Nb-0.5C	24, 48, 96, 168h @ 800°C, FC	HIPed & Annealed Ti-45Al-5Nb-0.5C
		24, 48, 96, 168h @ 900°C, FC	
		24, 48, 96h @ 1000°C, FC	
	Solution treated (5h @1250°C, OQ) Ti-45Al-5Nb-0.75C	24, 48, 96, 168, 1054h @ 800°C, FC	Solution Treated & Annealed Ti-45Al-5Nb-0.75C
		24, 48, 96, 168h @ 900°C, FC	
		24, 48, 96, 168h @ 1000°C, FC	
	Solution treated (5h @1250°C, OQ) Ti-45Al-5Nb-0.5C	24, 48, 96, 168, 1104h @ 800°C, FC	Solution Treated & Annealed Ti-45Al-5Nb-0.5C
		24, 48, 96, 168h @ 900°C, FC	
		24, 48, 96, 168h @ 1000°C, FC	

* OQ: oil quenching, WQ: water quenching, FC: furnace cooling. All the heat treatments were performed in an air except for the Ti-45Al-5Nb-0.5C alloy @ 800 and 900°C for 168h, which were implemented under vacuum.

HIPed & Annealed Ti-45Al-5Nb-0.75C and Ti-45Al-5Nb-0.5C were obtained by applying annealing treatments within the temperature range 800-1000°C for 24, 48, 96 and 168h, to the HIPed material. To obtain the **Solution Treated & Annealed** Ti-

45Al-5Nb-0.75C and Ti-45Al-5Nb-0.5C alloys, HIPed specimens were first solution treated at 1250°C for 5h to dissolve the primary carbides and obtain a more homogeneous carbon distribution in the matrix. Then the Solution treated materials were annealed at 800, 900 and 1000°C for 24, 48, 96 and 168h. Additionally, long-term annealing treatments at 800°C for 1054 and 1104h were performed to investigate the thermal stability of carbides in the Ti-45Al-5Nb-0.75C and Ti-45Al-5Nb-0.5C alloys.

2.3 Characterization techniques

2.3.1 Differential Scanning Calorimetry

In order to investigate the influence of carbon on phase transformations in the Ti-45Al-5Nb-xC alloys, Differential Scanning Calorimetry (DSC) experiments were conducted using a Dynamic High-Temperature Calorimeter Netzsch Pegasus 404C. DSC measurements were performed up to 1500°C with a heating rate of 20K/min under an Argon atmosphere (99.9999% purity). The specimens had a cube shape with dimensions of around $2\times2\times2mm^3$.

2.3.2 Macro hardness measurements

Macro hardness measurements were carried out to study the influence of carbon on the mechanical properties of Ti-45Al-5Nb-xC alloys. The specimens were ground using successive SiC abrasive papers to P2500 prior to the hardness measurements. In this study Vickers hardness was measured by applying a Vickers diamond pyramid indenter, at a load of 20Kg and with a dwelling time of 15s. Then the diagonal lengths of the square indentation were measured and the mean length was imported to the following equation to get the Vickers hardness:

$$Hv = \frac{1.854 \cdot P}{d^2} Kg/mm^2 \qquad \textbf{Eq. 1}$$

Where, P is the load (20Kg in this experiment), d is the average diagonal length in mm divided by 100). For each specimen, 3-5 indentations were carried out and an average value of Hv was obtained.

2.3.3 High Energy X-Ray Diffraction

The phase identification, phase fraction and lattice parameters of phases were determined by analyzing HEXRD patterns. HEXRD experiments using synchrotron radiation were conducted using the HEMS and HARWI-II beam lines run by the Helmholtz-Zentrum Geesthacht at the Deutsches Elektronen-Synchrotron (DESY). The X-ray beam had a cross section of $1\times1mm^2$ and a photon energy of 100keV for HEMS and 87.1keV for HARWI-II. These energies correspond to wavelengths of 0.12398Å and 0.1425Å respectively. The reflections were recorded by a mar345 image plate or a PerkinElmer XRD 1622 flat panel detector at the HEMS beamline and a mar555 flat panel detector at HARWI-II. Through applying the Rietveld

refinement method on the HEXRD patterns the lattice parameters of the γ and α_2 phases could be derived. However due to the low fraction of carbides the Rietveld method could not be used, so the lattice parameters of P-type carbides were calculated from the peak positions of the (111), (200) and (220) reflections and then the average value was taken. The fractions of γ and α_2 phases were obtained by Rietveld refinement, while the fraction of carbides was obtained by the Reference Intensity Ratios (RIRs) method.

The RIRs method is based on the following equations (Hubbard 1988):

$$W_X = \frac{I_X}{K_A^X \sum_{i=A}^{N} \frac{I_i}{K_A^i}} \qquad \textbf{Eq. 2}$$

$$K_A^X = \frac{K_X}{K_A} \qquad \textbf{Eq. 3}$$

Where, W_X is the weight fraction of phase *X*. I_X is the highest peak intensity of phase *X*. I_i is the highest peak intensity of phase *A*. K_X and K_A are scaling factors for phases *X* and *A*, defined by $K_X = I_X/I_C$ and $K_A = I_A/I_C$ respectively when the reference sample is corundum (Al_2O_3). I_C is the highest peak intensity of corundum. In this research, the scaling factors for γ, α_2 and P-Ti_3AlC phases are taken from the Powder Diffraction File (2004) and are given as 5.53, 5.72 and 5.20 respectively.

2.3.4 Scanning Electron Microscopy and Electron Back-Scatter Diffraction (EBSD)

The microstructure and grain size of the Ti-45Al-5Nb-xC alloys were determined by SEM investigation in a LEO Gemini 1530 Scanning Electron Microscope equipped with EBSD and energy-dispersive X-ray analysis (EDX). The method used for grain size measurement is the linear intercept method which was employed on SEM images that were taken in back-scattered electron mode. Images were taken from 5 different positions in each specimen at a magnification of 2000 times. SEM specimens were cut from HIPed billets, ground and then electro-polished with a solution composed of 26ml perchloric acid (70%), 359ml 2-butanol and 625ml methanol at 30V and -30ºC. After grinding some specimens were prepared by mechanical polishing using a vibration polisher to retain the carbides within the matrix.

The grain size of the Ti-45Al-5Nb-xC alloys was also characterized by EBSD in an AURIGA Scanning Electron Microscope. For EBSD investigations a TSL analysis system fitted to the AURIGA microscope was employed. The proprietary TSL software was used for EBSD data analysis. The EBSD specimens were prepared using the same procedure as for SEM specimens i.e. electro-polishing.

2.3.5 Transmission Electron Microscopy and HRTEM image simulation

The carbides in the Ti-45Al-5Nb-xC alloys were investigated in detail by TEM in a Philips CM200 Electron Microscope operated at 200KV (equipped with EDX), and a

FEI Titan 80-300 Transmission Electron Microscope with Cs corrector. TEM foils with a diameter of 2.3mm were first drilled, ground to a thickness below 120μm, and then thinned by twin-jet polishing at 25-35V and a temperature of -40°C with a solution composed of 26ml perchloric acid (70%), 359ml 2-butanol and 625ml methanol.

In order to gain information about the atomic arrangement of the phases and the interfaces between the matrix and precipitates, HRTEM was carried out in the FEI Titan 80-300 Transmission Electron Microscope. However, HRTEM images are very sensitive to many factors (Williams 2009, Zou 2012): (1) the precise alignment of the beam to the electron-optical axis and zone axes of the crystal, (2) the thickness of the specimen and the defocus of the objective lens, (3) chromatic aberration and spherical aberration, (4) accelerating voltage and the coherence of the beam, (5) crystal structure, atomic coordinates and occupancy.

The idea of simulating HRTEM images is important because it is not only used to interpret experimental HRTEM images, but also applied for other purposes: to find out the experimental conditions for the images taken, to determine the optimized experimental parameters of a microscope for a particular structure, and to predict the resolution required for a microscope to resolve specific atoms in a structure.

To obtain the simulated HRTEM image, it is important to calculate the exit-wave function. The exit-wave function is defined by the wave function of electrons after interaction with a specimen right below the specimen and contains the information about the arrangement of atoms in the specimen. After calculating the exit-wave function and image wave at focal plane, the contrast transfer function is applied to the image wave to simulate HRTEM images. There are two ways to obtain the exit-wave function: the multislice method and the Bloch wave method (Williams 2009, Zou 2012).

The multislice method was according to the physical-optical approach proposed by Cowley and Moodie in 1957 (Cowley 1957). A crystal with thickness t is divided into many thin slices each with thickness Δt, as shown in **Figure 11**. The potential of each slice is projected to a plane and the related projected potential is calculated. The propagation of the electron wave from the exit surface of one slice to the incident surface of the next slice is taken as Fresnel propagation in vacuum. When all slices are taken into account, the final exit-wave function is obtained.

The Bloch wave method: Electron propagates through the crystalline specimen as a Bloch wave. Fujimoto (Fujimoto 1978) and Kambe (Kambe 1982) showed that for a perfect crystal, the HRTEM image might be understood simply based on the image of Bloch waves. It is worth mentioning that only a small number of Bloch waves determine the appearance of the image if the crystal has a sufficiently high symmetry. The detailed mathematical calculation is overlooked here. For more information please refer to (Stadelmann 1993, Williams 2009, Zou 2012).

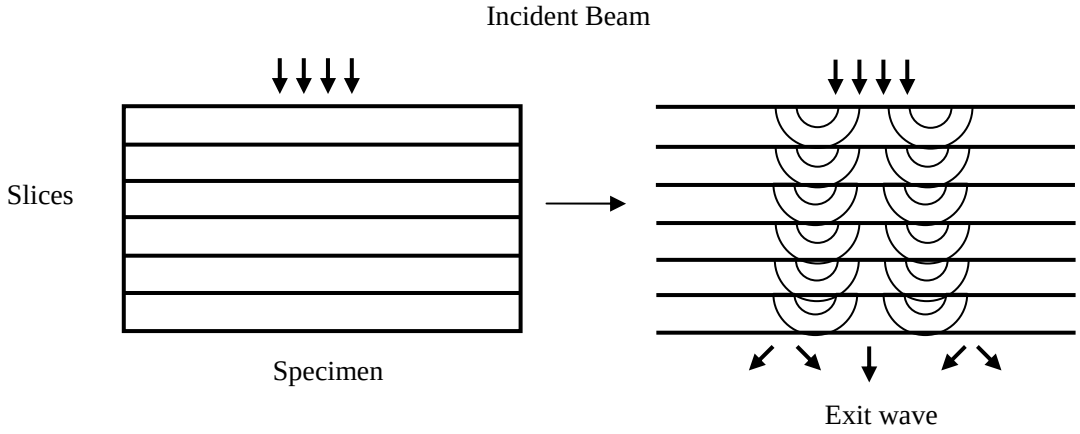

Figure 11 Schematic illustration of the multislice approximation method.

In this research JEMS software was used to simulate HRTEM images using the Bloch wave method. The multislice method was also applied to some cases and gives similar simulation results to the Bloch wave method. The following information is required for HRTEM image simulation.

(a) Definition of the crystals of γ-TiAl and P-Ti_3AlC phases, including space group and lattice parameters, atoms and their positions, as shown in **Table 6**.

Table 6 Crystal information of γ-TiAl and P-Ti_3AlC phases (Appel 2011)

Phases	Atoms	X-axis	Y-axis	Z-axis	Wyckoff	Occupancy
γ-TiAl	Al	0	0	0	1a	1
(P4/m m m)	Al	0.5	0.5	0	1c	1
a=4.012Å b=4.065Å	Ti	0	0.5	0.5	2e	1
P-Ti_3AlC	Al	0	0	0	1a	1
(P m -3 m)	Ti	0	0.5	0.5	3c	1
a=4.16Å	C	0.5	0.5	0.5	1b	1

(b) Parameters of the TEM equipment, as shown in **Table 7**.

Table 7 Parameters of the FEI Titan 80-300kV microscope

Acceleration voltage	Energy spread dE (FWHM)	Chromatic aberration Cc	Information limit	Half convergence angle
300kV	2.43/2.93nm	1.28mm	0.8Å	0.2mrad

(c) The parameters from the Cs corrector: defocus (C1), 2fold astigmatism (A1), 3fold astigmatism (A2), axial coma (B2), spherical aberration (C3), 4fold astigmatism (A3), star aberration (S3), 5fold astigmatism (A4). **Table 8** shows the parameters of the Cs corrector from the experiments. Three specimens were investigated during three sessions as indicated in **Table 8**.

Table 8 Parameters from the Cs corrector in experiments

	0.5C, @800°C,168h	0.75C, @800°C,168h	0.75C, @1250°C, 5h+@800°C,168h
C1(nm)	-447.5	-473.2	-535.9
A1(pm)	669.6	752.8	659.49
A2(nm)	5.065	5.56	14.12
B2(nm)	5.065	5.725	6.81
C3(nm)	1027	-49.35	644.2
A3(μm)	1.097	1.087	0.038
S3(nm)	210.4	205	357.8
A4(μm)	53.24	45.74	49.2

Before the HRTEM investigation was performed, it was necessary to check the atom projections and to do a test simulation to obtain the right experimental conditions, such as the right zone axis, the suitable spherical aberration. Since the P-Ti_3AlC phase has a similar crystal structure to the γ matrix, in order to distinguish these two phases, we should avoid taking images from $[110]_\gamma$, $[1\text{-}10]_\gamma$, $[\text{-}110]_\gamma$ and $[\text{-}1\text{-}10]_\gamma$ zone axes due to the similar atomic arrangement along these directions (ignoring carbon atoms because their intensities are too weak to be distinguished in HRTEM), as shown in **Figure 12**.

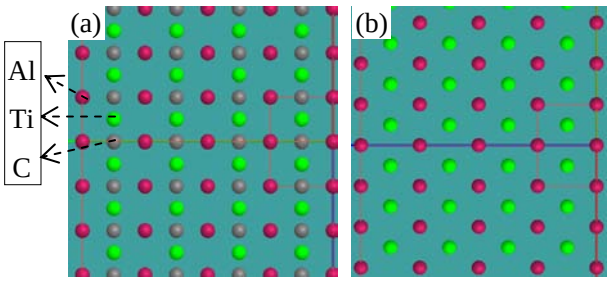

Figure 12 Atom projections of (a) P-Ti_3AlC in <110> and (b) γ phase in <110]. Red dots represent Al atoms, green dots represent Ti atoms and dark grey dots represent carbon atoms.

After importing the parameters given in **Tables 6-8** into the JEMS software, HRTEM images along different zone axes can be simulated for both γ and P-Ti_3AlC phases. These will be shown in **Section 5.2** together with the experimental HRTEM images.

3. Overview: influence of carbon content on phase transformations and microstructures

This chapter will talk about the influence of carbon on microstructures, phase transformations, and carbides in HIPed Ti-45Al-5Nb-xC alloys (x=0, 0.5, 0.75 and 1.0 at. %). The influence of carbon concentration on the hardness of Ti-45Al-5Nb-xC alloys in the HIPed condition is discussed.

3.1 High-energy X-ray diffraction of pre-alloyed powders

The high-energy X-ray diffraction (HEXRD) patterns in **Figure 13** exhibit no reflections from carbides in the pre-alloyed powders. Due to the fast cooling rate during powder manufacture, the high-temperature microstructure can be preserved to room temperature. This may suggest that at high temperatures close to the melting temperature, carbon solubility in these alloys may be higher than 1.0 at. %. The microstructure of Ti-45Al-5Nb powders is composed of a major α_2, a minor β and a trace amount of γ phases. With increasing carbon concentration, the amount of the β phase decreases and its reflections almost disappear in Ti-45Al-5Nb-0.75C and Ti-45Al-5Nb-1.0C powders, while the fraction of the γ phase increases. Carbon plays a role in changing the primary phase from the β phase to the α phase during the solidification process, which agrees well with the result reported by McCullough et al. (McCullough 1990).

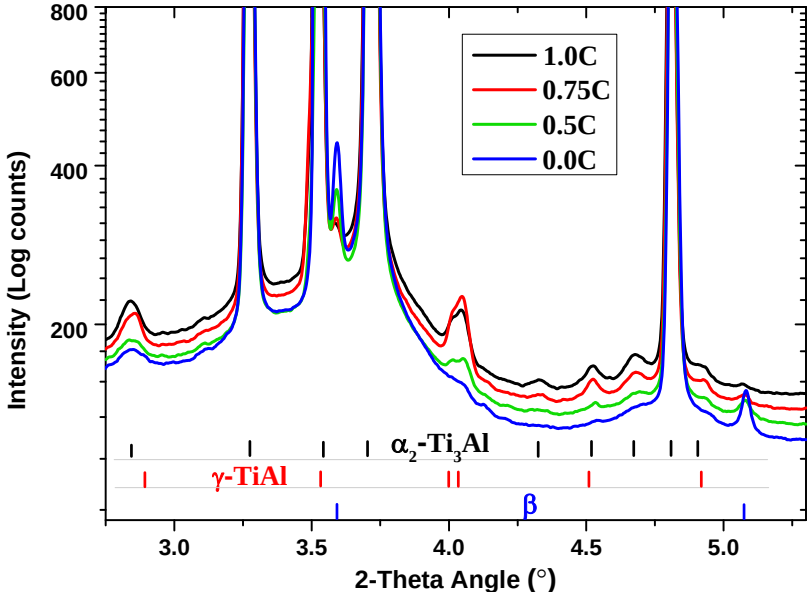

Figure 13 High-energy X-ray diffraction patterns of the pre-alloyed Ti-45Al-5Nb-xC (x=0, 0.5, 0.75 and 1.0 at. %) powders.

3.2 Influence of carbon on phase transformations

The influence of carbon on phase transformations in the HIPed Ti-45Al-5Nb-xC (x=0, 0.5, 0.75 and 1.0 at. %) alloys has been determined from DSC measurements, as shown in **Figure 14**. With increasing the carbon concentration to level of 0.75 at. %, both T_e ($\alpha_2+\gamma\rightarrow\alpha$) and T_β ($\alpha\rightarrow\beta$) increase, while T_α ($\gamma\rightarrow\alpha$) shows no obvious variation. As the carbon content further increases above 0.75 at. %, both T_e and T_α remain stable, but the peak of T_β disappears. At 1500°C the Ti-45Al-5Nb-0.75C and Ti-45Al-5Nb-1.0C alloys started to melt. These findings are in accordance with the HEXRD results. In the Ti-45Al-5Nb-0.75C and Ti-45Al-5Nb-1.0C alloys, the reflection intensity related to the β phase is very weak compared with those of the Ti-45Al-5Nb and Ti-45Al-5Nb-0.5C alloys.

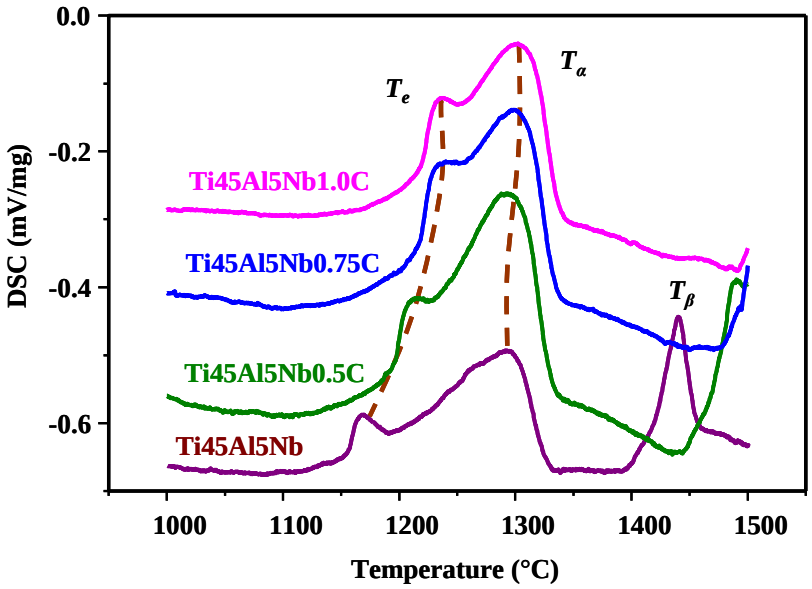

Figure 14 DSC analysis showing the influence of carbon on phase transformations in the Ti-45Al-5Nb-xC (x=0, 0.5, 0.75 and 1.0 at. %) alloys. Tests were performed under an Ar atmosphere at with a heating rate of 20K/min.

The carbon addition increasing T_β is further confirmed in **Figure 15**. Specimens were heat treated at 1400°C for 1h followed by oil quenching. The microstructure shows that the carbon-free alloy has much more refined grains. At 1400°C the carbon-free alloy is located within the α+β region and the grain growth of one phase is confined by the other. As carbon additions increase the T_β temperature, at 1400°C such alloys have less β phase than the carbon free alloy. Thus confinement of the α phase by the β phase is reduced and grain coarsening is enhanced. This explains why the carbon containing alloys have coarser grains.

In conclusion, carbon can stabilize α and α_2 phases, and shift the (α+β) phase field to a low Al concentration and a high temperature.

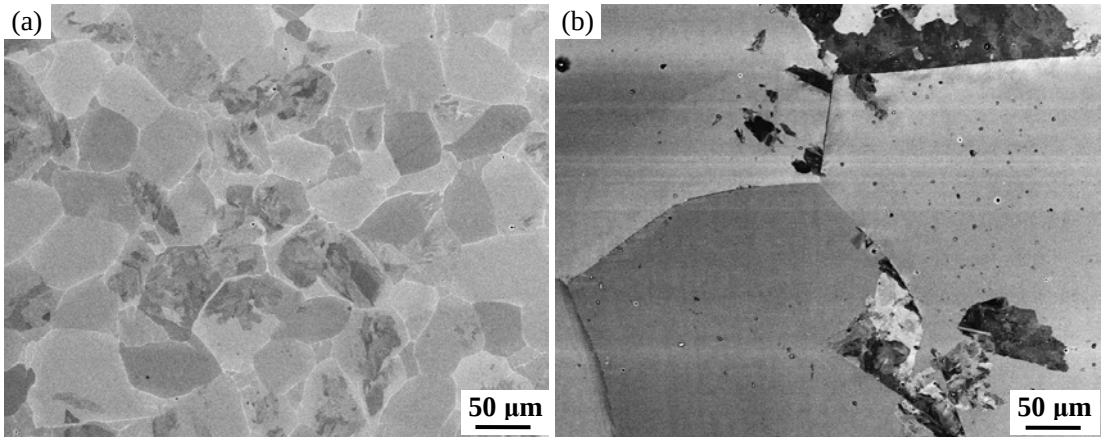

Figure 15 Microstructures of (a) Ti-45Al-5Nb and (b) Ti-45Al-5Nb-0.75C after heat treatment at 1400°C for 1h followed by Oil Quenching (OQ). The microstructures indicate that the carbon addition increases T_β temperature (see text) as the carbon free alloy has a more refined microstructure than the carbon containing alloy. SEM images were recorded in the back-scattered electron (BSE) mode.

3.3 Influence of carbon on grain size and phase fractions

The grain size of the γ and α_2 phases was measured by two methods, as shown in **Figure 16**. One is the linear intercept method using SEM images. The images were taken from 5 different positions in each specimen at a magnification of 2000 times. The second method was based on electron back-scatter diffraction (EBSD).

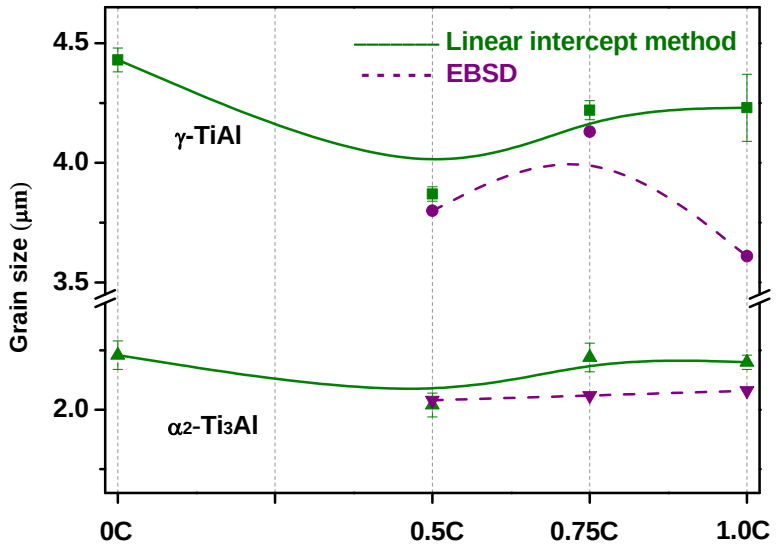

Figure 16 Grain size of the γ and α_2 phases in the HIPed Ti-45Al-5Nb-xC (x=0, 0.5, 0.75 and 1.0 at. %) alloys determined using the linear intercept method and EBSD method. The data is connected by guiding spline lines.

From the linear intercept method, the HIPed Ti-45Al-5Nb-0.5C has a slightly more refined microstructure than the HIPed Ti-45Al-5Nb. However with further increasing carbon concentration, the grain size seems to increase but is still slightly finer than that in the carbon free alloy. Here it should be noted that the Ti-45Al-5Nb-0.5C alloy

was not HIPed at the same time as the Ti-45Al-5Nb-0.75C and Ti-45Al-5Nb-1.0C alloys. Although the HIPing conditions should have been the same, this might have had an influence on the microstructure. From the EBSD results it seems that the grain size of the α_2 phase is unaffected by carbon, but this is not the case for the γ phase.

The phase fractions were determined by Rietveld analysis of HEXRD patterns. The measurements for the HIPed alloys were carried out twice to check reproducibility. In the Ti-45Al-5Nb alloy the amount of the α_2 phase decreases from about 21 wt. % to around 17 wt. % with a carbon addition of 0.5 at. %. However, with further increase of carbon concentration, the variation of the phase fraction shows no obvious tendency.

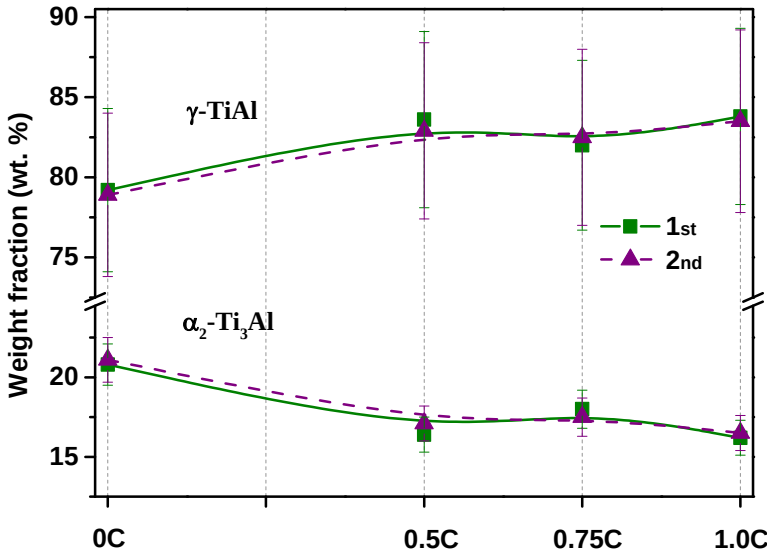

Figure 17 Phase fractions in the Ti-45Al-5Nb-xC (x=0, 0.5, 0.75 and 1.0 at. %) alloys determined by Rietveld analysis of HEXRD patterns. The data is connected by guiding spline lines.

From **Figures 16** and **17**, the influence of carbon concentration on the grain size and the phase fraction is not very significant, which is different from refs. (Yun 1997, Seo 1998, Perdrix 2001, Gerling 2008) which indicated that carbon decreased the size of lamellar colonies, reduced the lamellae spacing and increased the α_2 phase fraction. It is possible that carbon refinement on grain size is not obvious for heat treatments in the $\alpha+\gamma$ region, since the α and γ phases can block each other from growing.

3.4 Influence of carbon on lattice parameters of γ and α_2 phases

The lattice parameters were determined by Rietveld analysis from HEXRD patterns, as shown in **Figure 18**. The error bars cannot be seen due to their very small value for each data point. Two HEXRD measurements were made to ensure reproducibility and show a maximum difference in lattice parameters of about 0.002Å for both the γ and α_2 phases. This variation may be due to the different experimental setups, such as the wavelength and the distance between the specimen and the detector for example.

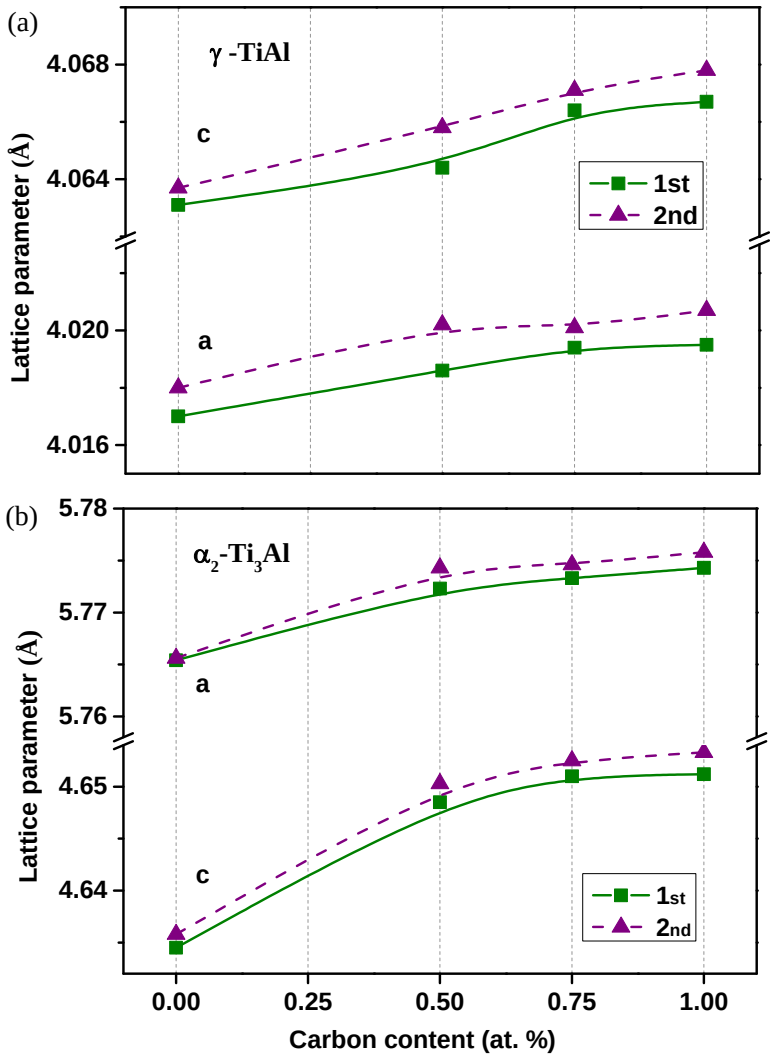

Figure 18 The influence of carbon concentration on the lattice parameters of (a) γ phase, and (b) α_2 phase in the HIPed Ti-45Al-5Nb-xC alloys (x=0, 0.5, 0.75 and 1.0 at. %) determined by Rietveld analysis of HEXRD patterns. Error bars for each data are too small to be seen on the graphs. The data is connected by guiding spline lines.

When the carbon content is lower than 0.75 at. %, lattice parameters of both α_2 and γ phases increase with increasing carbon concentration. The increase of the lattice parameters of the α_2 phase is larger than that of the γ phase, which agrees well with the results reported by Gerling et al. (Gerling 2008). It suggests that the carbon solubility in the α_2 phase is higher than in the γ phase. When the carbon concentration reaches above 0.75 at. %, interestingly the lattice parameters of both α_2 and γ phases start to become saturated, which might indicate the carbon content in both α_2 and γ phases reaches the solid-solution limit. From the research of Perdrix et al. (Perdrix 2001) on Ti-48Al-xC (x=20-6000 wt. ppm) alloys, when the carbon content was varied, the lattice parameters of the γ phase remained constant within the experimental error. While for the α_2 phase, the lattice parameters first increased and then remained stable at carbon concentrations ranging from 1000 to 6000 wt. ppm.

3.5 Influence of carbon on hardness

The influence of carbon concentration on the hardness shows a similar tendency to the lattice parameters, as shown in **Figure 19**. When the carbon content is lower than 0.75 at. %, the hardness increases linearly with increasing carbon concentration. For the carbon concentrations above 0.75 at. %, the hardness remains constant. This tendency is similar to the results reported by Perdrix et al. (Perdrix 2001) in Ti-48Al-xC (at. %) alloys. When the carbon content exceeded 1000 wt. ppm, the hardness became constant. They also considered the influence of the α_2 phase on the hardness. The amount of α_2 phase increased when the carbon content increased. Generally the hardness is related to several factors: carbon addition which introduces solid-solution hardening and precipitation hardening (depending on the precipitate size and distribution) and the microstructure including grain size and phase fraction. Since the microstructure does not vary too much after the addition of different carbon levels, the hardness increase may be attributed to solid-solution hardening and precipitation hardening. This has been investigated further by TEM investigation in **Section 3.6.2**.

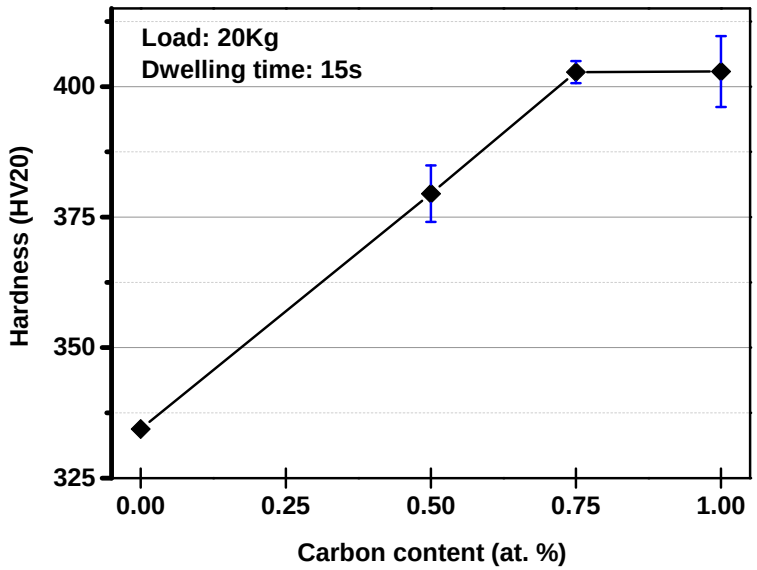

Figure 19 Influence of the carbon concentration on the Vickers hardness of the HIPed Ti-45Al-5Nb-xC (x=0, 0.5, 0.75 and 1.0 at. %) alloys.

3.6 Carbides in HIPed Ti-45Al-5Nb-xC alloys

3.6.1 Microstructure overview of the HIPed Ti-45Al-5Nb-xC alloys

Figure 20 shows the microstructure overview of the HIPed Ti-45Al-5Nb-xC (x=0, 0.5, 0.75 and 1.0 at. %) alloys. The four alloys have a similar microstructure, composed of a main γ phase and a minor α_2 phase. For the carbon-free alloy, some irregular lamellar structure is present, as marked in **Figure 20(a)**. For the carbon-doped alloys, especially for alloys with high carbon contents (0.75 and 1.0 at. %), this feature is seldom observed. The carbon concentration exhibits no obvious influence on the grain size and the phase fractions. In the Ti-45Al-5Nb-0.75C and Ti-45Al-

5Nb-1.0C alloys, pores are observed because carbides were removed during the electro-polishing process. The size and number of such pores in Ti-45Al-5Nb-0.75C are much smaller/fewer than those of Ti-45Al-5Nb-1.0C, which suggests that carbides in the 0.75C containing alloy should have a smaller size than those in the 1.0C containing alloy.

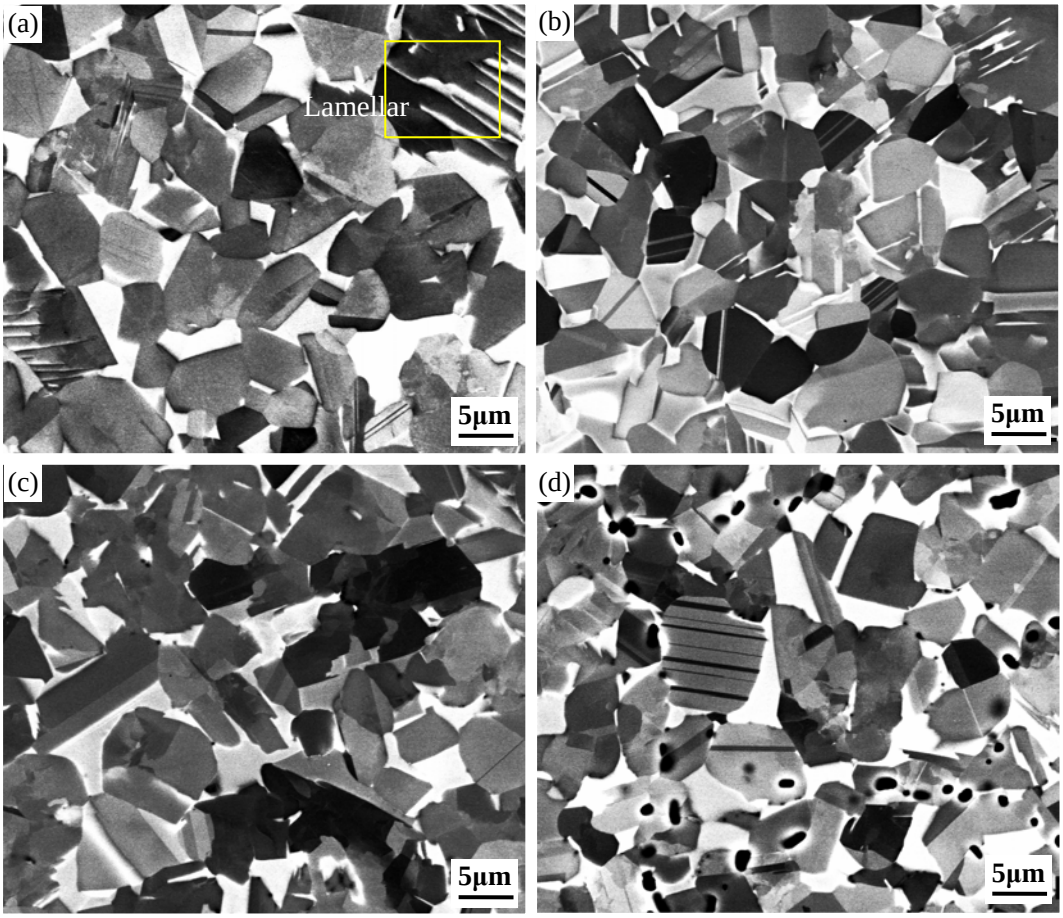

Figure 20 Microstructures of (a) Ti-45Al-5Nb, (b) Ti-45Al-5Nb-0.5C, (c) Ti-45Al-5Nb-0.75C, and (d) Ti-45Al-5Nb-1.0C alloys in the HIPed condition. SEM images were recorded using BSE mode. The γ phase shows a grey/dark contrast and the α_2 phase has a bright contrast. Specimens were prepared by electro-polishing. Carbides were removed during the electro-polishing process to leave holes.

From **Figure 21** it appears that carbides mainly form along primary powder grain boundaries, which might be explained by **Figure 22**. From the carbon element mapping of the surface of a Ti-45Al-5Nb-1.0C powder particle, carbon enriched regions are detected, where carbide nucleation and growth may take place more easily.

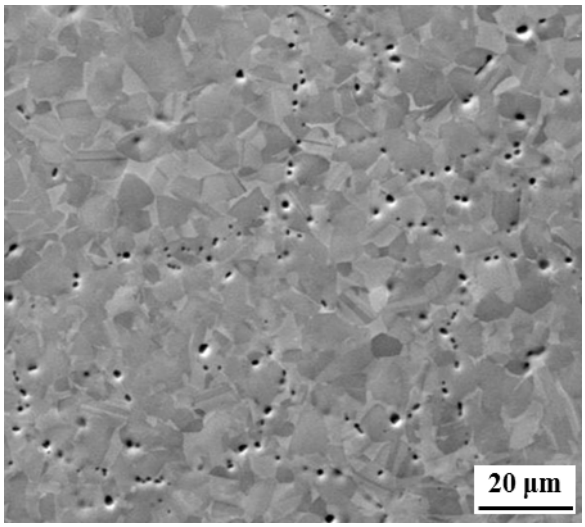

Figure 21 Microstructure of the HIPed Ti-45Al-5Nb-1.0C alloy showing that carbides obviously precipitate at primary powder boundaries. Specimen was prepared by electro-polishing. SEM image was recorded in the secondary electron (SE) mode.

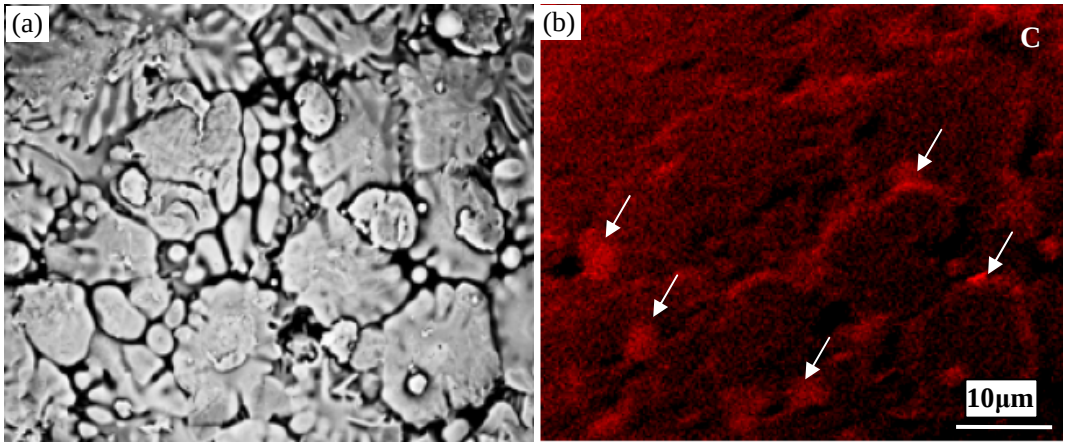

Figure 22 Carbon mapping analysis of the surface of a Ti-45Al-5Nb-1.0C powder particle, (a) SEM image of the powder surface, and (b) carbon mapping shows carbon enriched regions on the powder surface, as marked by arrows.

The enrichment of carbon at grain boundaries has been detected in the HIPed Ti-45Al-5Nb-0.75C alloy by TEM investigation using STEM mode, as shown in **Figure 23**. From the EDS line scan across a γ grain, the concentration of carbon tends to increase at the grain boundaries compared with the γ matrix. It seems that carbide nuclei might have already formed at these grain boundaries because the atomic ratio between Ti and Al there is close to the stoichiometric Ti/Al ratio of the P-Ti_3AlC phase (assuming that Nb is associated with Ti). One could argue that the Ti/Al ratio is also similar for the α_2-Ti_3Al phase. This can be excluded because the Nb level also decreases at the boundary, but it is usually enriched in α_2-Ti_3Al phase (see **Figure 95(b)**). Here it should be noted that the carbon distribution tendency in the γ grain is reliable but the detailed carbon concentration values should be treated with caution.

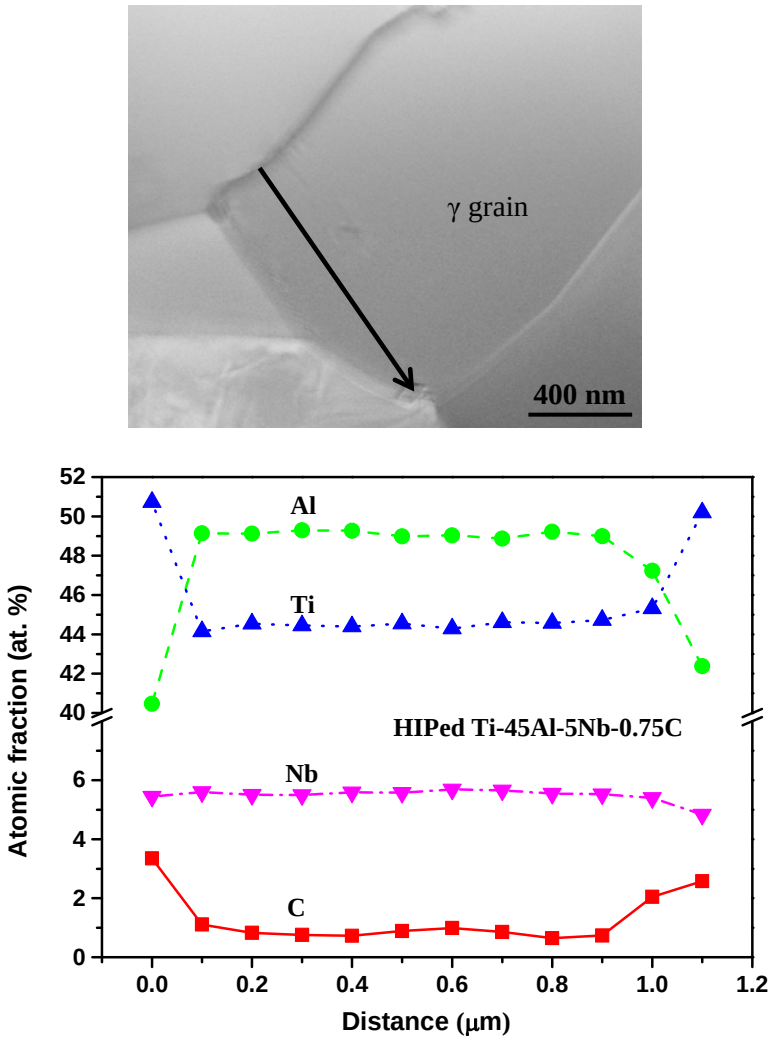

Figure 23 EDS line analysis across a γ grain in the HIPed Ti-45Al-5Nb-0.75C alloy using STEM mode. Specimen was prepared by electro-polishing. Carbon is found to be enriched at grain boundaries.

In order to preserve carbides in the matrix, vibration polishing was applied instead of electro-polishing to prepare SEM specimens. EDS analysis during SEM investigations on carbides was carried out to confirm their existence further, as shown in **Figure 24**. In the back-scattered electron mode, carbides show brighter contrast than the γ phase, while they are less bright than the α_2 phase. They appear to be standing out from the surface due to their higher hardness compared to the γ and the α_2 matrix phases (Wei 2002). The line scan indicates that the carbides are enriched in C and Ti, and are depleted in Al and Nb when compared with the matrix. However, the carbide types need be determined by further TEM investigation.

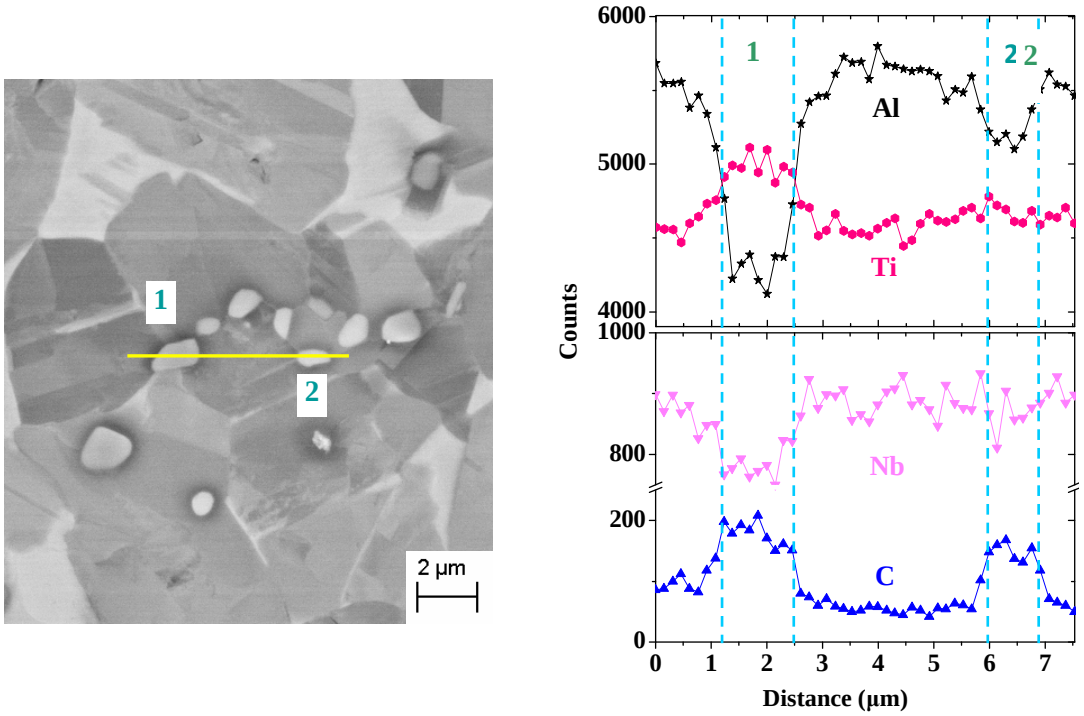

Figure 24 EDS line analysis in the HIPed Ti-45Al-5Nb-1.0C alloy. Specimen was prepared by vibration polishing. Carbides (position 1 and 2) are enriched in Ti and C, and are depleted in Al and Nb when compared to the γ matrix. SEM image was recorded in BSE mode. The brightest phase is the α_2 phase, the carbide phase is less bright, and the grey/dark phase is γ. Carbides stand out from the surface due to their higher hardness.

3.6.2 Carbide determination in the HIPed Ti-45Al-5Nb-xC alloys

In the HIPed Ti-45Al-5Nb-1.0C alloy, both H-Ti_2AlC and P-Ti_3AlC carbides have been detected.

Figure 25 shows a H-Ti_2AlC carbide existing at a grain boundary with a size about 2μm. The EDS analysis indicating that the ratio between Ti and Al is around 2:1, additionally the diffraction patterns from four zone axes which are not in the same plane, confirms the existence of H-Ti_2AlC carbides. What is more, H-Ti_2AlC carbides are found beside lamellae and twins, and in γ grains with a smaller size. No orientation relationship exists between α_2 or γ and H-Ti_2AlC carbides.

P-Ti_3AlC carbides with size about 100nm are found to be located at γ-γ grain boundaries, as shown in **Figure 26(a)**. Through analyzing the diffraction patterns in **Figure 26(b)**, P-Ti_3AlC phase have the following orientation relationship with one of the neighboring γ grain: $[001]_\gamma//[001]_P$, $(100)_\gamma//(100)_P$ and grow into this grain.

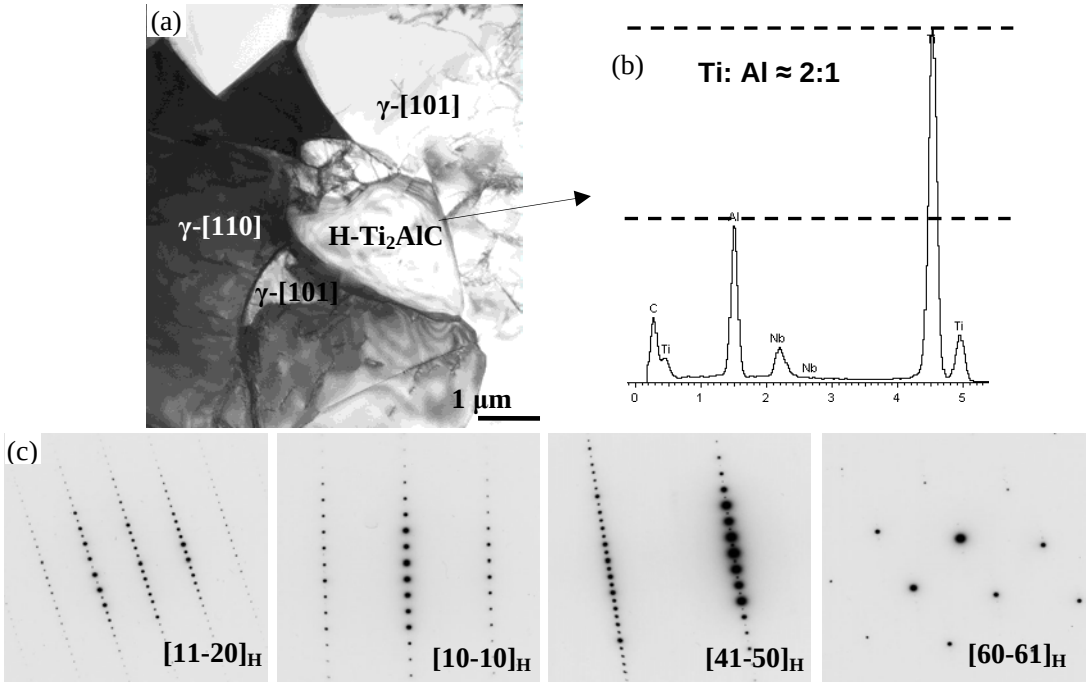

Figure 25 H-type carbides in the HIPed Ti-45Al-5Nb-1.0C alloy (a) at grain boundaries, (b) EDS analysis of the H-type carbide shows the atomic ratio between Ti and Al is about 2, (c) diffraction patterns of the H-type carbide along [11-20], [10-10], [41-50] and [60-61] zone axes.

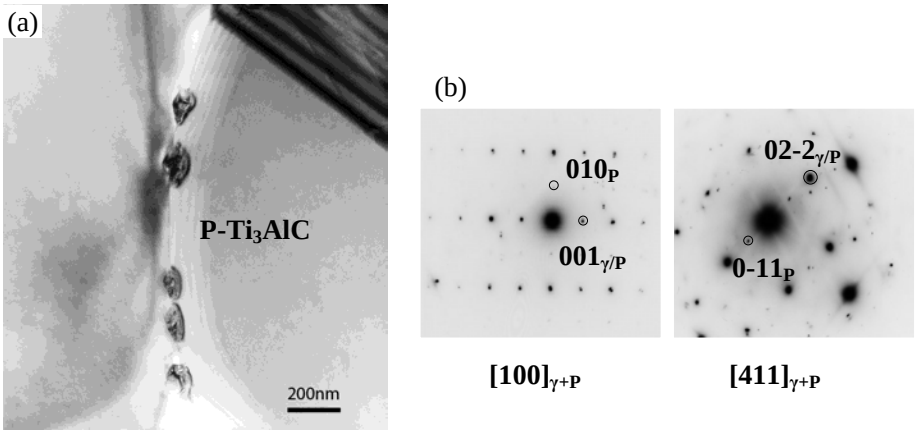

Figure 26 P-type carbides in the HIPed Ti-45Al-5Nb-1.0C alloy (a) at grain boundaries, (b) diffraction patterns of P-type carbide with γ matrix along [100] and [411] zone axes.

For comparison in the HIPed Ti-45Al-5Nb-0.75C alloy only several H-type carbides are occasionally observed at triple junctions, at grain boundaries, near lamellae and γ-twins. **Figure 27** shows an example of a H-type carbide at a grain boundary, which is confirmed by the diffraction pattern and the EDS result. However P-type carbides, see **Figure 28** for an example**,** have been commonly observed at triple junctions and at grain boundaries and hold the orientation relationship with one of the neighboring γ grains: $[001]_{\gamma}//[001]_{P}$, $(100)_{\gamma}//(100)_{P}$ and grow into this grain.

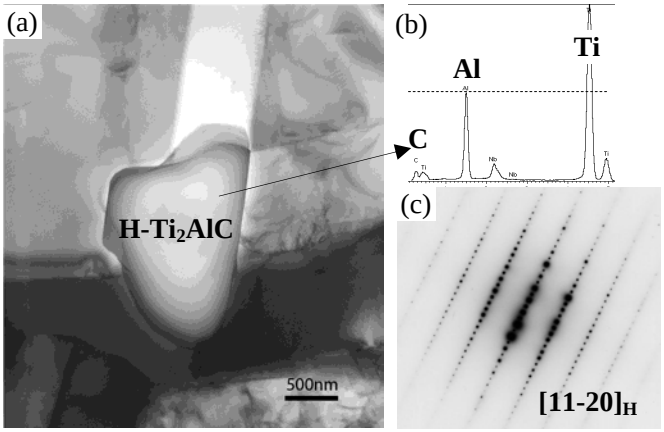

Figure 27 H-type carbide in the HIPed Ti-45Al-5Nb-0.75C alloy (a) at a grain boundary, (b) EDS analysis of the H-type carbide and (c) diffraction pattern of the H-type carbide along the [11-20] zone axis.

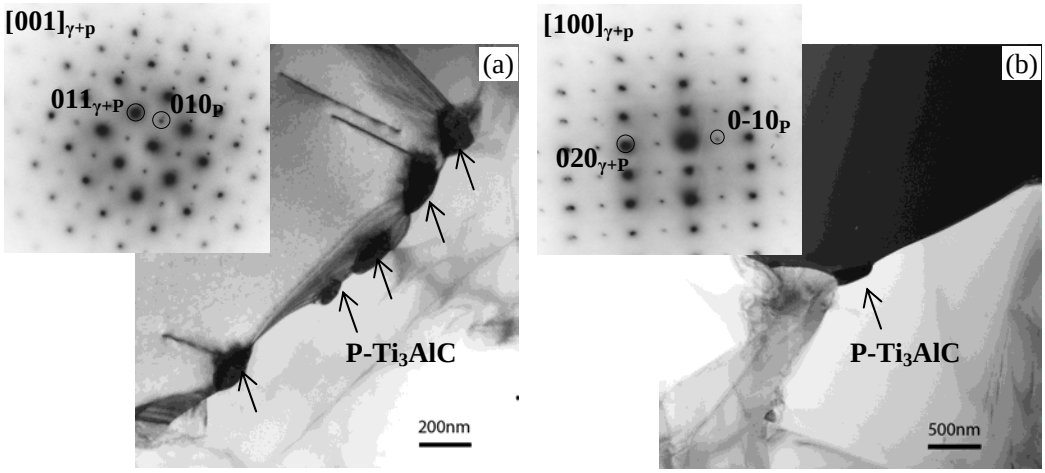

Figure 28 P-type carbides in the HIPed Ti-45Al-5Nb-0.75C alloy at (a) a grain boundary and (b) triple junction, together with diffraction patterns.

For Ti-45Al-5Nb-0.5C, the studies of Gerling et al. (Gerling 2008), Scheu et al. (Scheu 2009), and Staron et al. (Staron 2010) found no obvious evidence for the existence of carbides using TEM, atom probe (AP), and small angle neutron scattering (SANS) methods. However in our HRTEM investigation, occasionally some small P-type carbides were found to exist in the γ matrix, but this is not a typical feature (Gabrisch 2013).

3.6.3 Phase identification in the HIPed Ti-45Al-5Nb-xC alloys by HEXRD

In order to further confirm the existence of carbides, HIPed Ti-45Al-5Nb-xC alloys were also investigated by HEXRD at room temperature. **Figure 29** show that all the alloys have reflections from γ-TiAl and α_2-Ti_3Al phases. The HIPed Ti-45Al-5Nb-1.0C alloy has extra reflections which are indexed as H-Ti_2AlC (marked by red solid arrows) and P-Ti_3AlC (green dashed arrows). For HIPed Ti-45Al-5Nb-0.75C alloy reflections from the P-Ti_3AlC phase (green dashed arrows) are also detected, while H-Ti_2AlC reflections are missing except one broad peak (red solid arrow), which

suggests the fraction of the H-Ti_2AlC phase should be lower than the detection limit of the HEXRD method. The reflections of the P-Ti_3AlC phase appear to shift slightly to a higher scattering vector with increasing carbon concentration. This may be because there is less carbon in the interstices of the P-type carbides on account of the higher fraction of H-type carbides. It should be noted that extra reflections, as marked by a rectangle, show up due to a weak component of higher harmonic wavelength ($\lambda/2$) within the incident beam.

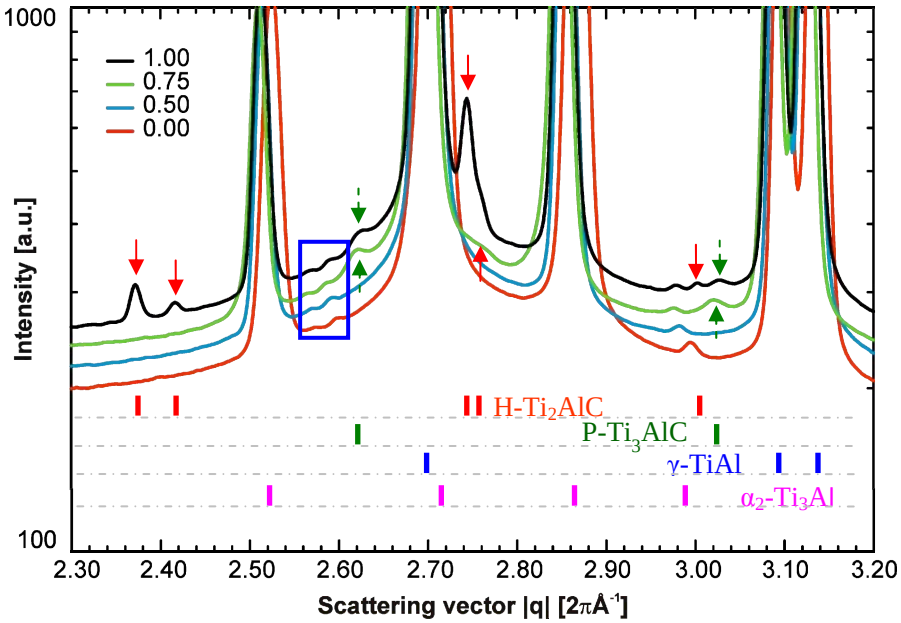

Figure 29 HEXRD patterns of the Ti-45Al-5Nb-xC (x = 0, 0.5, 0.75 and 1.0 at. %) alloys. $|\mathbf{q}| = 2\pi/d = (2\pi/\lambda)\cdot 2\sin\theta$.

The HEXRD results indicate that the carbon content might be close to the solid-solution limit in the HIPed Ti-45Al-5Nb-0.5C alloy (assuming that the HIPed alloy is in thermodynamic equilibrium, which is very likely not the case). H-Ti_2AlC carbides with a large size are formed predominately in alloys with higher carbon content, while P-Ti_3AlC carbides are more likely to form in lower carbon containing alloys. This may explain why nearly no pores were found in HIPed Ti-45Al-5Nb-0.5C, only small pores were observed in HIPed Ti-45Al-5Nb-0.75C and big holes were seen in HIPed Ti-45Al-5Nb-1.0C as shown in **Figure 20**.

4. Microstructural evolution and thermal stability of carbides

4.1 Dissolution of primary carbides via heat treatment

From literature it is well known that the H-Ti_2AlC phase is more thermally stable than the P-Ti_3AlC phase and that it forms at higher temperatures (Appel 2000). Exact details, on dissolution temperature for example, vary according to the different alloy systems investigated.

From **Section 3.6.2**, both H-Ti_2AlC and P-Ti_3AlC carbides are found in the HIPed Ti-45Al-5Nb-1.0C alloy. From the research of Christoph et al. (Christoph 1997), carbides (both P- and H-type) were dissolved in Ti-48.5Al-0.4C (at. %) after heat treatment at 1250°C. Therefore heat treatments at 1250°C for 5 to 96h were conducted for Ti-45Al-5Nb-1.0C, as shown in **Figure 30**. With increasing time, the microstructure coarsens. Additionally a number of holes are observed. They are formed by the removal of carbides from the matrix during the electro-polishing process. In the following the development of carbide size and number will be interpreted from the holes. Thus the number of carbides decreases and their size increases after longer solution times.

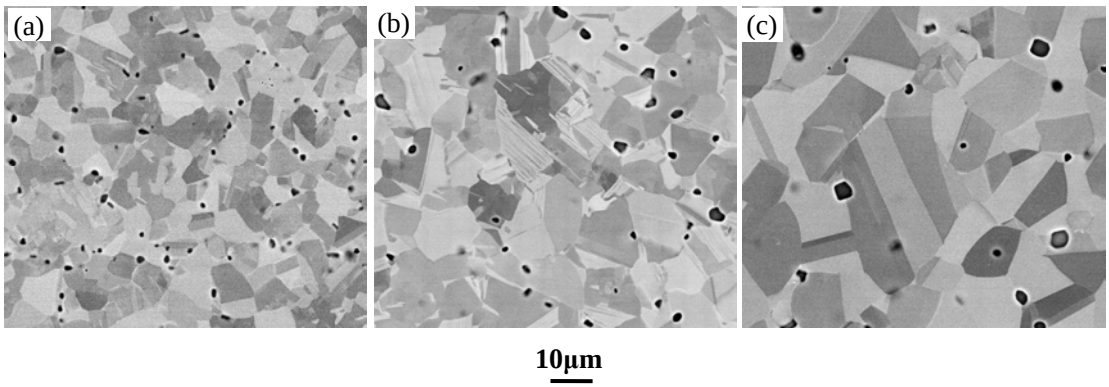

Figure 30 Microstructures of the Ti-45Al-5Nb-1.0C alloy after solution treatments at 1250°C for (a) 5h, (b) 48h, (c) 96h, oil quenched (OQ). Specimens were prepared by electro-polishing. Pores are left because carbides were removed during the electro-polishing process. All SEM images have the same scale bar and were recorded in the back-scattered electron (BSE) mode.

A specimen that had been solution treated at 1250°C for 96h was selected to be prepared by vibration polishing, as shown in **Figure 31**. The precipitates, with a larger size than those in the HIPed condition, are observed at grain boundaries and appear to have a plate-like morphology. So at 1250°C, carbides are thermally stable and coarsen.

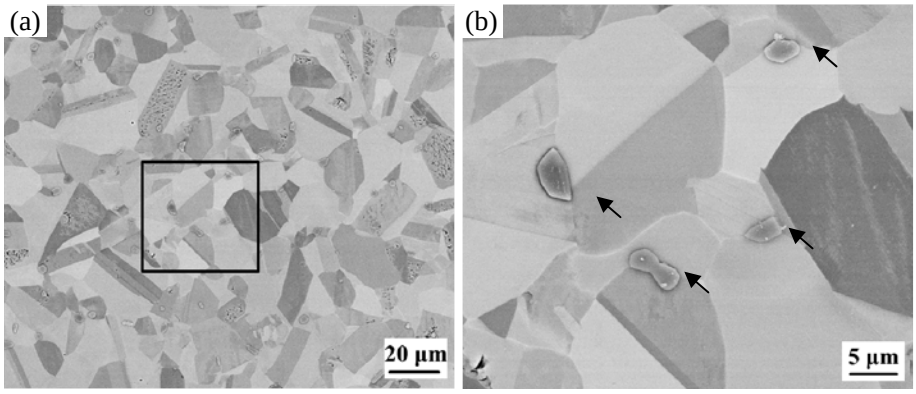

Figure 31 Microstructures of Ti-45Al-5Nb-1.0C after solution treatment at 1250°C for 96h, OQ (a) low magnification and (b) high magnification of the marked area in (a) The specimen was prepared by vibration polishing. SEM images were recorded in BSE mode.

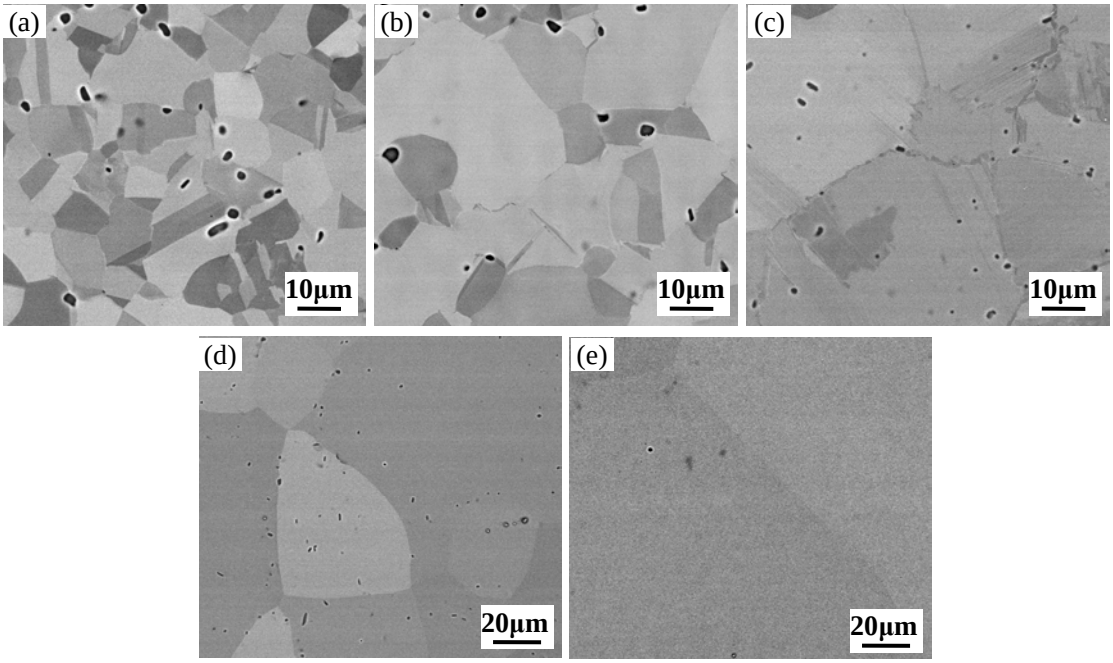

Figure 32 Microstructures of Ti-45Al-5Nb-1.0C after solution treatments at (a) 1280°C for 24h, OQ, (b) 1300°C for 24h, OQ, (c) 1320°C for 1h, water quenched (WQ), (d) 1350°C for 5h, WQ, and (e) 1400°C for 1h, OQ. Specimens were prepared by electro-polishing. SEM images were recorded in BSE mode.

Increasing the solution temperature from 1280 to 1400°C resulted in significant coarsening of the microstructure, as shown in **Figure 32**. For heat treatments at temperatures of 1320°C and above, the microstructure is mainly composed of the α_2 phase. As explained earlier the holes seen in the microstructure are formed by electro-polishing. Thus the number and size of carbides can be induced from the development of holes. On increasing the temperature from 1280 to 1300°C, after 24h the number of holes decreases and the hole size increases. After heat treatment above 1320°C for 1h the size of the holes is reduced (**Figure 32(c)**). But due to this short heat treatment time, it cannot be stated definitely that carbides start to dissolve at 1320°C. At 1350°C for 5h the hole size reduces and finally after 1h at 1400°C no holes are observed and

carbides appear to be dissolved. This is also confirmed by the in situ HEXRD investigation where reflections from carbides disappear at 1400°C.

In the HIPed Ti-45Al-5Nb-0.75C alloy, P-Ti_3AlC carbides were often observed while only several H-Ti_2AlC carbides were detected. **Figure 33** shows the microstructures of the alloy after being heat treated at 1250°C for 5, 24 and 48h. Grain coarsening is obvious after 24h and several big holes are observable.

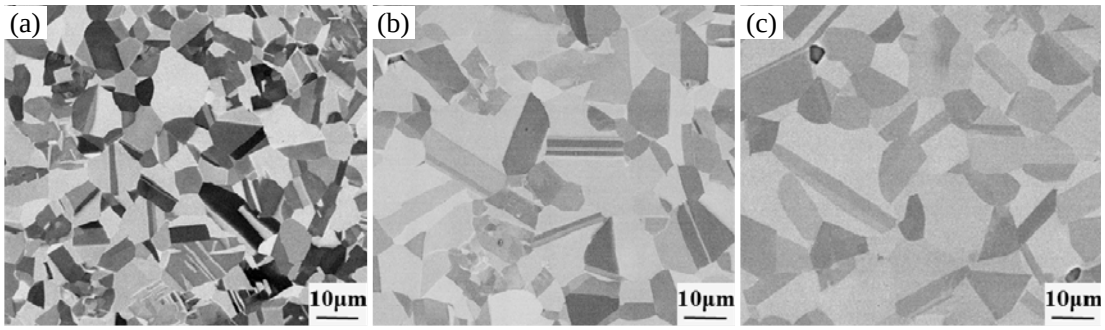

Figure 33 Microstructures of the Ti-45Al-5Nb-0.75C alloy after solution treatments at 1250°C for (a) 5h, (b) 24h and (c) 48h, OQ. Specimens were prepared by electro-polishing. SEM images were recorded in BSE mode.

TEM investigation of the Ti-45Al-5Nb-0.75C alloy after heat treatment at 1250°C for 5h indicates that small P-Ti_3AlC carbides are formed at grain boundaries (**Figure 34(a)**), during transfer of the specimen from the furnace to the oil. Two observations support this point, (1) the size of the P-Ti_3AlC carbides is very small, and (2) the in-situ HEXRD experiment shows that the P-Ti_3AlC phase is dissolved above 1100°C. Only one big H-Ti_2AlC carbide (**Figure 34(b)**), confirmed by diffraction along the $[41\text{-}50]_H$ direction (**Figure 34(c)**), is found in two TEM discs.

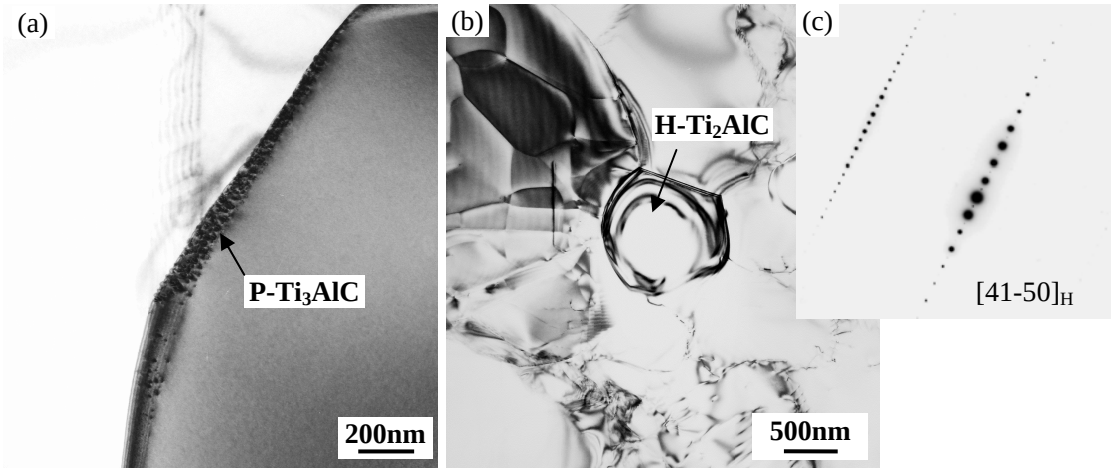

Figure 34 TEM investigation of the Ti-45Al-5Nb-0.75C alloy after solution treatment at 1250°C for 5h, OQ, (a) Small P-Ti_3AlC carbides form during transfer of the specimen from the furnace to the oil, (b) residual H-Ti_2AlC carbide at a triple junction, (c) diffraction pattern of the H-Ti_2AlC carbide along the [41-50] direction.

This specimen was investigated further by HEXRD, as shown in **Figure 35**. Only reflections from the γ and α_2 phases are present. The fraction of residual carbides in the heat-treated Ti-45Al-5Nb-0.75C alloy is lower than the detection limit of the HEXRD method (the detection limit is around 0.05-0.1 wt. %). From Rietveld analysis, the fractions of γ and α_2 phases are 54.2 and 45.8, wt. %, respectively. The lattice parameters of the phases are: a_γ=4.016Å, c_γ=4.068Å and $a_{\alpha 2}$=5.760Å, $c_{\alpha 2}$=4.637Å. Compared with those of the HIPed condition (a_γ=4.020Å, c_γ=4.067Å, and $a_{\alpha 2}$=5.775Å, $c_{\alpha 2}$=4.653Å), a_γ decreases very slightly, but c_γ remains almost constant. Both $a_{\alpha 2}$ and $c_{\alpha 2}$ are obviously reduced compared to the HIPed condition. After solution treatment, carbon may be redistributed and goes from the primary α_2 phase to newly formed α_2 phase. As a consequence the lattice parameters of the α_2 phase are decreased. The lattice parameters of the γ phase show no obvious variation which seems to support the view proposed by Menand et al. (Menand 1996) that the interstitial level in the γ phase is not lowered by the scavenging effect of the α_2 phase.

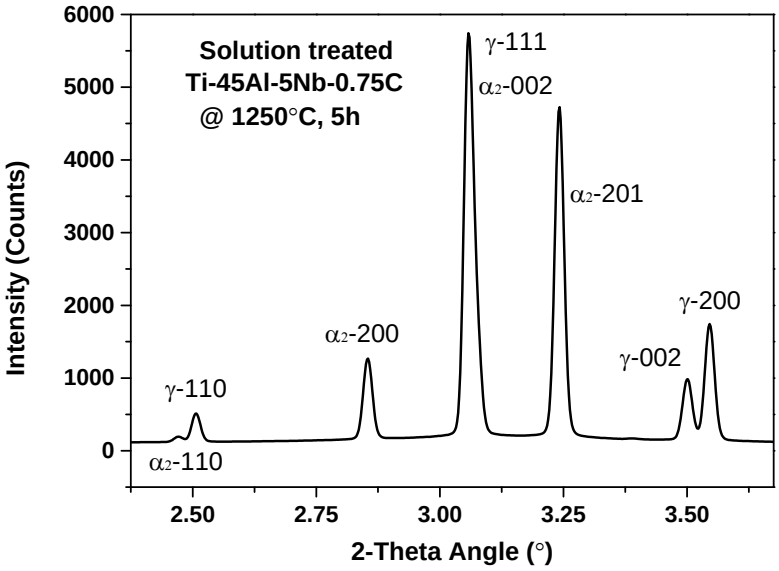

Figure 35 HEXRD pattern of the Ti-45Al-5Nb-0.75C alloy after heat treatment at 1250°C for 5h, OQ. The pattern shows reflections from γ-TiAl and α_2-Ti_3Al phases. Wavelength λ=0.12398Å.

After Ti-45Al-5Nb-0.75C was heat treated at 1280°C no big holes are found, however the microstructure obviously coarsens, see **Figure 36**. From HEXRD investigations no reflections from the P-Ti_3AlC and H-Ti_2AlC carbides were observed.

From the above results, in the Ti-45Al-5Nb-0.75C alloy carbides have lost stability and can thus be considered as being dissolved in the matrix at 1250°C. Therefore heat treatments performed at 1250°C for 5h were taken to dissolve primary carbides and to homogenize the carbon distribution in the matrix without resulting in excessive coarsening of the microstructure.

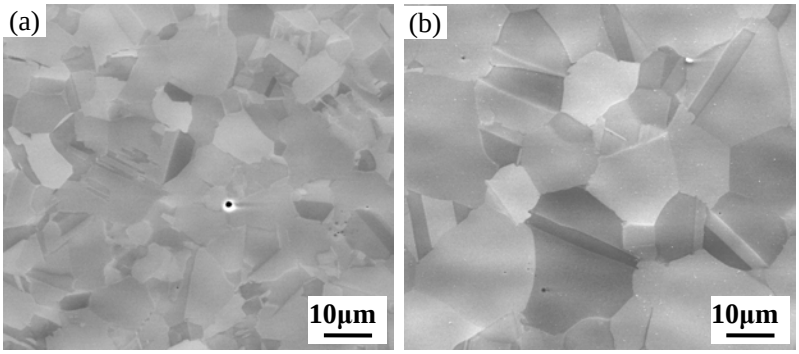

Figure 36 Microstructures of Ti-45Al-5Nb-0.75C after solution treatments at 1280°C for (a) 2h and (b) 24h, OQ. Specimens were prepared by electro-polishing. SEM images were recorded in SE mode.

For HIPed Ti-45Al-5Nb-0.5C, very few P-type carbides were observed by HRTEM. In order to compare with Ti-45Al-5Nb-0.75C at a similar metallurgical condition, heat treatment at 1250ºC for 5h was also applied to the HIPed Ti-45Al-5Nb-0.5C in order to dissolve primary carbides and homogenize the microstructure, as shown in **Figure 37**.

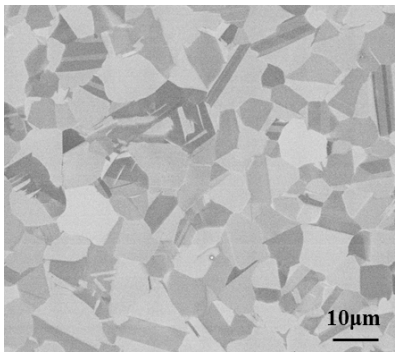

Figure 37 Microstructure of HIPed Ti-45Al-5Nb-0.5C after solution treatment at 1250°C for 5h, OQ. Specimens were prepared by electro-polishing. SEM image was recorded in BSE mode.

From the HEXRD investigation no diffractions peaks from carbides were observed for HIPed Ti-45Al-5Nb-0.5C after solution treatment at 1250°C for 5h. The microstructure is composed of γ and α_2 phases, with phase fractions of 53.3 and 46.7, wt. %. The corresponding lattice parameters are a_γ=4.016Å, c_γ=4.069Å and $a_{\alpha2}$=5.762Å, $c_{\alpha2}$=4.631Å respectively. Compared with those in the HIPed condition (a_γ=4.020Å, c_γ=4.066Å, and $a_{\alpha2}$=5.774Å, $c_{\alpha2}$=4.650Å), the lattice parameters of the γ phase remain relatively stable, while the lattice parameters of the α_2 phase have decreased. As explained above this could also be caused by carbon redistribution from the primary α_2 phase to the α_2 phase newly formed at 1250°C. Meanwhile it supports the idea that the interstitial level in the γ phase is not reduced by the scavenging effect of the α_2 phase.

To summarize, carbides are highly thermally stable in Ti-45Al-5Nb-1.0C and can remain in the matrix up to 1400°C. In Ti-45Al-5Nb-0.5C and Ti-45Al-5Nb-0.75C carbides go into solution at temperatures of 1250°C and above. Christoph et al.

(Christoph 1997) also reported that carbides went into solution in the Ti-48.5Al-0.4C alloy after being heat treated at 1250°C. Based on this finding it is proposed that the thermal stability of carbides is related to the carbon concentration in the alloy. However the research by Tian et al. (Tian 1997) on $(Ti_{0.5}Al_{0.5})_{99.7}C_{0.3}$, $(Ti_{0.5}Al_{0.5})_{99.5}C_{0.5}$, and $(Ti_{0.5}Al_{0.5})_{99}C$ alloys after solution treatment at 1250°C for 168h suggested that the maximum solid solubility of carbon in TiAl at 1250°C might be less than 0.5 mol%. The difference between this literature and the current research may be attributed to differences in chemical composition (Al and Nb contents).

4.2 Microstructure evolution in heat-treated alloys

From the work presented in **Section 4.1** on the HIPed Ti-45Al-5Nb-1.0C alloy, carbides are very stable and exist up to 1400°C. It is difficult to dissolve primary carbides without the microstructure coarsening too much. For the HIPed Ti-45Al-5Nb-0.5C and HIPed Ti-45Al-5Nb-0.75C alloys, carbides can be treated to go into solution after treatment at 1250°C for 5h. Moreover the 0.5C and 0.75C containing alloys may be more interesting for application. Therefore only these two alloys were used in further heat treatments to investigate carbide precipitation and their thermal stability. In **Section 4.2**, the microstructural evolution of heat-treated Ti-45Al-5Nb-xC alloys (x=0.5 and 0.75 at. %) is discussed.

4.2.1 Microstructure and phase identification

From **Section 3.6** it is known that the HIPed Ti-45Al-5Nb-0.5C alloy has a similar microstructure to the HIPed Ti-45Al-5Nb-0.75C alloy, except that many more primary P-type carbides and several H-type carbides are found in the HIPed Ti-45Al-5Nb-0.75C alloy. From **Section 4.1** after solution treatment at 1250°C for 5h, the solution treated Ti-45Al-5Nb-0.5C alloy also has a similar microstructure to that of the solution treated Ti-45Al-5Nb-0.75C alloy.

Figure 38 shows the microstructures for HIPed & Annealed Ti-45Al-5Nb-0.5C alloy after annealing at 800 to 1000°C, FC. The microstructures are composed mostly of γ phase and a minor amount of α_2 phase. The γ phase shows a grey contrast and the α_2 phase has a bright contrast in the back-scattered electron imaging mode. As increasing the temperature, the microstructure does not show any obvious grain growth. As earlier, holes exist at grain boundaries in some conditions because carbides are removed during the electro-polishing process. As explained earlier the development of carbides during annealing has been inferred from the development of holes. After 800°C at 24h, small holes have developed at grain boundaries. With increasing time, the number and the size of holes increase. At 900°C after 168h, the number of holes reduces and their size increases, which suggests that the grain boundary carbides have coarsened. However, after 96h at 1000°C, no holes are observed and grain boundary carbides are considered to be dissolved in the matrix.

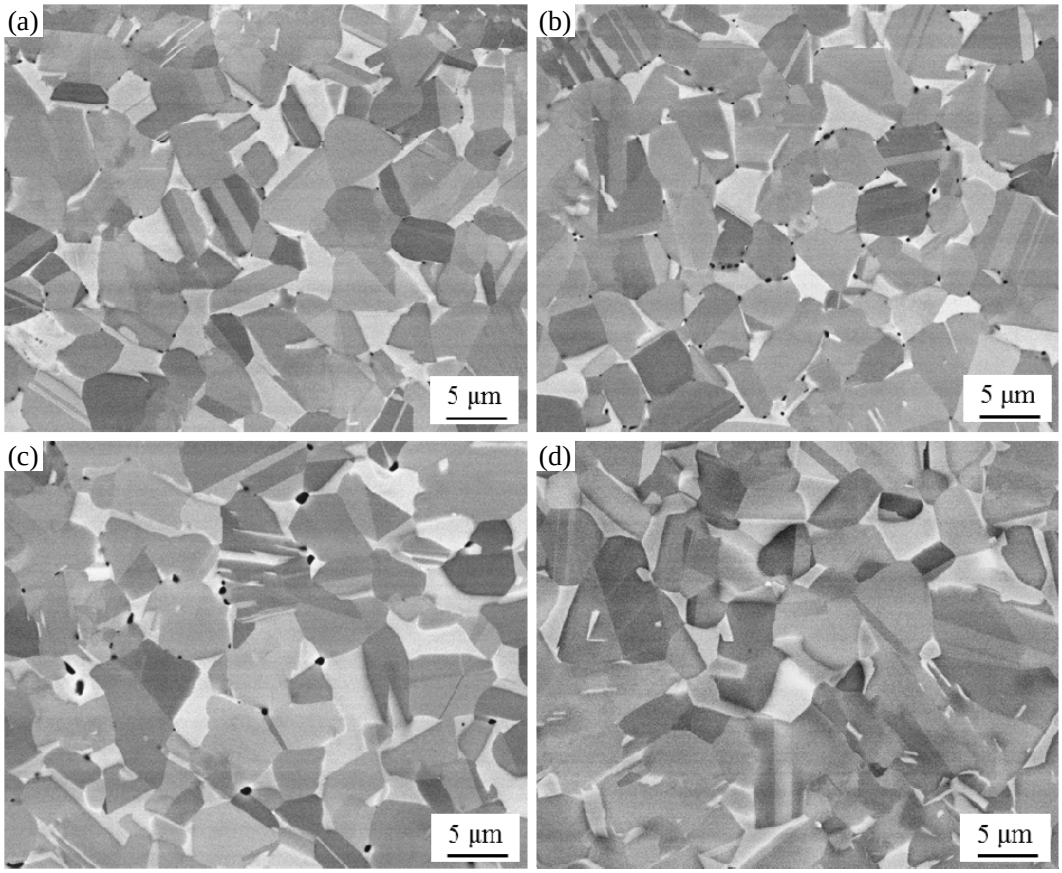

Figure 38 Microstructures of the HIPed & Annealed Ti-45Al-5Nb-0.5C alloy at (a) 800°C for 24h, (b) 800°C for 168h, (c) 900°C for 168h and (d) 1000°C for 96h (FC). SEM images were recorded in BSE mode. The γ phase shows a grey contrast and the α_2 phase has a bright contrast. Specimens were prepared by electro-polishing. Holes were formed because carbides were removed during the electro-polishing process.

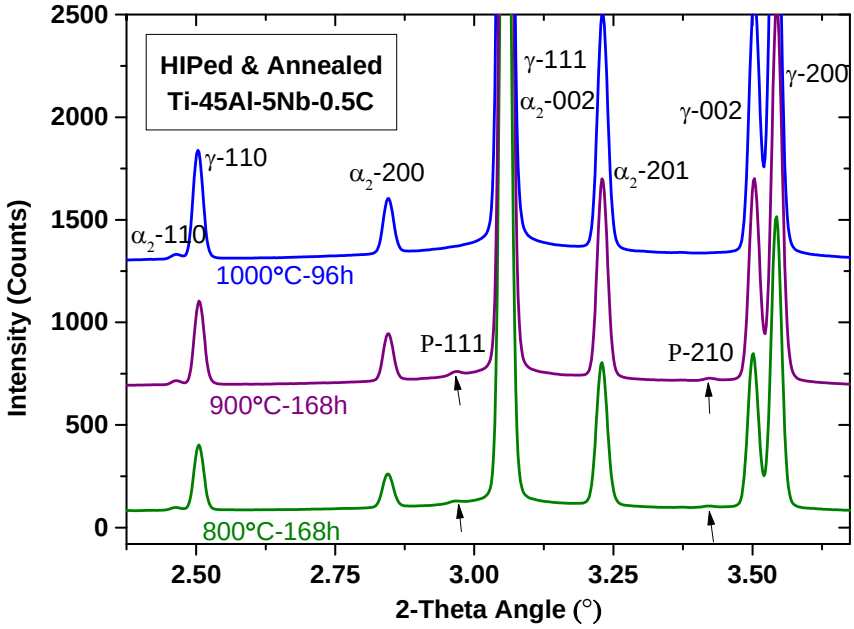

Figure 39 HEXRD diffractograms of the HIPed & Annealed Ti-45Al-5Nb-0.5C alloy after annealing at 800 and 900°C for 168h and at 1000°C for 96h. Wavelength λ=0.12398Å.

The alloy was also investigated by HEXRD. The diffractograms from HIPed & Annealed Ti-45Al-5Nb-0.5C alloy after annealing at 800 and 900°C for 168h and at 1000°C for 96h (FC) are shown in **Figure 39**. All the heat-treated conditions have reflections from γ and α_2 phases. After 168h at 800 and 900°C reflections from the P-Ti_3AlC phase are observed. However, at 1000°C carbide diffraction peaks disappear, which suggests that at this temperature the P-Ti_3AlC phase is dissolved or at least the amount of P-Ti_3AlC phase below the detection limit of the HEXRD method. This is in agreement with the SEM investigation.

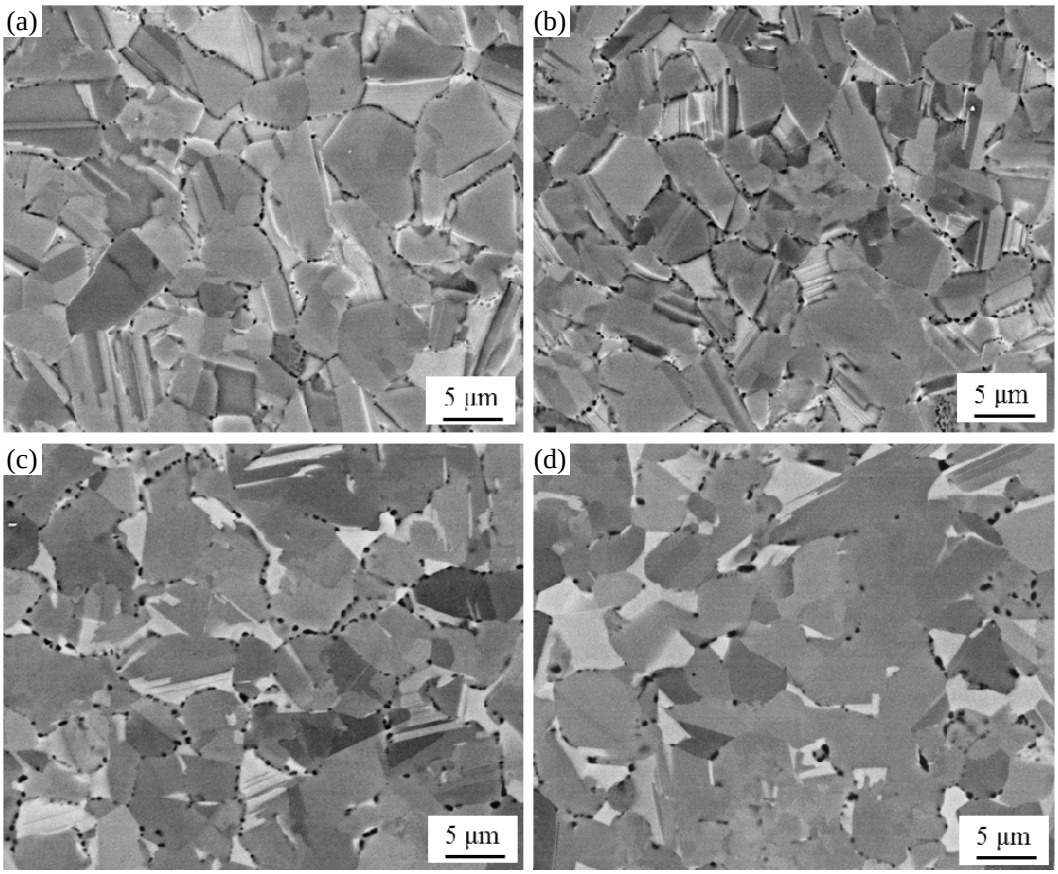

Figure 40 Microstructures of the HIPed & Annealed Ti-45Al-5Nb-0.75C alloy after annealing at (a) 800°C for 24h, (b) 800°C for 168h, (c) 900°C for 168h and (d) 1000°C for 168h. SEM images were recorded in BSE mode. Specimens were prepared by electro-polishing. Holes were left because carbides were removed during the electro-polishing process.

Figure 40 shows the microstructure of the HIPed & Annealed Ti-45Al-5Nb-0.75C alloy after various annealing treatments. As for the HIPed & Annealed Ti-45Al-5Nb-0.5C alloy, the different microstructures are composed mostly of γ phase and a small amount of α_2 phase. With increasing annealing time and temperature, the microstructure also shows no obvious grain growth. For all annealing conditions a higher density of holes, which are assumed to be where carbides were prior to electro-polishing, was observed when compared to the HIPed & Annealed Ti-45Al-5Nb-0.5C alloy. After 24h at 800°C, holes at grain boundaries are small in size. With the increasing annealing time at 800°C, the microstructure shows no obvious changes. After 168h at 900°C, holes become large, which suggests carbides at grain boundaries

grow. After 168h at 1000°C, grain boundary carbides coarsen further and this is associated with a decrease in the number of holes.

The phases in the HIPed & Annealed Ti-45Al-5Nb-0.75C alloy after the different annealing treatments were also identified by HEXRD, as shown in **Figure 41**. Reflections from γ, α_2 and P-Ti_3AlC phases can be observed for all conditions. With increasing annealing temperature, the intensity of the reflections from P-Ti_3AlC carbides tends to increase. Thus the fraction of carbides in the HIPed & Annealed Ti-45Al-5Nb-0.75C increases up to 1000°C. This suggests that the dissolution behavior of the P-Ti_3AlC phase depends on the carbon concentration because in the HIPed & Annealed Ti-45Al-5Nb-0.5C alloy the carbides have dissolved after similar annealing at 1000°C.

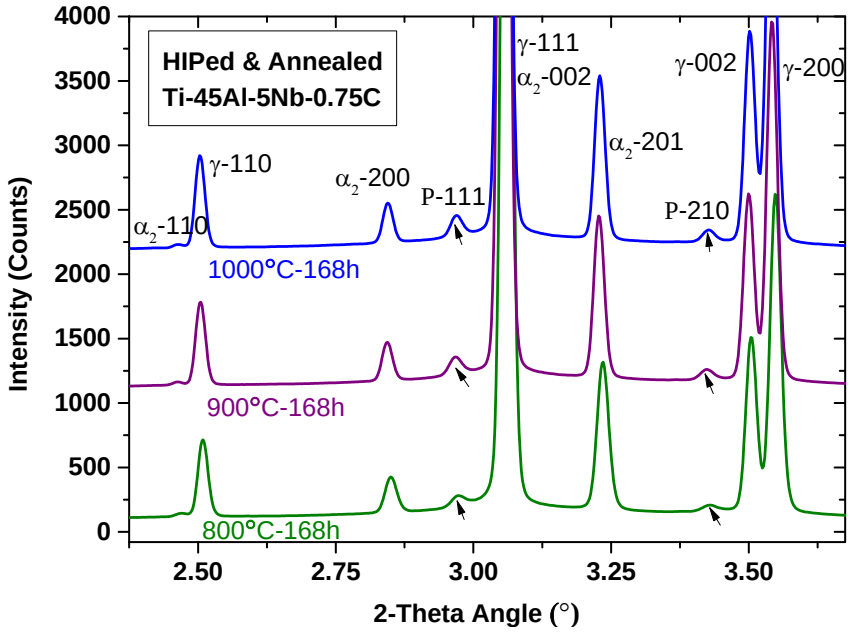

Figure 41 HEXRD patterns of the HIPed & Annealed Ti-45Al-5Nb-0.75C alloy after annealing at 800, 900 and 1000°C for 168h. Wavelength λ=0.12398Å.

Figure 42 shows an overview of the microstructures of Solution Treated & Annealed Ti-45Al-5Nb-0.5C after solution treatment at 1250°C for 5h and subsequent annealing at 800°C for 24, 168 and 1104h. The microstructures are composed of γ and α_2 phases. Compared with the HIPed & Annealed Ti-45Al-5Nb-0.5C alloy, the microstructures have large grains and a larger volume fraction of lamellar structure. From Rietveld analysis, as described in **Section 4.1**, the phase fractions of the γ and α_2 phases are 54.2 and 45.8, wt. %, respectively in Ti-45Al-5Nb-0.5C after solution treatment at 1250°C for 5h. During annealing the high-temperature α phase transforms to a lamellar structure. The lamellar spacing is very fine after 24h, as shown in the TEM image recorded using a [11-20]α_2/[110]γ direction (**Figure 42(b)**). After 168h, the lamellar spacing does not seem to coarsen too much. Some lamellar colonies tend to decompose (as marked by arrows), which is more obvious in the alloy after 1104h at 800°C. Most lamellar structures decompose into equiaxed grains and some grains

show strong bright contrast in the back-scattered electron mode. The primary equiaxed γ grains do not exhibit obvious growth. Meanwhile at grain boundaries, small holes that are introduced by the separation of carbides from the matrix are observed after 168h and are more obvious after 1104h. This may suggest that carbides at grain boundaries grow after long-time annealing. But in comparison with the HIPed & Annealed Ti-45Al-5Nb-0.5C alloy, holes are not as frequently observed, which suggests that grain boundary precipitates seem to have a smaller size and density in the Solution Treated & Annealed Ti-45Al-5Nb-0.5C alloy.

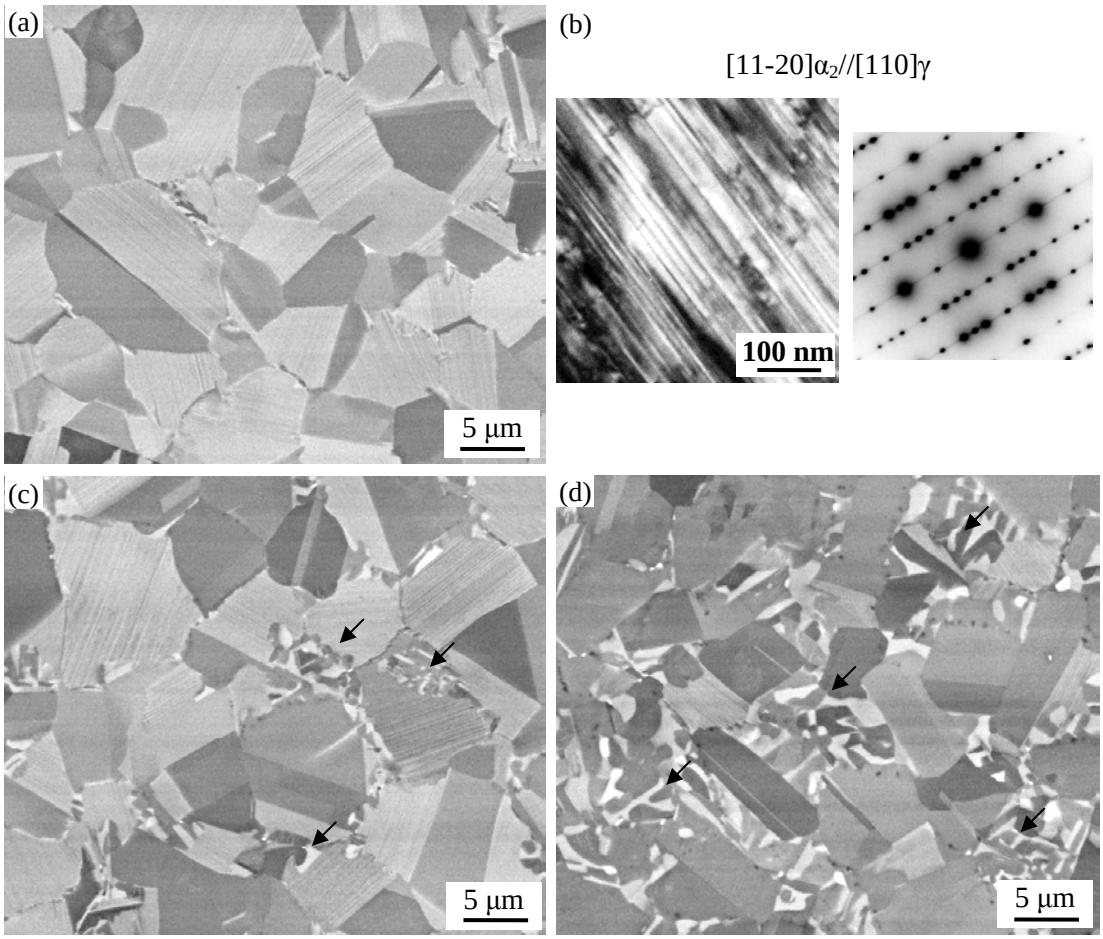

Figure 42 Microstructure of the Solution Treated & Annealed Ti-45Al-5Nb-0.5C alloy after solution treatment at 1250°C for 5h (OQ) and subsequent annealing at 800°C for (a) 24h, (b) TEM image illustrates the fine lamellae spacing after 24h, recorded along [11-20]α_2/[110]γ direction, (c)168h and (d) 1104h (FC). SEM images were recorded in BSE mode. Specimens were prepared by electro-polishing.

The alloy at heat-treated conditions was also investigated by HEXRD. **Figure 43** shows diffractograms from the Solution Treated & Annealed Ti-45Al-5Nb-0.5C alloy after solution treatment at 1250°C for 5h and subsequent annealing at 800°C for 24, 168 and 1104h. All the spectrums have reflections from γ-TiAl and α_2-Ti_3Al phases. However, only the condition with a long annealing time displays obvious diffraction peaks from the P-Ti_3AlC phase. Additionally the reflections shift to a lower diffraction angle with increased annealing time, especially for the α_2 phase.

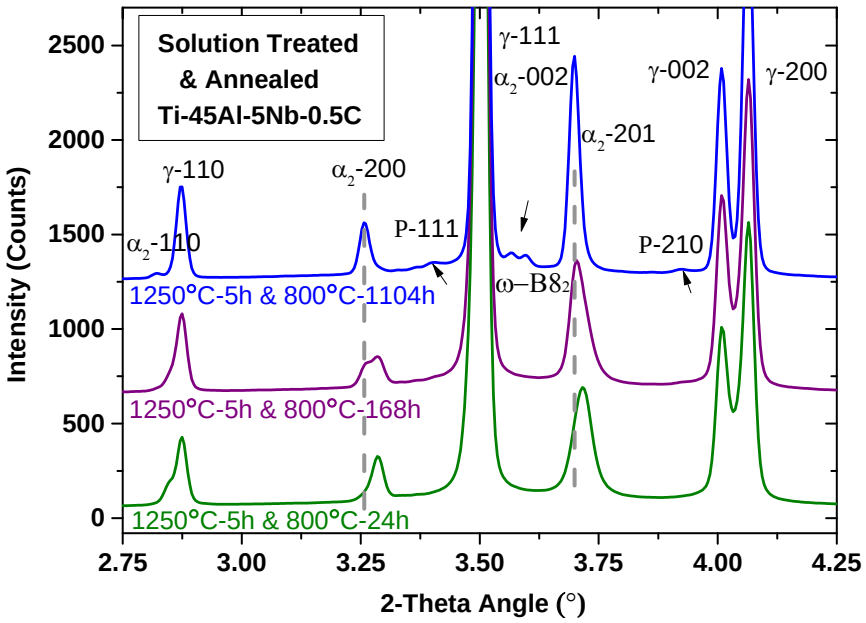

Figure 43 HEXRD diffractograms for the Solution Treated & Annealed Ti-45Al-5Nb-0.5C alloy after solution treatment at 1250°C for 5h (OQ) and subsequent annealing at 800°C for 24, 168 and 1104h (FC). Wavelength λ=0.1425Å.

After solution treatment at 1250°C (OQ) the alloy retains the high-temperature microstructure, which should have different phase fractions and phase compositions compared to the equilibrium low-temperature microstructure. During subsequent annealing at 800°C, the microstructure does not attain thermodynamic equilibrium after a short time due to the low temperature. With increasing annealing time, the microstructure gradually becomes equilibrium, thus diffraction peaks shift closer to their equilibrium positions after 1104h. The reason for the diffraction peak shift may be attributed to the variation of Al towards equilibrium condition. This will be discussed further in **Section 4.2.3**. The diffraction peaks after shorter annealing times are broader due to the formation of very fine lamellae. After annealing for 1104h, most of the lamellae structures decompose into equiaxed grains and lamellae with a coarse spacing, this results in that the reflections become narrower. As will be described in **Section 4.3**, P-Ti_3AlC carbides in the γ matrix have a very fine size. Thus the HEXRD reflections from the P-Ti_3AlC phase are also broadened and thus the height of the diffraction peaks is consequently reduced. Therefore after annealing at 800°C for 24 to 168h, P-Ti_3AlC reflections initially do not appear because they are submerged into the background (and their fraction may be low). However after annealing for 1104h, there are more carbides and they have also coarsened. The reflection peaks thus become narrower and are observable in the diffractograms.

As mentioned above, SEM investigations have shown that the lamellar structure decomposes after annealing for 1104h and some of the newly formed grains show bright contrast (**Figure 42(d)**). Considering its very bright contrast and the two characteristic neighboring reflections (110) and (201) at round 3.6° in HEXRD diffractograms, it is believed that this phase is the ω-$B8_2$ phase (Ti_4Al_3Nb), as

indicated in **Figure 43**. From the work of Stark et al. (Stark 2008) on Ti-45Al-(5, 7.5, 10) Nb (at. %) alloys, the formation of the ω-$B8_2$ phase was at the expense of the α_2 phase which also transformed to new γ grains.

After annealing at 900°C for 24h, the reflections become narrower compared to those after 24h at 800°C and are closer to the equilibrium position. Diffraction peaks of P-Ti_3AlC carbides are also hidden in the background. After 168h at 900 and 1000°C, the alloys are closer to equilibrium. The (111) and (210) reflections from the P-Ti_3AlC phase show intensity at 900°C, as shown in **Figure 44**. But at 1000°C, these diffraction peaks disappear, which implies that P-Ti_3AlC carbides dissolve and carbon goes back into solution. This agrees well with the results for the HIPed & Annealed Ti-45Al-5Nb-0.5C alloy.

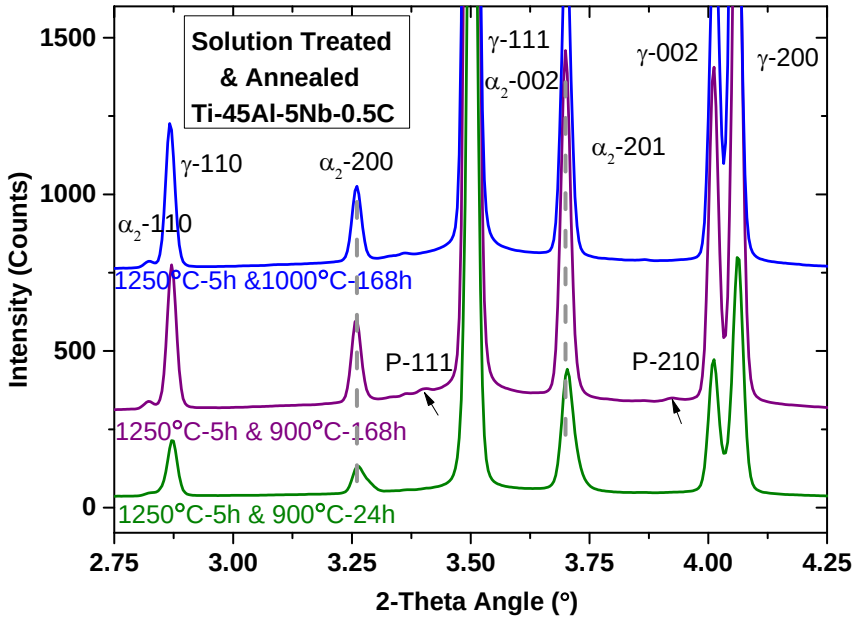

Figure 44 HEXRD patterns of the Solution Treated & Annealed Ti-45Al-5Nb-0.5C alloy after solution treatment at 1250°C for 5h (OQ) and subsequently annealed at 900°C for 24 and 168h, and at 1000°C for 168h (FC). Wavelength λ=0.1425Å.

Figure 45 shows the microstructure of the Solution Treated & Annealed Ti-45Al-5Nb-0.75C alloy. After 168h at 800°C, the microstructure is composed of equiaxed γ grains and γ/α_2 lamellar colonies. The lamellae spacing is very fine, as shown in the insert of **Figure 45(a)**. After annealing for 1104h, the lamellae coarsen and the lamellar structure starts to decompose. But this phenomenon is not as obvious as in the Solution Treated & Annealed Ti-45Al-5Nb-0.5C alloy. Small holes formed from carbide removal during electro-polishing are again observed. After 168h at 900°C, the lamellar structure has a larger lamellae spacing and seems to decompose. Holes are again observed to exist at grain boundaries but are larger in size than those after 1104h at 800°C. After 168h at 1000°C, the microstructure is composed of equiaxed γ and α_2 phases, together with a small amount of lamellar structure with a very coarse lamellae spacing. Some lamellae widths even reach around 200nm, as shown in **Figure 45(d)**. Holes at grain boundaries are larger in size but fewer in number. From

the development of holes it can be proposed that grain boundary carbides coarsen with increasing annealing temperature. Compared to the HIPed & Annealed condition, Solution Treated & Annealed Ti-45Al-5Nb-0.75C has significantly fewer and smaller holes at grain boundaries (assumed as grain boundary carbides). This is further confirmed in **Figure 46**.

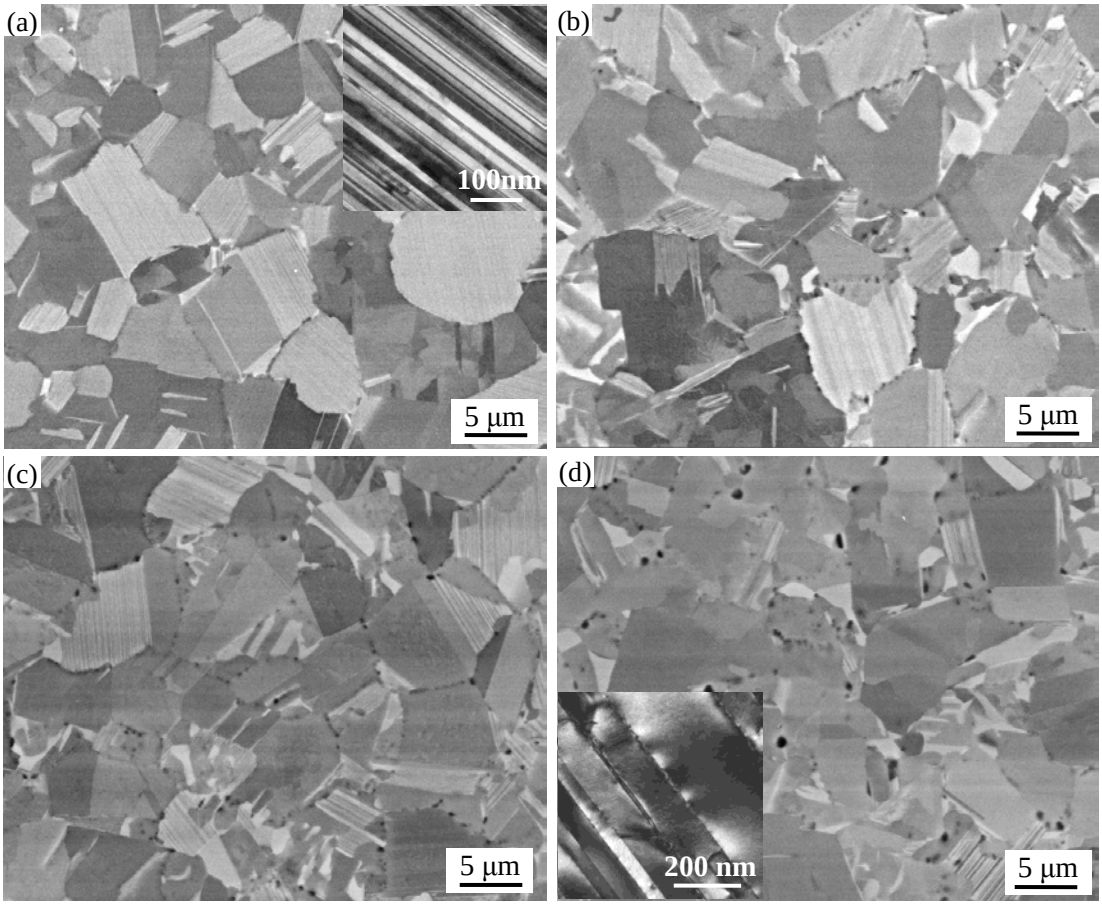

Figure 45 Microstructures of the Solution Treated & Annealed Ti-45Al-5Nb-0.75C alloy after solution treatment at 1250°C for 5h (OQ), and subsequent annealing at (a) 800°C for 168h, (b) 800°C for 1054h, (c) 900°C for 168h, and (d) 1000°C for 168h (FC). SEM images were recorded in BSE mode. Specimens were prepared by electro-polishing.

As mentioned in **Chapter 3**, vibration polishing retains carbides within the matrix. In order to compare the microstructures and carbides developed in the HIPed & Annealed alloys and the Solution Treated & Annealed alloys, the Ti-45Al-5Nb-0.75C alloy was chosen as an example alloy. Thus the HIPed & Annealed (168h @ 800°C, FC) condition was compared to the Solution Treated & Annealed (5h @ 1250°C, OQ + 168h @ 800°C, FC) condition (vibration-polished specimens). The microstructures are shown in **Figure 46**. The alloy at HIPed & Annealed condition has a finer grain size than that in the Solution Treated & Annealed condition. The carbides are imaged with a bright contrast. From **Figures 46(a)** and **(b)** the number and size of grain boundary carbides in the Solution Treated & Annealed condition are found to be much fewer and smaller than those in the HIPed & Annealed condition. From **Figures 46(c)** and **(d)**, the number of carbides in the γ grains of the HIPed & Annealed

condition is lower than that in the Solution Treated & Annealed condition. Moreover, in **Figures 46(e)** and **(f)**, carbides are observed to form in the lamellae structure of the alloy in the Solution Treated & Annealed condition, exhibiting bright contrast in both secondary electron and back-scattered electron modes.

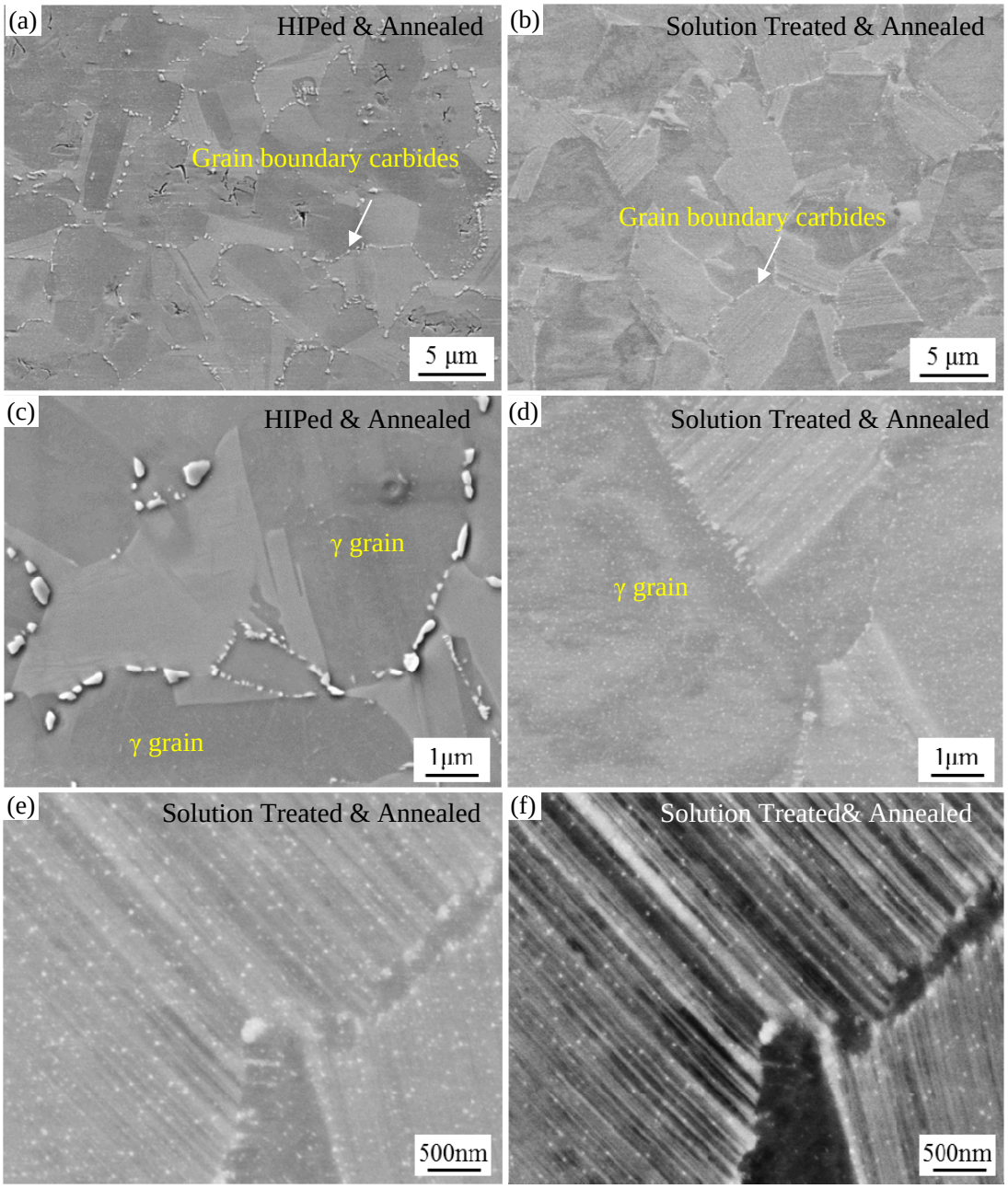

Figure 46 Microstructure of the heat-treated Ti-45Al-5Nb-0.75C alloy after (a) and (c) HIPed & annealed at 800°C for 168h, and (b), (d), (e), (f) solution treated at 1250°C for 5h (OQ) & annealed at 800°C for 168h (FC). SEM images (a), (b), (c), (d) and (e), were recorded in SE mode. SEM image (f) was recorded in BSE mode. Specimens were prepared by vibration polishing. Carbides remain in alloys and show bright contrast.

Further HEXRD investigations were performed to study the effect of increased annealing time at 800°C and increased annealing temperature on Solution Treated & Annealed Ti-45Al-5Nb-0.75C.

Figure 47 shows the influence of annealing time at 800°C. All the patterns show reflections from γ-TiAl and α_2-Ti_3Al phases. Similar to condition in the Solution Treated & Annealed Ti-45Al-5Nb-0.5C alloy, the Solution Treated & Annealed Ti-45Al-5Nb-0.75C alloy is not in thermodynamic equilibrium after annealing at 800°C for 24 to 168h. This is why the peak positions shift gradually with longer annealing times. This will be discussed later in **Section 4.2.3**. Due to the fine lamellar structure, diffraction peaks are also broadened. Despite broadening of the carbide diffraction peaks, they can be identified after annealing for 168h as the fraction of carbides is higher than in the Solution Treated & Annealed Ti-45Al-5Nb-0.5C alloy. After annealing for 1054h, the microstructure almost reaches equilibrium. The reflections become narrower and the diffraction peaks from P-Ti_3AlC carbides are obvious. Compared with the Solution Treated & Annealed Ti-45Al-5Nb-0.5C alloy that was annealed at 800°C for 1104h, no ω-$B8_2$ phase is detected in the Solution Treated & Annealed Ti-45Al-5Nb-0.75C alloy after 1054h at 800°C. This observation is consistent with the research of Stark et al. (Stark 2008) which showed that the addition of carbon can stabilize the α_2 phase and thus hinder the transformation of α_2 phase to ω phase.

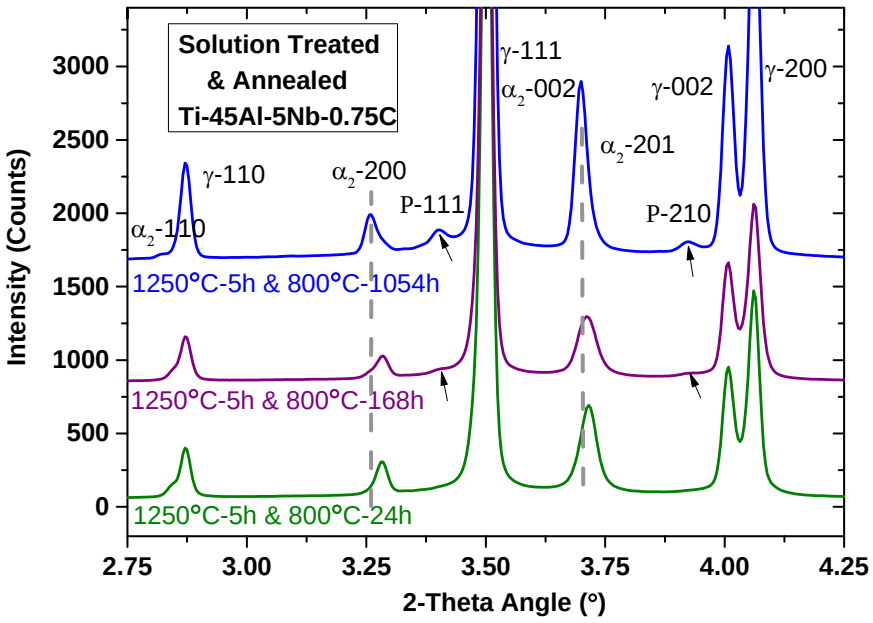

Figure 47 HEXRD patterns of the Solution Treated & Annealed Ti-45Al-5Nb-0.75C alloy after solution treatment at 1250°C for 5h (OQ) and subsequent annealing at 800°C for 24, 168 and 1054h (FC). Wavelength λ=0.1425Å.

After annealing at 900°C for 24h, the alloy has not reached the equilibrium condition, which is revealed by the shifting of reflection peaks, as shown in **Figure 48.** After annealing at 900 and 1000°C for 168h, the alloys are close to thermodynamic equilibrium because no reflection shift is observed. The diffraction intensity of carbides increases with increasing annealing time and temperature. This indicates that the fraction of carbides increases.

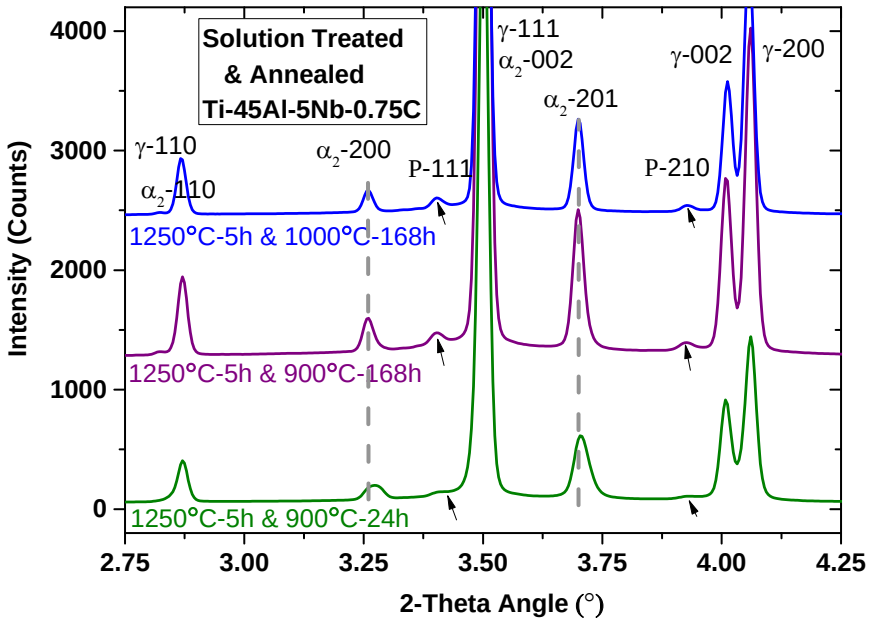

Figure 48 HEXRD patterns of the Solution Treated & Annealed Ti-45Al-5Nb-0.75C alloy after solution treatment at 1250°C for 5h (OQ) and annealing at 900°C for 24 and 168h, and at 1000°C for 168h (FC). Wavelength λ=0.1425Å.

4.2.2 Phase fractions

Because the α_2 phase can retain more carbon than the γ phase, it is important to know how the fraction of the α_2 phase develops during annealing.

Figure 49 shows the fraction of α_2 phase as a function of time and temperature for the Ti-45Al-5Nb-0.5C and Ti-45Al-5Nb-0.75C alloys in HIPed & Annealed condition. The fraction of α_2 phase in the HIPed & Annealed Ti-45Al-5Nb-0.5C alloy is reduced compared with the HIPed condition (annealing time = 0) and tends to decrease further with increasing time. In the HIPed & Annealed Ti-45Al-5Nb-0.75C alloy, the α_2 phase fraction also clearly decreases after annealing. With increasing temperature and time, the fraction of α_2 phase reduces further. As a whole, the HIPed & Annealed Ti-45Al-5Nb-0.75C alloy has a slightly lower α_2 phase fraction than the HIPed & Annealed Ti-45Al-5Nb-0.5C alloy.

Figure 50 shows the development of the α_2 phase during annealing of the Solution Treated & Annealed Ti-45Al-5Nb-0.5C and Ti-45Al-5Nb-0.75C alloys. The α_2 phase fractions in the solution treated condition for Ti-45Al-5Nb-0.5C and Ti-45Al-5Nb-0.75C alloys are around 46.7 and 45.8 wt. % respectively. After annealing, the fraction of α_2 phase decreases greatly. As for the HIPed & Annealed condition, the fraction of α_2 phase tends to slowly reduce further for both alloys as increasing temperature and time. The alloys in Solution Treated & Annealed conditions have a higher α_2 phase fraction than HIPed & Annealed alloy conditions after annealing at 800°C for 24 to 168h due to the non-equilibrium microstructure resulted from quenching. For each alloy the fraction of α_2 phase is roughly similar in the HIPed & Annealed and Solution Treated & Annealed conditions after the same annealing time

at 900 or 1000°C. For the Solution Treated & Annealed conditions, the Ti-45Al-5Nb-0.5C alloy always has a slightly higher α_2 phase fraction than the Ti-45Al-5Nb-0.75C alloy.

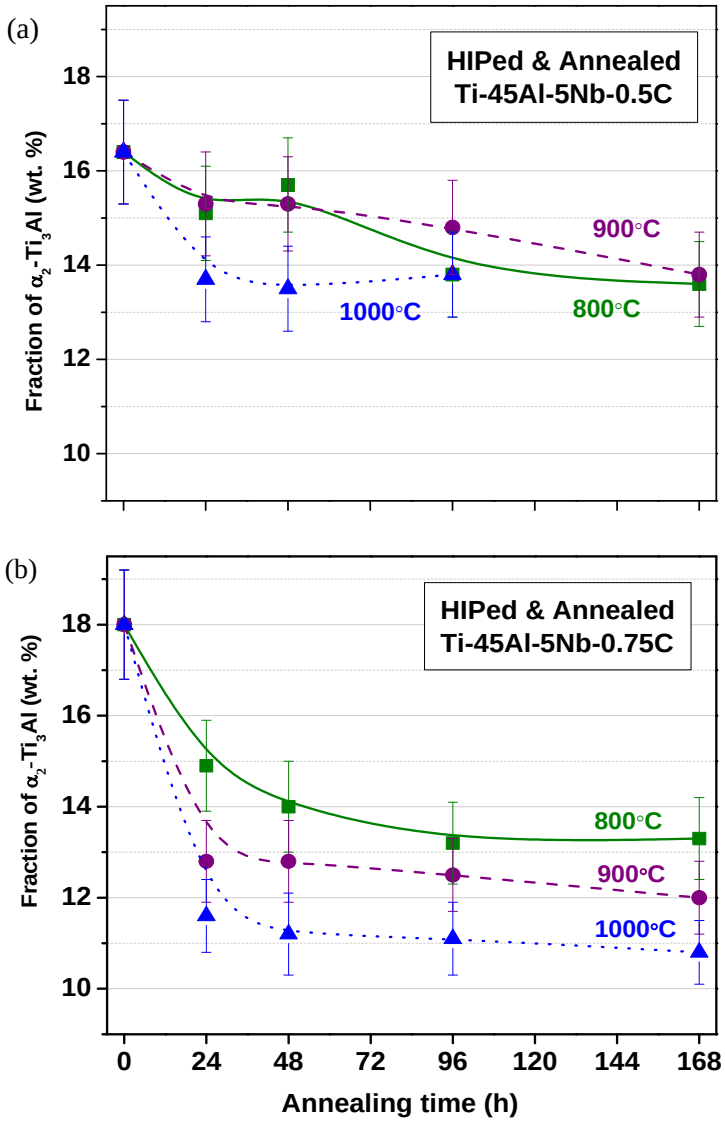

Figure 49 Weight fraction of the α_2-Ti_3Al phase determined using Rietveld analysis of HEXRD patterns from the HIPed & Annealed (a) Ti-45Al-5Nb-0.5C and (b) Ti-45Al-5Nb-0.75C alloys after annealing at 800, 900 and 1000°C for 0 (HIPed condition), 24, 48, 96 and 168h (FC). The data is connected by guiding spline lines.

In these alloys, the α_2 phase fraction decreases with increasing annealing time. This might be attributed to the formation of carbides which take up carbon atoms, as confirmed by the Ti-Al-C phase diagram (Bandyopadhyay 2000, Cornish 2009).

As mentioned above, after annealing, the Ti-45Al-5Nb-0.5C alloy always has a higher α_2 phase fraction than the Ti-45Al-5Nb-0.75C alloy with a similar treatment. This observation seems contary to **Figure 14** which shows that carbon can stabilize the α and α_2 phases. From literature (Perdrix 2001) carbon increased the volume fraction of α_2 phase in a Ti-48Al fully lamellar alloy that was slowly cooled from 1350°C. In the

current work it is speculated that the simultaneous addition of Nb and C may affect the fraction of the α_2 phase in Ti-45Al-5Nb-xC alloys.

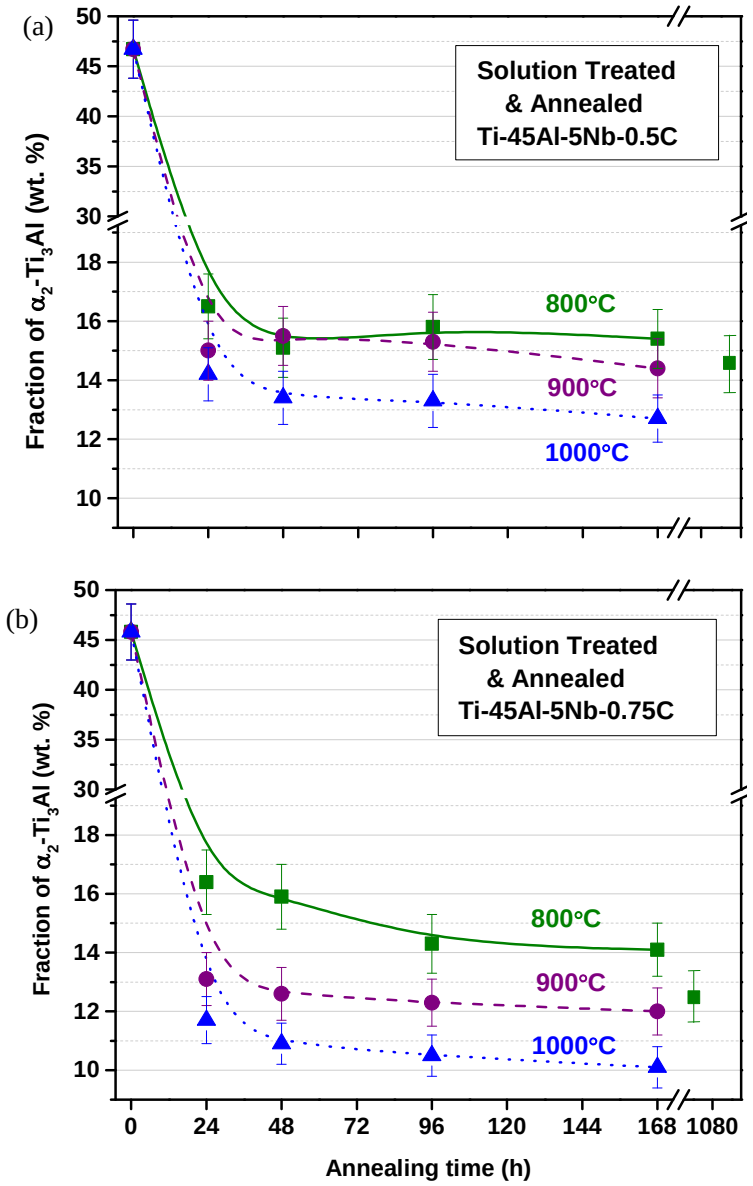

Figure 50 Weight fraction of the α_2-Ti_3Al phase determined using Rietveld analysis of HEXRD patterns of the Solution Treated & Annealed (a) Ti-45Al-5Nb-0.5C and (b) Ti-45Al-5Nb-0.75C alloys after solution treatment at 1250°C for 5h (OQ) and subsequent annealing at 800, 900 and 1000°C (FC). The data is connected by guiding spline lines.

4.2.3 Lattice parameters

The amount of carbon in solid solution is reflected by the variation of lattice parameters in both the γ and α_2 phases. The more carbon in the interstices of the lattice, the larger the lattice parameters. During annealing, the variation of phase fractions and the carbide precipitation will alter the amount of carbon in solid solution. Additionally, the change of lattice parameters of the γ phase will have influence on the lattice misfit between P-Ti_3AlC and γ phases. The variation of lattice parameters

of both the γ and α_2 phases in the Ti-45Al-5Nb-0.5C and Ti-45Al-5Nb-0.75C alloys during annealing is shown in **Figures 51-54**. These values were obtained by Rietveld analysis of HEXRD diffractograms. Here it is worth mentioning that the HEXRD experiments were conducted at room temperature, so the values relate to room temperature values. The error bar cannot be seen due to its small value (0.0001Å).

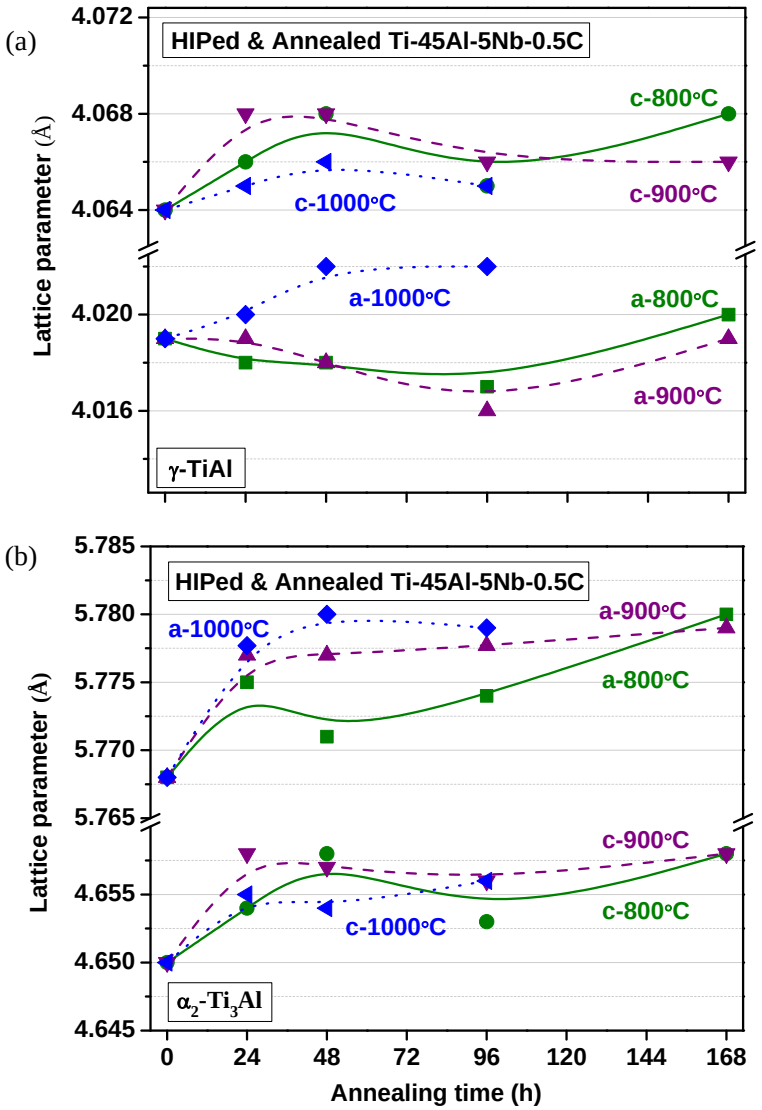

Figure 51 Lattice parameters of (a) γ and (b) α_2 phases determined using Rietveld analysis of HEXRD patterns from the HIPed & Annealed Ti-45Al-5Nb-0.5C alloy after annealing at 800 and 900°C for 0 (HIPed condition), 24, 48, 96 and 168h, and at 1000°C for 0 (HIPed condition), 24, 48 and 96h. The data is connected by guiding spline lines. The error bar cannot be seen due to its small value.

From **Figure 51(a)** it can be seen that the lattice parameter a_γ in the HIPed & Annealed Ti-45Al-5Nb-0.5C alloy decreases for annealing times up to 96h at 800 and 900°C, and then it starts to increase. However at 1000°C, it increases and then remains constant after 48h. For all temperatures the lattice parameter c_γ, increases up to 48h and then decreases at an annealing time of 96h. Thereafter c_γ increases again for 800°C but remains stable for 900°C.

The lattice parameter variation of the α_2 phase, shown in **Figure 51(b)** reveals some differences. Both the a and c lattice parameters are larger than those in the HIPed condition. After annealing at 800°C the lattice parameters of the α_2 phase show no clear tendency up to 96h, but are increased at 168h. For annealing at 900 and 1000°C they show no obvious variation with increasing time.

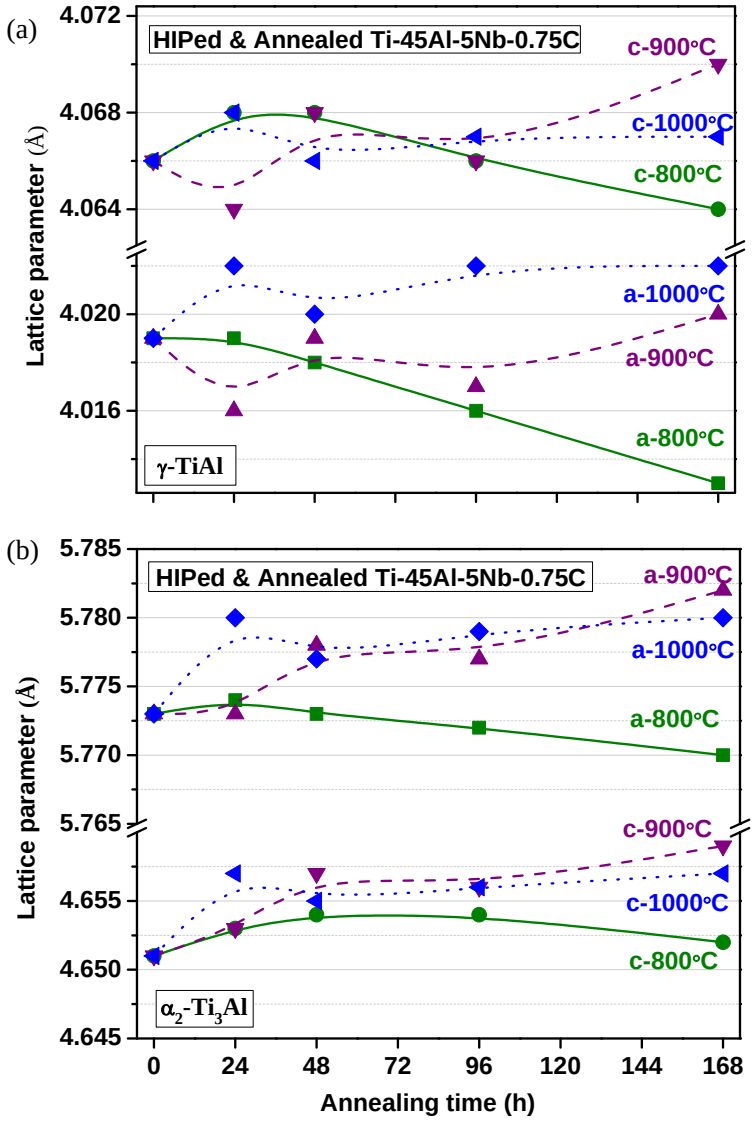

Figure 52 Lattice parameters of (a) γ and (b) α_2 phases obtained using Rietveld analysis of HEXRD patterns from the HIPed & Annealed Ti-45Al-5Nb-0.75C alloy after annealing at 800, 900 and 1000°C for 0 (HIPed condition), 24, 48, 96 and 168h respectively. The data is connected by guiding spline lines. The error bar cannot be seen due to its small value.

The influence of annealing time and temperature on HIPed & Annealed Ti-45Al-5Nb-0.75C is given in **Figure 52(a)**. For annealing at 800°C, a_γ decreases with increasing time. For 900°C a_γ decreases after 24h and then shows a tendency to increase over the time range investigated. For annealing at 1000°C, a_γ is larger than that of the HIPed condition and stabilizes after 168h. For all annealing temperatures c_γ has a similar tendency to that of a_γ.

The variation of $a_{\alpha 2}$ can be seen in **Figure 52(b)**. For annealing at 800°C, $a_{\alpha 2}$ decreases, while it increases for 900 and 1000°C with increasing annealing time. For annealing at 800°C, $c_{\alpha 2}$ first increases, then becomes stable and finally decreases. However it continually increases for annealing at 900 and 1000°C with increasing time.

As mentioned above both the precipitation of carbides and changes in the α_2 phase fraction result in a variation of parameters. The decrease of the a_γ lattice parameter in the HIPed & Annealed Ti-45Al-5Nb-0.5C alloy at 800 and 900°C for 24 to 96h may be attributed to the carbide precipitation. After 168h, the lattice parameter a_γ increases. This is probably because carbon has redistributed in the α_2 and γ phases due to a decrease in the α_2 phase fraction. When the annealing temperature is increased to 1000°C, carbon returns into solution and both a_γ and c_γ increase accordingly. On considering the α_2 phase, the lattice parameters are increased after annealing because carbon may redistribute in the α_2 phase.

For the HIPed & Annealed Ti-45Al-5Nb-0.75C alloy after annealing at 800°C, a possible explanation for the decrease of the γ phase lattice parameters may be attributed to the precipitation of carbides. Carbon was probably supersaturated in the γ phase and reduces to values closer to its equilibrium level (at a specific annealing temperature) as more and more carbides are precipitated. At 900 and 1000°C, the fraction of the α_2 phase decreases. While the fraction of carbides increases and their subsequent growth consumes carbon, carbon solute from dissolved α_2 grains would redistribute into the matrix to give rise to an increase of lattice parameters of both the γ and α_2 phases.

Figure 53(a) shows how the lattice parameters of the γ phase of the Solution Treated & Annealed Ti-45Al-5Nb-0.5C alloy change as a function of temperature and time. The a_γ lattice parameter increases with increasing temperature and reaches a maximum value at 1000°C. On the contrary c_γ is lowest at 1000°C and remains almost constant at 800 and 900°C.

The $a_{\alpha 2}$ lattice parameter in **Figure 53(b)** is lowest for 800°C and remains almost constant for 900 and 1000°C (except for the data point at 900°C for 24h). $a_{\alpha 2}$ increases with increasing annealing time at 800°C, while it remains almost constant at 900 and 1000°C. The $c_{\alpha 2}$ lattice parameter is highest at 800°C, and those after annealing at 900 and 1000°C are quite similar (except a small difference at 24h). Meanwhile with increasing annealing time at 800°C, $c_{\alpha 2}$ decreases, but it remains stable for annealing at 900 and 1000°C. It is worth noting that after 1104h at 800°C, the lattice parameters of the α_2 phase become closer to the values after annealing at 900 and 1000°C for 168h.

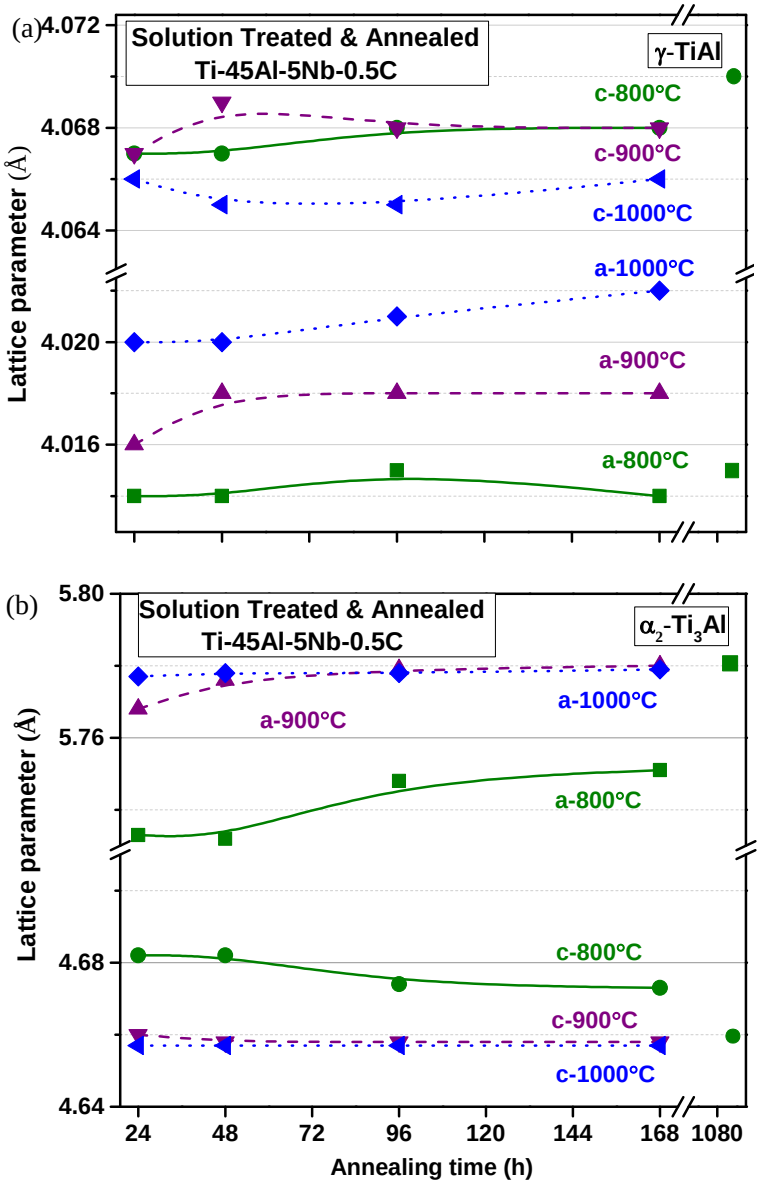

Figure 53 Lattice parameters of (a) γ phase and (b) α_2 phases obtained using Rietveld analysis of HEXRD patterns from the Solution Treated & Annealed Ti-45Al-5Nb-0.5C alloy after solution treatment at 1250°C for 5h (OQ) and subsequent annealing at 800, 900 and 1000°C for 24, 48, 96 and 168h, and at 800°C for 1104h. The data is connected by guiding spline lines. The error bar cannot be seen due to its small value.

Figure 54 shows the variation of the lattice parameters of both the γ and α_2 phase as a function of temperature and time for the Solution Treated & Annealed Ti-45Al-5Nb-0.75C alloy. The lattice variations show a similar tendency to those of the Solution Treated & Annealed Ti-45Al-5Nb-0.5C alloy. The a_γ lattice parameter decreases and c_γ increases with increasing annealing temperature. For the α_2 phase, $a_{\alpha 2}$ reaches a minimum and $c_{\alpha 2}$ has a maximum value for 800°C. After 1054h at 800°C, both $a_{\alpha 2}$ and $c_{\alpha 2}$ are close to the level at 1000°C. Extended annealing at 900°C results in the lattice parameters moving close to the values for 1000°C. At 1000°C, both $a_{\alpha 2}$ and $c_{\alpha 2}$ remain unchanged with the increased annealing time.

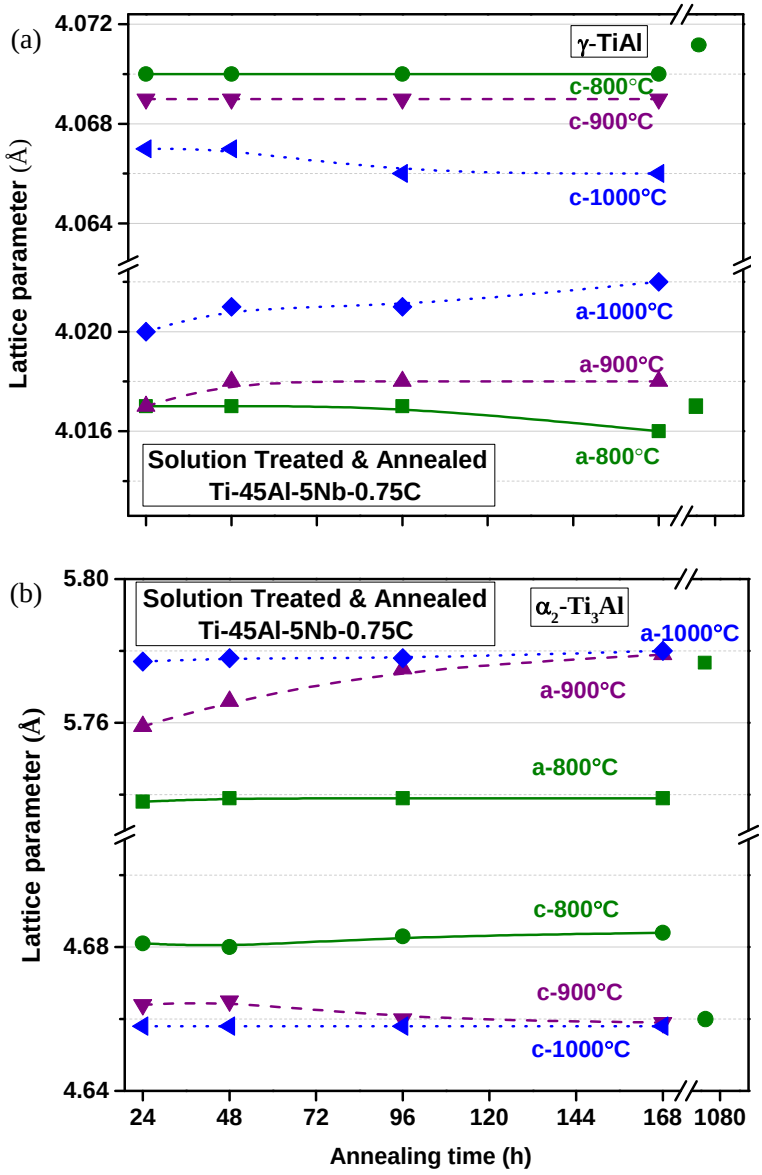

Figure 54 Lattice parameters of (a) γ and (b) α_2 phases obtained using Rietveld analysis of HEXRD patterns from the Solution Treated & Annealed Ti-45Al-5Nb-0.75C alloy after solution treatment at 1250°C for 5h (OQ) and subsequent annealing at 800, 900 and 1000°C for 24, 48, 96 and 168h, and at 800°C for 1054h. The data is connected by guiding spline lines. The error bar cannot be seen due to its small value.

From above results, the lattice parameters of both the γ and α_2 phases in each of Solution Treated & Annealed conditions are different from the HIPed & Annealed conditions, especially at 800°C. Compared to the HIPed & Annealed conditions, for both phases in the Solution Treated & Annealed conditions the lattice parameter c is increased but a is decreased. As a result of fast cooling (oil quenching) the microstructure at high temperature can be preserved at room temperature. It should be noted that the preserved high-temperature phases have higher Al content than room-temperature phases. After annealing at 800°C for 24 to 168h, the alloys cannot reach thermodynamic equilibrium due to the low temperature and short annealing time. This is confirmed by the shift of diffraction peaks in the diffractograms, see **Figure 47** for

example. Using EDS (energy-dispersive spectroscopy) measurements, the level of Al in the γ phase of the HIPed & Annealed Ti-45Al-5Nb-0.75C after 24h at 800°C is about 49-50 at. %. But it increases to 51-52 at. % in Solution Treated & Annealed Ti-45Al-5Nb-0.75C (annealed at 800°C for 24h). Thus the increase of Al content in the γ phase seems to have caused the small increase of c_γ and reduction of a_γ. This is supported by the work of Whang et al. (Whang 1988) who showed that Al atoms substituted for Ti atoms at Ti positions and this combined with the fact that the atomic radius of Al is smaller than that of Ti introduced a contraction of the a_γ lattice parameter. The increasing number of Al-Al atom pairs along the [001] direction, results in an increase of the c_γ lattice parameter because the Al-Al atomic distance is larger than the Ti-Al atomic distance (Whang 1988). However it is not completely understood why c_γ increases to 4.071Å after 1054h because it would be expected that it should decrease due to a lower Al content of γ at near-equilibrium conditions. It could be something to do with the formation of ω-$B8_2$ phase after long term annealing. The obvious increase of $c_{\alpha 2}$ and decrease of $a_{\alpha 2}$ seen in **Figures 53(b)** and **54(b)** might be attributed to an Al content higher than the equilibrium value. After long-term annealing, the microstructure may be near to equilibrium as indicated by the increased value of $a_{\alpha 2}$ and decreased value of $c_{\alpha 2}$. After annealing at a specific temperature the changes of lattice parameters are less obvious for the Solution Treated & Annealed conditions compared to the HIPed & Annealed conditions. This may be due to the more uniform distribution of carbon after solution treatment. Carbon supersaturation, like the case in HIPed & Annealed alloys is reduced or even disappears after solution treatment.

4.2.4 Lattice misfits

The lattice misfit between P-type carbides and the γ matrix is important when considering the development of carbide morphology and the interfaces between carbides and the matrix. The misfit along [100] and [001] directions is defined by:

$$\varepsilon_{100} = \frac{(a_\gamma - a_P)}{a_P} \qquad \textbf{Eq. 4}$$

$$\varepsilon_{001} = \frac{(c_\gamma - c_P)}{c_P} \qquad \textbf{Eq. 5}$$

a_γ and c_γ are lattices parameters of the γ phase, and a_P and c_P are the lattice parameters of the P-Ti_3AlC carbide phase.

We will only consider the lattice misfit in the heat-treated Ti-45Al-5Nb-0.75C alloy because in Solution Treated & Annealed Ti-45Al-5Nb-0.5C no reflections from the P-Ti_3AlC phase were present. **Table 9** gives the lattice parameters of the P-type carbides and γ phase as determined from HEXRD and the associated lattice misfit along the [100] and [001] directions.

The lattice misfit in the HIPed & Annealed conditions does not show an obvious variation from that of the Solution Treated & Annealed conditions, although misfit along the [001] direction is slightly lower for the Solution Treated & Annealed conditions due to a slightly higher value of c_γ. The misfit along the [001] direction is smaller compared to that along the [100] direction in heat-treated Ti-45Al-5Nb-0.75C alloy. Compared with literature data (Schuster 1980), the misfit difference between [100]/[010] and [001] directions is greatly reduced due to a lower Al content and the addition of Nb. The effect of lattice misfit on the carbide morphology development during annealing will be discussed in **Section 5.3.1**.

Table 9 Lattice misfit* between P-Ti_3AlC and γ phases in heat-treated Ti-45Al-5Nb-0.75C alloy

annealing conditions		phases	*a* (Å)	*c* (Å)	ε_{100} (%)	ε_{001} (%)
HIPed & Annealed	800ºC, 24h	P	4.155	4.155	-3.27	-2.09
		γ	4.019	4.068		
	800ºC, 48h	P	4.154	4.154	-3.27	-2.07
		γ	4.018	4.068		
	800ºC, 96h	P	4.154	4.154	-3.32	-2.12
		γ	4.016	4.066		
	800ºC, 168h	P	4.151	4.151	-3.33	-2.10
		γ	4.013	4.064		
Solution Treated & Annealed	1250ºC, 5h & 800ºC, 24h	P	4.154	4.154	-3.30	-2.02
		γ	4.017	4.070		
	1250ºC, 5h & 800ºC, 48h	P	4.154	4.154	-3.30	-2.02
		γ	4.017	4.070		
	1250ºC, 5h & 800ºC, 96h	P	4.154	4.154	-3.30	-2.02
		γ	4.017	4.070		
	1250ºC, 5h & 800ºC, 168h	P	4.154	4.154	-3.32	-2.02
		γ	4.016	4.070		
Ti-50Al (Schuster 1980)	/	P	4.162	4.162	-5.57	-2.11
		γ	3.930	4.074		

* It should be noted that due to the low fraction of P-Ti_3AlC phase, the value of the third decimal place of the lattice parameter measurement of the P-Ti_3AlC phase is not so precise.

4.3 Carbide precipitation and thermal stability of carbides in heat-treated alloys

In this section the formation, thermal stability, weight fraction, size and density of P-Ti_3AlC carbides are discussed. Here it should be noted that no H-Ti_2AlC carbides are found to form in Ti-45Al-5Nb-0.5C and Ti-45Al-5Nb-0.75C after annealing at 800 to 1000°C, although a few H-type carbides are detected in the HIPed Ti-45Al-5Nb-0.75C alloy. For the moment it is not confirmed whether these primary H-type carbides (formed during HIPing) are dissolved during annealing or occur in volume fractions too low to be observed. Additionally the development of precipitate free zones (PFZs) in Ti-45Al-5Nb-0.75C after annealing is discussed.

4.3.1 Carbide precipitation sequence and dissolution of carbides in HIPed & Annealed Ti-45Al-5Nb-0.5C

Figure 55 shows the carbide precipitation sequence in the HIPed & Annealed Ti-45Al-5Nb-0.5C alloy after annealing at 800ºC. P-type carbides first form at triple junctions (**Figure 55(a)**) and at grain boundaries (**Figure 55(c)**). Carbides have the crystallographic orientation relationship: $[001]_\gamma//[001]_P$, $(100)_\gamma//(100)_P$, with one of the neighboring γ grains and grow into this grain, as confirmed by the diffraction pattern in **Figure 55(b)**. Through the formation of lower energy facet (coherent interface), the total free energy is reduced. Thus nucleation at triple junctions is very fast. The same situation also applies for carbides at grain boundaries. Most grain boundary carbides either show a spherical cap or a faceted shape as illustrated in **Figure 55(c)**. The density and size of carbides vary at different grain boundaries. This is probably caused by a variation in boundary misorientations (Unwin 1969, Monzen 1990). Small carbides are found to start decorating dislocations after 48h at 800°C. After 96h more and more carbides nucleate at triple junctions, at grain boundaries and along dislocations. The unambiguous identification of carbides along dislocations is difficult because the particle size is very small, and the contrast from dislocations can make it difficult to identify the shape of carbides. **Figures 55(d)** and **(e)** show a detailed example of P-type carbides decorating dislocations. When tilting the specimen near to the [001] direction, using a $\boldsymbol{g}$=110 diffraction vector, the contrast from the dislocations disappears (Figure 55(e)). The carbides show "coffee bean" contrast (Ashby 1963) due to the elastic strain field of the spherical particles. As a typical feature of "coffee bean" contrast the line out of contrast is perpendicular to the $\boldsymbol{g}$ vector. As the annealing time at 800°C increases to 168h carbides grow at all precipitation sites. The P-type carbides are observed more frequently at the nodes of dislocation networks (**Figure 55(g)**). Under suited imaging conditions they show moiré fringe contrast visible as parallel black and white stripes, which can be seen more clearly in the enlarged inset in **Figure 55(g)**. According to the equation of translational moiré fringe, the spacing between fringes d_{tm} is given by: $d_{tm}=d_1/(1-d_2/d_1)$. d_1 and d_2 are the interplanar spacing of the P-type carbide and the γ matrix respectively. The $\boldsymbol{g}$ vector is parallel to the [010] direction but (010) is a forbidden diffraction for the γ phase. Thus the values of the spacing of the (020) planes: d_P=0.2078nm and d_γ=0.2010nm (which are calculated by analyzing HEXRD patterns) have been applied and an average value of 6.39nm is obtained for the fringe spacing. This is quite close to the measured value of 6.28nm. Most important is the fact that after 168h at 800°C carbides which exhibit a rod-like shape are observed in the γ matrix. It has been found by selected area diffraction analysis that they have an orientation relationship of $[001]_\gamma//[001]_P$ and $(100)_\gamma//(100)_P$ with the γ matrix. As shown in the weak-beam dark field image (**Figure 55(h)**), the growth direction of carbides is parallel to the [001] direction of the γ phase. The diffraction pattern (**Figure 55(i)**) shows weak diffraction spots from carbides. When viewed from the [101] direction some carbides possessing plate-like projections are observed, as shown later in HRTEM images.

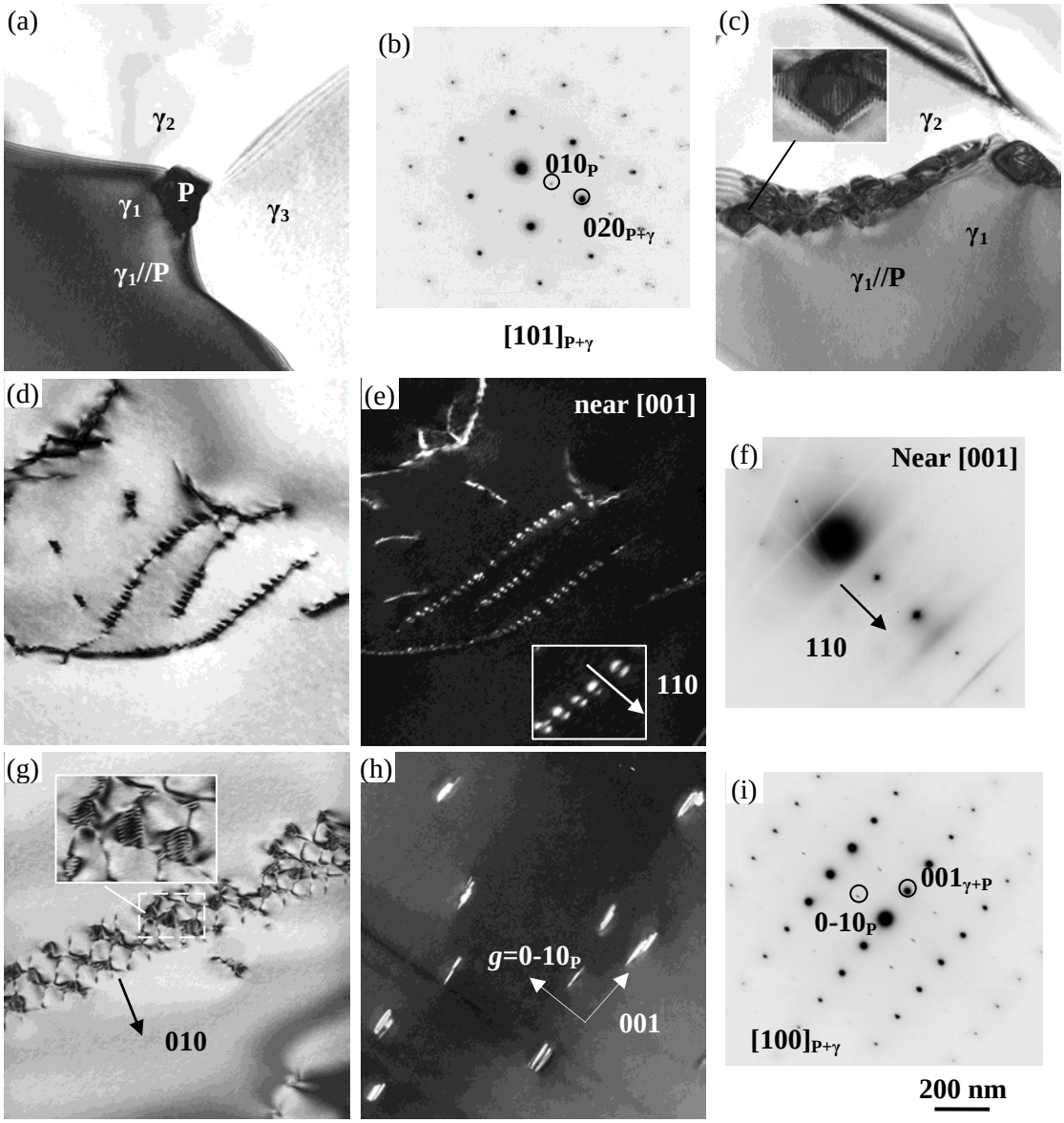

Figure 55 P-type carbides in the HIPed & Annealed Ti-45Al-5Nb-0.5C alloy (a) at triple junctions after annealing at 800°C for 48h, (b) diffraction pattern of (a), (c) at grain boundaries with faceted shape after 800°C for 48h, (d) and (e) at dislocations after annealing at 800°C for 96h, (e) recorded using the ***g***/3***g*** condition: ***g***=110, near the $[001]_\gamma$ direction, dislocations are out of contrast and carbides show "coffee bean" contrast, (f) is the ***g***/3***g*** condition of (e), (g) at nodes of dislocation networks after annealing at 800°C for 168h, carbides show moiré fringes, (h) in the γ matrix with a rod-like shape after 800°C for 168h, image was recorded using ***g***=$0\text{-}10_P$ in two-beam condition and (i) diffraction pattern in the $[100]_\gamma$ direction. All TEM images have the same scale bar.

In the HIPed & Annealed Ti-45Al-5Nb-0.5C alloy after annealing at 800°C, P-type carbides precipitate sequentially at sites with increasing nucleation free energy: at grain boundaries, at dislocations, and in the γ matrix. According to thermodynamics, when precipitates form the total free energy change is given by:

$$\Delta G = -V(\Delta G_v - \Delta G_s) + A\gamma - \Delta G_d \qquad \textbf{Eq. 6}$$

Where, $V\Delta G_v$ is the volume free energy, $V\Delta G_s$ is the misfit strain energy, $A\gamma$ is the surface energy, and ΔG_d is the released free energy from defects when building precipitates at the expense of defects (Porter 1992). Thereby the more free energy released by the defects, the easier the nucleation of precipitates. Here it is worth mentioning that carbides which first nucleate at grain boundaries might be aided by the possible carbon enrichment at grain boundaries.

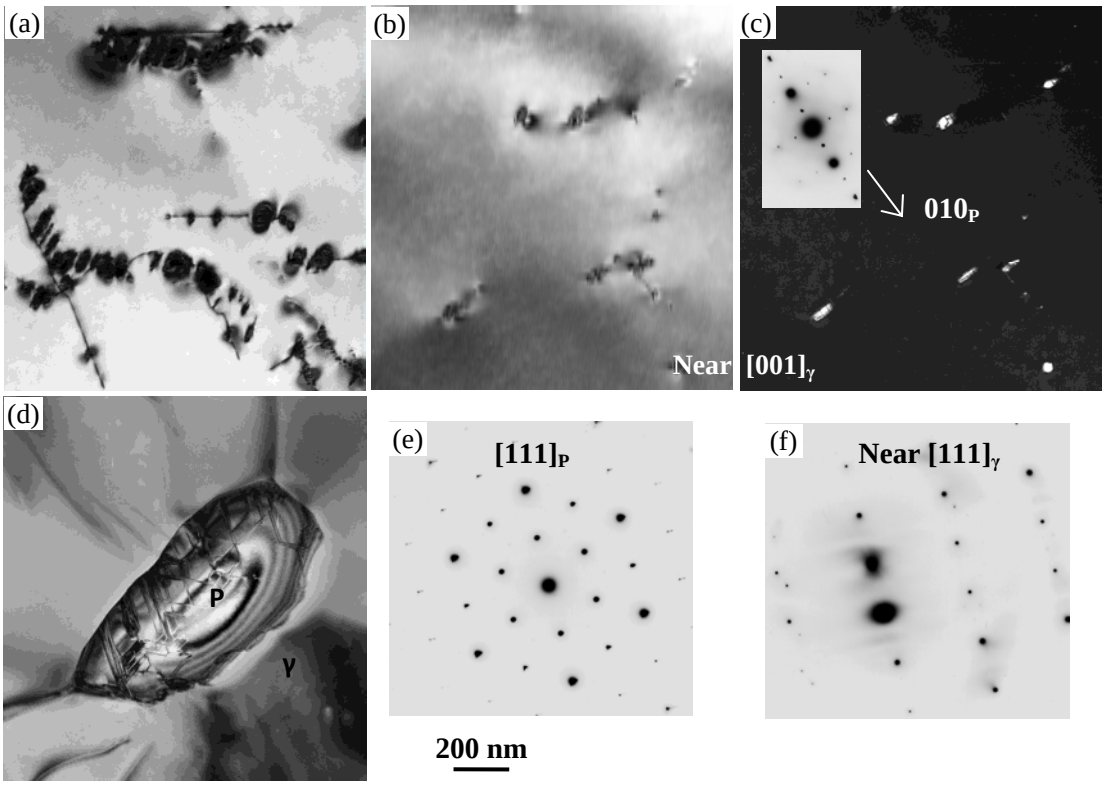

Figure 56 P-type carbides in the HIPed & Annealed Ti-45Al-5Nb-0.5C alloy (a) at dislocations after annealing at 900°C for 24h, (b) in TEM bright field, (c) in TEM dark field in the γ matrix both after annealing at 900°C for 48h, recorded using $\boldsymbol{g}$=**0-10**$_{\mathbf{P}}$ in two-beam condition, (d) at triple junctions after 900°C for 168h, carbides coarsen and lose crystallographic relationship with the γ matrix, (e) and (f) diffraction patterns of P and γ phases in (d) respectively. All TEM images have the same scale bar.

After annealing at 900ºC for 24h, P-type carbides are found at triple junctions, at grain boundaries and quite frequently at dislocations (**Figure 56(a)**). After 48h, P-type carbides start to form in the γ matrix (**Figure 56(b)**) in bright field and **(c)** in dark field). When the annealing time is extended to 96h, P-type carbides coarsen by Ostwald ripening and the number of carbides at dislocations and dislocation networks starts to decrease. After further annealing for 168h, only large P-type carbides exist at triple junctions (**Figure 56(d)**) and at grain boundaries. While the particles at triple junctions and at grain boundaries grow, the big carbides lose their crystallographic orientation relationship with the γ matrix. When the carbides are small, see **Figure 55(a)**, they possess an orientation relationship with one of the neighboring γ grains. As the carbide size reaches about 1μm (**Figure 56(d)**), the orientation relationship with the γ grain is lost. When tilting the specimen to the [111] direction of the P-

Ti_3AlC phase (**Figure 56(e)**), the orientation of the γ matrix is not exactly in $[111]_\gamma$ (**Figure 56(f)**). This is because as the carbides coarsen, the elastic strain field that is caused by the misfit between the carbides and the γ matrix increases. As a consequence it is energetically favorable for the carbide to become incoherent with the neighboring γ grains when the carbides exceed a certain size.

After annealing at 1000ºC for 24h, the number and size of carbides decreases significantly. Only a few small carbides can be found at triple junctions, at grain boundaries and along dislocations. This is confirmed by the absence of any diffraction peaks for carbides in the HEXRD patterns as their fraction is already below the detection limit of the HEXRD method. Thus when annealing at 1000°C carbides may initially nucleate and grow in regions where carbon is enriched locally. With increasing annealing time, diffusion processes gradually to bring the microstructure close to thermodynamic equilibrium and thus the carbides dissolve. Therefore after 96h at 1000°C no carbides exist and all carbon is back in solution.

At the start of annealing the carbides initially precipitate and grow with increasing temperature and annealing time. After a certain temperature dependent annealing time carbides at dislocations and in the γ matrix start to dissolve first as they are smaller than those at grain boundaries (it should be noted that this phenomenon does not happen at 800°C because diffusion is insufficient). The carbon that goes into solution then contributes to the growth of grain boundary carbides. This results in the overall energy of the system being reduced because the surface to volume ratio of large carbides is smaller than that of small carbides. This is the classical process of Ostwald ripening.

To summarize, in the HIPed & Annealed Ti-45Al-5Nb-0.5C alloy P-Ti_3AlC carbides are stable at 800°C, coarsen at 900°C and dissolve at 1000°C. It is thus suggested that the carbon solubility in Ti-45Al-5Nb-0.5C is higher than 0.5 at. % at 1000ºC and less than 0.5 at. % at 800ºC. No H-Ti_2AlC phase has been observed in this alloy after annealing at 1000°C. This provides evidence that H-type carbides do not form from P-type carbides.

4.3.2 Carbides and their thermal stability in HIPed & Annealed Ti-45Al-5Nb-0.75C

Unlike the HIPed & Annealed Ti-45Al-5Nb-0.5C alloy where carbide precipitation took place in a sequential manner during annealing at 800°C, in the HIPed & Annealed Ti-45Al-5Nb-0.75C alloy carbides were observed at all precipitation sites after 24h at 800°C. This is either due to the fact that small amount of carbides was already present in HIPed Ti-45Al-5Nb-0.75C prior to the annealing treatment or caused by the higher carbon content.

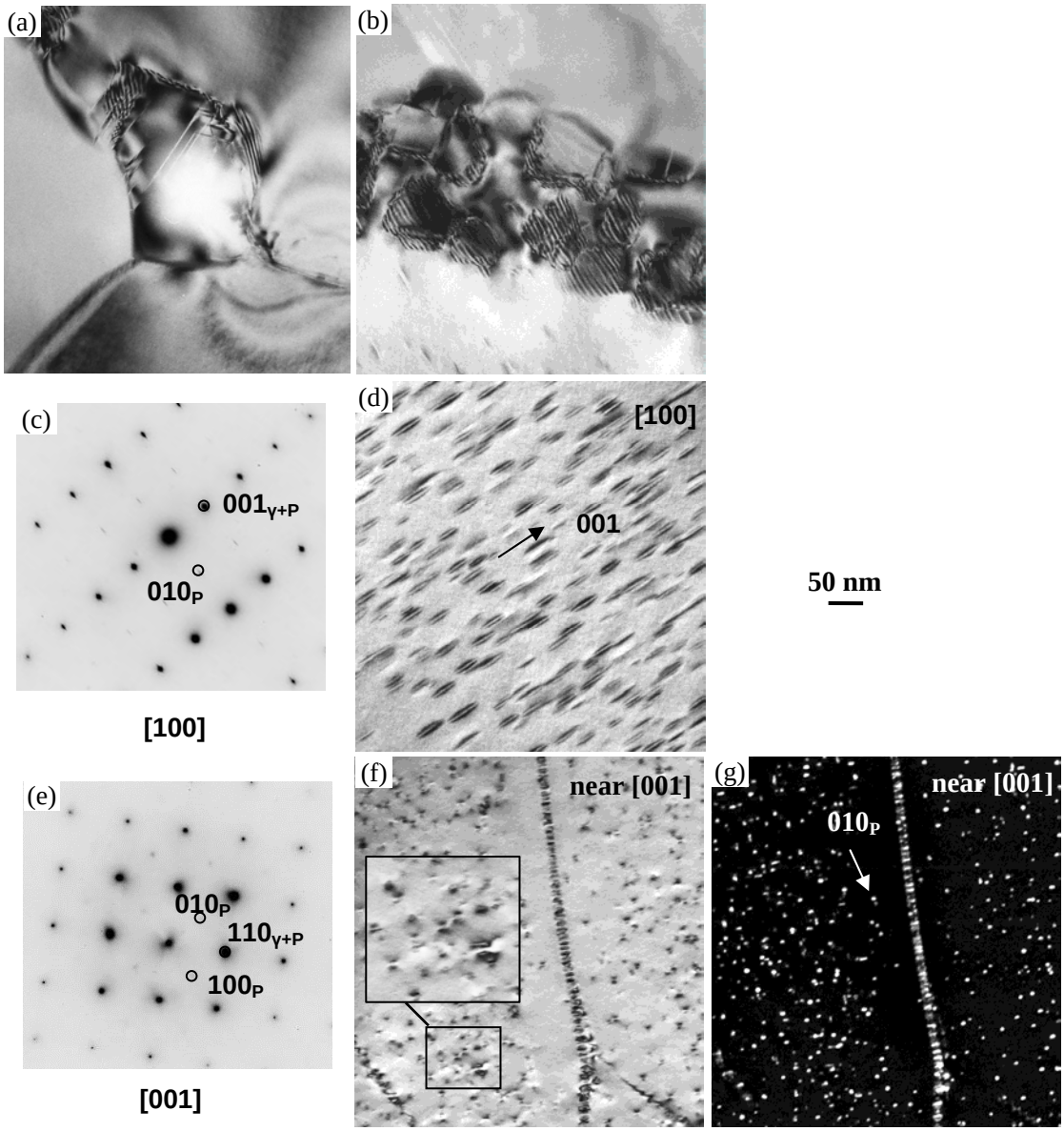

Figure 57 P-type carbides in the HIPed & Annealed Ti-45Al-5Nb-0.75C alloy after annealing at 800°C for 24h (a) at a triple junction, (b) at a grain boundary, (c) diffraction pattern of (d), (d) in the γ matrix viewed from the $[100]_\gamma$ direction showing needle-like projections, (e) diffraction pattern in the $[001]_\gamma$ direction, (f) in the γ matrix and at dislocations viewed from the $[001]_\gamma$ direction, enlarged image inset showing Ashby and Brown contrast, (g) dark field image of (f), recorded using a $\boldsymbol{g}/3\boldsymbol{g}$ condition, $\boldsymbol{g}=010_P$, showing dot-like projections. All TEM images have the same scale bar.

As shown in **Figure 57**, after 24h carbides are found at triple junctions (**Figure 57(a)**), at grain boundaries (**Figure 57(b)**), along dislocations (**Figure 57(f) and (g)**) and have formed in the γ matrix (**Figure 57(d), (f)**, and **(g)**) with a needle-like shape elongated along the $[001]_\gamma$ direction. Precipitate-free zones are present near both grain boundaries and carbide-decorated dislocations. The needle-like morphology of P-type carbides in the γ matrix is confirmed by TEM imaging along the $[100]_\gamma$ (**Figure 57(c)** and **(d)**) and the $[001]_\gamma$ (**Figure 57(e)**, **(f)** and **(g)**) directions. What is more, in the TEM bright field image (**Figure 57(f)**), ”coffee bean” contrast (Ashby 1963) is visible

around the carbides due to the strain field caused by coherency stresses. After 48h at 800°C, P-type carbides in the γ matrix grow and in particular carbides near γ grain boundaries change their shape to a plate-like morphology. After 800°C for 168h, carbides remain at grain boundaries, at dislocations and in the γ matrix. The change of carbide morphology in the γ matrix during annealing of the HIPed & Annealed Ti-45Al-5Nb-0.75C alloy will be discussed in **Section 5.1.1**.

After annealing at 900ºC for 24h, larger P-type carbides are observed at grain boundaries (**Figure 58(a)**), at dislocations (**Figure 58(b)**) and occasionally in the γ matrix (**Figure 58(c)**). The carbides decorating dislocations in **Figure 58(b)** show clear moiré fringe contrast. However, unlike the situation at 800ºC, the needle-like carbides are only observed in some γ grains and were larger in size. After 48h at 900°C the carbides in the γ matrix completely disappear. After annealing 168h a large number of carbides still remain at triple junctions, at grain boundaries and also at dislocations.

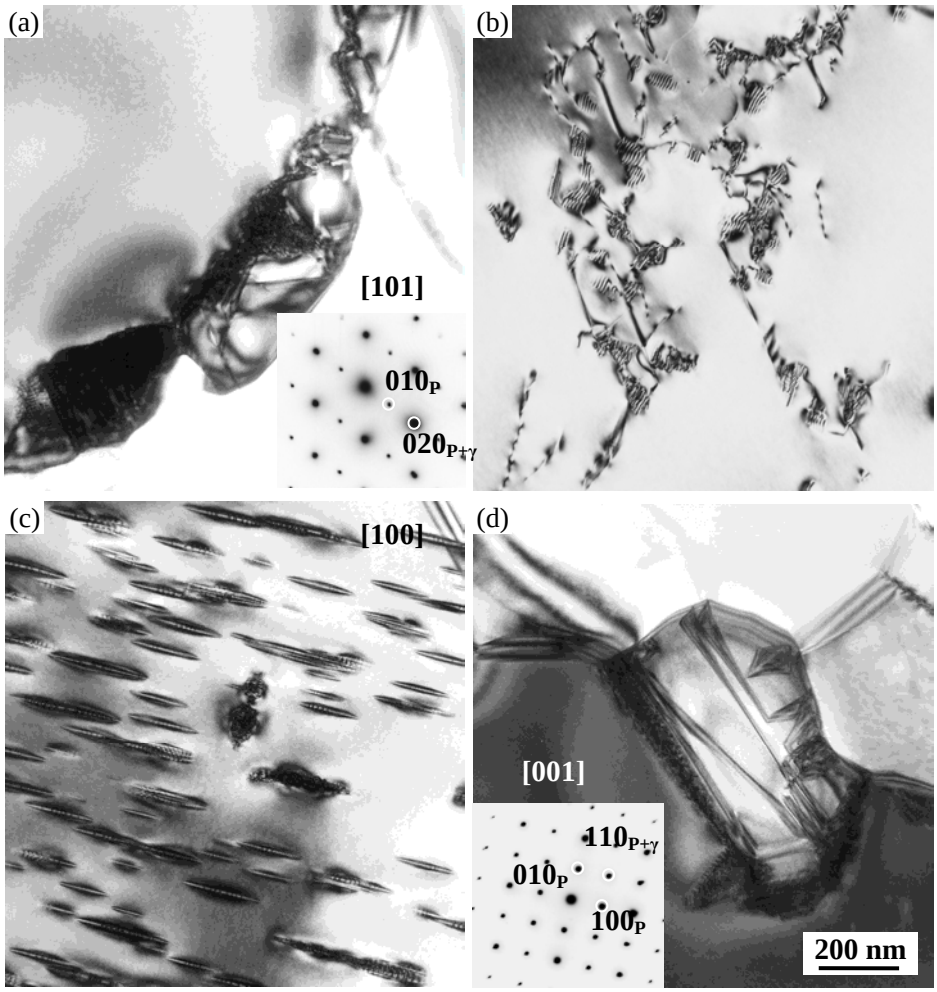

Figure 58 P-type carbides in the HIPed & Annealed Ti-45Al-5Nb-0.75C alloy (a) at grain boundaries after annealing at 900°C for 24h, (b) at dislocations after 900°C for 24h, (c) in γ grains appearing as large needles after 900°C for 24h, (d) coarsening at triple junctions after 1000°C for 168h. All TEM images have the same scale bar.

After annealing at 1000ºC, carbides at triple junctions and at grain boundaries coarsen after 168h. An obvious interface between the particle and the matrix can be seen and many planar defects exist in the particles, as shown in **Figure 58(d)**. However the carbides decorating dislocations decrease significantly in both number and size.

As a summary, in the HIPed & Annealed Ti-45Al-5Nb-0.75C alloy, carbides are stable at 800°C, and coarsen at 900 and 1000°C. This is different to the situation in the HIPed & Annealed Ti-45Al-5Nb-0.5C alloy in which the P-Ti_3AlC phase disappears at 1000°C. This supports the view that the dissolution temperature of carbides depends on the carbon concentration in alloys. It is proposed that the carbon solubility in Ti-45Al-5Nb-0.75C at 1000ºC is less than 0.75 at. %.

Carbon may be enriched at the grain boundaries of HIPed alloys. During subsequent annealing, carbides form preferentially at grain boundaries. Such grain boundary carbides might not be as effective as matrix precipitates for improving the mechanical properties of TiAl alloys, and even may worsen them. Therefore it is interesting to know the situation of carbide precipitation in the Solution Treated & Annealed alloys.

4.3.3 Carbide precipitation at 800°C in Solution Treated & Annealed Ti-45Al-5Nb-0.5C

In the Solution Treated & Annealed Ti-45Al-5Nb-0.5C alloy, after annealing at 800°C, P-type carbides are found at grain boundaries, at dislocations and in γ grains even after 24h. Compared with the HIPed & Annealed condition, grain boundary carbides are not detected so often and appear to have a smaller size. This has been confirmed during the SEM investigation when interpreting the observed holes as indication for the presence of carbides. P-type carbides in γ grains show a needle-like shape confirmed by needle projections along the $[100]_\gamma$ direction (**Figure 59(a)**) and dot cross-sections observed in the $[001]_\gamma$ direction (**Figure 59(b)**). The carbide density in γ grains measured from the $[001]_\gamma$ direction is about $(1.2\pm0.2) \times 10^{15} m^{-2}$, which is smaller than that in Ti-45Al-5Nb-0.75C (refer to **Section 4.4.2**).

After 168h at 800°C, P-type carbides are still present at grain boundaries, at dislocations, and with a decreased density of around $(0.45\pm0.05) \times 10^{15} m^{-2}$ in the γ matrix (measured from the $[001]_\gamma$ direction). **Figure 60** shows that most carbides in the γ grains retain a needle-like morphology. After careful investigation from the $[001]_\gamma$ direction, it can be seen that several dots are very close to each other and arranged very regularly, seemingly as though a large carbide has split, as shown in the insert in **Figure 60(b)**.

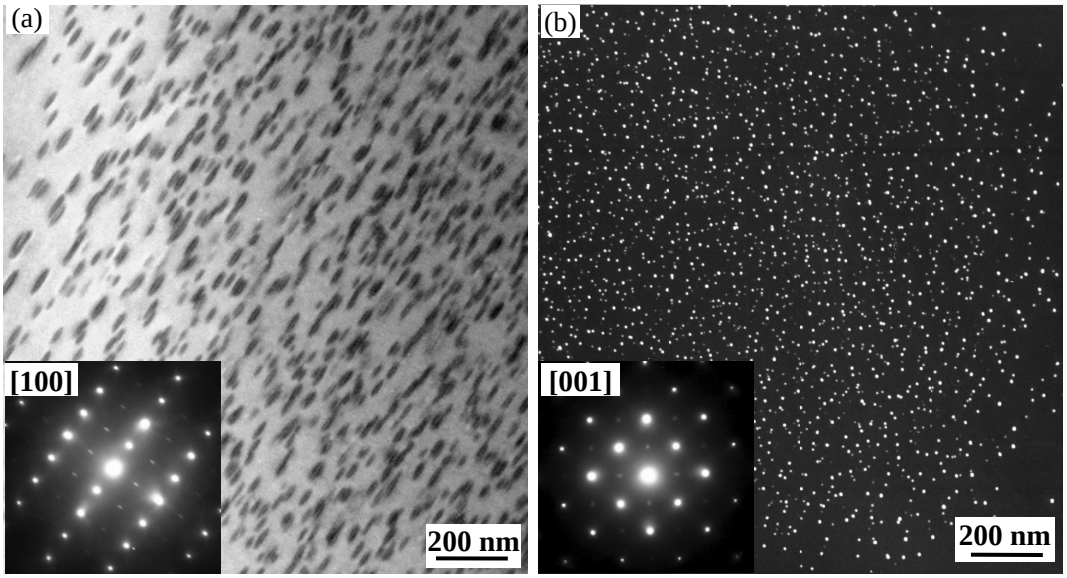

Figure 59 P-type carbides in the γ matrix of the Solution Treated & Annealed Ti-45Al-5Nb-0.5C alloy after solution treatment at 1250°C for 5h (OQ) and subsequent annealing at 800°C for 24h (FC), showing (a) needle-like projections in the $[100]_\gamma$ direction, (b) dot-like cross sections in the $[001]_\gamma$ direction. TEM dark field image was recorded using the $\mathbf{010_P}$ diffraction in two-beam condition.

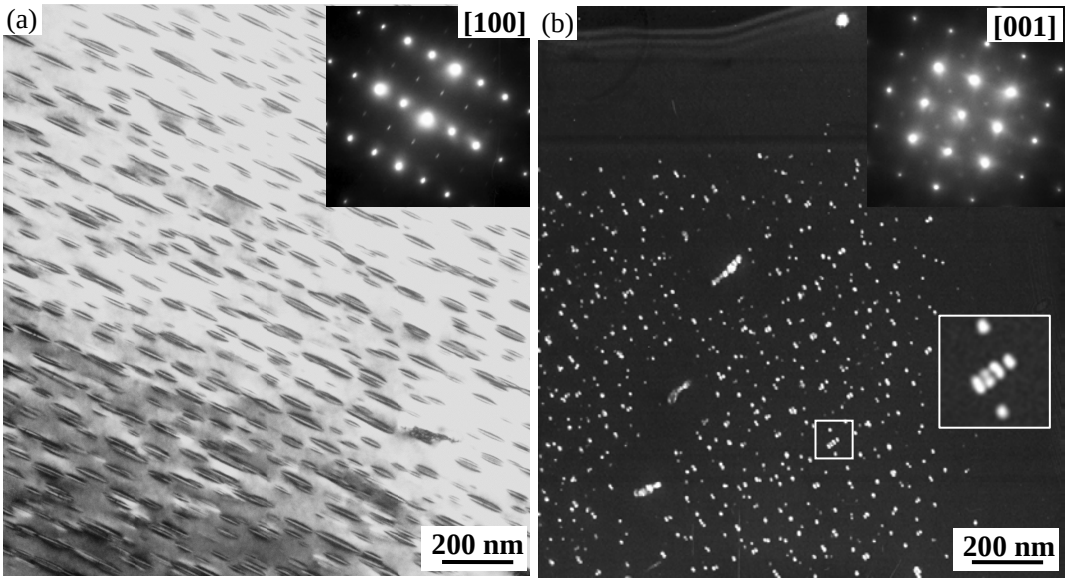

Figure 60 Most P-type carbides in the γ matrix of the Solution Treated & Annealed Ti-45Al-5Nb-0.5C alloy after solution treatment at 1250°C for 5h (OQ) and subsequent annealing at 800°C for 168h (FC), showing (a) needle-like projections in the $[100]_\gamma$ direction and (b) dot-like cross sections in the $[001]_\gamma$ direction. TEM dark field image was recorded using the $\mathbf{010_P}$ diffraction in two-beam condition. Some carbide starts to split, as shown in the insert of (b).

After 1104h at 800°C, P-Ti_3AlC carbides in γ grains significantly coarsen and change their morphology, as shown in **Figure 61**. From the $[100]_\gamma$ direction, carbides exhibit one set of needle projections and one set of plate projections with a large length/width ratio. Additionally, for the plate projections, fringes are observed not only vertically, but also parallel to the ***g*** vector. The fringes vertical to the ***g*** vector are more obvious.

For the needle projections, they show almost uniform contrast except for some discontinuity which is difficult to identify. From the $[001]_\gamma$ direction, the carbides show two sets of short rod projections. Meanwhile, fringes are also seen vertical to the ***g*** vector. Considering all the above, carbides may change their shape from needle-like to plate-like (with a larger length/width ratio compared to carbides in HIP & Annealed Ti-45Al-5Nb-0.75C). The broad faces of the plate-like carbide are parallel to $(100)_\gamma$ and $(010)_\gamma$ planes. Meanwhile carbides seem to split into many small substructures, which will be discussed for the Solution Treated & Annealed Ti-45Al-5Nb-0.75C alloy in **Section 5.1.2**.

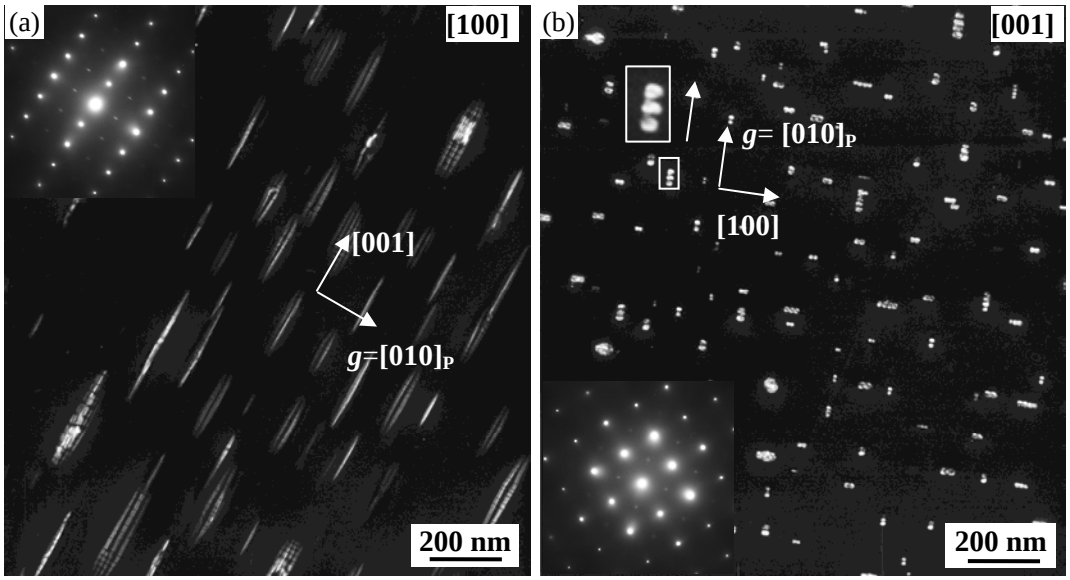

Figure 61 P-type carbides in the γ matrix in the Solution Treated & Annealed Ti-45Al-5Nb-0.5C alloy after solution treatment at 1250°C for 5h (OQ) and subsequent annealing at 800°C for 1104h (FC), coarsen and change their morphology, viewed from (a) the $[100]_\gamma$ direction and (b) the $[001]_\gamma$ direction respectively. TEM dark field images were recorded using the $\mathbf{010_P}$ diffraction in two-beam condition.

During the above TEM investigation it is mentioned that carbides are found at grain boundaries, at dislocations and in γ grains. Actually carbides have also been observed in lamellar colonies, as shown in **Figure 62** in the Solution Treated & Annealed Ti-45Al-5Nb-0.5C alloy after annealing at 800°C for 1104h. The dark field images were taken near the $[001]_\gamma$ direction using the $(010)_P$ diffraction in the two-beam condition. The projections near the $[001]_\gamma$ direction appear as short rods. However the exact morphology of the carbides in the lamellar colonies is not clear, although their size is definitely smaller than carbides in γ grains and at grain boundaries.

No investigation has been performed using TEM to study the carbides formed in the Solution Treated & Annealed Ti-45Al-5Nb-0.5C alloy after annealing at 900°C.

After annealing at 1000°C, several P-Ti_3AlC carbides are found at grain boundaries after 24h, but their number is lower than that in the HIPed & Annealed Ti-45Al-5Nb-0.5C alloy. This might confirm that after solution treatment, carbon supersaturation is

reduced and carbon is distributed more homogenously in the matrix. With increased annealing time, carbides are fully dissolved.

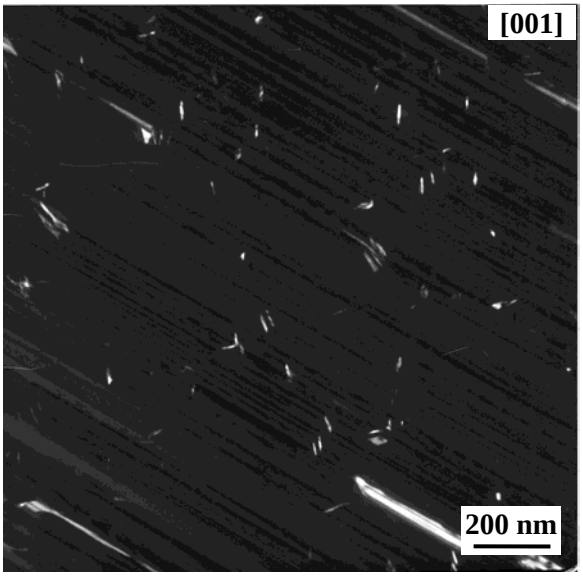

Figure 62 P-type carbides in the lamellar structure of the Solution Treated & Annealed Ti-45Al-5Nb-0.5C alloy after solution treatment at 1250°C for 5h (OQ) and subsequent annealing at 800°C for 1104h (FC). TEM dark field image was recorded using the $\mathbf{010_P}$ diffraction near the $[001]_\gamma$ direction. The morphology of P-type carbides in the lamellar colonies remains unclear at the moment.

To sum up, in Ti-45Al-5Nb-0.5C the thermal stability of P-type carbides in Solution Treated & Annealed conditions is similar to that in HIPed & Annealed conditions. Carbides are stable at 800°C but are dissolved at 1000°C.

4.3.4 Thermal stability of carbides in Solution Treated & Annealed Ti-45Al-5Nb-0.75C

The following will discuss carbide precipitation and thermal stability of carbides in the Solution Treated & Annealed Ti-45Al-5Nb-0.75C alloy.

P-Ti_3AlC carbides are found to be located at grain boundaries, at dislocations and in γ grains after annealing at 800°C. Compared with HIPed & Annealed Ti-45Al-5Nb-0.75C and Solution Treated & Annealed Ti-45Al-5Nb-0.5C, the carbide density in the γ grains of Solution Treated & Annealed Ti-45Al-5Nb-0.75C is significantly higher. **Figures 63** and **64** illustrate the development of P-Ti_3AlC carbides in the γ matrix during annealing at 800°C. The dark field images were recorded in the $[100]_\gamma$ and the $[001]_\gamma$ directions in order to observe the development of precipitate size and density clearly. Detailed values will be shown and discussed in **Section 4.4.2**.

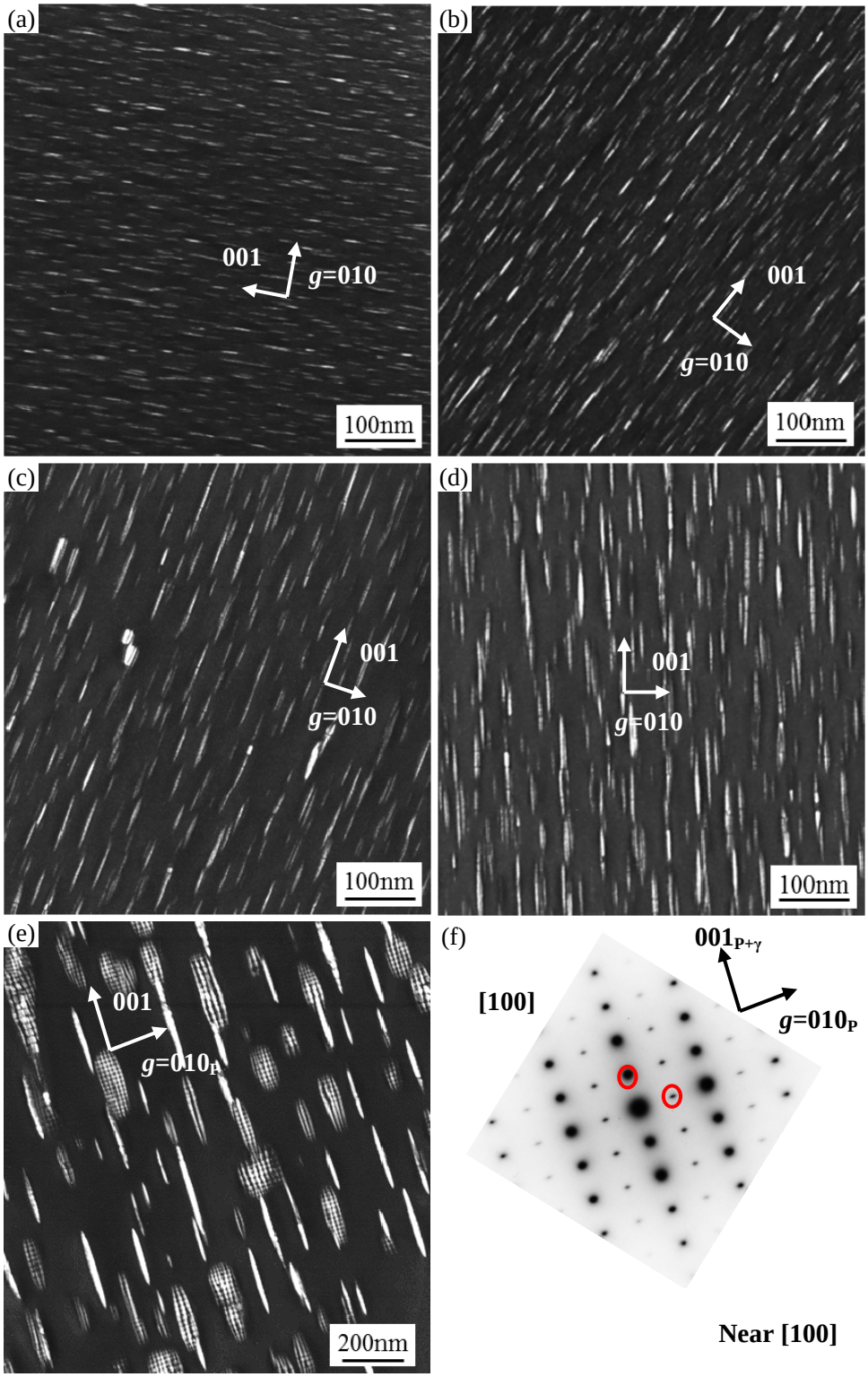

Figure 63 P-type carbides in the γ matrix of the Solution Treated & Annealed Ti-45Al-5Nb-0.75C alloy after solution treatment at 1250°C for 5h (OQ) and subsequent annealing at 800°C for (a) 24h, (b) 48h, (c) 96h, (d) 168h, (e) 1054h and (f) diffraction pattern for (e), (FC). All TEM images were recorded near the $[100]_{\gamma}$ direction using the $\mathbf{(010)_P}$ diffraction in two-beam condition.

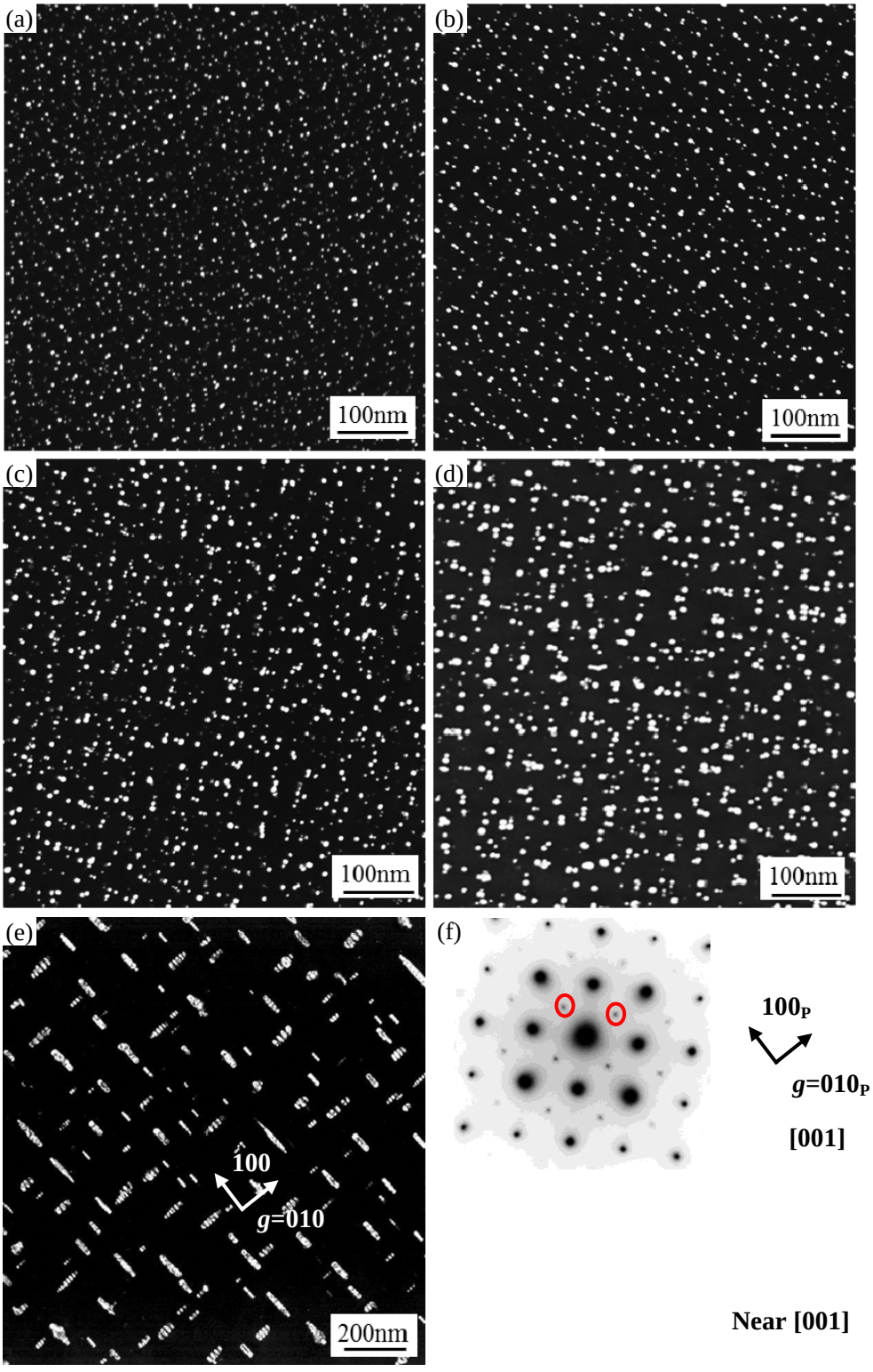

Figure 64 P-type carbides in the γ matrix of the Solution Treated & Annealed Ti-45Al-5Nb-0.75C alloy after solution treatment at 1250°C for 5h (OQ) and subsequent annealing at 800°C for (a) 24h, (b) 48h, (c) 96h, (d) 168h, (e) 1054h and (f) diffraction pattern for (e), (FC). All TEM images were recorded near the $[001]_{\gamma}$ direction using the $\mathbf{(010)_P}$ diffraction in two-beam condition.

Carbides in the γ matrix first appear with a normal needle-like morphology. With increasing annealing time, the density of particles tends to decrease and their size increases, as shown in **Figures 63-64**. However, after 168h at 800°C the P-Ti_3AlC

carbides in γ grains have not only grown. Some of them have changed their morphology and started to split, as is the case for Solution Treated & Annealed Ti-45Al-5Nb-0.5C. After 1054h, carbides remain at grain boundaries, at dislocations and in the γ matrix. Carbides in γ grains split into many substructures. The morphology change of γ matrix carbides and carbide splitting which occur during annealing of the Solution Treated & Annealed Ti-45Al-5Nb-0.75C alloy will be discussed in detail in **Section 5.1.2**.

After annealing at 900°C, P-Ti_3AlC carbides can be detected at grain boundaries, at dislocations and in γ grains. After annealing for 24h, carbides in the γ matrix have grown to a large size and have already split into substructures, as shown in **Figure 65**. Regions A and B of the larger micrographs in **Figure 65** show two γ grains that are oriented along the [100] and [001] directions respectively. Most plate shaped carbides in region A have split into several parallel needles along the [001] direction and have started to split further along the [100] or the [010] direction into even smaller domains.

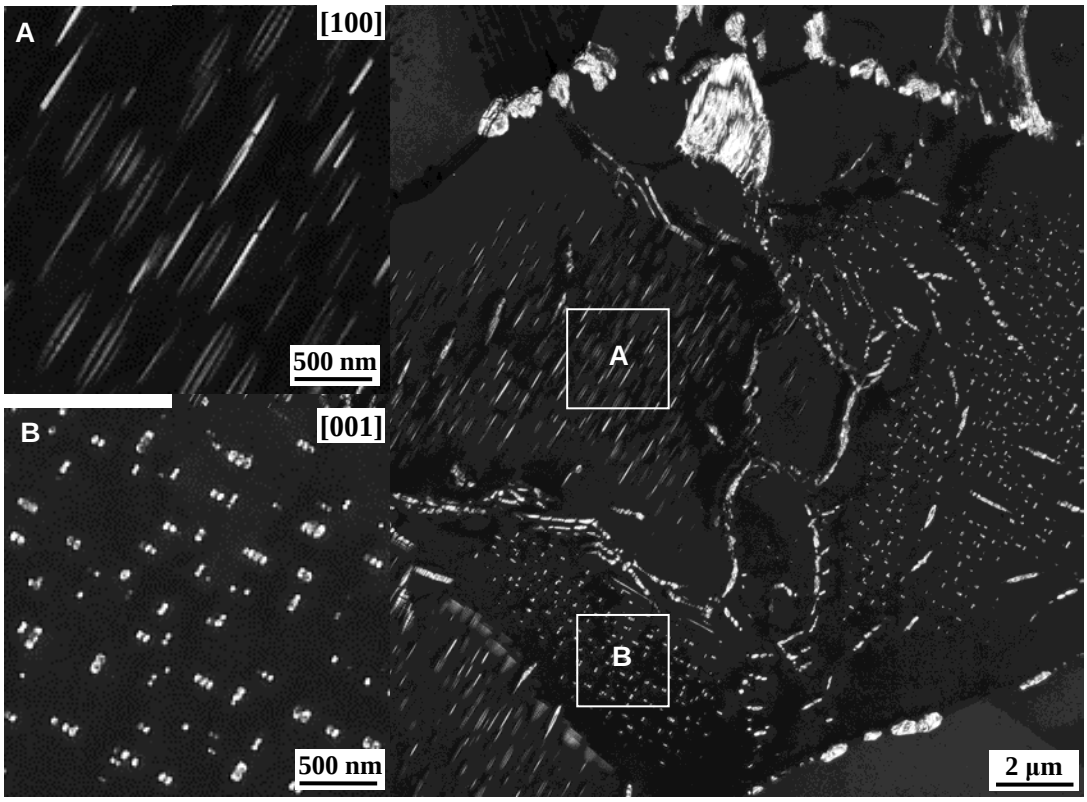

Figure 65 TEM investigation of P-type carbides in the γ matrix of the Solution Treated & Annealed Ti-45Al-5Nb-0.75C alloy after solution treatment at 1250°C for 5h (OQ) and subsequent annealing at 900°C for 24h (FC), using $\boldsymbol{g}$**=010** $_{\mathbf{P}}$ in two-beam condition.

After 168h at 900°C, P-Ti_3AlC carbides are observed to be present in the γ matrix accompanied by dislocations, marked in **Figure 66**, which may be treated as evidence of lost coherency (Iwamura 2004). Meanwhile the carbides are surrounded by "coffee bean" contrast which is caused by the strain field from the formation of plate-shaped carbides. Compared with the HIPed & Annealed condition, carbides still exist, remain in the γ phase and retain their orientation with the γ matrix after 168h at 900°C.

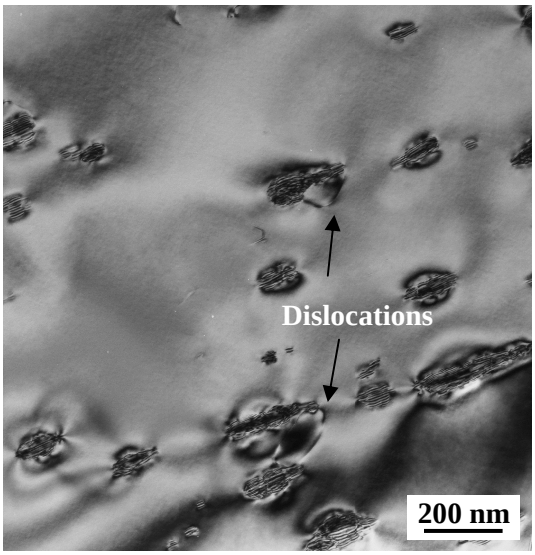

Figure 66 P-type carbides in the γ matrix of the Solution Treated & Annealed Ti-45Al-5Nb-0.75C alloy after solution treatment at 1250°C for 5h (OQ) and subsequent annealing at 900°C for 168h (FC), near the [101] direction. TEM bright field image was recorded in two-beam condition. Dislocations can be observed around the precipitates.

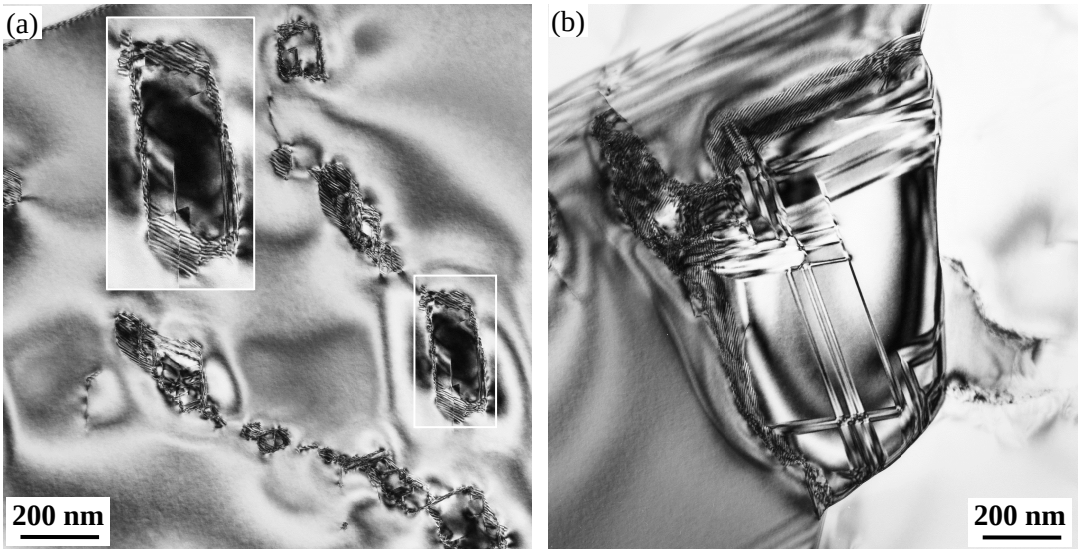

Figure 67 P-type carbides in the Solution Treated & Annealed Ti-45Al-5Nb-0.75C alloy after solution treatment at 1250°C for 5h (OQ) and subsequent annealing at 1000°C (a) for 24h (FC), at dislocations with plate-like morphology, and (b) for 168h (FC), at grain boundaries with a size of around 1μm.

At 1000°C, carbides coarsen significantly and only exist at grain boundaries and at dislocations. **Figure 67(a)** shows carbides at dislocations which have changed their morphology to plate-like shape with faceted edges. Moiré fringes are observed to surround these plate carbides, as shown in the insert. Moreover there is obvious contrast around the precipitates probably due to the elastic strain field caused by carbide precipitation. As seen in **Figure 67(b)** the size of the carbide at grain boundaries almost reaches 1μm after 168h. Obvious interfaces can be seen between

the carbide and the γ matrix. At the same time planar defects are observed in big carbides.

To summarize: similar to the HIPed & Annealed conditions, carbides in Solution Treated & Annealed Ti-45Al-5Nb-0.75C are stable at 800°C and coarsen at 900 and 1000°C.

4.4 Carbide fraction, size and density in the heat-treated alloys

4.4.1 Carbide fractions

From the relative intensity ratio (RIR) method the weight fraction of the P-Ti_3AlC phase in the Ti-45Al-5Nb-0.5C and Ti-45Al-5Nb-0.75C alloys in HIPed & Annealed and Solution Treated & Annealed conditions were obtained, as shown in **Figures 68** and **69** respectively.

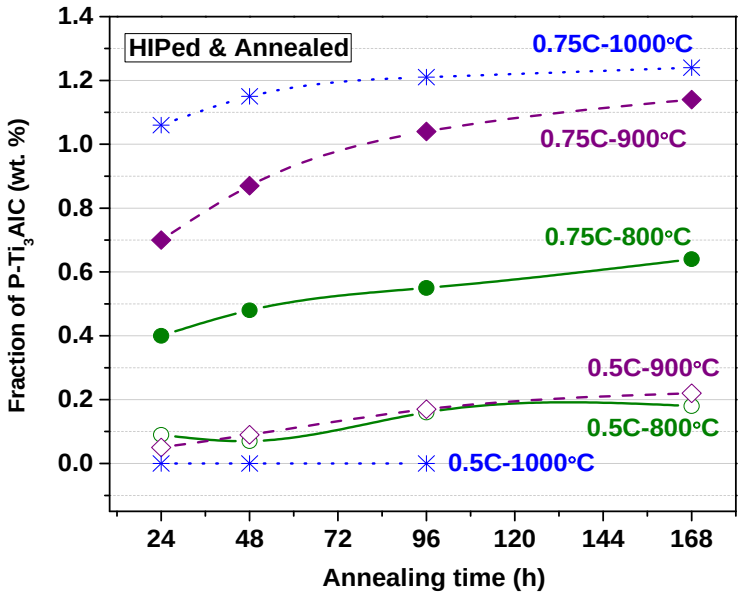

Figure 68 Weight fraction of the P-Ti_3AlC phase determined using the RIRs method based on HEXRD patterns for the HIPed & Annealed Ti-45Al-5Nb-0.5C and Ti-45Al-5Nb-0.75C alloys at 800 to 1000°C. The data is connected by guiding spline lines.

In the HIPed & Annealed Ti-45Al-5Nb-0.5C alloy the fraction of carbides tends to increase (except for an abnormal case after 24h at 800°C) after annealing at 800 and 900°C. However, at 1000°C no carbide reflections are detected.

In comparison to the HIPed & Annealed Ti-45Al-5Nb-0.5C alloy, the fractions of carbides are much higher in HIPed & Annealed Ti-45Al-5Nb-0.75C. With increasing temperature and time the carbide fraction in HIPed & Annealed Ti-45Al-5Nb-0.75C increases. For all temperatures, at the beginning of annealing, the carbide fraction in HIPed & Annealed Ti-45Al-5Nb-0.75C quickly increases. For longer annealing times the increase of carbide fraction slows down and is assumed to be saturated at 1000°C after 168h. The fraction of carbides in the alloy after 168h at 1000°C was also analyzed by Rietveld refinement to compare the results with that obtained using the

RIR method. The Rietveld method gives a P-Ti_3AlC phase fraction of about 1.8±0.1 wt. %, which is around 0.56 % higher than that determined from the RIR method. This may indicate that RIR method underestimates the fraction of carbides. However it should not change the tendency of the carbide fraction variation with temperature and time.

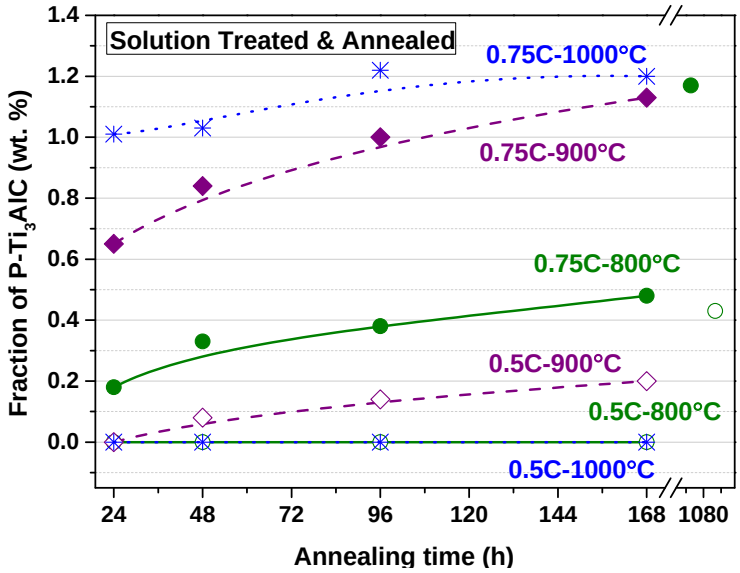

Figure 69 Weight fraction of the P-Ti_3AlC phase at 800 to 1000°C determined using RIR method on HEXRD patterns of the Solution Treated & Annealed Ti-45Al-5Nb-0.5C and Ti-45Al-5Nb-0.75C alloys. The data is connected by guiding spline lines.

In the Solution Treated & Annealed Ti-45Al-5Nb-0.5C alloy, no reflections from the P-Ti_3AlC phase are detected after annealing from 24 to 168h at 800°C due to the fine particle size in the γ matrix. As explained earlier reflections from the P-Ti_3AlC phase are broadened and thus submerged into the background. Thus the fraction of carbides cannot be determined from the HEXRD diffractograms, which is why the results are represented as zero in **Figure 69**. After 1104h at 800°C, the fraction of P-Ti_3AlC phase is around 0.4 wt. %. After 24h at 900°C, the carbide fraction is represented as zero for the same reason. After 48h at 900°C, the carbide fraction increases and is close to the level in the HIPed & Annealed Ti-45Al-5Nb-0.5C annealed under the same conditions. At 1000°C, carbides are dissolved in the Solution Treated & Annealed Ti-45Al-5Nb-0.5C alloy.

In the Solution Treated & Annealed Ti-45Al-5Nb-0.75C alloy, the fraction of P-Ti_3AlC phase is lower than that in the HIPed & Annealed conditions at 800°C. In the Solution Treated & Annealed conditions the reflections from the P-Ti_3AlC phase are broadened due to the fine precipitate size in the γ matrix, and thus the fraction of the P-Ti_3AlC phase might be underestimated. Another reason for the differences in carbide fraction could be that due to the more homogeneous distribution of carbon after solution treatment. This would reduce the fraction of carbides at grain boundaries (**Figure 46** in **Section 4.2.1**) and slow down the growth of carbides in γ grains (**Figure 74** in **Section 4.4.2**). With increasing annealing temperature and time,

the fraction of P-Ti_3AlC phase increases. As for the situation at 800°C, the carbide fraction is slightly smaller in the Solution Treated & Annealed alloys than in the HIPed & Annealed conditions after annealing at 900 and 1000°C. The fraction of P-Ti_3AlC phase at 900°C also increases with increasing time. The development of P-Ti_3AlC phase is slowed down at 1000°C and its fraction becomes saturated after 96h. Similar to the case for the HIPed & Annealed conditions, the fraction of P-Ti_3AlC phase may be underestimated for the Solution and Annealed conditions when calculated using the RIR method compared to the values determined by Rietveld analysis. For example after 168h at 1000°C the fraction of carbides is 1.2 wt. % according to the RIR method and 1.7±0.1 wt. % from Rietveld analysis.

4.4.2 Carbide size and density in heat-treated Ti-45Al-5Nb-0.75C

The growth and coarsening of carbides during annealing of Ti-45Al-5Nb-0.75C at 800°C is described in this section which concentrates on the size and the density of carbides in the γ matrix. The measurement of carbide size and density is based on TEM images and three γ grains were analyzed for each condition (except for the case at 800°C for 24h where five grains were measured in order to obtain better statistics).

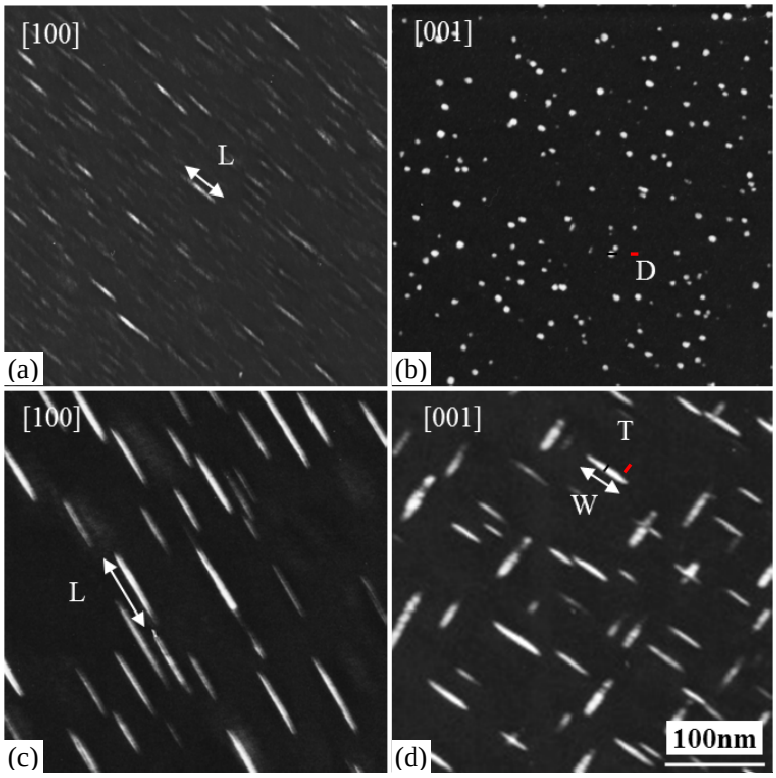

Figure 70 Examples of TEM images used for carbide size measurement in HIPed & Annealed Ti-45Al-5Nb-0.75C after annealing at 800°C, (a) length (*L*) of a needle in the $[100]_\gamma$ direction after 24h, (b) diameter (*D*) of a needle in the $[001]_\gamma$ direction after 24h, (c) length (*L*) of a plate in the $[100]_\gamma$ direction after 168h, and (d) thickness (*T*) and width (*W*) of a plate in the $[001]_\gamma$ direction after 168h. All the TEM dark field images have the same scale bar and were recorded using the diffraction from P-Ti_3AlC phase in two-beam condition.

From the TEM investigations described in **Section 4.3.2**, in HIPed & Annealed Ti-45Al-5Nb-0.75C the carbides in γ grains have a needle-like morphology after 24h at 800°C and start to change their morphology to plate-like after 48h. In Solution Treated & Annealed Ti-45Al-5Nb-0.75C (**Section 4.3.4**), carbides have a needle shape up to 96h and have started splitting after 168h. For this reason the carbide density and size were not determined for the condition at 168h. The TEM images were recorded from $[100]_\gamma$ and $[001]_\gamma$ directions in order to measure the length (L) and diameter (D) of needle-shaped carbides, and the length (L), width (W) and thickness (T) of plate-like carbides, as shown in **Figure 70**.

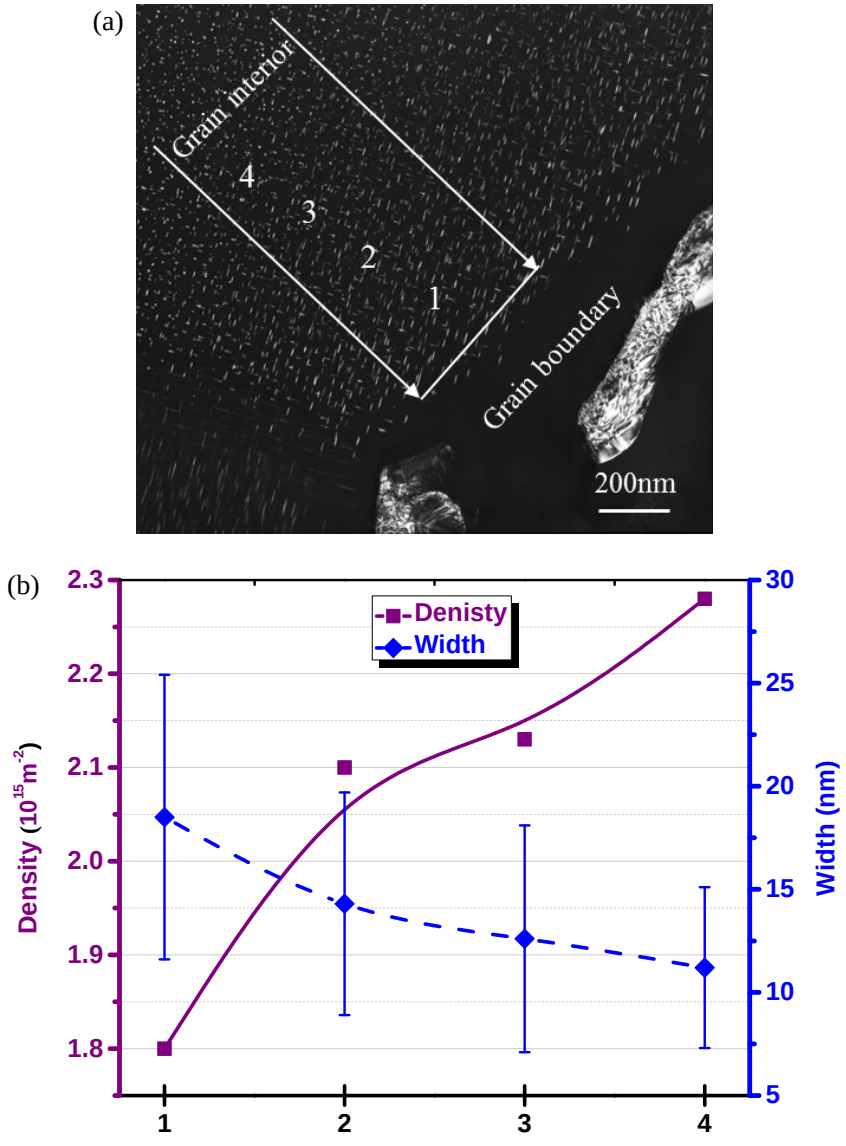

Figure 71 (a) TEM dark field image in the $[001]_\gamma$ direction of the HIPed & Annealed Ti-45Al-5Nb-0.75C alloy after annealing at 800°C for 48h, (b) data showing the variation of carbide size and density within a γ grain. The data is connected by guiding spline lines (with standard deviation bars).

As shown in **Figure 71**, in HIPed & Annealed Ti-45Al-5Nb-0.75C, there is a gradient in carbide size and density within the γ grains. The carbide density increases and their

size decreases with increasing distance from the grain boundary. In order to make the measurement more accurate but without introducing too much work, two regions (with dimension of 484.06×193.62nm^2), one near to a grain boundary (like position 1 in **Figure 71**), and the second within a grain interior (like position 4 in **Figure 71**) that was about 1.4μm away from the grain boundary, were examined (3 grains for each condition). There was an obvious difference between the carbides at the grain boundaries and grain interiors, especially after annealing for 24 to 48h. After annealing for 96h the differences were smaller. However for the Solution Treated & Annealed Ti-45Al-5Nb-0.75C, the differences in carbide size and density of grain boundary and grain interior carbides were not as obvious as for the HIPed & Annealed conditions. The numbers of particles measured in each region ranged from about 25-500. The density of carbides in the γ matrix is expressed as number per unit area (m^{-2}).

The variation of carbide size and density in γ grains shown in **Figure 71** suggests that carbides near to grain boundaries grow faster than those within the grain interiors (around 1-1.5μm away from the grain boundary). According to a rough estimate of the carbide volume in different regions, it can be determined that regions near to grain boundaries have a higher volume fraction of carbides than regions away from grain boundaries. This might be an explanation why the carbide morphology change first starts at grain boundaries, as discussed later in **Section 5.3.1**.

Figure 72 shows how the carbide density develops in the γ matrix as a function of annealing time at 800°C in the Ti-45Al-5Nb-0.75C alloy. Generally Solution Treated & Annealed conditions have a higher carbide density than HIPed & Annealed conditions. In HIPed & Annealed Ti-45Al-5Nb-0.75C, the average carbide density is $2.7\times10^{15}m^{-2}$ after 24h, decreases to around $2.2\times10^{15}m^{-2}$ after 48h, drops further to $0.6\times10^{15}m^{-2}$ after 96h and slowly reduces to $0.4\times10^{15}m^{-2}$ after 168h. It is worth mentioning that the carbide density in different grains has some variation, which is shown by the large standard deviation bar at 24h and might be attributed to the variation of carbon concentration in different grains. The carbide density in the Solution Treated & Annealed conditions is significantly higher than that of the HIPed & Annealed conditions, and will be discussed in **Section 4.6**. As the annealing time of the Solution Treated & Annealed alloy is increased, the average carbide density decreases almost linearly from around $4.8\times10^{15}m^{-2}$ at 24h to $2.8\times10^{15}m^{-2}$ at 96h. Again it should be noted that after 48 and 96h the standard deviation bars are very large because there is a large variation of precipitation in different grains. This also implies that the nucleation and growth of carbides may happen at the same time in γ grains.

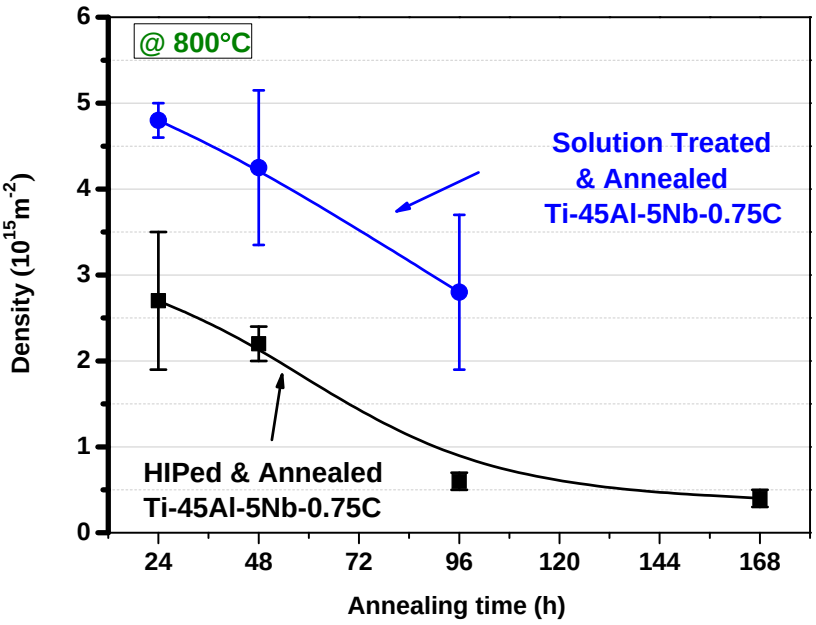

Figure 72 The development of carbide density in the γ matrix as a function of annealing time at 800°C for the Ti-45Al-5Nb-0.75C alloy. The data is connected by guiding spline lines (with standard deviation bars).

Figure 73 shows the development of carbide size in the γ matrix as a function of annealing time at 800°C for the Ti-45Al-5Nb-0.75C alloy. It is again worth mentioning that *L*, *W* and *T* represent Length, Width and Thickness of plates, and *L* and *D* represent the Length and Diameter of the needles. In the HIPed & Annealed condition after 24h at 800°C, carbides exhibit a needle-like shape with average dimensions of $D \approx 4.7$nm, and $L \approx 24.2$nm ($L/D \approx 5$). After 48h, carbides start to change shape to a plate-like morphology with average dimensions of $T \approx 3.4$nm, $W \approx 15.3$nm and $L \approx 34.8$nm ($L/T \approx 10$, $L/W \approx 2$). Here it should be noted that after the morphology changes from needle to plate, the atoms should be redistributed because the diameter of the needles is larger than the thickness of the plates. After 48h the plate-shaped carbides have grown. The carbides have average dimensions of $T \approx 4.6$nm, $W \approx 26.8$nm, and $L \approx 45.8$nm ($L/T \approx 10$, $L/W \approx 2$) after 96h. After 168h the growth tends to slow down and carbides have average dimensions of $T \approx 5.0$nm, $W \approx 30.4$nm, and $L \approx 51.1$nm ($L/T \approx 10$, $L/W \approx 2$). It should be noted that during carbide growth, the size ratios don't change significantly. These ratios will be used in the calculations presented in **Section 5.3.1**. The carbides have a smaller size in Solution Treated & Annealed conditions compared to those in HIPed & Annealed conditions. This is attributed to the higher density of carbides and stronger competition among carbides. With increasing annealing time it can be seen in **Figure 73** that the carbides grow. After 24h, the needles have an average *L* of about 20.8nm and *D* of around 3.5nm ($L/D \approx 6$). After 48h, the average *L* has increased to 26.7nm and the average *D* has increased to 4.4nm ($L/D \approx 6$) respectively. After 96h, the needles have grown to a size with an *L* of around 35.3nm and a *D* of about 5.6nm ($L/D \approx 6$). Although the L/D ratio remains at around 6 during the carbide growth, in fact it increases slightly for longer annealing times.

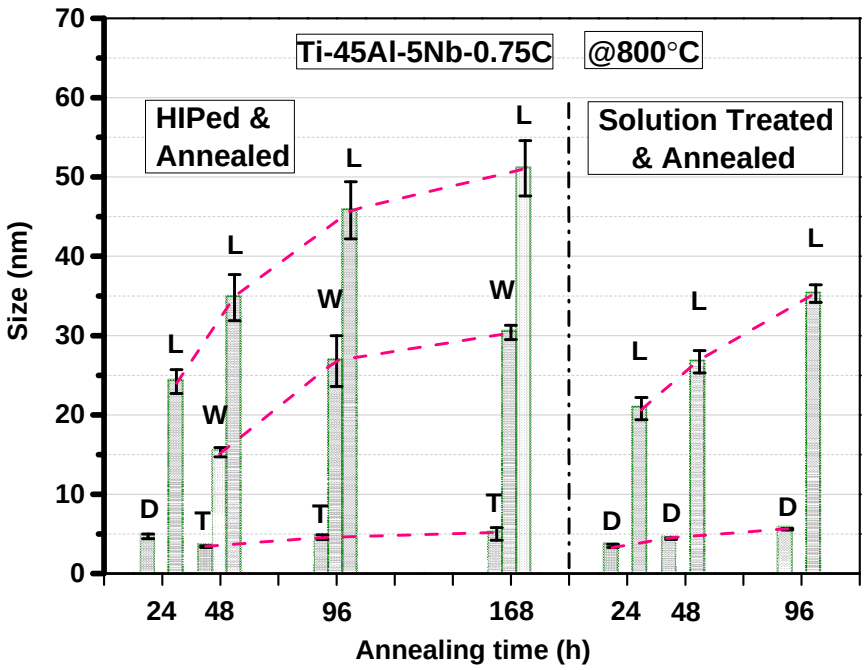

Figure 73 Development of carbide size (with standard deviation bars) in the γ matrix during annealing at 800°C in the heat-treated Ti-45Al-5Nb-0.75C alloy. *L*, *W* and *T* represent Length, Width and Thickness for the plates while *L* and *D* represent the Length and Diameter of the needles.

By integrating the carbide area density and the carbide size, it is possible to get a rough estimate for the volume of carbide in the γ matrix. The volume of carbides can be simply expressed as:

$$V = v' \cdot d' \qquad \textbf{Eq. 7}$$

Where, *v'* is the volume for a single precipitate and *d'* is the carbide number per unit area ($1m^2$). Thus the volume of carbides with needle-like and plate-like morphologies is given by **Eqs. 8** and **9** respectively:

$$V = \frac{4\pi}{3} \cdot \frac{L}{2} \cdot \frac{D}{2} \cdot \frac{D}{2} \cdot d' \text{ (Needle-like)} \qquad \textbf{Eq. 8}$$

$$V = 2\pi \cdot \frac{L}{2} \cdot \frac{W}{2} \cdot \frac{T}{2} \cdot d' \text{ (Plate-like)} \qquad \textbf{Eq. 9}$$

Using the data given in **Figures 72-73** in **Eqs. 8-9**, the development of carbide volume can be calculated and is plotted in **Figure 74**. In the HIPed & Annealed Ti-45Al-5Nb-0.75C alloy, the carbide volume appears to significantly increase between 24 and 48h, and then starts to decrease after 48h. This may suggest that after 48h the formation of carbides has finished and carbides start to coarsen. In the Solution Treated & Annealed Ti-45Al-5Nb-0.75C alloy, the volume of carbides in the γ matrix continues to increase slowly with increasing annealing time. This may be due to the higher carbide density in Solution Treated & Annealed Ti-45Al-5Nb-0.75C alloy. The

growth of the carbides could be slowed down due to competition from numerous precipitates.

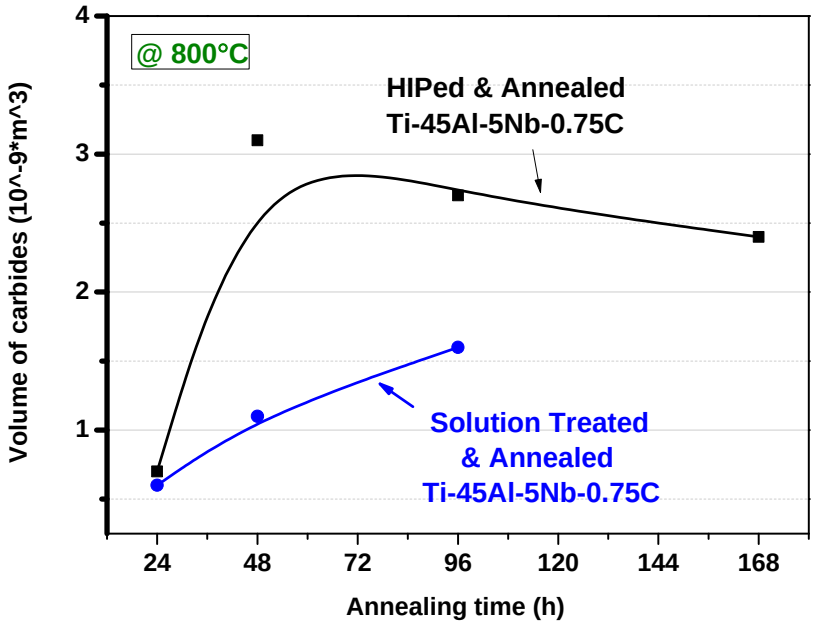

Figure 74 Development of carbide volume in the γ matrix as a function of annealing time at 800°C in the Ti-45Al-5Nb-0.75C alloy. The data is connected by guiding spline lines.

4.5 Precipitate-free zones in heat-treated Ti-45Al-5Nb-0.75C

In the heat-treated alloys in this research precipitate-free zones (PFZs) were often found to be located near to grain boundaries and dislocations. In the Ti-45Al-5Nb-0.75C alloy there are a number of types of boundaries which include γ-γ, γ-P-γ, γ-α_2, γ-P-α_2, γ-lamellar and γ-P-lamellar boundaries. The type of boundary has an influence on the width of the PFZs. γ-P-γ, γ-P-α_2 and γ-P-lamellar boundaries represent P-type carbides located at γ-γ, γ-α_2 and γ-lamellar grain boundaries. From literature PFZs played a role in mechanical properties (Abe 1973) and were reported to be harmful because cracks could form easily in soft PFZs (Krol 2004, Nembach 2005, Tolley 2005). However, Ryum et al. (Ryum 1968) found that PFZs increased the ductility of Al–Zn–Mg alloys and Park et al. (Park 1995) reported PFZs were beneficial to low-cycle fatigue life due to local stress relief in PFZs. Thus it is important to know the formation mechanism of the PFZs and their development during annealing treatments.

Figure 75 shows examples for PFZs width measurement near different grain boundaries in heat-treated Ti-45Al-5Nb-0.75C alloy. Five images for each condition were used to determine an average PFZ width, as shown in **Figure 76**.

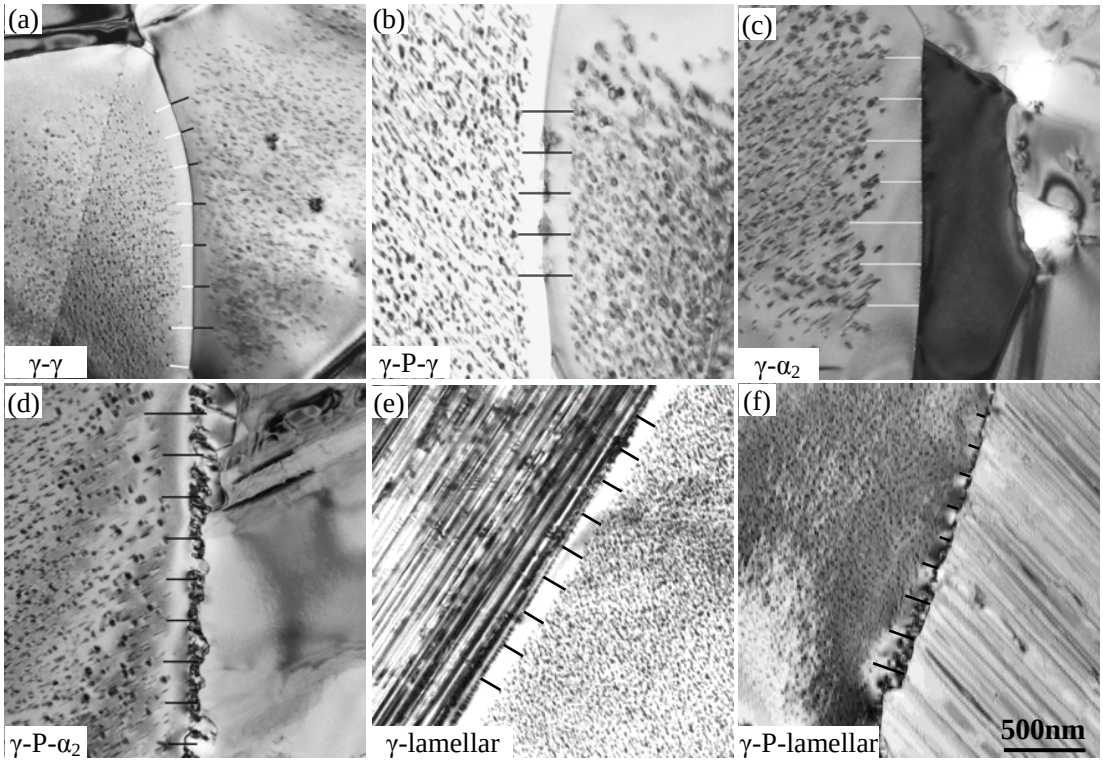

Figure 75 Examples of different PFZs near to: (a) a γ-γ grain boundary, 24h @ 800°C, (b) a γ-P-γ grain boundary, 168h @ 800°C, (c) a γ-α_2 grain boundary, 168h @ 800°C, (d) a γ-P-α_2 grain boundary, 96h @ 800°C, (all in HIPed & Annealed Ti-45Al-5Nb-0.75C), and (e) a γ-lamellar grain boundary and (f) a γ-P-lamellar grain boundary, 48h @ 800°C (both in Solution Treated & Annealed Ti-45Al-5Nb-0.75C). γ-P-γ, γ-P-α_2 and γ-P-lamellar boundaries, represent P-type carbides located at γ-γ, γ-α_2 and γ-lamellar grain boundaries. All TEM images have the same scale bar.

In the HIPed & Annealed Ti-45Al-5Nb-0.75C alloy, the width of the PFZs near to γ-γ and γ-P-γ grain boundaries is quite similar, and smaller than those near to γ-α_2 and γ-P-α_2 grain boundaries (these two are also quite similar). It may be that the γ-γ grain boundaries and γ-P-γ grain boundaries are actually identical since the precipitates lie at certain positions in the γ-γ grain boundaries. Thus, the γ-γ boundaries can be in foil material and are very close to precipitates that are no longer in the foil. This may also apply to γ-α_2 and γ-P-α_2 grain boundaries. During annealing only the width of PFZs near to γ-γ and γ-P-γ grain boundaries seems to increase slightly and remain stable after 96h. The width of PFZs near to γ-α_2 and γ-P-α_2 grain boundaries shows no obvious tendency.

In the Solution Treated & Annealed Ti-45Al-5Nb-0.75C alloy, PFZs appear narrower than those in the HIPed & Annealed alloy. Again the width of PFZs near to γ-γ grain boundaries are close to those of γ-P-γ grain boundaries and smaller than the width of PFZs near to γ-lamellar and γ-P-lamellar grain boundaries. In the Solution Treated & Annealed condition the lamellar structure was formed during annealing from retained high-temperature α phase. The width of PFZs near γ-lamellar grain boundaries is smaller than that of PFZs near to γ-P-lamellar grain boundaries. Here it should be mentioned that for the case of PFZs near to γ-lamellar grain boundaries, the γ phase

has an orientation relationship of [11-20]α_2//[110]γ with the lamellar structure. However, for the situation of PFZs near to γ-P-lamellar grain boundaries, the γ phase has no orientation relationship with the lamellar structure. The PFZs width increases slowly with increasing annealing time.

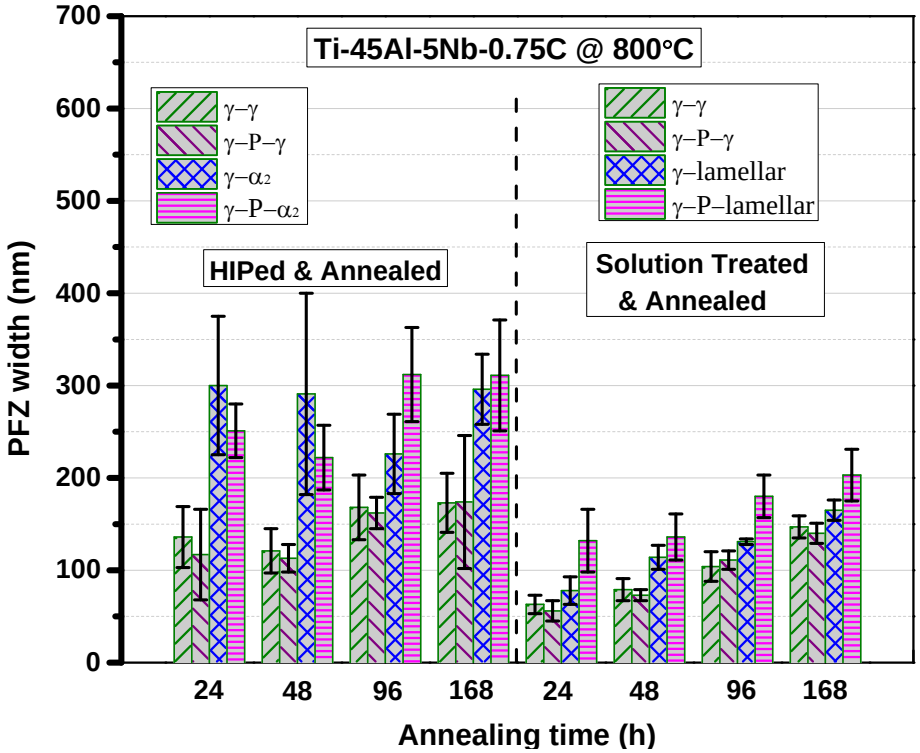

Figure 76 Development of PFZs width (with standard deviation bars) in heat-treated Ti-45Al-5Nb-0.75C alloy during annealing at 800°C. γ-P-γ, γ-P-α_2 and γ-P-lamellar grain boundaries represent P-type carbides located at γ-γ, γ-α_2 and γ-lamellar grain boundaries.

Precipitate-free zones (PFZs) have often been observed adjacent to grain boundaries and dislocations in other annealed alloys systems (Unwin 1969, Shastry 1971, Jha 1987, Maldonado 1997). The explanations for these zones were attributed to localized depletion of solute caused by preferential precipitation at grain boundaries (Rosenbaum 1959), the depletion of vacancies (Geisler 1951), or a combination of both. In the HIPed & Annealed alloy the width of PFZs near to γ-γ (γ-P-γ) grain boundaries is smaller than that of PFZs near to γ-α_2 (γ-P-α_2) grain boundaries. In TiAl alloys, the α_2 phase has been shown to accommodate much more carbon than the γ phase. During annealing, neighboring α_2 grains in Ti-45Al-5Nb-0.75C may absorb carbon solute from γ grains. The growth of big grain boundary carbides may also continuously take carbon from the γ matrix. Therefore regions near to grain boundaries probably have less carbon solute than within γ grain interiors. When the carbon solute content is lower than its solubility, the formation of carbides will not proceed. Therefore precipitate free zones near to γ-α_2 (γ-P-α_2) grain boundaries occur. In the case of PFZs near to γ-γ (γ-P-γ) grain boundaries, small precipitates at grain boundaries also can consume carbon solute from the matrix and grain boundaries can work as a sink for carbon solute. However, compared with the α_2 phase, their ability to

consume carbon from the matrix is weak. So PFZs near to γ-γ (γ-P-γ) grain boundaries appear narrower than those near to γ-α_2 (γ-P-α_2) grain boundaries. Similarly in the Solution Treated & Annealed alloy, PFZs near to γ-γ (γ-P-γ) grain boundaries are again the narrowest. But the width of PFZs near to γ-lamellar grain boundaries is smaller than that of PFZs near to γ-P-lamellar grain boundaries, and may be due to the growth of P-type carbides at γ-lamellar grain boundaries.

In the HIPed & Annealed alloy the width of PFZs near to γ-γ (γ-P-γ) grain boundaries tends to increase slightly up to 96h while those near to γ-α_2 (γ-P-α_2) grain boundaries show no obvious variation. This might be explained by the near-equilibrium condition of the HIPed & Annealed microstructure. However, in the Solution Treated & Annealed alloy the width increases for all types of PFZs with increasing annealing time. With longer annealing time, the grain boundary and γ matrix carbides can grow by taking carbon from the neighboring matrix. This might imply that the microstructure of the Solution Treated & Annealed alloy conditions may not be close to thermodynamic equilibrium and gradual elemental redistribution is necessary to reach equilibrium. The width of all types of PFZs is apparently reduced in Solution Treated & Annealed conditions compared to HIPed & Annealed conditions. This may be explained by the larger number of grain boundary carbides in the HIPed & Annealed alloy which thus take carbon from the matrix. Hence PFZs in the Solution Treated & Annealed condition are narrower, as schematically illustrated in **Figure 96**.

4.6 Comparison of carbides in Ti-45Al-5Nb-0.5C and Ti-45Al-5Nb-0.75C

In both alloys under investigation carbides exist at grain boundaries, at dislocations and in the γ matrix after annealing at 800°C. The typical morphology of P-Ti_3AlC carbides at triple junctions is shown in **Figures 55(a)** and **57(a)**. P-type carbides have an orientation relationship of: $[001]_P//[001]_\gamma$, $(100)_P//(100)_\gamma$ with one of the neighboring γ grains. As the carbides coarsen, the orientation relationship is gradually lost and the interface between the P-Ti_3AlC carbides and the γ phase becomes incoherent. The same situation applies for carbides at grain boundaries. Carbides at dislocations in γ grains always possess the orientation relationship of $[001]_P//[001]_\gamma$, $(100)_P//(100)_\gamma$ with the γ matrix, as evidenced by the diffraction patterns and moiré fringes. At the beginning of annealing, very small carbides start to nucleate at dislocations. Their intensity in diffraction patterns is usually too weak to be identified. As annealing progresses, carbides decorating dislocations become evident. Under special tilting conditions they show ”coffee bean” contrast (Ashby 1963) which is caused by the elastic strain field of the particles. As the carbides grow further, moiré fringes are observed, which is evidence that P-type carbides keep their orientation relationship with the γ matrix. Carbides in γ grains always possess the orientation relationship $[001]_P//[001]_\gamma$, $(100)_P//(100)_\gamma$ with the γ matrix, no matter if the carbides change their morphology from needle-like to plate-like in the HIPed & Annealed and Solution Treated & Annealed alloy conditions, or after splitting into substructures during coarsening in the Solution Treated & Annealed alloy conditions.

An overview of carbide precipitation and thermal stability in heat-treated Ti-45Al-5Nb-0.5C and Ti-45Al-5Nb-0.75C alloys is illustrated in **Figure 77**. In the HIPed & Annealed Ti-45Al-5Nb-0.5C alloy, carbides form sequentially at grain boundaries, at dislocations and in the γ matrix during annealing at 800°C. Carbide coarsening takes place at 900°C and carbides only exist at grain boundaries after annealing for 168h. After annealing at 1000°C they dissolve. For the Solution Treated & Annealed Ti-45Al-5Nb-0.5C, carbides form at grain boundaries, at dislocations and in the γ matrix after 24h at 800°C. Carbides with needle-like morphology grow and start to split after 168h. In HIPed & Annealed Ti-45Al-5Nb-0.75C at 800°C, more carbides are formed than in the HIPed & Annealed Ti-45Al-5Nb-0.5C alloy and the carbides in the γ matrix change shape from a needle-like to plate-like morphology with increasing annealing times. Carbides coarsen in the Ti-45Al-5Nb-0.75C alloy at 900 and 1000°C. In Solution Treated & Annealed Ti-45Al-5Nb-0.75C, fewer grain boundary carbides are found and there is a higher density of carbides in the γ matrix compared to the HIPed & Annealed condition. As for the Solution Treated & Annealed Ti-45Al-5Nb-0.5C, at 800°C carbides in the γ matrix initially have a needle-like morphology and start to split after 168h.

The variation of carbide precipitation and thermal stability in Ti-45Al-5Nb-0.5C and Ti-45Al-5Nb-0.75C alloys may be attributed to the different carbon concentrations: with more carbides forming in higher carbon containing alloys. The dissolution temperature of the P-Ti_3AlC phase may also depend on the carbon concentration. This would explain why carbides disappear at 1000°C in Ti-45Al-5Nb-0.5C but still exist in Ti-45Al-5Nb-0.75C. The variation of carbide precipitation in the HIPed & Annealed and Solution Treated & Annealed conditions might be caused by the carbon distribution variation in the matrix. In the HIPed & Annealed conditions, carbides preferentially form at grain boundaries on account of a higher local carbon concentration and consume carbon from the matrix. Thus the formation of carbides in the γ matrix is reduced. After solution treatment, carbon is redistributed more homogenously in the matrix and thus fewer grain boundary carbides are formed during annealing. This results in the increased density of carbides in the γ matrix. Meanwhile, grain boundaries can work as a carbon sink. Comparing **Figures 40** and **45**, it can be seen that the alloy in the Solution Treated & Annealed condition has larger grains, which suggests that the grain boundary area is reduced compared to the HIPed & Annealed condition. Therefore more carbon would be available for distribution in the γ matrix, resulting in a higher carbide density in the γ grains of alloys in the Solution Treated & Annealed conditions.

The differences between carbide morphology development in HIPed & Annealed and Solution Treated & Annealed conditions will be interpreted in **Sections 5.1** and **5.3**.

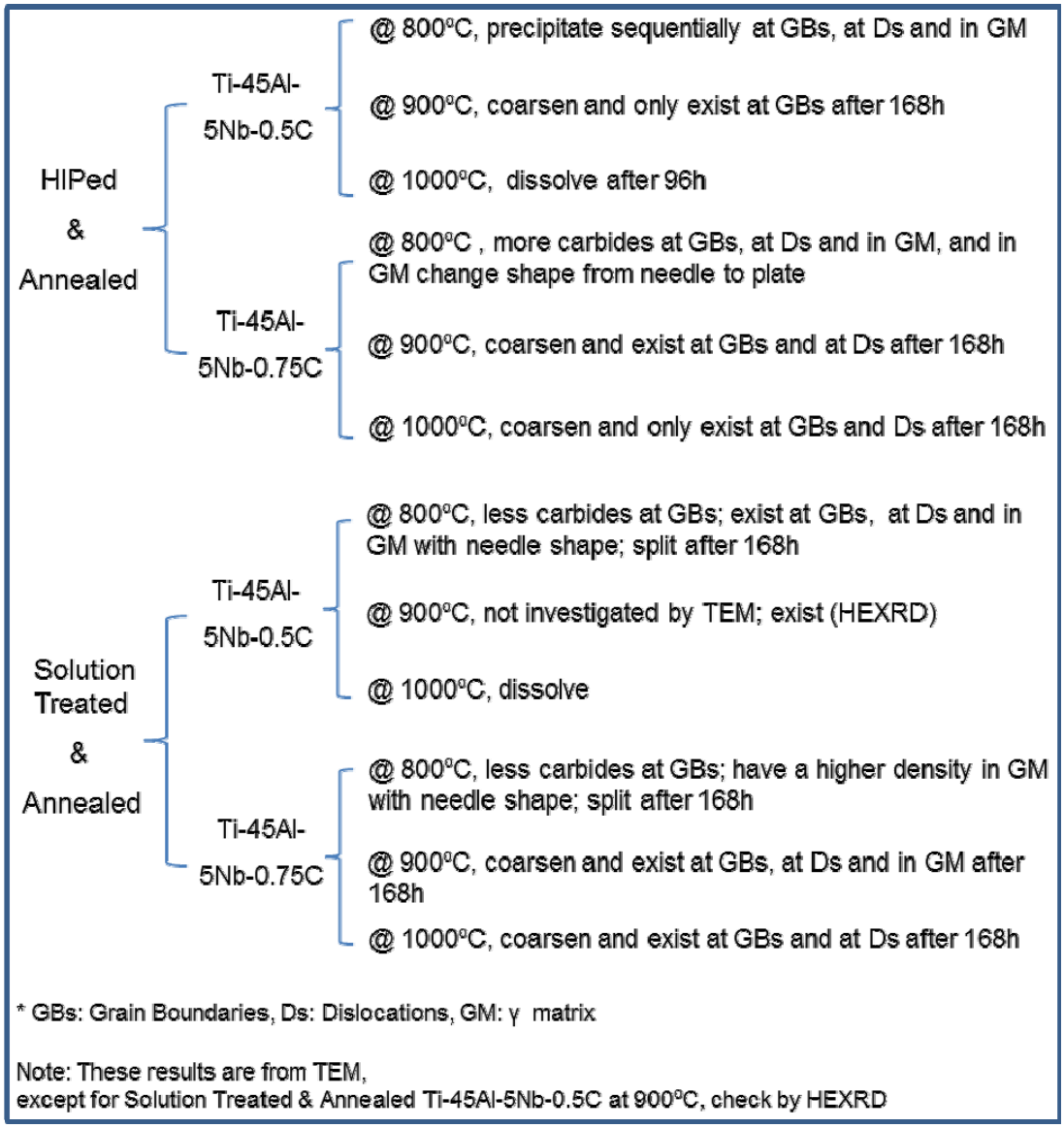

Figure 77 Overview of carbide precipitation and existence in heat-treated Ti-45Al-5Nb-0.5C and Ti-45Al-5Nb-0.75C alloys.

In the Ti-45Al-5Nb-0.5C and Ti-45Al-5Nb-0.75C alloys no H-type carbides have been observed to form during annealing, although in Ti-45Al-5Nb-0.75C, several H-Ti_2AlC carbides were detected in the HIPed condition. It is not yet clear whether the primary H-type carbides are dissolved during annealing or are too few to be observed.

5. Development of carbide morphology and interfaces between carbides and the γ matrix

5.1 Morphology development of P-type carbides in γ grains

5.1.1 In HIPed & Annealed Ti-45Al-5Nb-0.75C

In the HIPed & Annealed Ti-45Al-5Nb-0.75C alloy after annealing at 800°C, carbides in the γ matrix have a needle-like morphology elongated along the $[001]_\gamma$ direction after 24h, which is confirmed by TEM micrographs along $[100]_\gamma$ and $[001]_\gamma$ directions. In the $[100]_\gamma$ direction, carbides appear as needle-like projections (**Figure 78(a)**), and in the $[001]_\gamma$ direction they exhibit as dot-like projections (**Figure 78(b)**). The carbide morphology is illustrated schematically in **Figure 78(c)**.

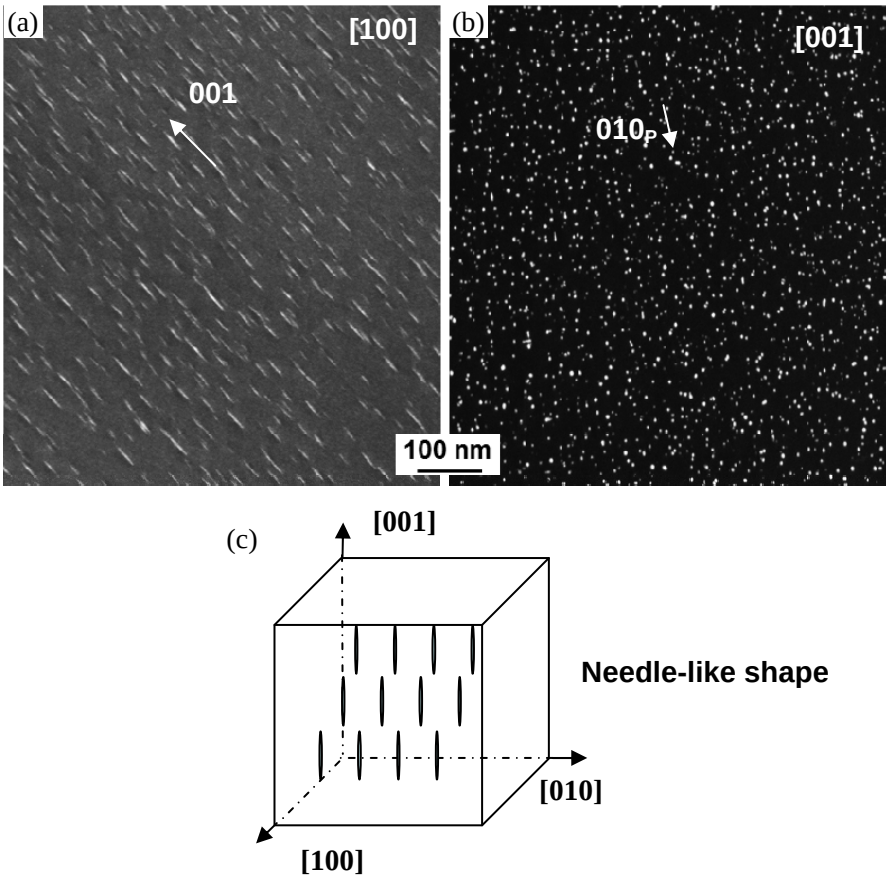

Figure 78 P-type carbides in the γ matrix of HIPed & Annealed Ti-45Al-5Nb-0.75C after annealing at 800°C for 24h (a) appearing as needle-like projections near the $[100]_\gamma$ direction, (b) showing dot-like projections near the $[001]_\gamma$ direction, and (c) schematic illustration of the needle-like shape. TEM dark field images were recorded using $\boldsymbol{g}=010_P$ in two-beam condition and have the same scale bar.

After 48h at 800°C, the carbides near to γ grain boundaries start to change their morphology, as shown in **Figure 79(a)**. Along the $[001]_\gamma$ direction, carbides away

from grain boundaries (position B) still appear as dot-like cross-sections, as shown in the insert B. However particles near γ grain boundaries (position A) show two sets of needle-like or rod-like projections parallel to the $[100]_\gamma$ and $[010]_\gamma$ directions. **Figure 79(b)** shows an example of two γ twins viewed along the $[101]_\gamma$ direction after annealing for 96h at 800°C. In each γ grain a number of the carbides appear as needle-like projections (P_1) while other carbides exhibit near round plate-like projections (P_2).

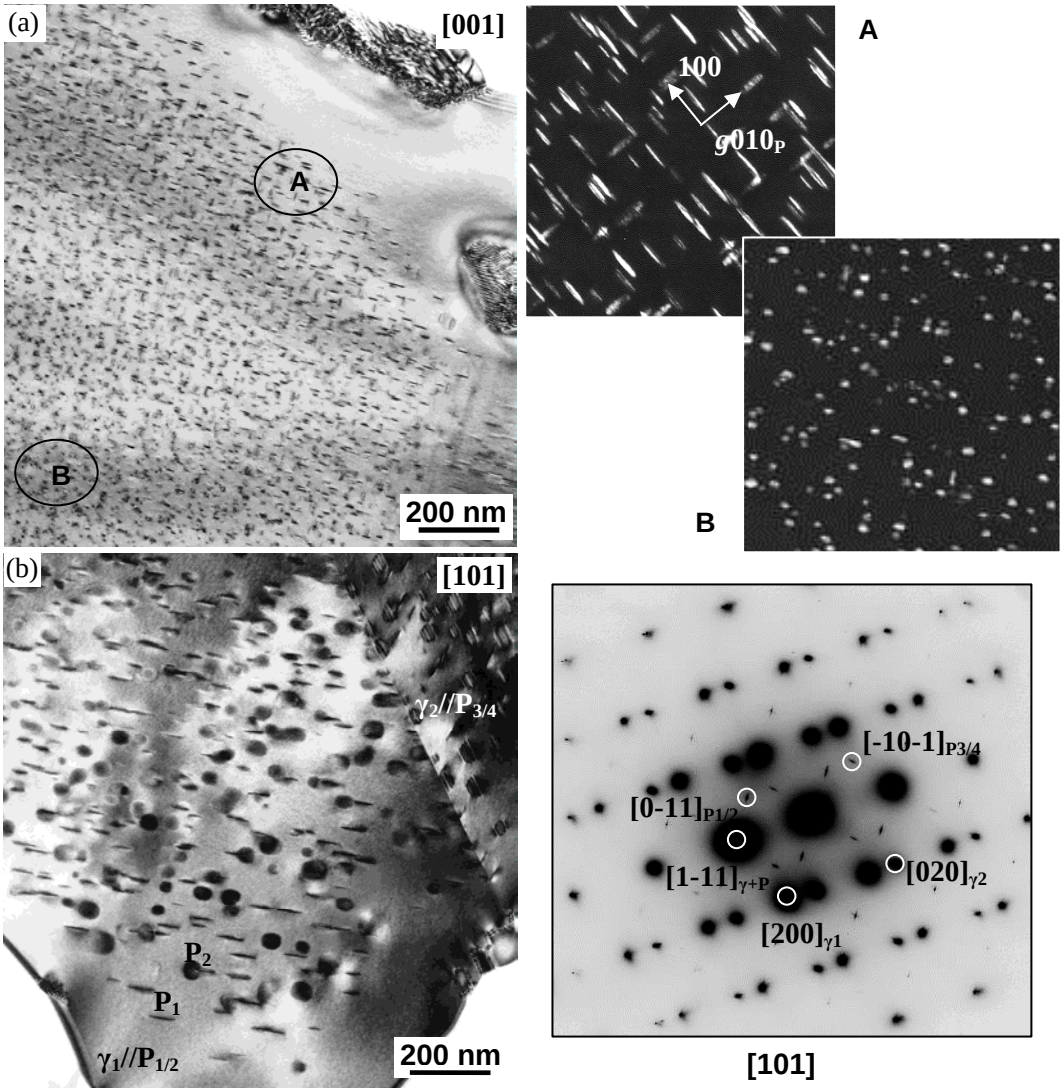

Figure 79 P-type carbides in the γ matrix of HIPed & Annealed Ti-45Al-5Nb-0.75C (a) after annealing at 800°C for 48h, viewed along the $[001]_\gamma$ direction, carbides near to the grain boundary (position A) appear as two sets of needle or rod-like projections, while carbides away from the grain boundary (position B) show dot-like projections, and (b) after annealing at 800°C for 96h, viewed from the $[101]_\gamma$ direction carbides exhibit one set of needle-like or rod-like and another set of plate-like projections, together with the corresponding diffraction pattern. TEM dark field images were recorded using $\boldsymbol{g}=\mathbf{010_P}$ in two-beam condition.

In order to determine the exact morphology of carbides, tilting experiments were carried out for the specimen annealed for 168h at 800°C, as shown in **Figure 80**. In the $[001]_\gamma$ beam direction, P-type carbides appear as two sets of needle-like or rod-like projections perpendicular to each other (**Figure 80(a)**). As pictured along $[101]_\gamma$

and $[0\text{-}11]_\gamma$ beam directions, only one set of carbides appears with needle-like or rod-like projections. The other set of carbides exhibits weak plate-like projections (**Figures 80(b)** and **(c)**). Thus the morphology of carbides gradually changes from a needle-like to a plate-like shape. The habit planes of the carbide plates are the (100) and (010) crystallographic planes of the γ matrix, as illustrated in **Figure 80(d)**. In some grains carbides far away from grain boundaries, still appear with a needle-like morphology. The change of carbide morphology from needle-like to plate-like first starts at grain boundaries and is discussed further in **Section 5.3.1**.

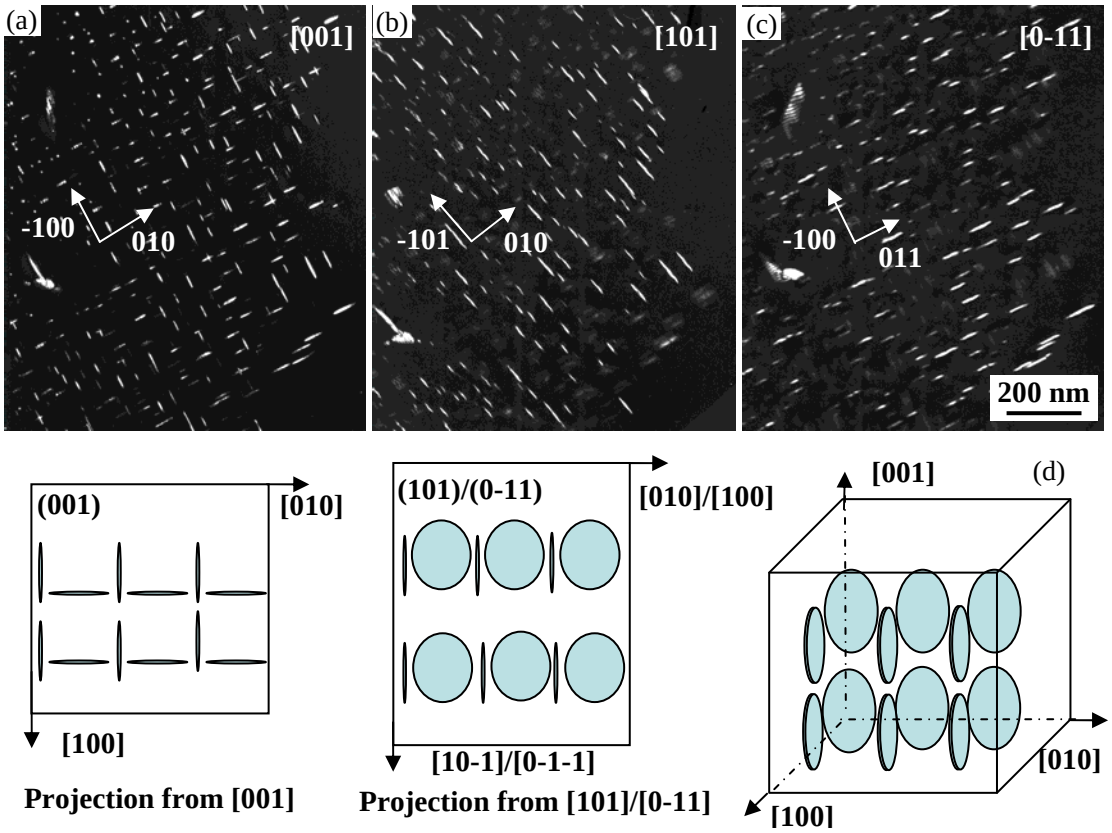

Figure 80 P-type carbides in the γ matrix of HIPed & Annealed Ti-45Al-5Nb-0.75C after annealing at 800°C for 168h, viewing near (a) the $[001]_\gamma$ direction, showing two sets of needle-like or rod-like projections, (b) the $[101]_\gamma$ direction and (c) the $[0\text{-}11]_\gamma$ direction showing one set of needle-like or rod-like projections and another set of plate-like projections, (d) schematic illustration of the plate-like morphology. TEM dark field images have the same scale bar.

It is worth noting that after 168h at 800°C some carbides also start to split in the HIPed & Annealed Ti-45Al-5Nb-0.75C alloy, as marked in **Figure 81**. This splitting phenomenon will be discussed in detail in the Solution Treated & Annealed condition.

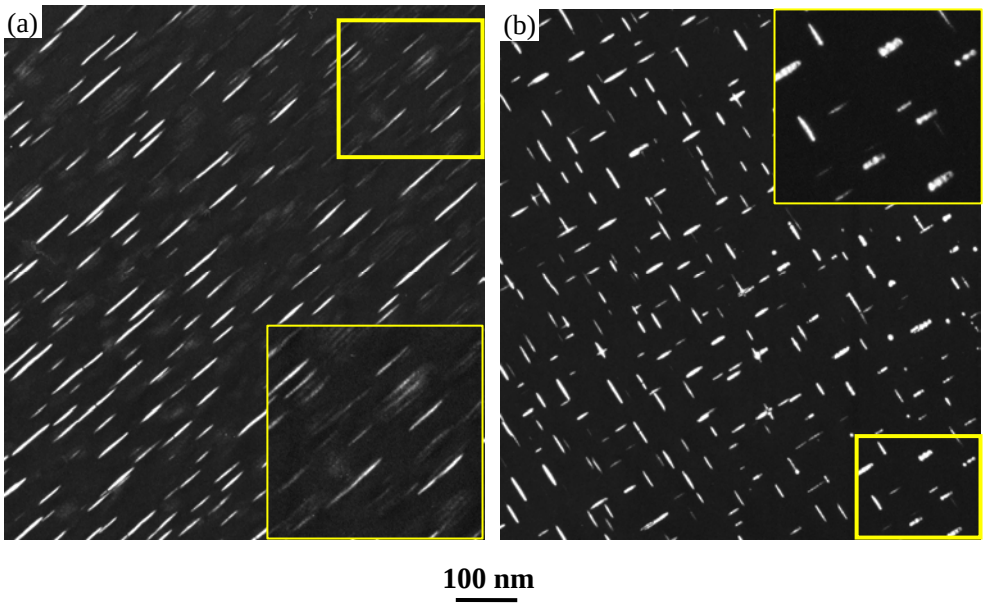

Figure 81 P-type carbides in the γ matrix of HIPed & Annealed Ti-45Al-5Nb-0.75C after annealing at 800°C for 168h, recorded near (a) the $[100]_\gamma$ direction and (b) the $[001]_\gamma$ direction. Some carbides start to split. TEM dark field images have the same scale bar.

5.1.2 In Solution Treated & Annealed Ti-45Al-5Nb-0.75C

In the Solution Treated & Annealed Ti-45Al-5Nb-0.75C alloy after annealing at 800°C for 24h, P-Ti_3AlC carbides in the γ matrix exhibit a needle-like morphology, as confirmed in **Figures 82(a)** and **(b)**. However, after 168h some P-Ti_3AlC carbides start to change their morphology and split (as marked by arrows in **Figures 82(c)** and **(d)**). After 1054h the carbides have split into many substructures. This phenomenon has also been observed in the Solution Treated & Annealed Ti-45Al-5Nb-0.5C alloy. The split carbides continue to exhibit the orientation relationship: $[001]_\gamma//[001]_P$, $(100)_\gamma//(100)_P$ with the γ grains. From the $[100]_\gamma$ direction (**Figure 82(e)**), carbides show one set of needle-like projections and one set of plate-like projections. For the plate-like projections there are many fringes parallel and vertical to the ***g*** vector. It should be noted that fringes vertical to the ***g*** vector are more obvious. Meanwhile it is worth paying attention to particles A, B and C marked by arrows in **Figure 82(e)**. Particles A, B and C seem to exhibit different stages of the splitting process. Particle A appears to have split into two parts along the $[001]_\gamma$ direction. For particle B it seems that the carbide first split in a similar manner to particle A, and the split structures subsequently start splitting along the $[010]_\gamma$ direction. Particle C appears to have split along the [001] and [010] directions and is divided into many small domains. From the $[001]_\gamma$ direction (**Figure 82(f)**), carbides show two sets of short rod-like projections, and one of these sets of carbides has fringes vertical to the ***g*** vector, as seen for particle D. The second set of carbides does not exhibit fringes, as exhibited by particle E. In order to understand the structure after splitting, the following tilting experiment was carried out.

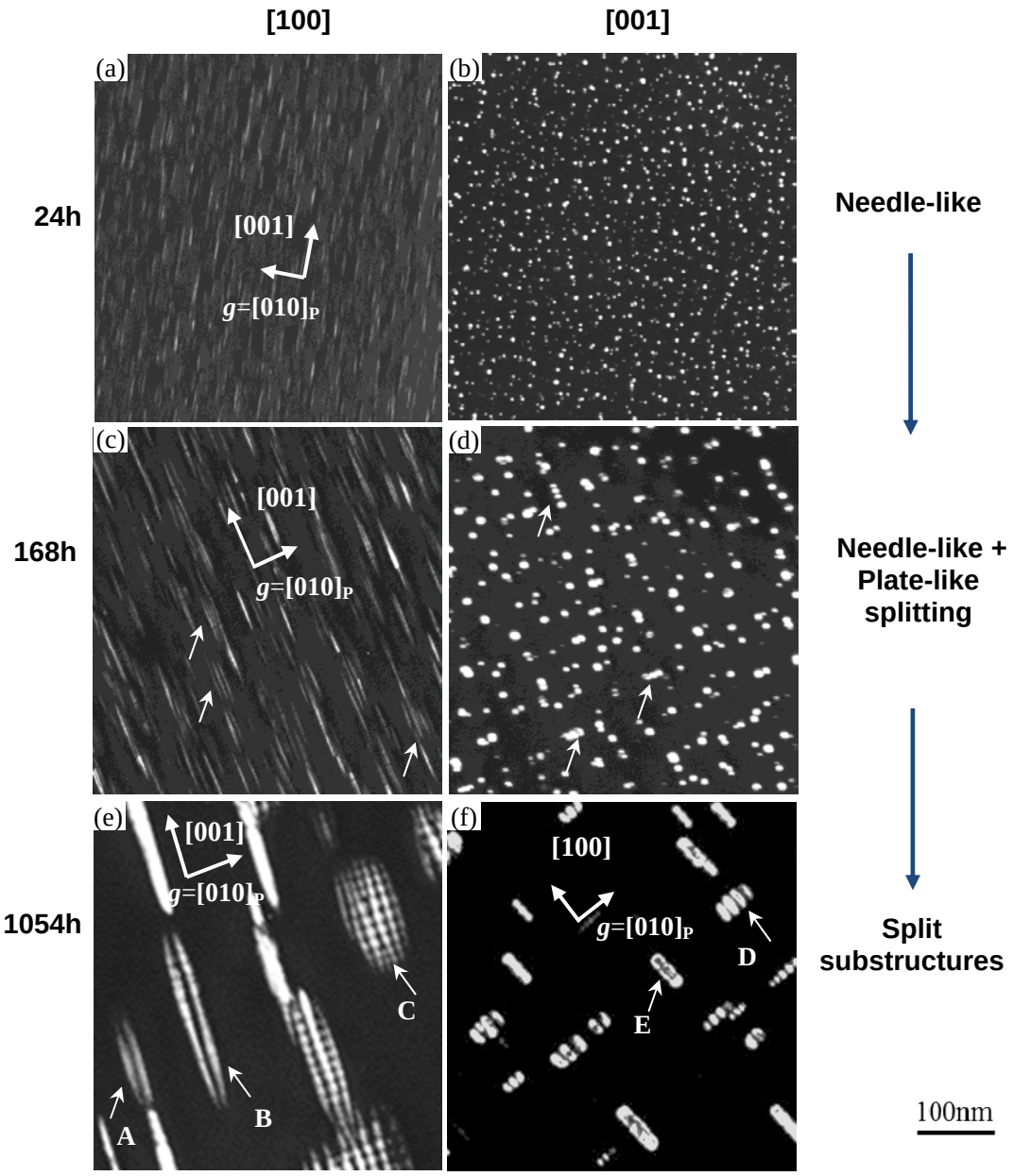

Figure 82 P-Ti_3AlC carbides in the γ matrix of the Solution Treated & Annealed Ti-45Al-5Nb-0.75C alloy after solution treatment at 1250°C for 5h (OQ) and subsequent annealing at 800°C for (a) 24h near $[100]_\gamma$, (b) 24h near $[001]_\gamma$, (c) 168h near $[100]_\gamma$, (d) 168h near $[001]_\gamma$, (e) 1054h near $[001]_\gamma$ and (f) 1054h near $[001]_\gamma$ directions. TEM dark field images were recorded using $\boldsymbol{g}=\mathbf{010_P}$ in two-beam condition. All images have the same scale bar.

Through the tilting experiment in **Figure 83** (images taken in the same γ grain), the fringes vertical to the $\boldsymbol{g}$ vector always appear in carbides which are parallel to the $\boldsymbol{g}$ vector. When using the $(100)_P$ diffraction, carbides parallel to $\boldsymbol{g_{100}}$ have fringes, while using the $(010)_P$ diffraction, the other set of carbides parallel to $\boldsymbol{g_{010}}$ shows fringes. This feature is quite similar to the translational moiré fringes. However after measuring the fringe spacing, it ranges from 10 to 18nm, which is larger than the translational moiré fringe spacing 6.39nm when using (010) diffraction. Additionally, images using different diffractions at different zone axis under two-beam conditions were taken and these fringes in carbides are proved to be no moiré fringes. This

confirms that big carbides split into small substructures and the regions between the substructures appear black when using diffractions from the P-Ti_3AlC phase in two-beam condition. However when the specimen is tilted in two-beam condition, in one set of carbides no fringes are observed because the dark regions are not viewed edged on anymore but overlap with the bright regions. Therefore it also explains why the intensity of these carbides is not uniform (particle E in **Figure 82(f)**).

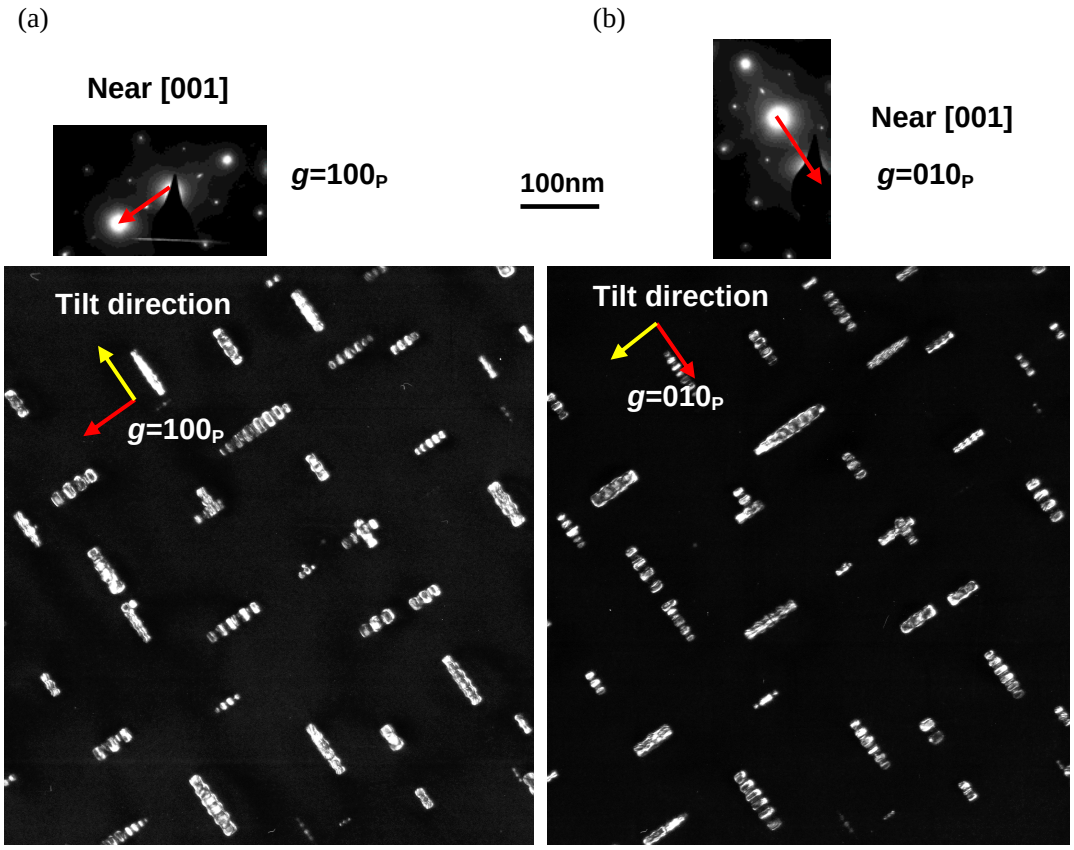

Figure 83 TEM investigation on the substructures of P-Ti_3AlC carbides in the γ matrix in the Solution Treated & Annealed Ti-45Al-5Nb-0.75C alloy after solution at 1250°C for 5h and annealed at 800°C for 1054h viewed near the $[001]_\gamma$ direction, using (a) $\boldsymbol{g=100_P}$ and (b) $\boldsymbol{g=010_P}$ in two-beam condition. All images have the same scale bar.

Figure 84 was taken from another γ grain. When using the $(011)_P$ and $(0\text{-}11)_P$ diffractions in the $[100]_\gamma$ direction, the plate projections of most carbides are composed of many small dots which are arranged very regularly. Most of the needle projections are also composed of dots except for a few that show uniform contrast. In this grain shown in **Figure 84**, most precipitates seem to have split along the $[001]_\gamma$ and $[100]_\gamma/[010]_\gamma$ directions already. It is worth noting that some of the carbides, as marked by red arrows, have split along the $[001]_\gamma$ direction but splitting along the $[100]_\gamma$ /$[010]_\gamma$ directions has not finished completely.

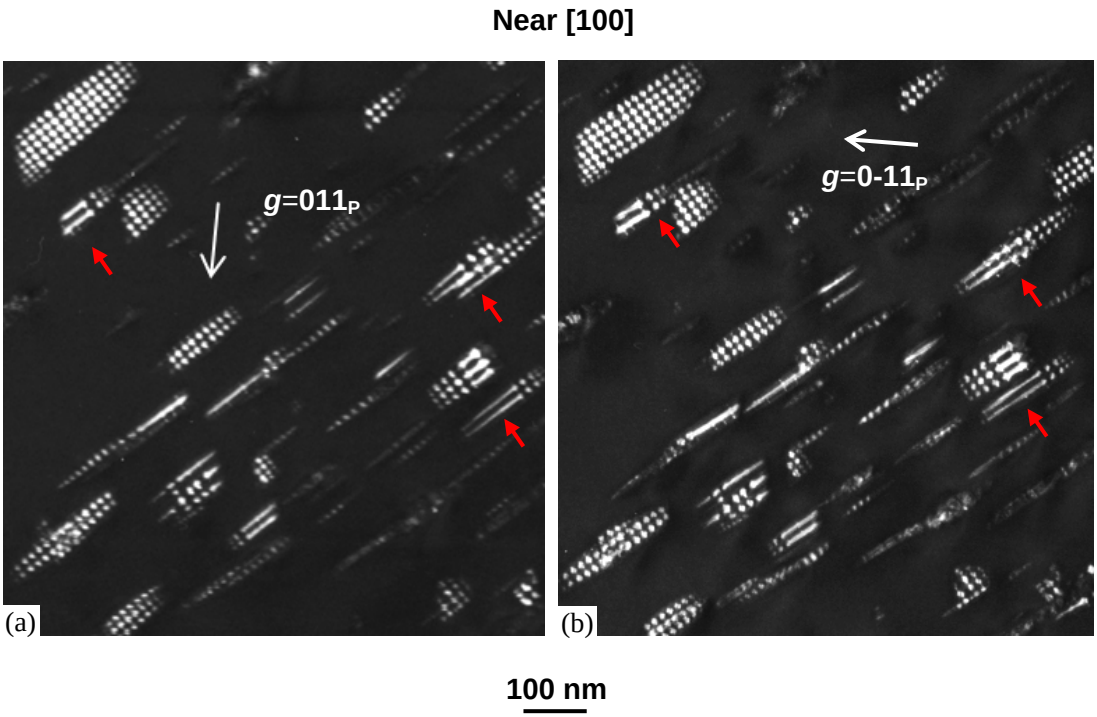

Figure 84 TEM investigation on the substructure of P-Ti_3AlC carbides in the γ matrix of the Solution Treated & Annealed Ti-45Al-5Nb-0.75C alloy after solution treatment at 1250°C for 5h (OQ) and subsequent annealing at 800°C for 1054h near the $[100]_\gamma$ direction, using $\boldsymbol{g=011_P}$ and $\boldsymbol{g=0\text{-}11_P}$ respectively in two-beam condition.

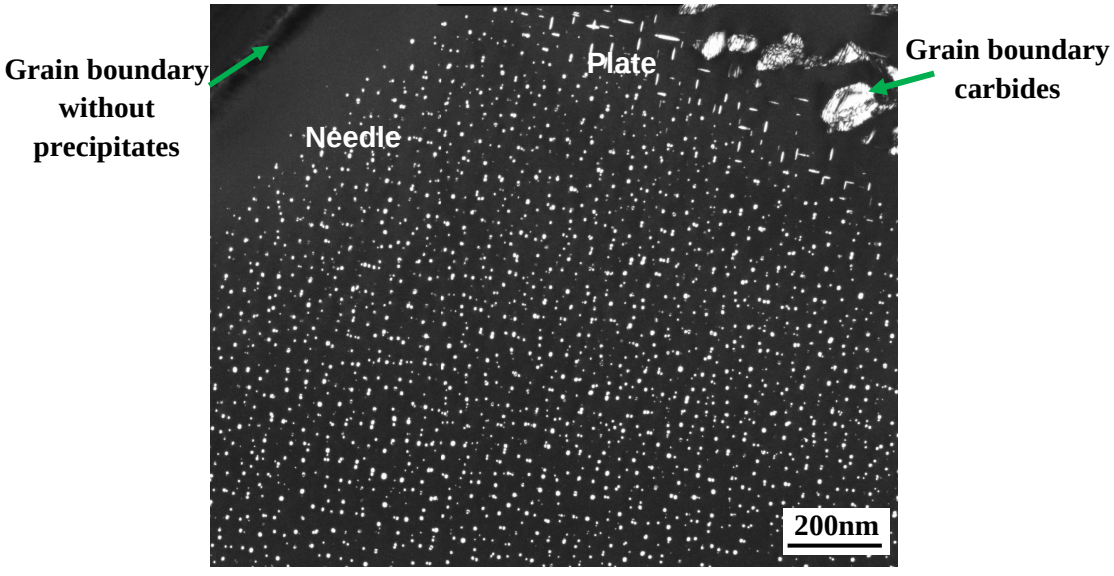

Figure 85 TEM investigation of the Solution Treated & Annealed Ti-45Al-5Nb-0.75C alloy after solution treatment at 1250°C for 5h (OQ) and subsequent annealing at 800°C for 96h near the $[001]_\gamma$ direction, using $\boldsymbol{g}=010_P$ in two-beam condition. Carbides near to the grain boundary which is decorated by precipitates change their morphology to plate-like, while carbides near to an undecorated grain boundary retain the needle-like shape.

Here it is worth mentioning that after careful observation, some plate-shaped carbides similar to those seen in the HIPed & Annealed Ti-45Al-5Nb-0.75C alloy, are found near to grain boundaries which were decorated by carbides. However carbides near to

grain boundaries which are not decorated by carbide precipitates still exhibit a needle-like morphology, as seen in **Figure 85**. As will be shown by EDS measurement in **Figure 95** (**Section 5.3.1**), Al and Nb are enriched in regions near big carbides while Ti is slightly depleted. It seems that the big carbides absorb Ti atoms from the neighboring matrix area but exclude Al and Nb atoms into neighboring regions. In **Figure 85**, the chemical composition of regions near to the grain boundary decorated by carbides may thus be altered due to the formation of carbides. Any local composition change might result in a variation of the elastic modulus and lattice parameters, and then further locally influence carbide precipitation.

5.2 Interfaces between carbides and the matrix, and split substructures

5.2.1 Interface between carbides and the matrix in HIPed & Annealed alloys

In order to obtain further details about the carbides in the γ matrix, and especially the interfaces between the carbides and the γ matrix, the alloys were investigated by HRTEM. Since the P-Ti_3AlC phase has a similar structure to the γ phase, it is difficult to distinguish the atomic arrangement of carbides from that of the γ phase in HRTEM images. By simulating the atomic positions under different specimen orientations using JEMS software, it was found that investigation along the $<101]_\gamma$ zone axis is preferred because the atomic arrangement of the P-type carbides with respect to the positions of Al and Ti atoms can be distinguished from that of the γ phase. Furthermore, there are 8 equivalents for the $[101]_\gamma$ direction in the γ-TiAl phase. The HRTEM images in this section have been recorded from the $<101]_\gamma$ zone axis.

Plate-like and rod-like carbides with a length of about 50-100nm have been found to form in the γ matrix of the HIPed & Annealed Ti-45Al-5Nb-0.5C alloy after annealing at 800°C for 168h. An example of a plate-like carbide is shown in **Figure 86**. It is difficult to record HRTEM micrographs of big carbides and their surroundings as the optimal thickness to achieve good imaging conditions in both the carbide and the matrix are different. Even the contrast within the carbide varies in different regions due to local changes in specimen thickness. In **Figure 86**, the possible interface between the carbide and γ matrix is weakly displayed by the contrast difference. The size of the carbide projection is measured to be around 30nm. Compared with the FFT pattern of the γ phase, the FFT pattern of the carbide shows additional intensities which correspond to forbidden reflections in a pure fcc diffraction pattern. The atom planes of the matrix and the precipitate are well aligned except for where the dislocations, labeled in position 1 and 2, exist. The resolved Burgers vector of these dislocations on the (101) plane is ½[010], and they are probably ordinary dislocations pinned at the carbide.

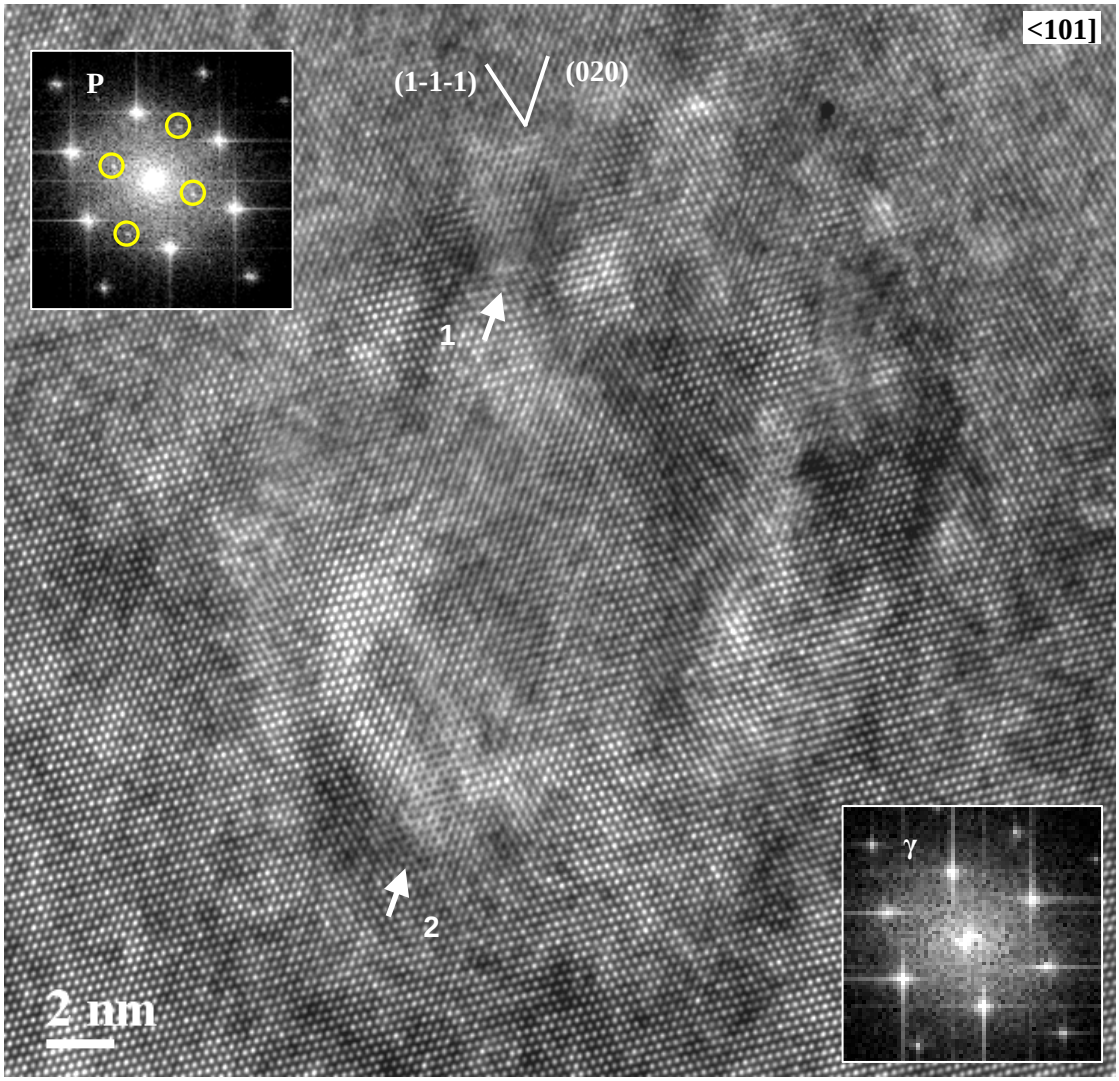

Figure 86 HRTEM investigation of a P-type carbide with a plate-like projection in the γ matrix. The image was taken along the $<101]_{\gamma}$ direction in the HIPed & Annealed Ti-45Al-5Nb-0.5C alloy after annealing at 800°C for 168h (FC). Dislocations are located at positions 1 and 2.

Additionally, small precipitates are often observed near to defects, as seen in **Figure 87** for example. It is very difficult to identify the defect type due to the poor quality of the image at the defect position. After close observation in the region of the precipitate it can be seen that there is a variation in contrast between adjacent rows of atoms as marked by arrows. The presence of P-type carbide is further confirmed by the FFT pattern.

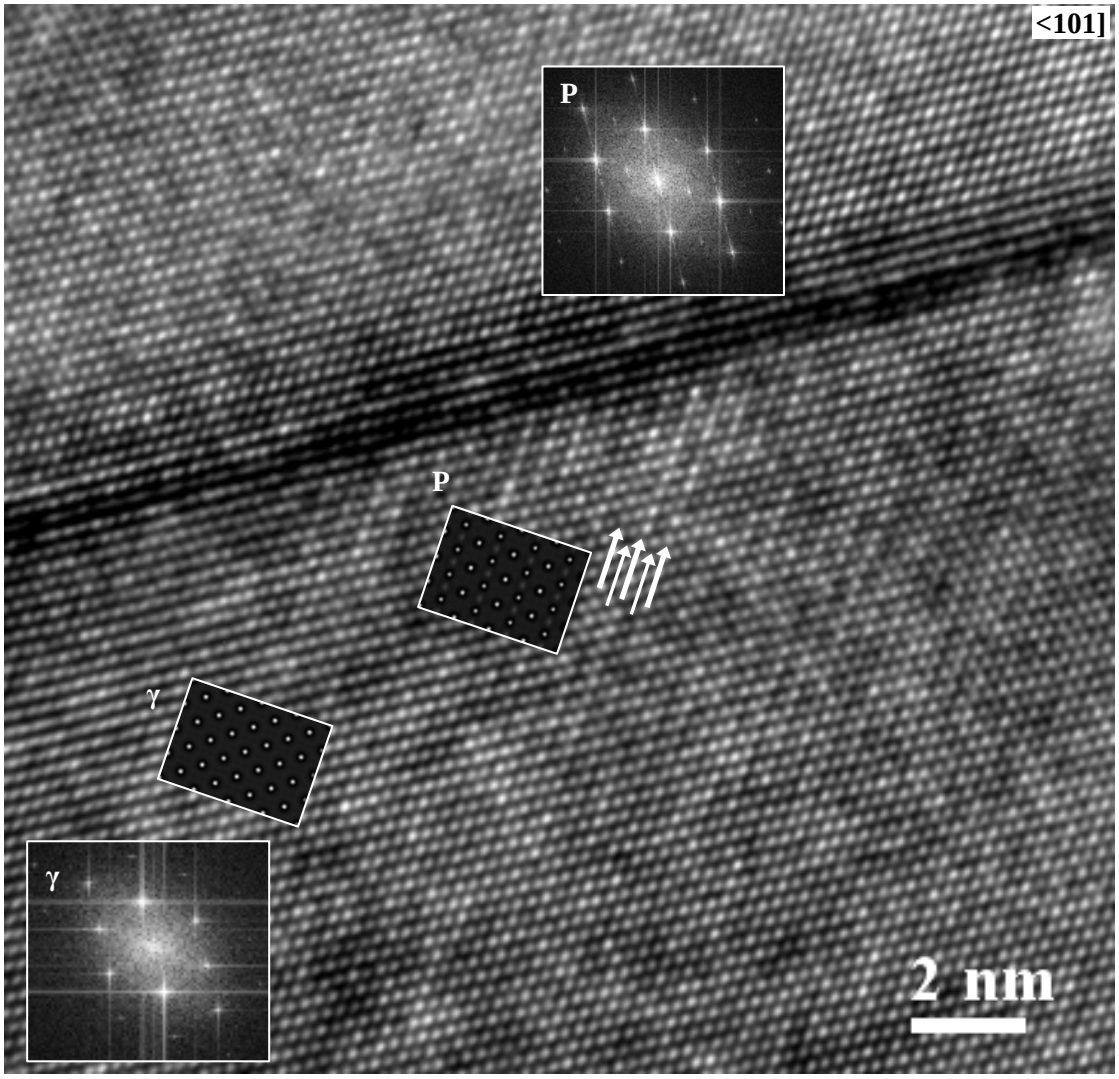

Figure 87 HRTEM investigation of a P-type carbide at a planar defect in the γ matrix of the HIPed & Annealed Ti-45Al-5Nb-0.5C alloy after annealing at 800°C for 168h (FC). The image was taken in the $<101]_{\gamma}$ direction.

In the HIPed & Annealed Ti-45Al-5Nb-0.75C alloy after annealing at 800°C for 24h, small needle-like carbides nucleate in γ grains and remain coherent with the γ matrix. After 168h, the carbides grow and the needle-like carbides gradually develop into plate-like carbides. When imaged along the $<101]_{\gamma}$ zone axis, the carbides show both plate-like and needle-like or rod-like projections. The image of the plate-like projection is similar to that shown in **Figure 86**.

Figure 88 shows an example of the side view of a plate-shaped carbide that appears as a needle-like or rod-like projection. The needle-like projection has a size about 40nm length and 4nm width. No dislocations have been observed in the interface. Interestingly near the precipitate ends obvious ledges are found, as marked by arrows. Additionally the interface between the carbides and the γ matrix is not straight. Shiflet et al. (Merwe 1991, Shiflet 1991, Shiflet 1994) reported that ledges could accommodate mismatch in cubic systems, and this has also been published by Appel

et al. (Appel 2011) in the TiAl system. However in this case it is not confirmed whether the ledges result from misfit accommodation or are growth ledges.

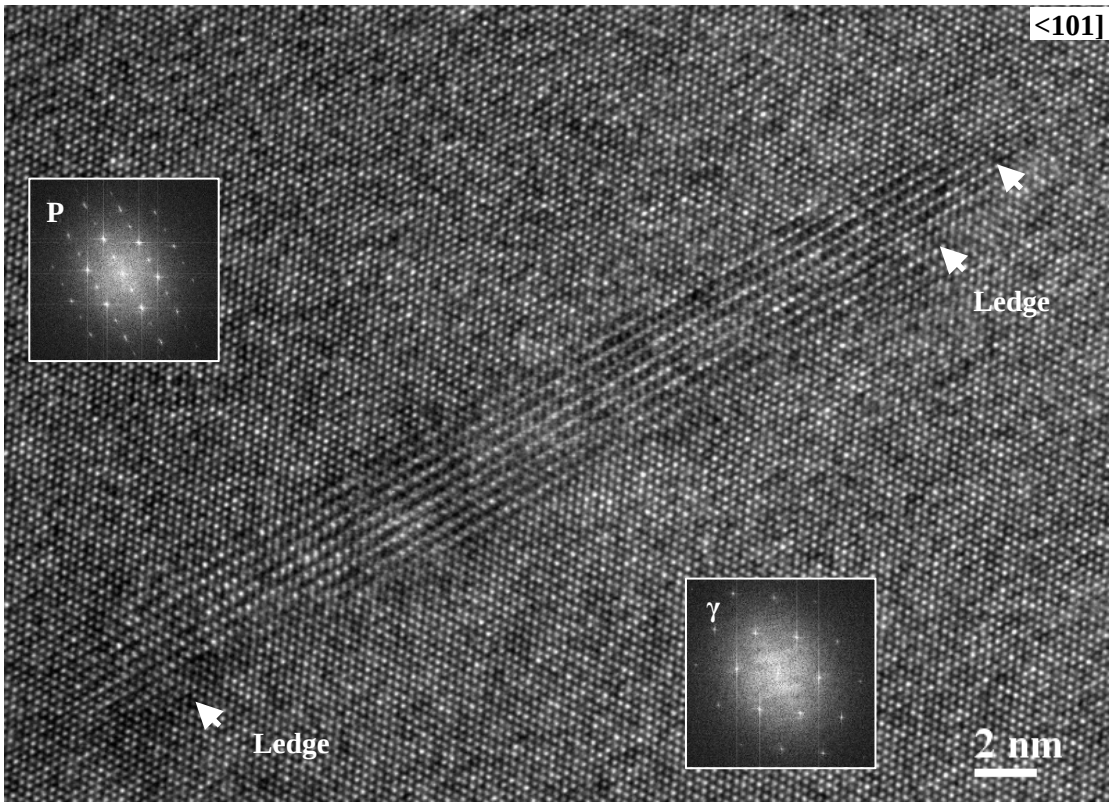

Figure 88 HRTEM investigation of a P-type carbide imaged along the $<101]_{\gamma}$ direction of the HIPed & Annealed Ti-45Al-5Nb-0.75C alloy after annealing at 800°C for 168h (FC). The carbide has a needle-like or rod-like projection. No misfit dislocations are found and ledges form at the interface.

Simulations of the HRTEM images at certain defocus (d) and foil thickness (t) values show good agreement with the experimental HRTEM images as illustrated in **Figure 89**. Simulated in the [101] direction and varying the thickness, the image of the P-Ti_3AlC carbide shows different contrast. At a foil thickness of 4nm for example, the image shows almost uniform contrast for different atomic rows. With increasing thickness, the intensity variation between atomic planes becomes clear as the mixed Ti/Al rows show strong contrast compared to Ti/C rows. The intensity of carbon atoms is too weak to be distinguished. For comparison, the γ phase shows uniform contrast in the simulated images along the [101] direction with varying thickness.

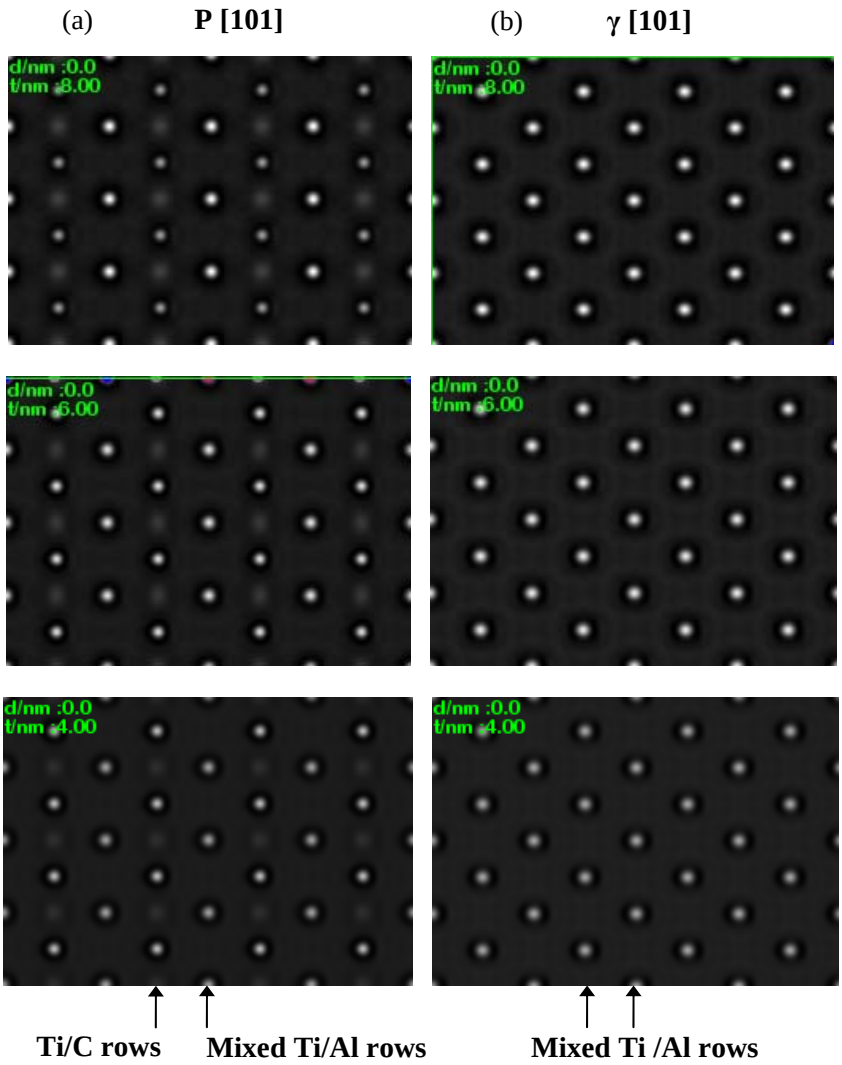

Figure 89 HRTEM image simulation in the [101] direction of the (a) P-Ti_3AlC and (b) γ phases shows agreement with experimental results. The images are simulated at different foil thicknesses (t) and show a varying contrast for the P-Ti_3AlC phase, while a uniform contrast is observed for the γ-TiAl phase.

From the above HRTEM investigation, it can be concluded that when carbides are small and have a needle-shaped morphology, they remain coherent with the γ matrix. As annealing continues, the carbides in γ grains grow and gradually change morphology to plate-like. It is believed that they remain coherent with the γ matrix because no misfit dislocations are observed at the interface between the carbides and the γ matrix. Appel et al. (Appel 2007) pointed out that in a Ti-48.5Al-0.36C alloy the perovskite precipitates lost coherency and misfit dislocations were introduced when the particle width was in a range of 4nm. This was also the critical precipitate size for the transition between a coherent and an incoherent interface proposed by Benedek et al. (Benedek 2002) through first-principle calculations. Compared to the results of Appel (Appel 2007), the critical size for coherency loss of carbides seem to be larger in the current work.

The total energy for a coherent precipitate is expressed as (Mott 1940, Nabarro 1940, Nabarro 1940, Porter 1992, Iwamura 2004):

$$\Delta E_{(coherent)} = E_{elas} + E_{surf} = E_{elas} + S \cdot \gamma_{(coherent)} \quad \textbf{Eq. 10}$$

Where $\Delta E_{(coherent)}$ is the total energy, E_{elas} is the elastic strain energy, E_{surf} is the surface energy, S is the surface area and $\gamma_{(coherent)}$ is the coherent surface energy density for a coherent precipitate.

If the precipitate has an incoherent or a semi-coherent interface with the matrix, then the misfit strain energy will be relived, but an extra structural contribution to the surface energy will be introduced. Thus the total energy for a semi-coherent or an incoherent precipitate is given by (Porter 1992):

$$\Delta E_{(incoherent)} = 0 + E'_{surf} = S \cdot \gamma_{incoherent} = S \cdot (\gamma_{(coherent)} + \gamma_{st}) \quad \textbf{Eq. 11}$$

Where $\Delta E_{(incoherent)}$ is the total energy, and $\gamma_{(incoherent)}$ is the incoherent surface energy density for an incoherent precipitate. $\gamma_{(st)}$ is an extra structural contribution to the surface energy.

When the precipitate size reaches the critical value then:

$$\Delta E_{(coherent)} = \Delta E_{(incoherent)} \quad \textbf{Eq. 12}$$

and

$$E_{elas} = S \cdot \gamma_{(st)} \quad \textbf{Eq. 13}$$

According to **Eqs. 23-24** in **Section 5.3.1**, the elastic strain energy of the precipitate is related to the third power of the particle size and the square of the misfit. The surface area is related to the square of the particle size. Thereby the critical size for coherency loss has an inverse relationship with misfit. Based on **Table 10** and the work of Christoph et al. (Christoph 1997), the misfit between P-Ti_3AlC particles and the γ phase in Ti-48.5Al-0.36C might be higher than that in Ti-45Al-5Nb-0.5C and in Ti-45Al-5Nb-0.75C due to the higher Al content. As a consequence in our alloys the critical size for coherency loss is increased.

5.2.2 Split substructures in Solution Treated & Annealed alloys

From the TEM investigation of Solution Treated & Annealed alloys, carbides maintain their orientation with respect to the γ phase after splitting into substructures. In order to get more information about the interface between the P-Ti_3AlC carbides and the γ matrix, and to understand the substructures after splitting, the Solution Treated & Annealed Ti-45Al-5Nb-0.75C alloy after annealing at 800°C for 1054h was investigated by HRTEM. **Figures 90-92** illustrate the substructures of carbides along the $<101]_\gamma$, $[001]_\gamma$ and $[100]_\gamma$ directions, respectively.

Figure 90 is a side view of the carbide recorded from the <101]$_\gamma$ direction. The carbide is easily seen by the contrast variation and is further confirmed by FFT patterns. The width of the carbide in this projection is about 12nm. Meanwhile, atom planes between the matrix and the carbide are aligned, which suggests that the carbide remains coherent with the γ matrix.

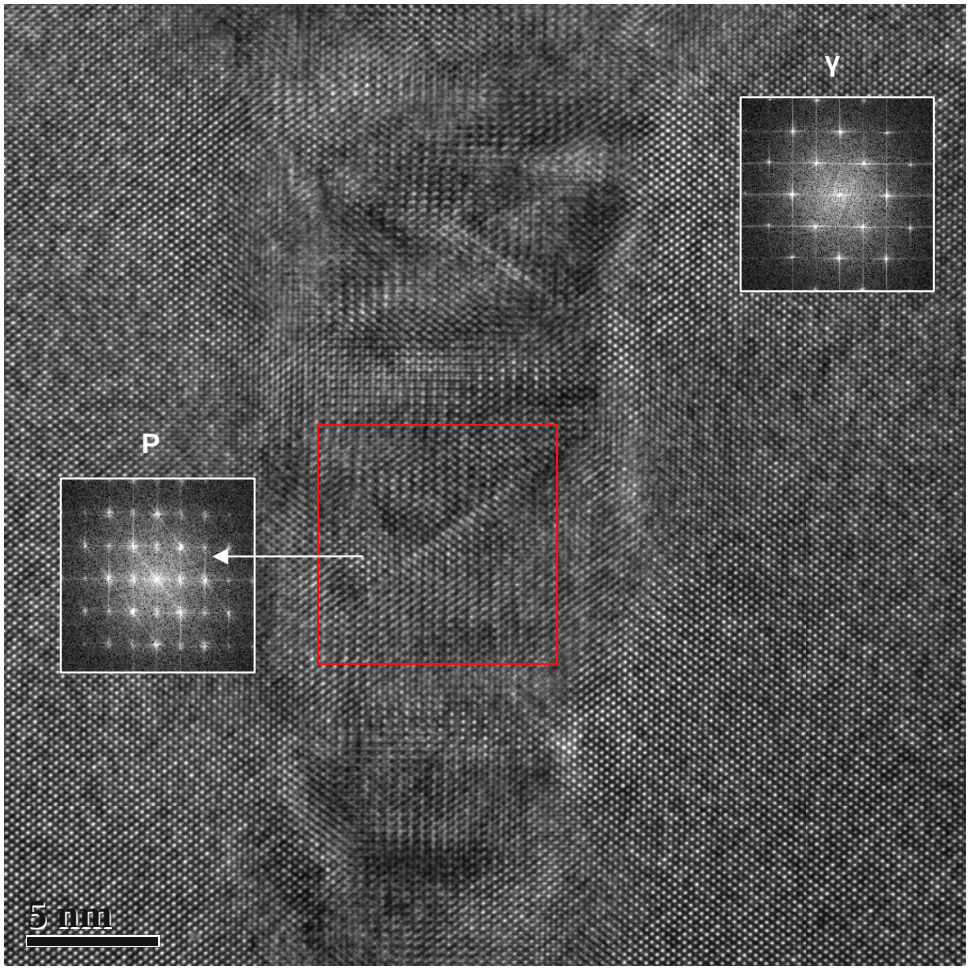

Figure 90 HRTEM investigation on the substructure of P-Ti_3AlC carbides in the Solution Treated & Annealed Ti-45Al-5Nb-0.75C alloy after annealing at 800°C for 1054h (FC) in the <101]$_\gamma$ direction.

Figure 91 illustrates the side view of the plate-like carbide from the [001]$_\gamma$ direction. The carbide is easily identified by its contrast variation from the γ matrix and further by FFT patterns. From this direction it seems that the atomic arrangement of the matrix is different from the carbide and atomic planes between the matrix and the carbide are not aligned. After simulating HRTEM images of both phases, the atom columns show different contrast variation, as exhibited in the small images at the top and bottom left of the diagram. Due to this contrast difference it is very difficult to determine the type of interface between the carbide and matrix. The carbide projection in the (001) plane appears as a rod with a width of around 90nm and a thickness of about 20nm. On observation at a higher magnification, the interface between the carbide and the matrix is not planar but appears as plane-convex-plane-

convex. The rod projection can be treated as being composed of rectangular blocks (block A) and curved-sided blocks (block B). Blocks of type A have a size of about 5nm×13nm, and B Blocks are around 10nm×17nm, as measured from **Figure 91**. In dark field, A blocks seem to lose contrast when using diffractions from the P-Ti_3AlC phase. After carefully checking the atomic planes in block A it seems as though they are shifted compared with those in block B, as marked by the white rectangle and shown in the insert (i). Meanwhile, in the region marked by an ellipse, enlarged in insert (ii), a quite different atomic arrangement is found.

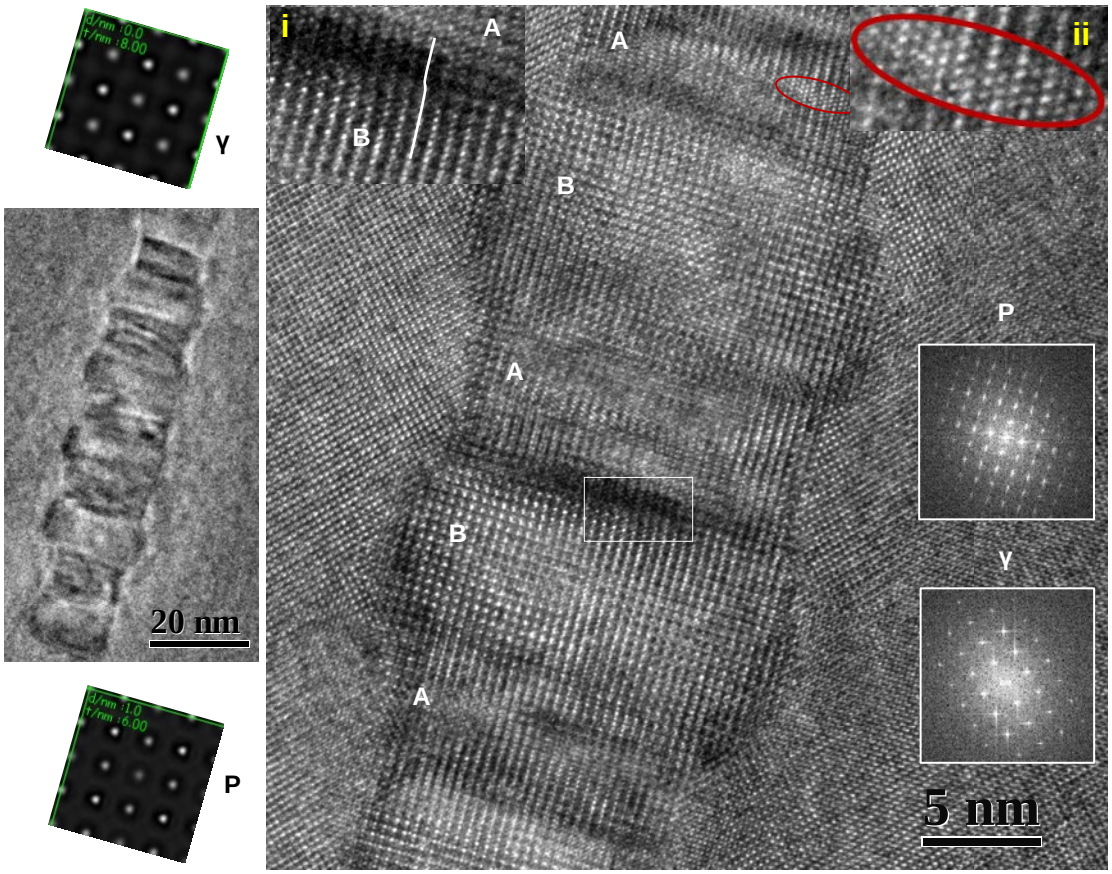

Figure 91 HRTEM investigation on the substructure of P-Ti_3AlC carbides in the Solution Treated & Annealed Ti-45Al-5Nb-0.75C alloy after solution treatment at 1250°C for 5h (OQ) and subsequent annealing at 800°C for 1054h (FC) in the $[001]_\gamma$ direction.

Figure 92 illustrates a needle-like projection in the $[100]_\gamma$ direction. Again the carbide stands out from the matrix due to the different contrast variation of atomic planes. The FFT patterns further confirm the existence of the carbide. The HRTEM image simulation shows agreement with the experimental result. At a low magnification (**Figure 92(a)**), the needle-like projection is also divided into blocks that are aligned along the $[100]_\gamma$ direction and have a size about 13nm×15nm. The regions between adjacent blocks are small and are not as obvious as A type blocks when viewed in the $[001]_\gamma$ direction. On observation at a higher magnification (**Figure 92(b)**), no dislocations are found at the interface between the carbide and the matrix or between the blocks. Interestingly it is found that the contrast of atomic rows in the region

between two blocks (strong-weak-strong) shows a variation that is different to that in block regions (weak-strong-weak), as clearly shown in the enlarged insert of region A (**Figure 92(c)**).

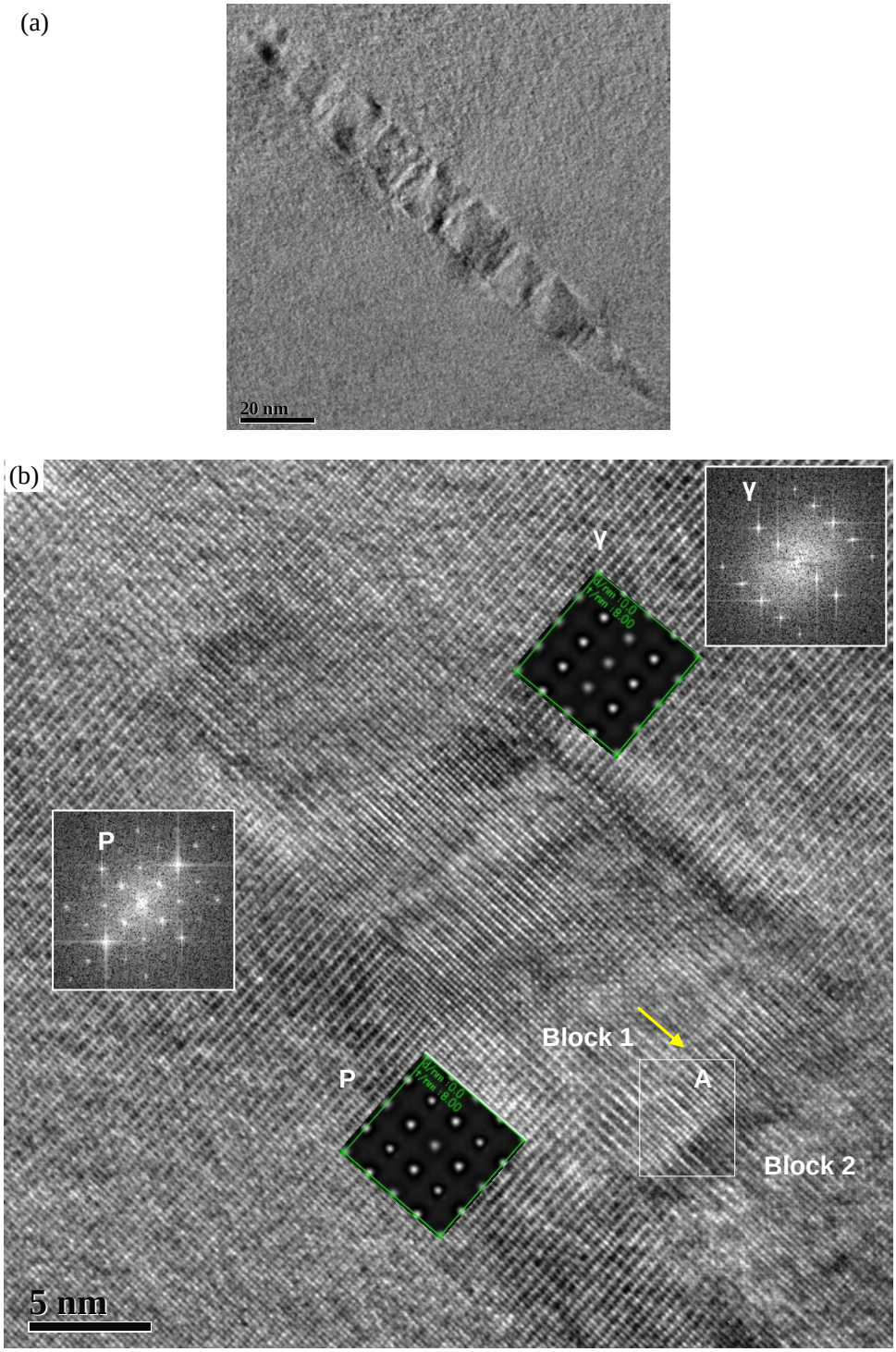

Figure 92 HRTEM investigation on the substructure of P-Ti_3AlC carbides in the Solution Treated & Annealed Ti-45Al-5Nb-0.75C alloy after solution treatment at 1250°C for 5h (OQ) and subsequent annealing at 800°C for 1054h (FC) in the $[100]_\gamma$ direction. (a) At a smaller magnification, (b) at a higher magnification (to be continued)

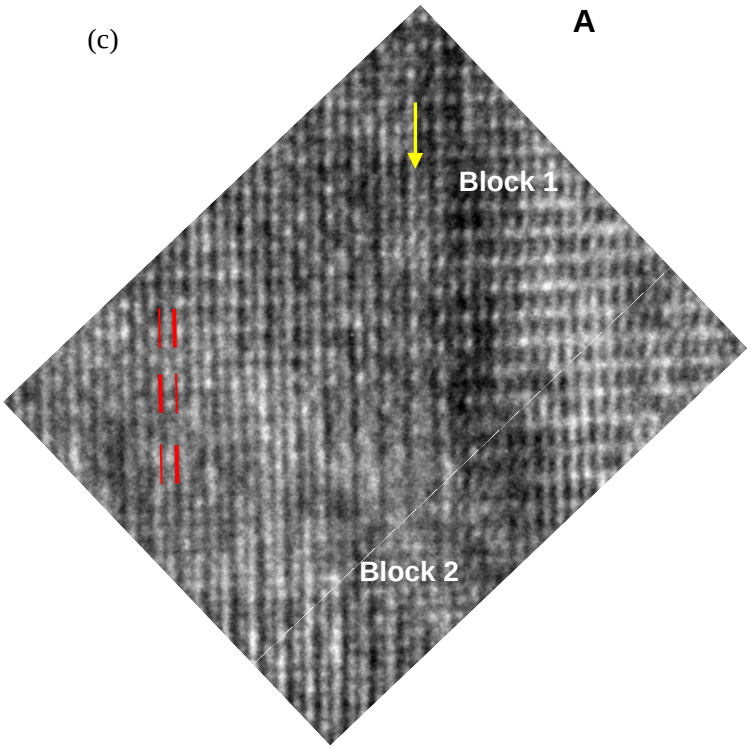

Figure 92 (continued) (c) region A in (b) at a higher magnification.

Figure 93 illustrates the top view of a plate-shaped carbide which appears as plate-like projection in the $[100]_{\gamma}$ direction. In this case the projection has a length of about 140nm and a width of around 45nm. At a low magnification (**Figure 93(a)**) the carbide seems to be composed of small domains with a shape near to a circle or plate (with a size of about 11nm×12nm), which seem to show contrast in the dark field with the $[010]_{P}$ diffraction. Meanwhile in each small domain there appears a pillar with strong contrast. After careful observation at a higher magnification (**Figure 93(b)**), the contrast varies for different regions, which makes interpretation very difficult. The variation of the thickness might be one reason for such contrast variations. This is supported by positions P-1 and P-2 where carbides are located, as marked by arrows in **Figure 93(b)**. The simulated results confirm that under the same defocus but at different thicknesses conditions the HRTEM images exhibit such variations. Similar to the case shown in **Figure 92**, in the region A marked by an ellipse, the atomic arrangement is quite different from other regions. In region B of **Figure 93(b)** that is shown more clearly in **Figure 93(c)**, it can be seen that the two squares on the left side of the micrograph have four atoms at each corner. However, on the right side of the micrograph, the shape of unit changes to a parallelogram gradually (two of which are indicated). It is proposed that this region is under a large distortion.

(a)

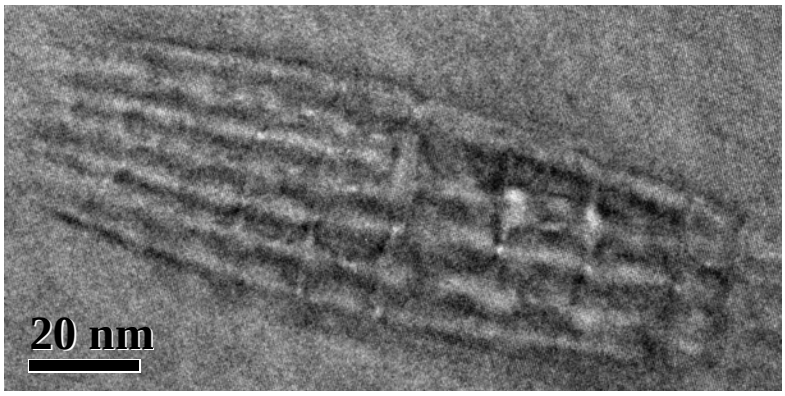

(b)

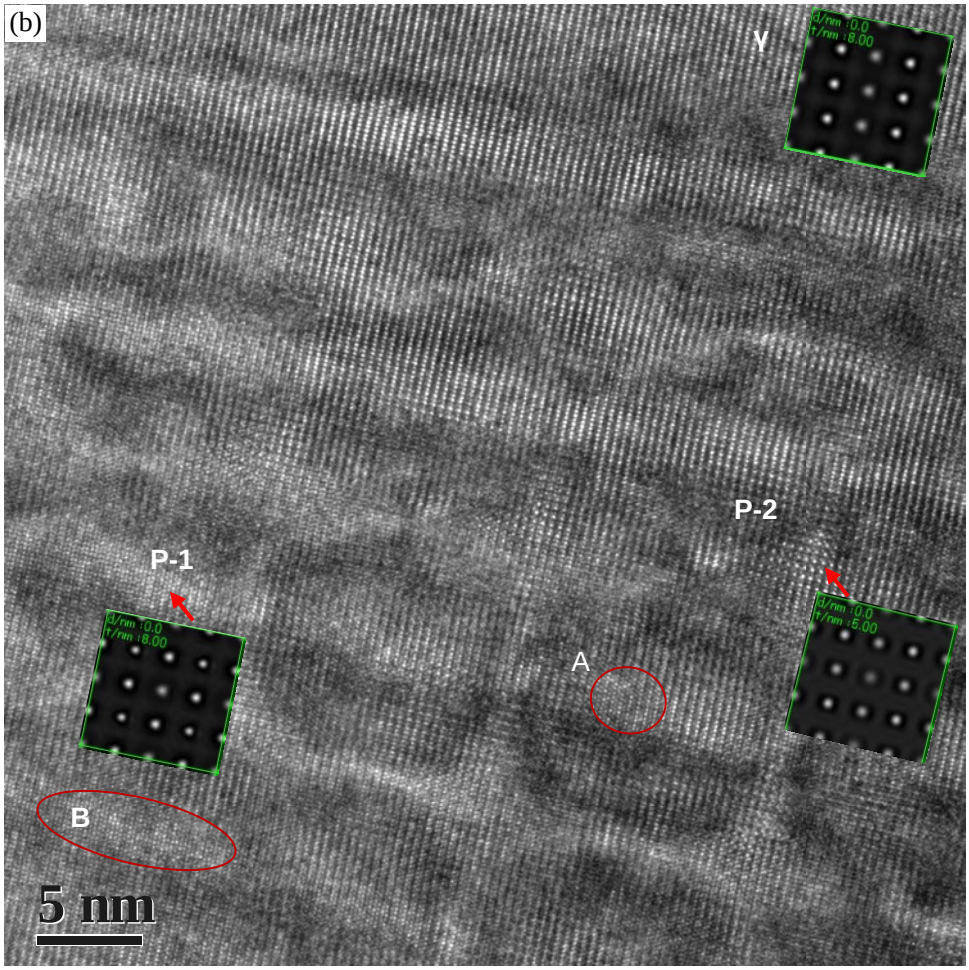

Figure 93 HRTEM investigation on the substructure of P-Ti_3AlC carbides in the Solution Treated & Annealed Ti-45Al-5Nb-0.75C alloy after solution treatment at 1250°C for 5h (OQ) and subsequent annealing at 800°C for 1054h in the $[100]_\gamma$ direction. (a) At a smaller magnification, (b) at a higher magnification (to be continued)

(c)

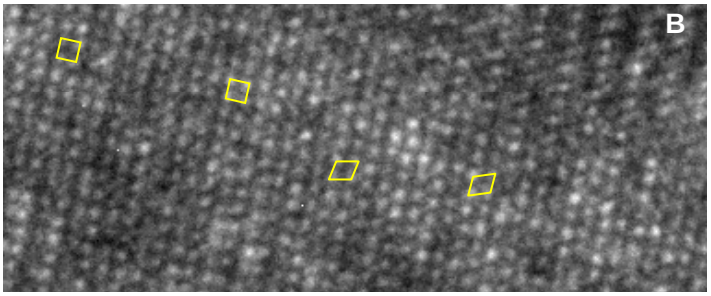

Figure 93 (continued) (c) region B in (b) at a higher magnification.

In conclusion, from the above HRTEM investigation, it is confirmed that during coarsening the carbides split into small domains with a size in each of the three directions of around 10-17nm. Integrating the projections from the $<101]_{\gamma}$, $[001]_{\gamma}$ and $[100]_{\gamma}$ directions, it is proposed that the domains have a superspherical shape. The inter domain distance along the $[100]_{\gamma}$ or the $[010]_{\gamma}$ direction is about half the size of the domains, but along the $[001]_{\gamma}$ direction the inter domain distance is smaller. From diffraction analysis the substructures retains its orientation relationship $[001]_{\gamma}//[001]_{P}$, $(100)_{\gamma}//(100)_{P}$ with the γ matrix. At the interface between carbides and the γ matrix no misfit dislocations have been identified. Meanwhile atom planes appear to traverse through all small domains but some atomic plane shift exists (**Figure 91**). There is also an intensity variation of atomic rows that can be observed in regions between domains (**Figure 92**). Due to a local variation of thickness, there is a variation of contrast between different regions. In some regions where elastic strain concentration may be located, a big distortion of the atomic arrangement can be observed (**Figure 93(c)**). However it is worth reminding that when using TEM dark field imaging, the regions between the domains lose contrast when using diffractions from the P-Ti_3AlC phase. It has not yet been confirmed using HRTEM that these regions are newly formed γ-TiAl matrix or other transient phases. It is proposed that when big carbides split into small substructures, the Ti_3AlC domains exist probably with higher carbon levels that are close to stoichiometric ratio. In regions between domains, the elements are redistributed and atoms are rearranged gradually, so they lose contrast when using diffractions from the Ti_3AlC phase in dark field imaging with a two-beam condition.

5.3 Interpretation of the morphology change and the splitting of carbides

5.3.1 Carbide morphology change

In the HIPed & Annealed Ti-45Al-5Nb-0.75C alloy, the needle-shaped carbides in γ grains are found to be coherent with the γ phase and grow preferentially along the [001] direction at the beginning of annealing. From **Table 9** it is obvious that the lattice misfit in the [001] direction is smaller than that in the [100] and [010] directions. Additionally the elastic constant of the γ phase is also smaller in this direction, thereby the misfit stress along the [001] direction should be reduced further (Tian 1993). Consequently P-type carbides in the γ matrix grow preferentially along the [001] direction. After further annealing the carbides change morphology to plate-

like. The shape of coherent precipitates is controlled by the interfacial energy and the misfit strain energy (Johnson 1987, Onaka 2002, Onaka 2003, Watanabe 2008, Watanabe 2009, Miyazawa 2011). Tian et al. (Tian 1993) reported that for basically similar crystal structures of the precipitate and the matrix and small misfit, the shape of the precipitate would change from spherical to needle-like and finally to plate-like with increasing misfit. In the TiAl-(0.5%, mol) C alloy investigated by them, they did not observe such a morphology change from needle to plate, but rather the formation of long-range ordering of carbon-vacancy or nitrogen-vacancy within the needles.

To explain the morphology change of the precipitates, we calculated the elastic strain energy and interfacial energy for the precipitates with both the needle and plate shapes using Eshelby's inclusion theory. The morphology of the precipitates is considered as an ellipsoid of revolution.

When the precipitate is coherent with the matrix, the total energy is given by (Miyazaki 1982, Doi 1984, Doi 1985):

$$E_{total} = E_{elas} + E_{surf} + E_{\text{int}} \qquad \textbf{Eq. 14}$$

Where, E_{elas} is the elastic strain energy due to the lattice mismatch, E_{surf} is the surface (interfacial) energy, and E_{int} is the elastic interaction energy caused by the overlap of elastic strain fields from individual coherent precipitates (which is ignored in our calculation). So the total energy can be expressed as:

$$E_{total} = E_{elas} + E_{surf} \qquad \textbf{Eq. 15}$$

In order to simplify the calculation, we first calculated the elastic strain energy using Eshelby's theory for the case of an elastically isotropic precipitate in an elastically isotropic matrix (Eshelby 1957). The elastic strain energy density is expressed as (Kato 1996):

$$E_{elas} = -\frac{1}{2}\sigma_{ij}\varepsilon_{ij}^{M} \qquad \textbf{Eq. 16}$$

Where σ_{ij} is the stress inside the inclusion and ε_{ij}^{M} is the stress-free strain. According to Eshelby (Eshelby 1957, Kato 1996) the stress can be calculated by the following equation:

$$\sigma_{ij} = C_{ijkl}^{*}(S_{klmn}\varepsilon_{mn}^{*} - \varepsilon_{kl}^{M}) = C_{ijkl}(S_{klmn}\varepsilon_{mn}^{*} - \varepsilon_{kl}^{*}) \qquad \textbf{Eq. 17}$$

Where C_{ijkl}^{*} and C_{ijkl} are the elastic constants of the precipitates and the matrix respectively. S_{klmn} is the Eshelby tensor and ε_{mn}^{*} is the eigenstrain. The Eshelby tensors for the needle and plate are from ref. (Pineau 1976).

The surface energy is given by:

$$E_{surf} = S \cdot \gamma$$ **Eq. 18**

S is the surface area of the precipitate, γ is the interfacial energy density. For a_γ=3.96Å and c_γ=4.08Å, γ equals 0.46 J·m^{-2} calculated by Benedek et al. (Benedek 2004) using the first principles density function theory code VASP.

In the HIPed & Annealed Ti-45Al-5Nb-0.75C alloy annealed at 800ºC for 24 to 48h, the lattice misfits between the P-Ti_3AlC and the γ matrix phases along [100], [010] and [001] directions are $\varepsilon_{100}=\varepsilon_{010}$=-0.033, and ε_{001}=-0.021 respectively. The elastic constants of the P-Ti_3AlC phase are calculated from ref. (Zhang 2009) and given as C_{11}=251.6GPa, C_{12}=84.8GPa, C_{44}=83.4GPa. The elastic constants of γ-TiAl are C_{11}=182.8GPa, C_{12}=75.2GPa, C_{44}=103.5GPa (He 1997). All the elastic constant values are for room-temperature as no elevated temperature values are available in literature for the P-Ti_3AlC phase. v is Poisson's ratio and is equal to 0.25 (Schafrik 1977, Du 2009, Kanchana 2009, Zhang 2009) for both phases. Based on the size measurements presented earlier for the HIPed & Annealed Ti-45Al-5Nb-0.75C alloy after annealing at 800°C for 24 and 48h, the ratio between the diameter (a_1 and b_1) and the length (c_1) of needles is $5a_1=5b_1=c_1$ and the size ratios for the plate are $10a_2=2b_2=c_2$ (Where a_2 is half of the thickness, b_2 is half of the width and c_2 is half of the length).

The surface area of the ellipsoid is given by the Knud Thomsen's formula:

$$S = 4\pi[\frac{a_1^p b_1^p + a_1^p c_1^p + b_1^p c_1^p}{3}]^{\frac{1}{p}}$$ **Eq. 19**

Where p is a constant and is about 1.6075 which yields a relative error of 1.061% at most.

The volume of the ellipsoid is expressed as:

$$V = \frac{4\pi}{3} abc$$ **Eq. 20**

When the morphology of the precipitates changes from needle to plate, the volume of both shapes should be equal resulting in the following relationship:

$$V_1 = \frac{4\pi}{3} a_1 b_1 c_1 = V_2 = \frac{4\pi}{3} a_2 b_2 c_2$$ **Eq. 21**

After inserting the size ratios given above, a ratio between c_1 and c_2 can be obtained from **Eq. 21** c_2=0.9283c_1.

Using the Eshelby's inclusion method, carbides with a needle-like morphology have a smaller elastic strain energy density ($1.26\times10^{-3}E$) than plate shaped precipitates ($(1.61\text{-}2.3)\times10^{-3}E$). Meanwhile the surface energy of needles ($0.92c_1^2$·J·m^{-2}) is also smaller than that of plate ($1.33c_1^2$·J·m^{-2}). So the needle is the more stable morphology.

However the prediction contradicts with our experimental findings. This could be because the γ matrix is elastically anisotropic, which could affect the elastic strain energy.

The elastic strain energy of coherent ellipsoidal precipitates in an anisotropic crystalline solid with a pure dilatational stress-free strain was calculated by Lee et al. (Lee 1977) also using the theory of Eshelby (Eshelby 1957), as shown in **Figure 94**. A^* and A, μ^* and μ, ν^* and ν are the anisotropic factors, shear modulus and Poisson's ratios of the precipitate and the matrix respectively. The results were represented as a normalized quantity W/W_0, where W_0 was the strain energy per unit volume in the isotropic homogeneous case and was taken as (Lee 1977):

$$W_0 = 2\mu\frac{1+\nu}{1-\nu}\varepsilon^2 \qquad \textbf{Eq. 22}$$

Where, μ was the shear modulus (C_{44}) and ν was the Poisson's ratio ($C_{12}/2(C_{12}+C_{44})$) of the matrix phase.

In order to understand that the morphology of the elastically isotropic P-Ti_3AlC phase changes from needle-like to plate-like when embedded in the anisotropic γ-TiAl matrix, we conducted a rough calculation for the elastic strain energy of both needle- and plate-like shapes based on the results of Lee et al. (Lee 1977). The shear moduli are 83.4GPa and 103.5GPa for the P-Ti_3AlC phase and the γ-TiAl matrix respectively. So μ^* equals around $\mu/1.24$. The anisotropic factor A^* ($2C_{44}/(C_{11}-C_{12})$) of the P-Ti_3AlC phase is 1, which is smaller than that of the γ-TiAl matrix (A=1.92). So our case is more similar to the case represented as dotted lines in **Figure 94**. Then the elastic strain energy per unit volume for a needle (β=0) is W=0.4085W_0 (Line 1), for a plate using the aspect ratio in our experimental results is W=0.3768W_0 (Line 2), and for a disc/plate (β=∞) is W=0.3415W_0 (Line 3), when $\mu^*=\mu/3$.

Thus the elastic strain energy for the P-Ti_3AlC carbides is assumed as W=0.4085W_0 with needle shape and as W=0.3768W_0 with plate shape. The interfacial energy can be simply calculated by **Eq. 18**. Hence, the total energy of the precipitates can be given by,

Needle:

$$E_{total} = 0.4085W_0 \cdot V_N + S_N \cdot \gamma = 0.4085 \cdot 2 \cdot \mu \cdot \frac{1+\nu}{1-\nu} \cdot \varepsilon^2 \cdot \frac{4}{3\pi}c_1^3 + 1.9973c_1^2 \cdot \gamma \quad \textbf{Eq. 23}$$

Plate:

$$E_{total} = 0.3768W_0 \cdot V_P + S_P \cdot \gamma = 0.3768 \cdot 2 \cdot \mu \cdot \frac{1+\nu}{1-\nu} \cdot \varepsilon^2 \cdot \frac{4}{3\pi}c_2^3 + 2.8991c_2^2 \cdot \gamma \quad \textbf{Eq. 24}$$

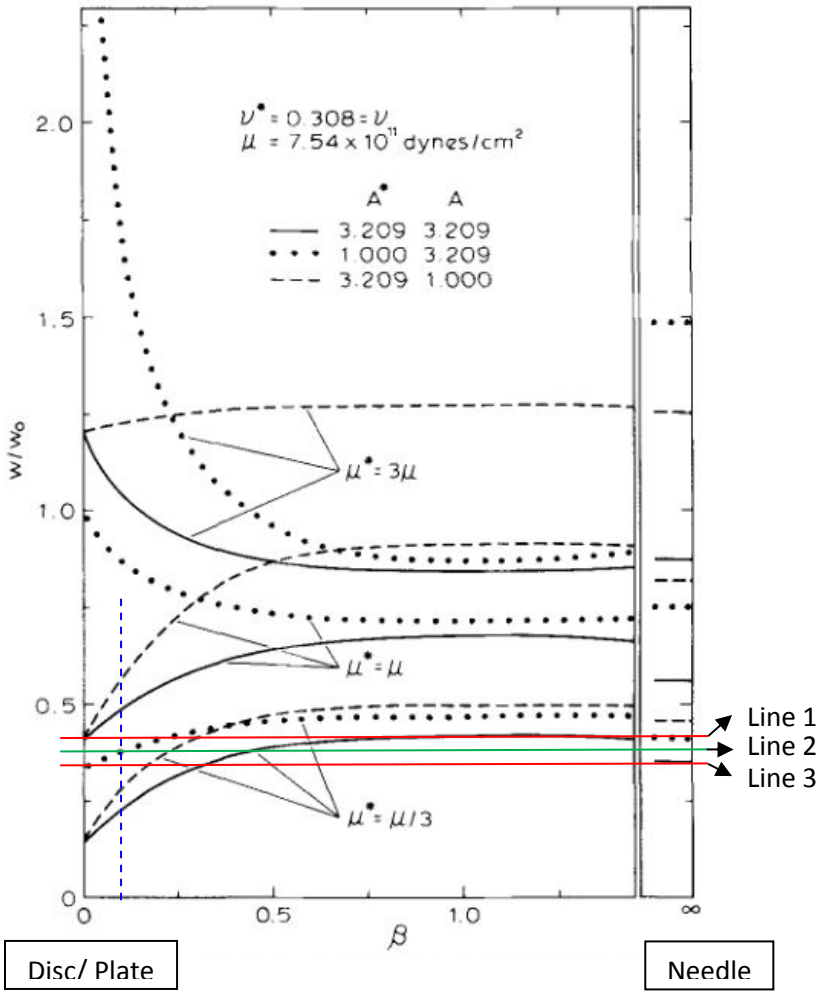

Figure 94 Normalized strain energy of a coherent precipitate as a function of aspect ratio calculated by computational procedure. A^* and A, μ^* and μ, ν^* and ν are the anisotropic factors, shear modulus and Poisson's ratios of the precipitate and the matrix respectively. β is the aspect ratio and equals c/a. W_0 is the strain energy density in an isotropic homogenous case. The dotted lines show the results for an isotropic precipitate in an anisotropic matrix, which is similar to our case. For extreme cases (β=0 and β=∞) the elastic strain energy per volume for a needle is W=0.4085W_0 (Line 1) and W=0.3415W_0 (Line 3) for a disc/plate. When the aspect ratio from our experimental results is used the elastic strain energy of a plate is W=0.3768W_0 (Line 2). All these values are derived for $\mu^*=\mu/3$ (Lee 1977).

From the assumption that when the morphology changes from needle-like to plate-like the volume of both shapes is the same, it follows c_2=0.9283c_1. After inserting this ratio and the properties of the γ-TiAl phase ($\mu=C_{44}$=103.5GPa, $\nu=C_{12}/2(C_{12}+C_{44})$=0.21, ε=(0.033+0.033+0.021)/3=0.029 and γ=0.46 J·m^{-2}) into **Eqs. 22-24**, the following equations can be obtained,

Needle: $E_{total} = 0.4560 \cdot 10^9 \cdot c_1^3 \cdot J \cdot m^{-3} + 0.9188 \cdot c_1^2 \cdot J \cdot m^{-2}$ **Eq. 25**

Plate: $E_{total} = 0.3365 \cdot 10^9 \cdot c_1^3 \cdot J \cdot m^{-3} + 1.3336 \cdot c_1^2 \cdot J \cdot m^{-2}$ **Eq. 26**

From **Eqs. 25-26**, it is clearly suggested that carbides with a needle shape have a higher elastic strain energy and lower surface energy than plate-shaped carbides. As the total energy changes with the growth of carbides the carbide morphology switches from needle-like to plate-like at a critical precipitate size $c_{1\text{-}cri}$=3.5nm (critical needle length=7nm). When c_1 is smaller than $c_{1\text{-}cri}$, a needle-like carbide is more stable because the interfacial energy is predominant. While when carbides grow and c_1 is larger than $c_{1\text{-}cri}$, the plate-like morphology becomes more stable due to its relatively smaller elastic strain energy. Although this critical size is less than the experimental data which shows that carbides retain a needle-like morphology up to an average length of about 24nm after 24h at 800°C and start to change to a plate-like morphology after 48h, it is in the same magnitude as the experimental data. The prediction of too low a critical size for shape change is probably caused by using data for the elastic strain energy coming from a calculation which assumes a ratio of shear moduli of $\mu^*=\mu/3$. It can be seen from **Figure 94** that a less pronounced difference in shear moduli favors the needle shape which should result in a larger critical size.

In the experiments on the HIPed & Annealed Ti-45Al-5Nb-0.75C alloy, it is found that plate-like carbides first form near to grain boundaries and carbides away from grain boundaries initially retain their needle-like shape. There are several possible explanations.

- Explanation 1: variation of elements in regions near grain boundaries

Figure 95 illustrates the chemical composition distribution in the matrix.

In **Figure 95(a)**, the EDS line scan was started within the grain interior, then crossed a precipitate free zone (PFZ) and ended near a grain boundary in the HIPed & Annealed Ti-45Al-5Nb-0.75C alloy after annealing at 800°C for 48h. The results show that the levels of Al and Nb in regions near the grain boundary increase slightly by about 0.5 at. %, while Ti is reduced compared to the grain interior. This might be attributed to the formation of large grain boundary carbides absorbing Ti atoms from neighboring regions and increasing the contents of Al and Nb atoms in the surrounding matrix.

Figure 95(b) is an example of PFZ near to a γ/α_2 grain boundary in the HIPed & Annealed Ti-45Al-5Nb-0.75C alloy after annealing at 800°C for 168h. The line scan was started in an α_2 grain, crossed a PFZ, and terminated in a γ grain. The results show that Nb is enriched in both the α_2 grain and the PFZ (by around 0.5 at. %). Additionally, the PFZ is also slightly enriched in Al (about 1.0 at. %) and depleted in Ti compared with the γ matrix.

Figure 95(c) is an example of a PFZ near to a γ/γ grain boundary in HIPed & Annealed Ti-45Al-5Nb-0.75C after annealing at 800°C for 168h. The result also shows that Al and Nb levels are increased slightly, while Ti is decreased slightly in the PFZ.

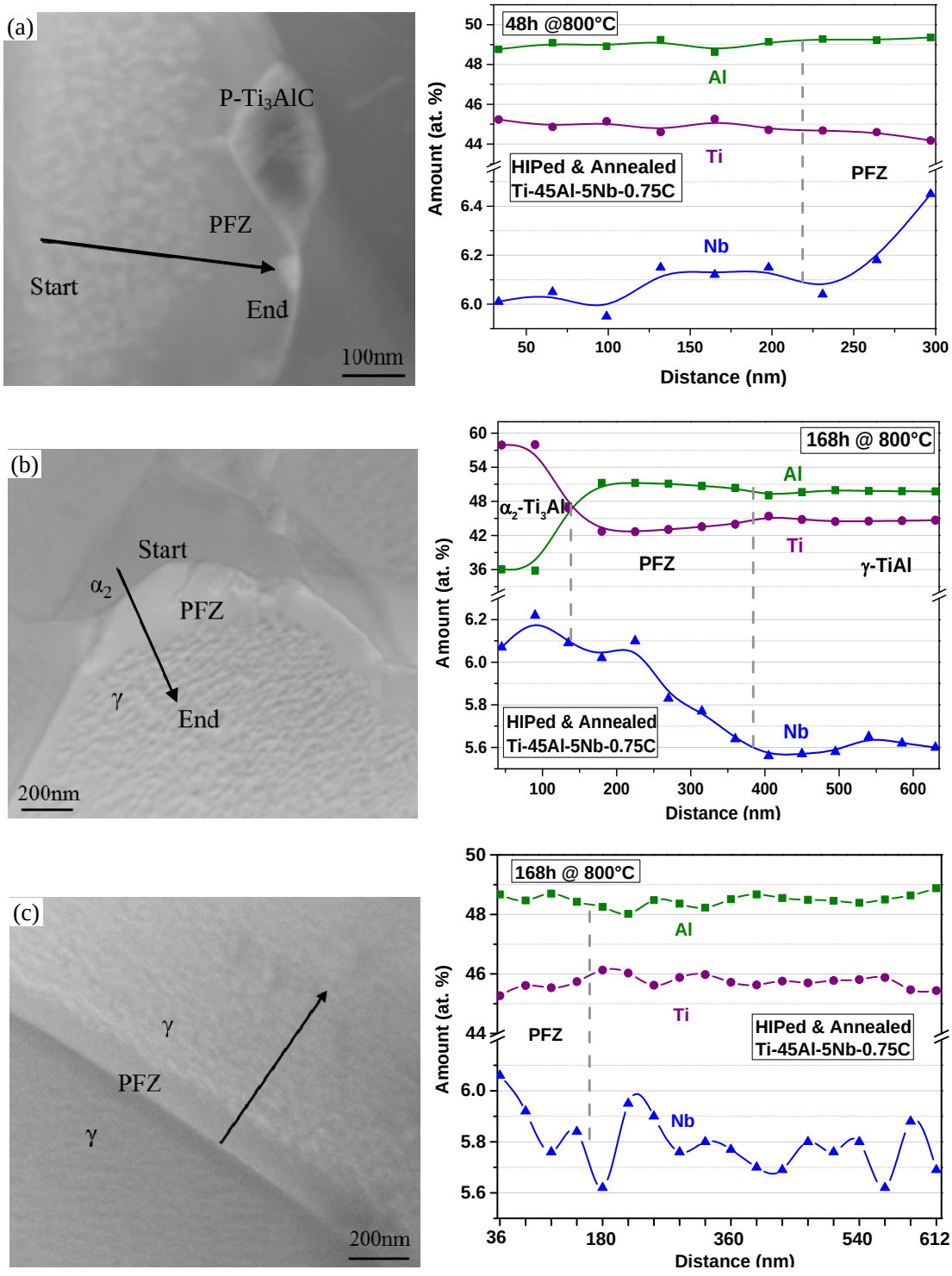

Figure 95 Ti, Al and Nb distribution in the matrix in different cases, (a) a PFZ near to a γ/P/γ grain boundary, (b) a PFZ near to a γ/α_2 grain boundary and (c) a PFZ near to a γ/γ grain boundary.

Since the local chemical composition can influence the lattice parameters of the matrix phase, the lattice misfit between carbides and the γ matrix may also be changed locally and thus can influence carbide precipitation in the alloy. From literature it is known that the lattice parameters of the γ phase vary depending on the Al and Nb levels, as shown in **Table 10**. Although the variation is not consistent in literature from different sources, they all suggest that Al has a more significant

influence on lattice parameters than Nb. From **Figure 95**, it can be seen that the increase of Nb is about 0.2-0.5 at. % at regions near grain boundaries, which is smaller than the increase of Al (around 0.3-1.0 at. %). As a consequence, the influence of Al on the lattice parameters exceeds that of Nb. This causes a reduced carbide-matrix misfit along the [001] direction and a slightly increased misfit along the [100] and [001] directions. From **Eqs. 23-26**, the critical size (c_1) at which needles transform to plates might thus be decreased slightly due to the small increment of the misfit strain. Therefore carbides near to grain boundaries may change their morphology to plate-like earlier than those within grain interiors.

Table 10 Effects of Al and Nb additions on the lattice parameters of the γ phase in TiAl alloys (from literature)

Literature	Effects of increment of Al and Nb contents on lattice parameters
(Kawabata 1998)	Al: $\downarrow a_\gamma$, $\downarrow c_\gamma$ and Nb: $\uparrow a_\gamma$, $\uparrow c_\gamma$. effects (Al) > effects (Nb)
(Whang 1988)	Al: $\downarrow a_\gamma$, $\uparrow c_\gamma$ and Nb: $\downarrow a_\gamma$, $\downarrow c_\gamma$.
(Oehring) unpublished results	Al: $\downarrow a_\gamma$, $\uparrow c_\gamma$ and Nb: $\uparrow a_\gamma$, $\rightarrow c_\gamma$ a_γ: decrement (Al) > increment (Nb)

* "↓" means decreasing, "↑" means increasing and "→" means remaining constant

- Explanation 2: Possible carbon distribution gradient in γ grains

In **Section 3.6** it is mentioned that due to the possible carbon enrichment at grain boundaries, the primary carbides are preferentially observed at grain boundaries in the HIPed & Annealed Ti-45Al-5Nb-0.75C alloy. This is shown in **Figure 23** in a HIPed alloy. From **Figure 71** in **Section 4.4.2**, the carbide size and density gradient suggests that there should be a carbon distribution gradient within γ grains. Carbon is enriched at grain boundaries, where carbides form first and absorb carbon from the neighboring γ matrix. Therefore the carbon concentration in the interior of γ grains should be higher than in regions near to grain boundaries. This leads to higher nucleation density of carbides in the grain interiors and in consequence to an increased competition among growing precipitates compared to the situation near grain boundaries. Thus in regions near grain boundaries carbides grow fast due to a low nucleation density and low growth competition and they first change their morphology to plate-like in such regions. This explanation is further supported by a comparison with the Solution Treated & Annealed Ti-45Al-5Nb-0.75C alloy. No such morphology change, and no obvious particle size and density gradient was observed. It is thought that after solution treatment, carbon is more homogeneously distributed in the matrix. During subsequent annealing treatments, grain boundaries carbides are thus smaller in size, as confirmed in **Figure 46**. Thereby carbides in regions near grain boundaries have similar characteristics to those at grain interiors. The nucleation and growth of carbides are more uniform in the γ grains. As a consequence carbides keep growing as a needle before their size reaches the critical value. **Figure 96** schematically illustrates the influence of the possible carbon distribution gradient on the carbide morphology and PFZs. It is worth mentioning that due to the low

concentration of carbon in the matrix and the difficulty in detecting the light element carbon, attempts to determine the carbon concentration were not successful.

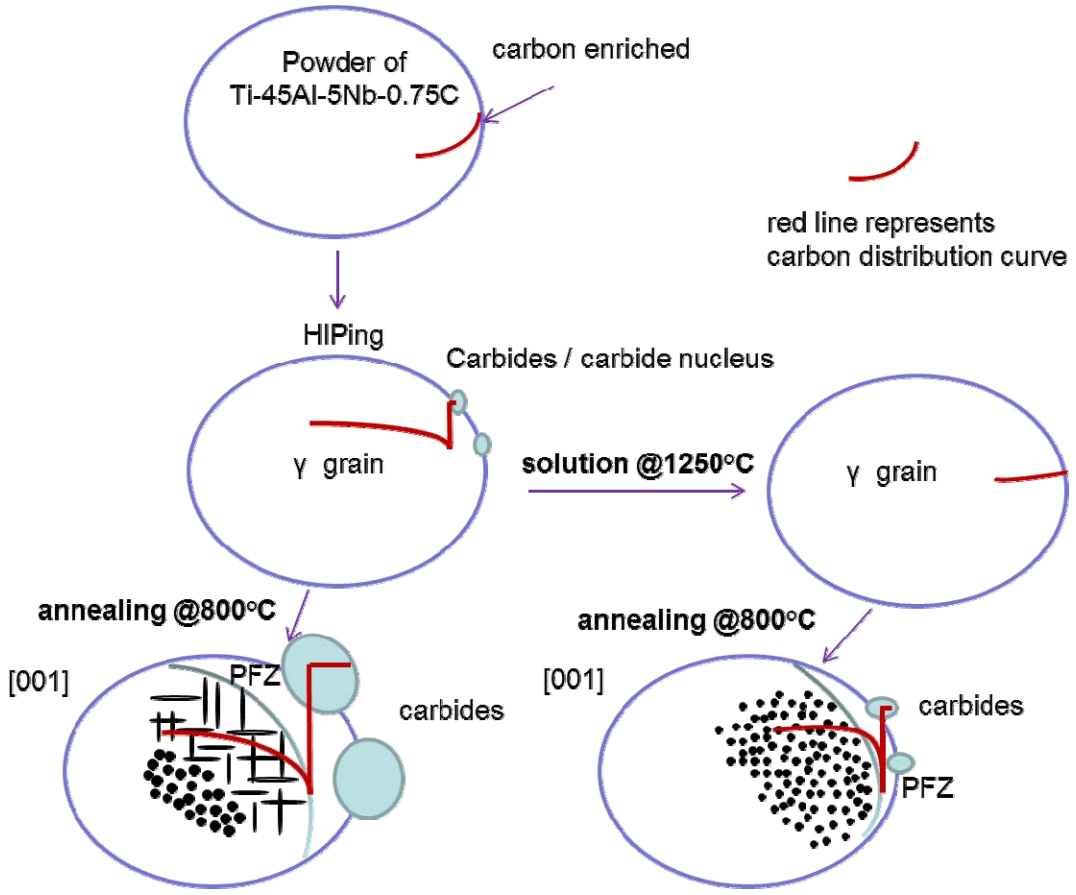

Figure 96 Schematic image illustrates the possible carbon distribution in γ grains in Ti-45Al-5Nb-0.75C alloy and its influence on the morphology of carbides and width of PFZs.

- Explanation 3: Possible different stress states in γ grains

It is possible that in each γ grain the stress states in regions near the grain boundary and within the grain interior are possibly different. In regions near the grain boundary, the stress state will be influenced by the strain field induced by the grain boundary. What is more, the stress state will also be influenced by strain fields from carbides that are within the γ grains. Although for the moment this point is not supported by experiments, it cannot be excluded as a possible reason for the carbide morphology change first starting near grain boundaries.

5.3.2 Carbide splitting

In the Solution Treated & Annealed alloys, carbides split into substructures after long-term annealing (some carbides in the HIPed & Annealed Ti-45Al-5Nb-0.75C alloy also start to split after annealing at 800°C for 168h, **Figure 81**). This is different from the phenomena observed by Tian et al. (Tian 1993) that ordered domains existed in a single needle-like perovskite carbide. Before splitting, the carbides in the γ matrix retain their needle-like morphology and can reach a length of around 35nm, which is

larger than the value for the shape change from needles to plates in the HIPed & Annealed condition. After comparing these two conditions, it is shown that the carbide density in γ grains of the Solution Treated & Annealed condition is much higher than that of the HIPed & Annealed one. It is reported that when the interparticle distances become very small, it is necessary to consider the interaction energy induced from the overlapping elastic strain fields from neighboring particles (Miyazaki 1982, Doi 1984, Doi 2004). The interaction energy between precipitates can play a significant role in the morphology change of precipitates during annealing (Ardell 1966, Johnson 1987, Doi 1992). Therefore, in the Solution Treated & Annealed alloys, the interaction energy between carbides needs to be considered. For a coherent carbide in the γ matrix, the total energy can be given by:

$$E_{total} = E_{elas} + E_{surf} + E_{\text{int}} \qquad \textbf{Eq. 27}$$

Presuming that the calculation for the self-elastic strain energy (elastic strain energy for a single particle) and the surface energy does not change and that for carbides with needle and plate morphologies, the total energies can be obtained by **Eqs. 28-29** respectively, we obtain modified equations for the total energy:

Needle: $$E_{total} = 0.1177 \cdot 10^{9} \cdot c_1^3 \cdot J \cdot m^{-3} + 0.9188 \cdot c_1^2 \cdot J \cdot m^{-2} + E_{\text{int}} \qquad \textbf{Eq. 28}$$

Plate: $$E_{total} = 0.0915 \cdot 10^{9} \cdot c_1^3 \cdot J \cdot m^{-3} + 1.2350 \cdot c_1^2 \cdot J \cdot m^{-2} + E_{\text{int}}^{'} \qquad \textbf{Eq. 29}$$

When the precipitate morphology changes, the total energy of the needle should be equal to that of the plate, as given by:

$$0.1177 \cdot 10^{9} \cdot c_1^3 \cdot J \cdot m^{-3} + 0.9188 \cdot c_1^2 \cdot J \cdot m^{-2} + E_{\text{int}} = 0.0915 \cdot 10^{9} \cdot c_1^3 \cdot J \cdot m^{-3} + 1.2350 \cdot c_1^2 \cdot J \cdot m^{-2} + E_{\text{int}}^{'} \qquad \textbf{Eq. 30}$$

or

$$0.0262 \cdot 10^{9} \cdot c_1^3 \cdot J \cdot m^{-3} - 0.3162 \cdot c_1^2 \cdot J \cdot m^{-2} = E_{\text{int}}^{'} - E_{\text{int}} \qquad \textbf{Eq. 31}$$

In the Solution Treated & Annealed condition, the critical size $c_{1\text{-}cri}$ is increased if the interaction energy between plates is higher than that between needles. This may suggest that the interaction energy can stabilize carbides with a needle-like morphology. With increasing annealing time, the carbides grow and coarsen. The interparticle distance increases and the interaction energy between particles is reduced and thus can be omitted. The total energy is then controlled by elastic strain energy and surface energy.

In order to stabilize the precipitates the process of carbide splitting occurs. P-Ti_3AlC carbides first split along the [001] direction to form parallel needles, and then these needles split further along the [100] or the [010] direction into small domains with a superspherical shape. From refs. (Ardell 1966, Johnson 1979, Miyazaki 1981,

Miyazaki 1982, Doi 1984, Miyazaki 1984, Doi 1985, Johnson 1987, Khachaturyan 1988, Kaufman 1989, Doi 1992, Banerjee 1999), it is well known that precipitate splitting into plates or cuboids can occur in Ni-base alloys.

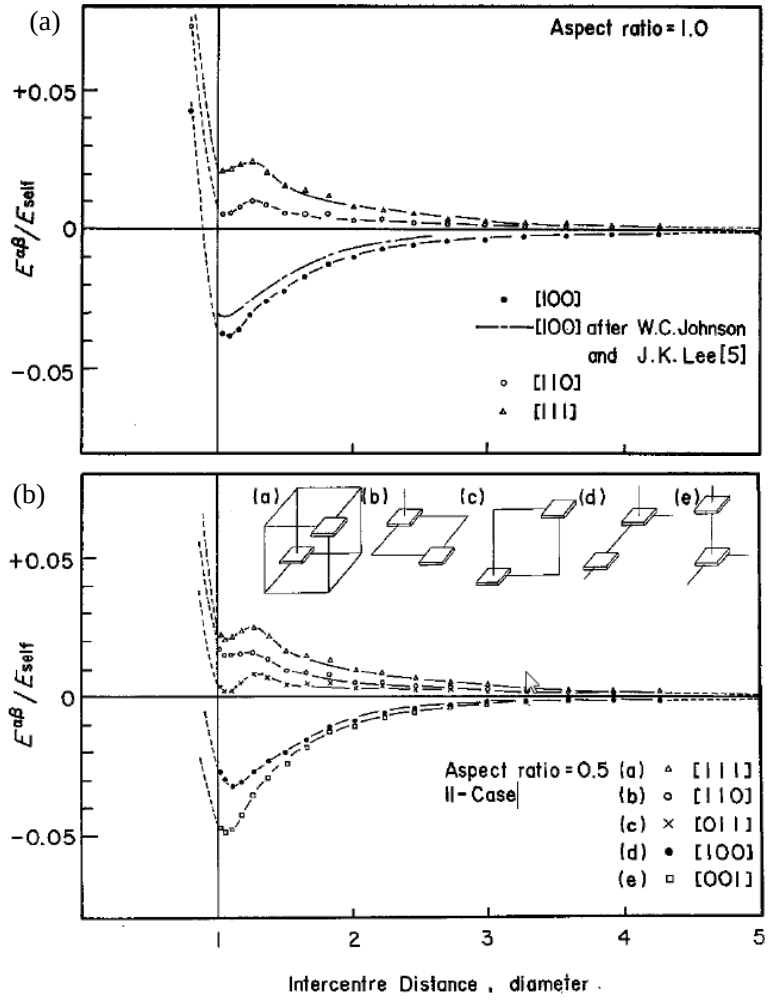

Figure 97 Elastic interaction energy between (a) spherical and (b) plate-shaped γ' precipitates as a function of interparticle distance and alignment direction (Miyazaki 1981). $E^{\alpha\beta}$ is the interaction energy between the precipitates and E_{self} is the elastic strain energy for a single precipitate.

In the research published by Doi et al. (Doi 1984) for Ni-base alloys, the coherent γ' precipitate split into substructures during coarsening and thus the surface energy of the precipitates was certainly increased. There must be some counteracting process which nevertheless caused a reduction in the total energy. In refs. (Johnson 1979, Yamauchi 1979, Miyazaki 1981) the interaction energy between two γ' precipitates was reported to be negative when they were adjacent to each other along <100> directions. Thus the interaction energy between the split substructures compensated for the increase of surface energy. Johnson et al. (Johnson 1979) treated the elastic interaction energy between two spherical precipitates in Ni-base superalloys embedded in an infinite cubic anisotropic matrix in dependence of the interparticle distance and alignment direction. When the anisotropy factor $A=2C_{44}/(C_{11}-C_{12})$ was larger than one, an attractive elastic interaction occurring along the <100> directions

could decrease the total energy of the precipitates. Miyazaki et al. (Miyazaki 1981, Miyazaki 1982) performed numerical calculations on the interaction energy as a function of interparticle distance and alignment direction for both spherical and plate-shaped γ' precipitates, as shown in **Figure 97**. When the γ' precipitates were aligned along the <100> directions (elastically soft directions), the interaction energy between the precipitates was negative and reached a minimum when they were separated by an interparticle distance of 1.090D in the <100> directions (D is the precipitate diameter).

Doi et al. (Miyazaki 1982, Doi 1984, Doi 1985, Doi 1992) summarized two splitting procedures in Ni-base alloys. One was for a Ni-Al alloy in which a single precipitate split into a doublet and the other was for a Ni-Si alloy in which one single precipitate split into eight cuboidal particles. They performed theoretical calculations and showed that a split doublet would further split into an octet (as shown in **Figure 98**), although in experiments this phenomenon was not observed.

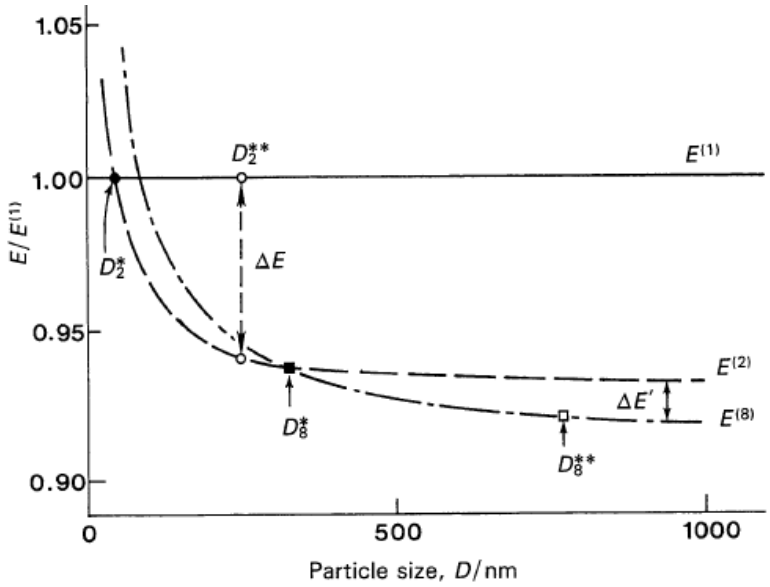

Figure 98 Total energies of γ' precipitates in a Ni-Al alloy as a single particle $E^{(1)}$, a split doublet $E^{(2)}$, and as a split octet $E^{(8)}$ based on microelasticity theory (Doi 1985, Doi 1992).

Although in our research we did not caculate the interaction energy, it can be assumed that the splitting of P-type carbides observed here is also due to the interaction energy between the precipitates. In our alloy system, the misfit between the P-Ti_3AlC carbides and the γ phase is small along the [001] direction and this is also the elastically softest direction for the γ matrix phase. Meanwhile the anisotropy factor for the γ matrix is also larger than one. This is similar to the situation in Ni-base superalloys. Thus through splitting into small domains, the total energy of a single carbide is reduced by the probable negative interaction energy among the domains. The splitting process is shown schematically in **Figure 99**.

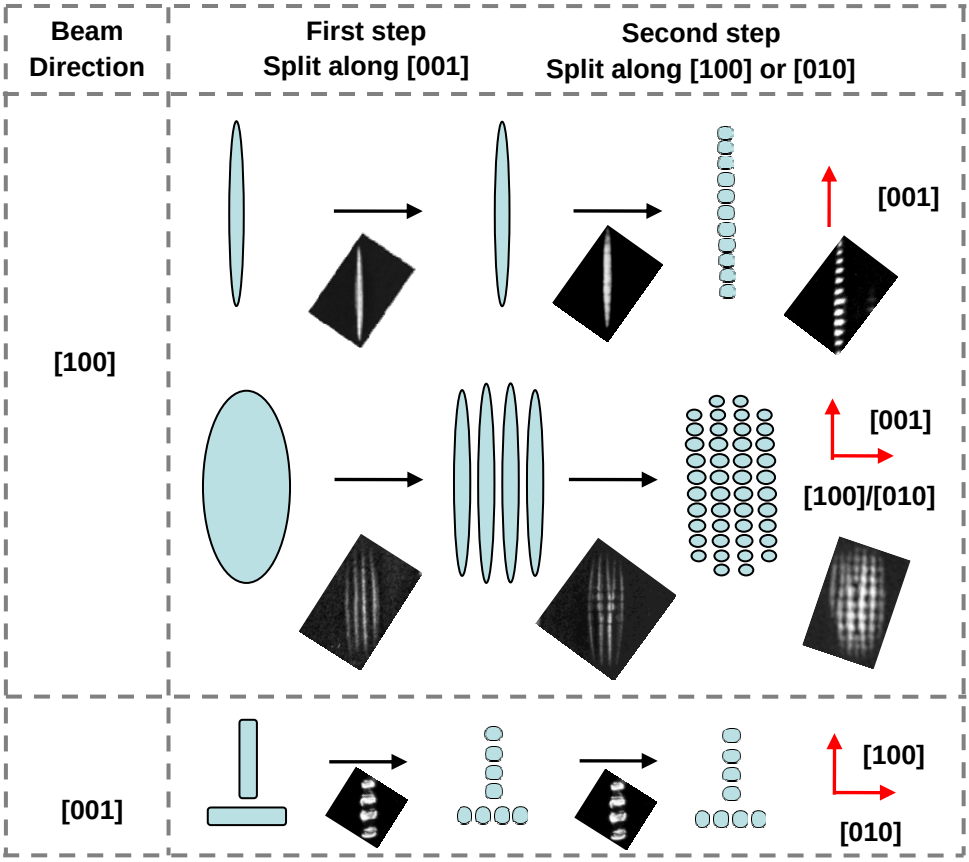

Figure 99 Schematic illustration of the P-Ti_3AlC carbide splitting process during coarsening. Carbides first split along the [001] direction, and then split further along the [100] or [010] directions into superspherical domains.

6 The influence of Nb on carbon solubility and carbide precipitation, comparison with literature

It is very interesting to know the carbon solubility and carbide precipitation in high Nb containing TiAl alloys because these alloys have potential for application in a higher temperature range. Although EDS and WDS methods in our research were not able to successfully measure the exact carbon concentration in the matrix, we can still obtain some information about the influence of Nb on carbon solubility and carbide precipitation by comparing our results with literature data.

In this research, no carbides are detected in Ti-45Al-5Nb-1.0C pre-alloyed powder. In the HIPed Ti-45Al-5Nb-1.0C alloy, carbides are dissolved after solution treatment at 1400°C. In the Ti-45Al-5Nb-0.75C and Ti-45Al-5Nb-0.5C alloys, carbides are considered as being in solution at 1250°C. In rapidly solidified Ti-45Al and Ti-48Al powders investigated by McCullough et al. (McCullough 1990), no carbides were observed in Ti-45Al-xC (x< 0.64 at. %) and in Ti-48Al-xC carbides (x< 1 at. %). In another Ti-48Al alloy investigated by Perdrix et al (Perdrix 2001), the carbon solubility was about 0.96 at. % in the α_2 phase and H-type carbides appeared in the alloy with a carbon concentration above 0.32 at. %. For as-cast Ti-39Al-1.0C, reported by Cam et al. (Cam 1988), the α_2 phase could accommodate more than 1 at. % carbon. Even as the temperature dropped from 1250 to 750ºC no carbides precipitation was detected. Tian et al. (Tian 1997) reported that in $(TiAl)_xC_y$ the maximum solid solubility of carbon at 1250°C was less than 0.5 mol%. Summarizing this data, it seems that Al content has significant role on carbon solubility in TiAl alloys. The lower the Al content, the higher the carbon solubility in the alloy. Addition of Nb seems to affect the solubility of carbon at high temperature.

Scheu et al. (Scheu 2009) carried out atom probe investigations on a Ti-45Al-5Nb-0.5C alloy after hot rolling and annealing at 1050ºC for 2h. The carbon content in the γ phase was about 0.25 at. %, which was almost ten times higher than that (200-350 at. ppm) reported in Ti-46Al and Ti-48Al alloys (Menand 1996). More importantly they did not find carbides in this alloy. However it is worth noting that the alloy investigated may be not in thermodynamic equilibrium. In the current work on Ti-45Al-5Nb-0.5C, carbides exist at 800ºC but dissolved at 1000ºC. But in Ti-45Al-5Nb-0.75C, carbides remain present at 800-1000ºC. Therefore it is proposed that in Ti-45Al-5Nb the carbon solubility at 1000ºC is higher than 0.5 at. % but less than 0.75 at. %, and is less than 0.5 at. % at 800ºC.

In this research, as summarized in **Section 4.6**, in the HIPed & Annealed Ti-45Al-5Nb-0.5C alloy, P-Ti_3AlC carbides precipitate sequentially at grain boundaries, at dislocations and in the γ matrix at 800°C. They coarsen at 900°C and dissolve at 1000°C. In the HIPed & Annealed Ti-45Al-5Nb-0.75C, carbides in the γ matrix change their morphology from needle-like to plate-like gradually at 800°C. Carbides coarsen at 900 and 1000°C. In the Solution Treated & Annealed Ti-45Al-5Nb-0.5C alloy, carbides form at all locations after 24h at 800°C. Carbides in the γ matrix

appear as needle-shape and split after further annealing. The carbides in the Solution Treated & Annealed Ti-45Al-5Nb-0.75C alloy annealed at 800°C show the same splitting phenomenon as those in Solution Treated & Annealed Ti-45Al-5Nb-0.5C at 800°C. Carbides coarsen at 900-1000°C. In both alloys, no H-type carbides are observed to form during annealing at 800-1000°C. These results are quite different from the literature, where P-type carbides formed at lower temperatures (ranging from 750 to 900°C) and then H-type carbides formed at the expense of P-type carbides (at 900-1000°C) or at lower temperatures with longer annealing times. For example, in the Ti-(48-50)Al-2.1Nb alloy with a carbon level of 0.06-0.07 at. % that was investigated by Chen et al. (Chen 1992), both P- and H-type carbides were observed after HIPing at 1250ºC and subsequent annealing within the temperature range of 750-1000ºC. Worth et al. (Worth 1995) pointed out that in Ti-48Al-1V-0.3C no carbides existed after a stabilization heat treatment at 1000ºC and P-type carbides nucleated at grain boundaries, at dislocations and in the γ matrix after annealing at 750 and 815ºC. Tian et al. (Tian 1993, Tian 1997) mentioned in $(TiAl)_xC_y$ at 1250ºC the maximum solid solubility should be less than 0.5 mol %, and that after 1000h at 800ºC, P-type carbides retained a needle-like morphology and had carbon-vacancy long-range ordering. Karadge et al. (Karadge 2003) detected elongated H-type carbides that formed at γ/γ interfaces in the K5SC alloy (Ti-46.2Al-2Cr-3Nb-0.2W-0.Si-0.1C, at. %) after creep deformation at 760 and 870ºC. McQuay et al. (McQuay 1999) added a series of carbon levels (0.02, 0.12, 0.21 and 0.36 at. %) to the 47XD alloy (Ti-47Al-2Mn-2Nb-1B, at. %) and found when the carbon content was ≥0.12 at. %, carbides could be observed.

More information about carbide formation from literatures has been discussed in **Section 1.4.1**. By comparison of our results with literature data it is found that the carbide precipitation in Ti-45Al-5Nb-xC alloys seems to be slowed down. This might be explained by the high Nb addition, the diffusion of elements being retarded (Herzig 2001) and the precipitation process becoming sluggish. However Divinski et al. (Divinski 2005) proposed that a high Nb addition (10 at. %) could enhance the diffusivities of both Ti and Nb in ternary alloys at $T > 1000K$ due to the elastic distortion of the $L1_0$ structure of the γ phase introduced by Nb alloying. Meanwhile the observed morphological development of carbides in the present study is different to ref. (Tian 1993), which may be also attributed to the addition of Nb and the different Al contents. Together these can influence the lattice parameters of the γ phase which affect the mismatch between the P-Ti_3AlC and γ phases and thus play a role in carbide precipitation. Furthermore, the thermal stability of P-type carbides and the formation temperature of H-type carbides are increased. As observed in **Sections 4.1** and **4.3**, the dissolution temperature of carbides is influenced by carbon concentration of the TiAl alloys. The references reported up to now are mainly concerned with TiAl alloys that were doped with low carbon concentrations (≤ 0.5 at. %) and a low Nb addition (≤ 3 at. %). It is probable that the addition of high amounts of Nb and carbon affect the thermal stability of carbides simultaneously.

7. Conclusions and future work

(1) Influence of C on phase transformations

Carbon influences the phase transformations in Ti-45Al-5Nb-xC alloys. The addition of carbon increases T_β (α→β) and shifts the (α+β) phase field to a lower Al concentration and a higher temperature. Carbon increases T_e (α_2+γ→α), but it has little influence on T_α (γ→α). However, when the carbon concentration reaches levels above 0.75 at. %, T_e remains constant.

(2) Influence of Nb on carbon solubility

The addition of Nb to TiAl alloys seems to influence the carbon solubility at high temperatures, but the effects of Nb on the solid solubility of carbon at low temperatures are unclear.

The carbon solubility in Ti-45Al-5Nb-xC is >1.0 at. % at 1400°C, >0.5 but <0.75 at. % at 1000°C, and <0.5 at. % at 800°C.

The carbon concentration in the γ phase is not lowered by the scavenging effect of the α_2 phase.

(3) Carbides precipitation and thermal stability of carbides

Carbide precipitation in high Nb containing TiAl alloys is different to that in low Nb or Nb-free TiAl alloys as reported in literature. The thermal stability of P-Ti_3AlC carbides in Ti-45Al-5Nb-xC alloys is increased compared to that reported in literature. These variations may be attributed to the addition of high amounts of Nb, or the high amount of carbon, or a combined effect from both Nb and C.

Carbides in the HIPed conditions are preferentially formed at grain boundaries due to a probable carbon enrichment at grain boundaries. P-Ti_3AlC carbides are preferred to form in alloys with lower carbon concentrations, while H-Ti_2AlC carbides are formed predominantly in alloys with higher carbon contents. The P-Ti_3AlC phase has an orientation relationship with the γ grains of: $[001]_\gamma//[001]_P$, $(100)_\gamma//(100)_P$, but H-Ti_2AlC carbides have no orientation relationship with the γ or α_2 phases.

In the HIPed & Annealed Ti-45Al-5Nb-0.5C alloy, P-type carbides form sequentially at grain boundaries, along dislocations and in the γ matrix at 800°C. P-type carbides coarsen at 900°C and lose stability and dissolve at 1000°C. More P-type carbides are present in the HIPed & Annealed Ti-45Al-5Nb-0.75C alloy. With increasing annealing time P-type carbides in the γ matrix gradually change morphology from

needle-like to plate-like to reduce the elastic strain energy and remain coherent with the γ matrix. At 900 and 1000°C P-type carbides coarsen and are stable.

In the Solution Treated & Annealed Ti-45Al-5Nb-0.5C alloy, carbides form at grain boundaries, at dislocations and in the γ matrix with a needle-like shape on annealing at 800°C. After long-term annealing, carbides split into small substructures and retain their orientation relationship with the γ grains. This is the same situation as for carbides in the Solution Treated & Annealed Ti-45Al-5Nb-0.75C alloy after annealing at 800°C. The carbide splitting may be attributed to the introduction of interaction energy between the carbides which results in a reduction of the total energy of a single precipitate. At 900 and 1000°C carbides coarsen and are stable. Compared with the HIPed & Annealed conditions, the carbide density in the γ grains is significantly increased, which is probably due to a more homogeneous carbon distribution in the γ matrix.

The dissolution temperature of carbides depends on the carbon concentration in the alloys. In the Ti-45Al-5Nb-1.0C alloy the carbides cannot be dissolved until solution treatment at 1400°C. However in Ti-45Al-5Nb-0.75C and Ti-45Al-5Nb-0.5C, the carbides are considered as being in solution after heat treatment at 1250°C.

In heat-treated Ti-45Al-5Nb-0.5C and Ti-45Al-5Nb-0.75C alloys, H-type carbides are not detected to form during annealing. It is believed that the addition of Nb may increase the formation temperature of the H-Ti_2AlC phase.

This work has concentrated on carbide precipitation and carbide stability in high Nb containing TiAl alloys. An attempt can be made to investigate the development of carbon concentration in the matrix during annealing. It may be valuable to investigate the interaction between plate-shaped carbides and dislocations during application. It would also be interesting to further understand the carbide splitting and split substructures as it may be possible to improve mechanical properties of high Nb containing TiAl alloys further via such precipitation.

References

Abe, M., Asano, K., Fujiwara, A. (1973). "Influence of the precipitate-free zone width on the tensile properties of an Al-6 Wt pct Zn-1.2 Wt pct Mg alloy." Metallurgical Transactions **4**(6): 1499-1505.

Appel, F., Fischer, F. D., Clemens, H. (2007). "Precipitation twinning." Acta Materialia **55**(14): 4915-4923.

Appel, F., Oehring, M., Paul, J. D H (2006). "Nano-Scale Design of TiAl Alloys Based on β-Phase Decomposition." Advanced Engineering Materials **8**(5): 371-376.

Appel, F., Oehring, M., Wagner, R. (2000). "Novel design concepts for gamma-base titanium aluminide alloys." Intermetallics **8**(9–11): 1283-1312.

Appel, F., Paul, J. D. H., Oehring, M. (2011). Constitution. Gamma Titanium Aluminide Alloys, Wiley-VCH Verlag GmbH & Co. KGaA**:** 5-23.

Appel, F., Paul, J. D. H., Oehring, M. (2011). Deformation Behavior of Two-Phase $\alpha_2(Ti_3Al)$ + γ(TiAl) Alloys. Gamma Titanium Aluminide Alloys, Wiley-VCH Verlag GmbH & Co. KGaA**:** 125-248.

Appel, F., Paul, J. D. H., Oehring, M. (2011). Strengthening Mechanisms. Gamma Titanium Aluminide Alloys, Wiley-VCH Verlag GmbH & Co. KGaA**:** 249-299.

Appel, F., Paul, J. D. H., Oehring, M., Fröbel, U., Lorenz, U. (2003). "Creep behavior of TiAl alloys with enhanced high-temperature capability." Metallurgical and Materials Transactions A **34**(10): 2149-2164.

Appel, F., Paul, Jonathan David Heaton, Oehring, Michael (2011). Introduction. Gamma Titanium Aluminide Alloys, Wiley-VCH Verlag GmbH & Co. KGaA**:** 1-3.

Ardell, A. J., Nicholson, R. B., Eshelby, J. D. (1966). "On the modulated structure of aged Ni-Al alloys: with an Appendix On the elastic interaction between inclusions by J. D. Eshelby." Acta Metallurgica **14**(10): 1295-1309.

Ashby, M. F., Brown, L. M. (1963). "Diffraction contrast from spherically symmetrical coherency strains." Philosophical Magazine **8**(91): 1083-1103.

Austin, C. M., Kelly, T. J. (1995). Progress in Implementation of Cast Gamma Titanium Aluminide. TMS Gamma titanium aluminide. Y.-W. Kim, Wagner, R., and Yamaguchi, M. Warrendale**:** 21-32.

Badami, M., Marino, F. (2006). "Fatigue tests of un-HIP'ed γ-TiAl engine valves for motorcycles." International Journal of Fatigue **28**(7): 722-732.

Bandyopadhyay, D., Sharma, R. C., Chakraborti, N. (2000). "The Ti- Al- C system (titanium - aluminum - carbon)." Journal of Phase Equilibria **21**(2): 195-198.

Banerjee, D., Banerjee, R., Wang, Y. (1999). "Formation of split patterns of γ' precipitates in Ni-Al via particle aggregation." Scripta Materialia **41**(9): 1023-1030.

Benedek, R., Seidman, D. N., Woodward, C. (2002). Interface Structure and Energy Calculations for Carbide Precipitates in γ-TiAl. High-temperature ordered intermetallic alloys VI. E. George, Inui, H., Mills, M. J., Eggeler, G. Pittsburgh (PA), MRS symposium proceedings. **753:** BB3.5

Benedek, R., Seidman, D. N., Woodward, C. (2004). "Interface Energies for Carbide Precipitates in TiAl." Interface Science **12**(1): 57-71.

Bewlay, B. P., Weimer, M., Kelly, T., Suzuki, A., Subramanian, P. R. (2013). "The Science, Technology, and Implementation of TiAl Alloys in Commercial Aircraft Engines." MRS Online Proceedings Library **1516**: 49-58.

Blackburn, M. J., Smith, M. P. (1981). Titanium Alloys of the TiAl Type. U.S. **No. 4, 294, 615**.

Blackburn, M. J., Smith, M. P. (1982). R&D on Composition and Processing of Titanium Aluminide Alloys for Turbine Engine. Technical Report AFWAL-TR-82-4086, U.S. Air Force Wright Aeronautical Laboratories.
Blum, M., Choudhury, A., Scholz, H., Pleier, S., Busse, P., Frommeyer, G., Knippscheer, S. (1999). Properties of low cost TiAl automotive valves produced by cold wall induction melting and permanent mold centrifugual casting. TMS Gamma Titanium Aluminides. Y.-W. Kim, Dimiduk, D. M., Loretto, M. H. California**:** 35-39.
Çam, G., Bohm, K. H., Müllauer, J., Koçak, M. (1996). "The fracture behavior of diffusion-bonded duplex gamma TiAl." JOM **48**(11): 66-68.
Cam, G., Flower, H. M., West, D. R. F. (1988). The alloying of titanium aluminides with carbon. High-Temperature Ordered Intermetallic Alloys III. C. C. Koch, Liu, C.T., Stoloff, N. S., Taub, A. I. , MRS Proceedings. **133:** 663.
Chaudhari, G. P., Acoff, V. L. (2010). "Titanium aluminide sheets made using roll bonding and reaction annealing." Intermetallics **18**(4): 472-478.
Chen, G. L., Zhang, L. C. (2002). "Deformation mechanism at large strains in a high-Nb-containing TiAl at room temperature." Materials Science and Engineering A **329-331**: 163-170.
Chen, G. L., Zhang, W. J. , Yang, Y., Wang, J., Sun, Z. (1993). TMS Structural Intermetallics. R. Darolia, Lewandowski, J. J., Liu, C. T., Martin, P. L., Miracle, D. B., Nathal, M. V. Warrendale**:** 319.
Chen, G. L., Zhang, W. J., Liu, Z. C., Li, S. J., Kim, Y-W. (1999). Microstructure and properties of high-Nb containing TiAl-base alloys. TMS Gamma Titanium Aluminides. Y. W. Kim, Dimiduk, D. M., Loretto, M. H. California**:** 371-380.
Chen, S., Beaven, P. A., Wagner, R. (1992). "Carbide precipitation in γ-TiAl alloys." Scripta Metallurgica et Materialia **26**(8): 1205-1210.
Chladil, H. F., Clemens, H., Leitner, H., Bartels, A., Gerling, R., Marketz, W. T (2005). "Experimental Studies of Phase Transformations in a Carbon Containing Ti-45Al-7.5Nb Alloy and Related Thermodynamic Simulations." Advanced Engineering Materials **7**(12): 1131-1134.
Chladil, H. F., Clemens, H., Leitner, H., Bartels, A., Gerling, R., Schimansky, F. P., Kremmer, S. (2006). "Phase transformations in high niobium and carbon containing γ-TiAl based alloys." Intermetallics **14**(10–11): 1194-1198.
Chladil, H. F., Clemens, H., Otto, A., Güther, V., Kremmer, S., Bartels, A., Gerling, R. (2006). "Charakterisierung einer β-erstarrenden γ-TiAl-Basislegierung." BHM Berg- und Hüttenmännische Monatshefte **151**(9): 356-361.
Christoph, U., Appel, F., Wagner, R. (1997). "Dislocation dynamics in carbon-doped titanium aluminide alloys." Materials Science and Engineering: A **239–240**(0): 39-45.
Clemens, H. (1995). "Intermetallic γ-TiAl based alloy sheet materials: processing and mechanical properties." Zeitschrift fur Metallkunde **86**(12): 814-822.
Clemens, H., Kestler, H. (2000). "Processing and Applications of Intermetallic γ-TiAl-Based Alloys." Advanced Engineering Materials **2**(9): 551-570.
Clemens, H., Lorich, A., Eberhardt, N., Glatz, W., Knabl, W., Kestler, H. (1999). "Technology, properties and applications of intermetallic γ-TiAl based alloys." Zeitschrift fuer Metallkunde/Materials Research and Advanced Techniques **90**(8): 569-580.
Clemens, H., Wallgram, W., Kremmer, S., Güther, V., Otto, A., Bartels, A. (2008). "Design of Novel β-Solidifying TiAl Alloys with Adjustable β/B2-Phase Fraction and Excellent Hot-Workability." Advanced Engineering Materials **10**(8): 707-713.
Cornish, L., Cacciamani, G., Cupid, D. M., De Keyzer, J. (2009). Aluminium-Carbon-Titanium. Refractory Metal Systems: Phase Diagrams, Crystallographic and Thermodynamic Data. G. Effenberg, Ilyenko, Svitlana, Springer-Verlag Berlin Heidelberg. **11E1**.

Couret, A., Molénat, G., Galy, J., Thomas, M. (2008). "Microstructures and mechanical properties of TiAl alloys consolidated by spark plasma sintering." Intermetallics **16**(9): 1134-1141.
Cowley, J. M., Moodie, A. F. (1957). "The scattering of electrons by atoms and crystals. I. A new theoretical approach." Acta Crystallographica **10**(10): 609-619.
Dimiduk, D. M. (1999). "Gamma titanium aluminide alloys—an assessment within the competition of aerospace structural materials." Materials Science and Engineering: A **263**(2): 281-288.
Divinski, S., Herzig, C., Klinkenberg, C. (2005). "Tracer diffusion of niobium and titanium in binary and ternary titanium aluminides." Journal of Phase Equilibria and Diffusion **26**(5): 452-457.
Djanarthany, S., Viala, J-C., Bouix, J. (2001). "Development of SiC/TiAl composites: processing and interfacial phenomena." Materials Science and Engineering: A **300**(1–2): 211-218.
Doi, M. (1992). "Coarsening Behaviour of Coherent Precipitates in Elastically Constrained Systems -With Particular Emphasis on Gamma-Prime Precipitates in Nickel-Base Alloy." Materials Transactions, JIM **33**(7): 637-649.
Doi, M., Miki, D., Moritani, T., Kozakai, T. (2004). Gamma/gamma-prime microstructure formed by phase separation of gamma-prime precipitates in a Ni-Al-Ti alloy. TMS (The Minerals, Metals & Materials Society), Superalloys 2004. K. A. Gree, Pollock, T. M., Harada, H., Howson, T. E., Reed, R. C., Schirra, J. J., Walston, S.**:** 109-114.
Doi, M., Miyazaki, T., Wakatsuki, T. (1984). "The effect of elastic interaction energy on the morphology of γ' precipitate in Ni-based alloys." Materials Science and Engineering **67**: 247-253.
Doi, M., Miyazaki, T., Wakatsuki, T. (1985). "The effects of elastic interaction energy on the γ' precipitate morphology of continuously cooled Nickel-base alloys." Materials Science and Engineering **74**: 139-145.
Du, Y.-L. (2009). "Electronic Structure and Elastic Properties of Ti_3AlC from First-Principles Calculations." Chinese Physics Letters **26**(11): 117102.
Eshelby, J. D. (1957). "The Determination of the Elastic Field of an Ellipsoidal Inclusion, and Related Problems." Proceedings of the Royal Society of London. Series A. Mathematical and Physical Sciences **241**(1226): 376-396.
Eylon, D., Keller, M. M., Jones, P. E. (1998). "Development of permanent-mold cast TiAl automotive valves." Intermetallics **6**(7–8): 703-708.
Fu, P. X., Kang, X. H., Ma, Y. C., Liu, K., Li, D. Z., Li, Y. Y. (2008). "Centrifugal casting of TiAl exhaust valves." Intermetallics **16**(2): 130-138.
Fujimoto, F. (1978). "Periodicity of crystal structure images in electron microscopy with crystal thickness." physica status solidi (a) **45**(1): 99-106.
Gabrisch, H., Stark, A., Schimansky, F. -P., Wang, L., Schell, N., Lorenz, U., Pyczak, F. (2013). "Investigation of carbides in Ti – 45Al – 5Nb – xC alloys ($0 \leqslant x \leqslant 1$) by transmission electron microscopy and high energy-XRD." Intermetallics **33**(0): 44-53.
Gebauer, K. (2006). "Performance, tolerance and cost of TiAl passenger car valves." Intermetallics **14**(4): 355-360.
Geisler, A., H. (1951). Phase Transformations in Solids. New York, John Wiley & Sons, Inc.
Gerling, R., Aust, E., Limberg, W., Pfuff, M., Schimansky, F. P. (2006). "Metal injection moulding of gamma titanium aluminide alloy powder." Materials Science and Engineering: A **423**(1–2): 262-268.
Gerling, R., Bartels, A., Clemens, H., Kestler, H., Schimansky, F. P. (2004). "Structural characterization and tensile properties of a high niobium containing gamma TiAl sheet obtained by powder metallurgical processing." Intermetallics **12**(3): 275-280.
Gerling, R., Clemens, H., Schimansky, F. P. (2004). "Powder Metallurgical Processing of Intermetallic Gamma Titanium Aluminides." Advanced Engineering Materials **6**(1-2): 23-38.

Gerling, R., Schimansky, F. P. (2002). "Prospects for metal injection moulding using a gamma titanium aluminide based alloy powder." Materials Science and Engineering A **329-331**: 45-49.
Gerling, R., Schimansky, F. P., Stark, A., Bartels, A., Kestler, H., Cha, L., Scheu, C., Clemens, H. (2008). "Microstructure and mechanical properties of Ti 45Al 5Nb+(0–0.5C) sheets." Intermetallics **16**(5): 689-697.
Gerling, R., Schimansky, F. P., Wegmann, G. (2001). "Metal Injection Moulding Using Intermetallic γ-TiAl Alloy Powder." Advanced Engineering Materials **3**(6): 387-390.
Gosslar, D., Günther, R., Hecht, U., Hartig, C., Bormann, R. (2010). "Grain refinement of TiAl-based alloys: The role of TiB2 crystallography and growth." Acta Materialia **58**(20): 6744-6751.
Gouma, P. I., Davey, S. J., Loretto, M. H. (1998). "Microstructure and mechanical properties of a TiAl-based powder alloy containing carbon." Materials Science and Engineering: A **241**(1–2): 151-158.
Gouma, P. I., Mills, M. J., Kim, Y. W. (1998). "Characterization of the precipitation process in a TiAl-based alloy with carbon and silicon additions." Philosophical Magazine Letters **78**(1): 59-66.
Gouma, P. I., Subramanian, K., Kim, Y. W., Mills, M. J. (1998). "Annealing studies of γ-titanium aluminides alloyed with light elements for creep strengthening." Intermetallics **6**(7–8): 689-693.
Guyon, J., Hazotte, A., Monchoux, J. P., Bouzy, E. (2013). "Effect of powder state on spark plasma sintering of TiAl alloys." Intermetallics **34**(0): 94-100.
Hashimoto, K., Doi, H., Kasahara, K., Tsujimoto, T., Suzuki, T. (1990). "Effect of Mn on the room-temperature/ductility of TiAl based alloy." Nippon Kinzoku Gakkai-si **54**(5): 539-548.
He, Y., Schwarz, R. B., Darling, T., Hundley, M., Whang, S. H., Wang, Z. M. (1997). "Elastic constants and thermal expansion of single crystal γ-TiAl from 300 to 750 K." Materials Science and Engineering: A **239–240**(0): 157-163.
Hecht, U., Witusiewicz, V., Drevermann, A., Zollinger, J. (2008). "Grain refinement by low boron additions in niobium-rich TiAl-based alloys." Intermetallics **16**(8): 969-978.
Herzig, C., Przeorski, T., Friesel, M., Hisker, F., Divinski, S. (2001). "Tracer solute diffusion of Nb, Zr, Cr, Fe, and Ni in γ-TiAl: effect of preferential site occupation." Intermetallics **9**(6): 461-472.
Hodge, A. M., Hsiung, L. M., Nieh, T. G. (2004). "Creep of nearly lamellar TiAl alloy containing W." Scripta Materialia **51**(5): 411-415.
Hu, D. (2001). "Effect of composition on grain refinement in TiAl-based alloys." Intermetallics **9**(12): 1037-1043.
Huang, S. C. (1991). Method of processing titanium aluminum alloys modified by chromium and niobium. U.S. **No. 5, 076, 858**.
Huang, S. C. (1993). Alloying considerations in gamma-based alloys.
Huang, S. C., Hall, E. L. (1991). "Characterization of the effect of vanadium additions to TiAl base alloys." Acta Metallurgica Et Materialia **39**(6): 1053-1060.
Huang, Z. H. (2005). "Workability and microstructure evolution of Ti–47Al–2Cr–1Nb alloy during isothermal deformation." Intermetallics **13**(3–4): 245-250.
Hubbard, C. R., Snyder,R. L. (1988). "RIR - Measurement and Use in Quantitative XRD." Powder Diffraction **3**(02): 74-77.
Iwamura, S., Miura, Y. (2004). "Loss in coherency and coarsening behavior of Al_3Sc precipitates." Acta Materialia **52**(3): 591-600.
Jabbar, H., Monchoux, J. P., Houdellier, F., Dollé, M., Schimansky, F. P., Pyczak, F., Thomas, M., Couret, A. (2010). "Microstructure and mechanical properties of high niobium containing TiAl alloys elaborated by spark plasma sintering." Intermetallics **18**(12): 2312-2321.

Jabbar, H., Monchoux, J. P., Thomas, M., Couret, A. (2011). "Microstructures and deformation mechanisms of a G4 TiAl alloy produced by spark plasma sintering." Acta Materialia **59**(20): 7574-7585.
Jha, S. C., Sanders Jr, T. H., Dayananda, M. A. (1987). "Grain boundary precipitate free zones in Al-Li alloys." Acta Metallurgica **35**(2): 473-482.
Johnson, W., Lee, JongK (1979). "Elastic interaction energy of two spherical precipitates in an anisotropic matrix." Metallurgical Transactions A **10**(8): 1141-1149.
Johnson, W. C., Voorhees, P. W. (1987). "Elastic interaction and stability of misfitting cuboidal inhomogeneities." Journal of Applied Physics **61**(4): 1610-1619.
Jovanović, M. T., Dimčić, B., Bobić, I., Zec, S., Maksimović, V. (2005). "Microstructure and mechanical properties of precision cast TiAl turbocharger wheel." Journal of Materials Processing Technology **167**(1): 14-21.
Kambe, K. (1982). "Visualization of bloch waves of high energy electrons in high resolution electron microscopy." Ultramicroscopy **10**(3): 223-227.
Kanchana, V. (2009). "Mechanical properties of Ti_3AlX (X = C, N): Ab initio study." EPL (Europhysics Letters) **87**(2): 26006.
Karadge, M., Gouma, P. I., Kim, Y. W. (2003). "Precipitation strengthening in K5-series γ-TiAl alloyed with silicon and carbon." Metallurgical and materials transactions A **34**(10): 2129-2138.
Karadge, M., Gouma, P., Kim, Y. (2003). "Precipitation strengthening in K5-series γ -TiAl alloyed with silicon and carbon." Metallurgical and materials transactions A **34**(10): 2129-2138.
Kato, M., Fujii, T., Onaka, S. (1996). "Elastic state and orientation of needle-shaped inclusions." Acta Materialia **44**(3): 1263-1269.
Kaufman, M. J., Voorhees, P. W., Johnson, W. C., Biancaniello, F. S. (1989). "An elastically induced morphological instability of a misfitting precipitate." Metallurgical Transactions A **20**(10): 2171-2175.
Kawabata, T., Fukai, H., Izumi, O. (1998). "Effect of ternary additions on mechanical properties of TiAl." Acta Materialia **46**(6): 2185-2194.
Kawabata, T., Tamura, T., Izumi, O. (1993). "Effect of Ti/Al ratio and Cr, Nb, and Hf additions on material factors and mechanical properties in TiAl." Metallurgical Transactions A **24**(1): 141-150.
Keller, M. M., Jones, P. E., Porter, W. J., Eylon, D. (1997). "The development of low-cost TiAl automotive valves." JOM **49**(5): 42-44.
Kennedy, S., Kumaran, S., Srinivasa Rao, T. (2013). "Effect of Milling on Sintering Behavior of γ-TiAl by Spark Plasma Sintering." Materials and Manufacturing Processes **28**(8): 928-932.
Kestler, H., Clemens, H. (2005). Production, Processing and Application of γ(TiAl)-Based Alloys. Titanium and Titanium Alloys, Wiley-VCH Verlag GmbH & Co. KGaA**:** 351-392.
Khachaturyan, A. G., Semenovskaya, S. V., Morris Jr, J. W. (1988). "Theoretical analysis of strain-induced shape changes in cubic precipitates during coarsening." Acta Metallurgica **36**(6): 1563-1572.
Kim, Y.-W. (1989). "Intermetallic alloys based on gamma titanium aluminide." JOM **41**(7): 24-30.
Kim, Y.-W. (1992). "Microstructural evolution and mechanical properties of a forged gamma titanium aluminide alloy." Acta Metallurgica et Materialia **40**(6): 1121-1134.
Kim, Y.-W. (1994). "Ordered intermetallic alloys, part III: Gamma titanium aluminides." JOM **46**(7): 30-39.
Kim, Y.-W. (1995). "Alloy Design of Gamma (TiAl) Alloys." Acta Metallurgica Sinica (English letters) **8**(z1): 319-328.
Kim, Y.-W. (1995). "Effects of microstructure on the deformation and fracture of γ-TiAl alloys." Materials Science and Engineering: A **192–193, Part 2**(0): 519-533.

Kim, Y.-W. (1995). "Gamma titanium aluminides: Their status and future." JOM **47**(7): 39-42.
Kim, Y.-W., Dimiduk, DennisM (1991). "Progress in the understanding of gamma titanium aluminides." JOM **43**(8): 40-47.
Krol, T., Baither, D., Nembach, E. (2004). "The formation of precipitate free zones along grain boundaries in a superalloy and the ensuing effects on its plastic deformation." Acta Materialia **52**(7): 2095-2108.
Kumpfert, J., Leyens, C. (2005). Orthorhombic Titanium Aluminides: Intermetallics with Improved Damage Tolerance. Titanium and Titanium Alloys, Wiley-VCH Verlag GmbH & Co. KGaA**:** 59-88.
Larsen, D. E., Christodoulou, L., Kampe, S. L., Sadler, R. (1991). "Investment-cast processing of XDTM near-γ titanium aluminides." Materials Science and Engineering: A **144**(1–2): 45-49.
Lee, J., Barnett, D. M., Aaronson, H. I. (1977). "The elastic strain energy of coherent ellipsoidal precipitates in anisotropic crystalline solids." Metallurgical Transactions A **8**(6): 963-970.
Lin, J. P., Zhao, L. L., Li, G. Y., Zhang, L. Q., Song, X. P., Ye, F., Chen, G. L. (2011). "Effect of Nb on oxidation behavior of high Nb containing TiAl alloys." Intermetallics **19**(2): 131-136.
Liu, C. T., Schneibel, J. H., Maziasz, P. J., Wright, J. L., Easton, D. S. (1996). "Tensile properties and fracture toughness of TiAl alloys with controlled microstructures." Intermetallics **4**(6): 429-440.
Liu, Y., Huang, B. Y., He, Y. H., Deng, Z. Y. (1998). "Heat treatment behavior of can-forged titanium aluminide alloy in (α+γ) region." Journal of Central South University of Technology **5**(2): 86-89.
Liu, Z. C., Lin, J. P., Li, S. J., Chen, G. L. (2002). "Effects of Nb and Al on the microstructures and mechanical properties of high Nb containing TiAl base alloys." Intermetallics **10**(7): 653-659.
Lu, X., He, X. B., Zhang, B., Zhang, L., Qu, X. H., Guo, Z. X. (2009). "Microstructure and mechanical properties of a spark plasma sinteredTi-45Al-8.5Nb-0.2W-0.2B-0.1Y alloy." Intermetallics **17**(10): 840-846.
Maldonado, R., Nembach, E. (1997). "The formation of precipitate free zones and the growth of grain boundary carbides in the nickel-base superalloy NIMONIC PE16." Acta Materialia **45**(1): 213-224.
Matsugi, K., Ishibashi, N., Hatayama, T., Yanagisawa, O. (1996). "Microstructure of spark sintered titanium-aluminide compacts." Intermetallics **4**(6): 457-467.
McAndrew, J. B., Kessler, H. D. (1956). "Ti-36 pct Al as a Base for High Temperature Alloys." Journal of Metals: 1348-1353.
McCullough, C., Valencia, J. J., Levi, C. G., Mehrabian, R. (1990). "Microstructural analysis of rapidly solidified Ti-Al-X powders." Materials Science and Engineering: A **124**(1): 83-101.
McQuay, P. A., Simpkins, R., Seo, D. Y., Bishop, T. R. (1999). Alloy and processimprovements for cast TiAl alloy applications. Gamma Titanium Aluminides Y.-W. Kim, Dimiduk, D. M., Loretto, M. H. San Diego, California, TMS**:** 197-207.
Menand, A., Huguet, A., Nérac-Partaix, A. (1996). "Interstitial solubility in γ and α2 phases of TiAl-based alloys." Acta Materialia **44**(12): 4729-4737.
Menand, A., Zapolsky-Tatarenko, H., Nérac-Partaix, A. (1998). "Atom-probe investigations of TiAl alloys." Materials Science and Engineering: A **250**(1): 55-64.
Merhar, J. R. (1990). "Overview of metal injection moulding." Metal Powder Report **45**(5): 339-342.
Merwe, J., Shiflet, GaryJ, Stoop, P. M. (1991). "Structural ledges in interphase boundaries." Metallurgical Transactions A **22**(6): 1165-1175.
Miyazaki, T., Doi, M. (1984). Influences of the elastic interaction energy on morphologies of gamma-prime precipitates in Ni-base alloys. Spueralloys 1984: proceedings of the Fifth International Symposium on Superalloys, Warrendale.

Miyazaki, T., Imamura, H., Kozakai, T. (1982). "The formation of "γ' precipitate doublets" in Ni-Al alloys and their energetic stability." Materials Science and Engineering **54**: 9-15.
Miyazaki, T., Imamura, H., Mori, H., Kozakal, T. (1981). "Theoretical and experimental investigations on elastic interactions between γ' -precipitates in a Ni-Al alloy." Journal of Materials Science **16**(5): 1197-1203.
Miyazawa, T., Fujii, T., Onaka, S., Kato, M. (2011). "Shape and elastic state of nano-sized Ag precipitates in a Cu–Ag single crystal." Journal of Materials Science **46**(12): 4228-4235.
Molénat, G., Thomas, M., Galy, J., Couret, A. (2007). "Application of Spark Plasma Sintering to Titanium Aluminide Alloys." Advanced Engineering Materials **9**(8): 667-669.
Monzen, R., Kitagawa, K., Miura, H., Kato, M., Mori, T. (1990). "Correlation between the boundary energy and preipitation in copper-[011] symmetric titl boundaries " J. Phys. Colloques **51**(C1): C1-269-C261-274.
Mott, N. F., Nabarro, F. R. N. (1940). "An attempt to estimate the degree of precipitation hardening, with a simple model." Proceedings of the Physical Society **52**(1): 86.
Nabarro, F. R. N. (1940). "The influence of elastic strain on the shape of particles segregating in an alloy." Proceedings of the Physical Society **52**(1): 90.
Nabarro, F. R. N. (1940). "The Strains Produced by Precipitation in Alloys." Proceedings of the Royal Society of London. Series A. Mathematical and Physical Sciences **175**(963): 519-538.
Nembach, E., Pesicka, J., Mohles, V., Baither, D., Vovk, V., Krol, T. (2005). "The effects of a second aging treatment on the yield strength of γ' -hardened NIMONIC PE16-polycrystals having γ' -precipitate free zones." Acta Materialia **53**(8): 2485-2494.
Nemoto, M., Tian, W. H., Harada, K., Han, C. S., Sano, T. (1992). "Microstructure of precipitation strengthened Ni3Al and TiAl." Materials Science and Engineering: A **152**(1–2): 247-252.
Noda, T. (1998). "Application of cast gamma TiAl for automobiles." Intermetallics **6**(7–8): 709-713.
Noda, T., Okabe, M., Isobe, S., Sayashi, M. (1995). "Silicide precipitation strengthened TiAl." Materials Science and Engineering: A **192–193, Part 2**(0): 774-779.
Oehring, M. unpublished work.
Onaka, S., Kobayashi, N., Fujii, T., Kato, M. (2002). "Simplified energy analysis on the equilibrium shape of coherent γ' precipitates in γ matrix with a superspherical shape approximation." Intermetallics **10**(4): 343-346.
Onaka, S., Kobayashi, N., Fujii, T., Kato, M. (2003). "Energy analysis with a superspherical shape approximation on the spherical to cubical shape transitions of coherent precipitates in cubic materials." Materials Science and Engineering: A **347**(1–2): 42-49.
Park, D. S., Nam, S. W. (1995). "Effect of precipitate free zones on iow cycle fatigue life of Al-Zn-Mg alloy." Materials Science and Technology **11**(9): 921-925.
Park, H. S., Hwang, S. K., Lee, C. M., Yoo, Y. C., Nam, S. W., Kim, N. J. (2001). "Microstructural refinement and mechanical properties improvement of elemental powder metallurgy processed Ti-46.6Al-1.4Mn-2Mo alloy by carbon addition." Metallurgical and Materials Transactions A **32**(2): 251-259.
Park, H. S., Nam, S. W., Kim, N. J., Hwang, S. K. (1999). "Refinement of the lamellar structure in TiAl-based intermetallic compound by addition of carbon." Scripta Materialia **41**(11): 1197-1203.
Paul, J. D. H., Appel, F., Wagner, R. (1998). "The compression behaviour of niobium alloyed γ-titanium alumindies." Acta Materialia **46**(4): 1075-1085.
Perdrix, F., Trichet, M. F., Bonnentien, J. L., Cornet, M., Bigot, J. (2001). "Relationships between interstitial content, microstructure and mechanical properties in fully lamellar Ti-48Al alloys, with special reference to carbon." Intermetallics **9**(9): 807-815.

Pietzka, M. A., Schuster, J. C. (1994). "Summary of constitutional data on the Aluminum-Carbon-Titanium system." Journal of Phase Equilibria **15**(4): 392-400.
Pineau, A. (1976). "Influence of uniaxial stress on the morphology of coherent precipitates during coarsening—elastic energy considerations." Acta Metallurgica **24**(6): 559-564.
Porter, D. A., Easterling, K. E. (1992). Crystal interfaces and microstructure. Phase transformations in metals and alloys. London, UK, Chapman & Hall, 2-6 Boundary Raw, London SEl 8HN, UK**:** 160-161.
Porter, D. A., Easterling, K. E. (1992). Diffusional transformations in solids. Phase transformations in metals and alloys. London, UK, Chapman & Hall, 2-6 Boundary Raw, London SEl 8HN, UK**:** 271-285.
Rao, K. P., Du, Y. J. (2000). "In situ formation of titanium silicides-reinforced TiAl-based composites." Materials Science and Engineering A **277**(1-2): 46-56.
Rosenbaum, H. S., Turnbull, D. (1959). "Metallographic investigation of precipitation of silicon from aluminum." Acta Metallurgica **7**(10): 664-674.
Ryum, N. (1968). "The influence of a precipitate-free zone on the mechanical properties of an Al-Mg-Zn alloy." Acta Metallurgica **16**(3): 327-332.
Schafrik, R. (1977). "Dynamic elastic moduli of the titanium aluminides." Metallurgical Transactions A **8**(6): 1003-1006.
Scheu, C., Stergar, E., Schober, M., Cha, L., Clemens, H., Bartels, A., Schimansky, F. P., Cerezo, A. (2009). "High carbon solubility in a γ-TiAl-based Ti–45Al–5Nb–0.5C alloy and its effect on hardening." Acta Materialia **57**(5): 1504-1511.
Schuster, J. C., Nowotny, H., Vaccaro, C. (1980). "The ternary systems: CrAlC, VAlC, and TiAlC and the behavior of H-phases (M_2AlC)." Journal of Solid State Chemistry **32**(2): 213-219.
Seo, D., Y., Everard, T., McQuay, P. A., Bieler, T. R. (1998). The Effect of Carbon Concentration on Primary Creep of an Investment Cast Ti-47Al-2Mn-2Nb+0.8vol%TiB_2 Alloy. Interstitial and substitutional solute effects in intermetallics. I. Baker, Noebe, R. D., George, E. P. Warrendale TMS , Warrendale 227-246.
Shastry, C. R., Judd, G. (1971). "A study of grain boundary precipitate-free zone formation in an Al−Zn−Mg alloy." Metallurgical and Materials Transactions B **2**(12): 3283-3287.
Shida, Y., Anada, H. (1993). "The influence of ternary element addition on the oxidation behaviour of TiAl intermetallic compound in high temperature air." Corrosion Science **35**(5-8): 945-953.
Shiflet, G. J., Merwe, J. H. (1991). "Misfit accommodation by steps in cubic materials." Journal of Electronic Materials **20**(7): 785-791.
Shiflet, G. J., Merwe, J. H. (1994). "The role of structural ledges as misfit- compensating defects: fcc-bcc interphase boundaries." Metallurgical and Materials Transactions A **25**(9): 1895-1903.
Simpkins II, R. J., Rourke, M. P., Bieler, T. R., McQuay, P. A. (2007). "The effects of HIP pore closure and age hardening on primary creep and tensile property variations in a TiAl XD™ alloy with 0.1wt.% carbon." Materials Science and Engineering: A **463**(1–2): 208-215.
Smarsly, W., Singheiser, L. (1994). Potential of intermetallics to replace superalloys for advanced operation conditions in gas turbines. Materials for Advanced Power Engineering, Part II. D. Coutsouradis, Wagner, R., Yamaguchi, M. . Netherlands, Kluwer Academic Publishers**:** 1731-1756.
Stadelmann, P. (1993). "Image calculation techniques." from http://www-hrem.msm.cam.ac.uk/hrem/local/ems/ImageCalculationTechniques.pdf.
Stark, A., Bartels, A., Clemens, H., Schimansky, F. P. (2008). "On the Formation of Ordered ω-phase in High Nb Containing γ-TiAl Based Alloys." Advanced Engineering Materials **10**(10): 929-934.

Staron, P., Schimansky, F. P., Scheu, C., Clemens, H. (2010). "SANS study of carbon addition in Ti-45Al-5Nb." Fall Meeting of the Materials Research Society, Mater. Res. Soc. Proc: 195-200.
Taniguchi, S., Uesaki, K., Zhu, Y. C., Zhang, H. X., Shibata, T. (1998). "Influence of niobium ion implantation on the oxidation behaviour of TiAl under thermal cycle conditions." Materials Science and Engineering A **249**(1-2): 223-232.
Terauchi, S., Teraoka, T., Shinkuma, T., Sugimoto, T. (2000). "Development of TiAl-type Intermetallic Compounds by Metal Powder Injection Molding Process." Journal of the Japan Society of Powder and Powder Metallurgy **47**(12): 1283-1287.
Tetsui, T. (1999). The effect of composition on the endurance of TiAl alloys in turbocharger applications. TMS Gamma Titatnium Aluminides. Y.-W. Kim, Dimiduk, D. M., Loretto, M. H. California**:** 15-23.
Tetsui, T. (2001). "Application of TiAl in a Turbocharger for Passenger Vehicles." Advanced Engineering Materials **3**(5): 307-310.
Tetsui, T. (2002). "Development of a TiAl turbocharger for passenger vehicles." Materials Science and Engineering: A **329–331**(0): 582-588.
Tetsui, T. (2007). Development of a second generation TiAl turbocharger. **561-565:** 379-382.
Tetsui, T., Kobayashi, T., Ueno, T., Harada, H. (2012). "Consideration of the influence of contamination from oxide crucibles on TiAl cast material, and the possibility of achieving low-purity TiAl precision cast turbine wheels." Intermetallics **31**(0): 274-281.
Tetsui, T., Ono, S. (1999). "Endurance and composition and microstructure effects on endurance of TiAl used in turbochargers." Intermetallics **7**(6): 689-697.
Tetsui, T., Shindo, K., Kaji, S., Kobayashi, S., Takeyama, M. (2005). "Fabrication of TiAl components by means of hot forging and machining." Intermetallics **13**(9): 971-978.
Tetsui, T., Shindo, K., Kobayashi, S., Takeyama, M. (2003). "Strengthening a high-strength TiAl alloy by hot-forging." Intermetallics **11**(4): 299-306.
Tian, W. H., Nemoto, M. (1995). Strengthening of γ-TiAl by carbide and nitride precipitation.
Tian, W. H., Nemoto, M. (1997). "Effect of carbon addition on the microstructures and mechanical properties of γ-TiAl alloys." Intermetallics **5**(3): 237-244.
Tian, W. H., Sano, T., Nemoto, M. (1993). "Structure of perovskite carbide and nitride precipitates in $L1_0$-ordered TiAl." Philosophical Magazine A **68**(5): 965-976.
Tolley, A., Mitlin, D., Radmilovic, V., Dahmen, U. (2005). "Transmission electron microscopy analysis of grain boundary precipitate-free-zones (PFZs) in an AlCuSiGe alloy." Materials Science and Engineering: A **412**(1–2): 204-213.
Unwin, P. N. T., Lorimer, G. W., Nicholson, R. B. (1969). "The origin of the grain boundary precipitate free zone." Acta Metallurgica **17**(11): 1363-1377.
Unwin, P. N. T., Nicholson, R. B. (1969). "The nucleation and initial stages of growth of grain boundary precipitates in Al-Zn-Mg and Al-Mg alloys." Acta Metallurgica **17**(11): 1379-1393.
Voisin, T., Monchoux, J.-P., Clemens,H., Couret, A. (2013). "First Investigations on a TNM TiAl Alloy Processed by Spark Plasma Sintering." MRS Online Proceedings Library **1516**: 17-22.
Vojtěch, D., Popela, T., Kubásek, J., Maixner, J., Novák, P. (2011). "Comparison of Nb- and Ta-effectiveness for improvement of the cyclic oxidation resistance of TiAl-based intermetallics." Intermetallics **19**(4): 493-501.
Wang, L., Liu, Y., Zhang, W., Wang, H., Li, Q. (2011). "Optimization of pack parameters for hot deformation of TiAl alloys." Intermetallics **19**(1): 68-74.
Watanabe, D., Watanabe, C., Monzen, R. (2008). "Effect of coherency on coarsening of second-phase precipitates in Cu-base alloys." Journal of Materials Science **43**(11): 3946-3953.
Watanabe, D., Watanabe, C., Monzen, R. (2009). "Determination of the interface energies of spherical, cuboidal and octahedral face-centered cubic precipitates in Cu–Co, Cu–Co–Fe and Cu–Fe alloys." Acta Materialia **57**(6): 1899-1911.

Wei, Z. J., Wang, H. W., Jin, Y. Y., Zhang, H., Zeng, S. Y. (2002). "Microstructures and mechanical properties of as-cast TiAl alloys with higher C additions." Journal of Materials Science **37**(9): 1809-1812.
Whang, S. H., Li, Z. X. (1988). "Tetragonal distortion and its relaxation in rapidly quenched L10 TiAl compounds." Materials Science and Engineering **98**(0): 269-272.
Williams, D., Carter, C. B. (2009). Image Simulation. Transmission Electron Microscopy, Springer US**:** 533-548.
Woodward, C., MacLaren, J. M., Dimiduk, D. M. (1992). "Energy of Planar Faults as a Function of Composition in Binary and Ternary Tial Alloys." MRS Online Proceedings Library **288**: null-null.
Worth, B., Jones, J., Allison, J. (1995). "Creep deformation in near-γ TiAl: II. influence of carbon on creep deformation in Ti-48Al-1V-0.3C." Metallurgical and materials transactions A **26**(11): 2961-2972.
Worth, B. D., Jones, J. W., Allison, J. E. (1995). "Creep deformation in near-γ TiAl: II. influence of carbon on creep deformation in Ti-48Al-1V-0.3C." Metallurgical and materials transactions A **26**(11): 2961-2972.
Wrzesinski, W. R., Rawers, J. C. (1990). "Self-propagating high-temperature synthesis of TiAl-SiC and TiAl-Al2O3 intermetallic composites." Journal of Materials Science Letters **9**(4): 432-435.
Wu, H., Cui, X. P., Geng, L., Fan, G. H., Pang, J. C., Wei, L. S. (2013). "Fabrication and characterization of in-situ TiAl matrix composite with controlled microlaminated architecture based on SiC/Al and Ti system." Intermetallics **43**(0): 8-15.
Wu, Y., Park, Y. W., Park, H. S., Hwang, S. K. (2003). "Microstructural development of indirect-extruded TiAl-Mn-Mo-C intermetallic alloys during aging." Materials Science and Engineering A **347**(1-2): 171-179.
Xiao, S. Q., Foitzik, A. H., Pirouz, P., Heuer, A. H. (1992). "Heterogeneous nucleation of Ti_2AlC precipitates at TiAl grain boundaries." physica status solidi (a) **131**(2): 333-344.
Yamaguchi, M., Inui, H., Ito, K. (2000). "High-temperature structural intermetallics." Acta Materialia **48**(1): 307-322.
Yamauchi, H., De Fontaine, D. (1979). "Elastic interaction of defect clusters with arbitrary strain fields in an anisotropic continuum." Acta Metallurgica **27**(5): 763-776.
Yoshihara, M., Miura, K. (1995). "Effects of Nb addition on oxidation behavior of TiAl." Intermetallics **3**(5): 357-363.
Yuan, Y., Liu, H. W., Zhao, X. N., Meng, X. K., Liu, Z. G., Boll, Torben, Al-Kassab, Talaat (2006). "Dissociation of super-dislocations and the stacking fault energy in TiAl based alloys with Nb-doping." Physics Letters A **358**(3): 231-235.
Yun, J. H., Oh, M. H., Nam, S. W., Wee, D. M., Inui, H., Yamaguchi, M. (1997). "Microalloying effects in TiAl+Mo alloys." Materials Science and Engineering: A **239–240**(0): 702-708.
Zhang, H., He, Xinbo, Qu, Xuanhui, Zhao, Liming (2009). "Microstructure and mechanical properties of high Nb containing TiAl alloy parts fabricated by metal injection molding." Materials Science and Engineering: A **526**(1–2): 31-37.
Zhang, W. J., Appel, F. (2002). "Weak-beam TEM study on planar fault energies of Al-lean TiAl-base alloys." Materials Science and Engineering: A **334**(1–2): 59-64.
Zhang, W. J., Deevi, S. C., Chen, G. L. (2002). "On the origin of superior high strength of Ti-45Al-10Nb alloys." Intermetallics **10**(5): 403-406.
Zhang, X., Wang, Xiaohui, Li, Fangzhi, Zhou, Yanchun (2009). "Mechanical and Thermal Properties of Antiperovskite Ti_3AlC Prepared by an In Situ Reaction/Hot-Pressing Route." Journal of the American Ceramic Society **92**(11): 2698-2703.
Zou, X. D., Hovmöller, S., Oleynikov, P. (2012). Simulation of images and electron diffraction patterns. Electron Crystallography: Electron Microscopy and Electron Diffraction, Oxford Scholarship Online**:** 245-253.

Appendix

List of figures

Figure 50 Weight fraction of the α_2-Ti_3Al phase determined using Rietveld analysis of HEXRD patterns of the Solution Treated & Annealed (a) Ti-45Al-5Nb-0.5C and (b) Ti-45Al-5Nb-0.75C alloys after solution treatment at 1250°C for 5h (OQ) and subsequent annealing at 800, 900 and 1000°C (FC). The data is connected by guiding spline lines. **P54**

Figure 51 Lattice parameters of (a) γ and (b) α_2 phases determined using Rietveld analysis of HEXRD patterns from the HIPed & Annealed Ti-45Al-5Nb-0.5C alloy after annealing at 800 and 900°C for 0 (HIPed condition), 24, 48, 96 and 168h, and at 1000°C for 0 (HIPed condition), 24, 48 and 96h. The data is connected by guiding spline lines. The error bar cannot be seen due to its small value. **P55**

Figure 52 Lattice parameters of (a) γ and (b) α_2 phases obtained using Rietveld analysis of HEXRD patterns from the HIPed & Annealed Ti-45Al-5Nb-0.75C alloy after annealing at 800, 900 and 1000°C for 0 (HIPed condition), 24, 48, 96 and 168h respectively. The data is connected by guiding spline lines. The error bar cannot be seen due to its small value. **P56**

Figure 53 Lattice parameters of (a) γ phase and (b) α_2 phases obtained using Rietveld analysis of HEXRD patterns from the Solution Treated & Annealed Ti-45Al-5Nb-0.5C alloy after solution treatment at 1250°C for 5h (OQ) and subsequent annealing at 800, 900 and 1000°C for 24, 48, 96 and 168h, and at 800°C for 1104h. The data is connected by guiding spline lines. The error bar cannot be seen due to its small value. **P58**

Figure 54 Lattice parameters of (a) γ and (b) α_2 phases obtained using Rietveld analysis of HEXRD patterns from the Solution Treated & Annealed Ti-45Al-5Nb-0.75C alloy after solution treatment at 1250°C for 5h (OQ) and subsequent annealing at 800, 900 and 1000°C for 24, 48, 96 and 168h, and at 800°C for 1054h. The data is connected by guiding spline lines. The error bar cannot be seen due to its small value. **P59**

Figure 55 P-type carbides in the HIPed & Annealed Ti-45Al-5Nb-0.5C alloy (a) at triple junctions after annealing at 800°C for 48h, (b) diffraction pattern of (a), (c) at grain boundaries with faceted shape after 800°C for 48h, (d) and (e) at dislocations after annealing at 800°C for 96h, (e) recorded using the $\boldsymbol{g}/3\boldsymbol{g}$ condition: $\boldsymbol{g}$=110, near the $[001]_\gamma$ direction, dislocations are out of contrast and carbides show "coffee bean" contrast, (f) is the $\boldsymbol{g}/3\boldsymbol{g}$ condition of (e), (g) at nodes of dislocation networks after annealing at 800°C for 168h, carbides show moiré fringes, (h) in the γ matrix with a rod-like shape after 800°C for168h, image was recorded using $\boldsymbol{g}$=0-10_P in two-beam condition and (i) diffraction pattern in the $[100]_\gamma$ direction. All TEM images have the same scale bar. **P63**

Figure 56 P-type carbides in the HIPed & Annealed Ti-45Al-5Nb-0.5C alloy (a) at dislocations after annealing at 900°C for 24h, (b) in TEM bright field, (c) in TEM dark field in the γ matrix both after annealing at 900°C for 48h, recorded using $\boldsymbol{g}$=$\mathbf{0\text{-}10_P}$ in two-beam condition, (d) at triple junctions after 900°C for 168h, carbides coarsen and lose crystallographic relationship with the γ matrix, (e) and (f) diffraction patterns of P and γ phases in (d) respectively. All TEM images have the same scale bar. **P64**

Figure 57 P-type carbides in the HIPed & Annealed Ti-45Al-5Nb-0.75C alloy after annealing at 800°C for 24h (a) at a triple junction, (b) at a grain boundary, (c) diffraction pattern of (d), (d) in the γ matrix viewed from the $[100]_\gamma$ direction showing needle-like projections, (e) diffraction pattern in the $[001]_\gamma$ direction, (f) in the γ matrix and at dislocations viewed from the $[001]_\gamma$ direction, enlarged image inset showing Ashby and Brown contrast, (g) dark field image of (f), recorded using a $\boldsymbol{g}/3\boldsymbol{g}$ condition, $\boldsymbol{g}$=010_P, showing dot-like projections. All TEM images have the same scale bar. **P66**

List of tables

Publications and conferences

Publications for this work

Preparing a paper on “Precipitation and Thermal Stability of Carbides in High Nb Containing TiAl Alloys”

Preparing a paper on “Carbide Morphology Development in High Nb containing TiAl alloys”

Heike Gabrisch, Andreas Stark, Frank-Peter Schimansky, Li Wang, Norbert Schell, Uwe Lorenz, Florian Pyczak. Investigation of carbides in Ti-45Al-5Nb-xC alloys by transmission electron microscopy and high energy-XRD. Intermetallics, 33 (2013) 44-53.

Conferences for this work

Nov. 2012: 2012 MRS Fall Meeting, Boston, USA

Presentation: Investigation on Carbon Solubility and Carbide Precipitation in Ti-45Al-5Nb-xC alloys

Sept. 2012: Materials Science and Engineering, Darmstadt, Germany

Oral Poster: Carbon solubility and thermal stability of carbides in high Nb containing TiAl alloys

“The Best Poster in Intermetallics Symposium”

Jun. 2012: Gamma (TiAl) alloy Technology, Beijing, China

Poster and presentation: The carbon solubility and carbide precipitation in high Nb containing TiAl alloys

Sept. 2011: 4th International Workshop on Titanium Aluminides, Nuremberg, Germany